Synthesis and characterisation of nanofibre supports for platinum as electrodes for polymer electrolyte fuel cells

Iuliia Maciejasz

Collège Doctoral du Languedoc-Roussillon

THÈSE

Pour obtenir le grade de

Docteur

Délivré par **l'Université Montpellier 2**
Sciences et Techniques du Languedoc

Préparée au sein de l'école doctorale
Sciences Chimiques Balard
Et de l'unité de recherche **UMR5253**

Spécialité: **Chimie et Physicochimie des Matériaux**

Présentée par **Iuliia SAVYCH MACIEJASZ**

SYNTHESE ET CARACTERISATION DE NANOCOMPOSITES PLATINE/NANOFIBRES POUR ELECTRODES DE PILES A COMBUSTIBLE A ELECTROLYTE POLYMERE

16 Juillet 2014

M. N. ALONSO-VANTE, Professeur, Université de Poitiers	**Rapporteur**
M. P. KULESZA, Professeur, Université de Varsovie	**Rapporteur**
M. J. ROZIÈRE, Professeur, UM 2	**Directeur de thèse**
Mme S. CAVALIERE, Maître de conférences, UM 2	**Co-Directeur**
Mme D. J. JONES, Directeur de Recherche, UM 2	**Examinateur**
M. J. J. ZAJĄC, Professeur, UM 2	**Président du jury**
M. P. KNAUTH, Professeur, Aix-Marseille Université	**Examinateur**
Mme M. L. DI VONA, Professeur, Université de Rome	**Examinateur**

UNIVERSITÉ MONTPELLIER 2
SCIENCES ET TECHNIQUES

Collège Doctoral du Languedoc-Roussillon

THÈSE

Pour obtenir le grade de

Docteur

Delivered by University of Montpellier 2

Prepared within the doctoral school
Sciences Chimiques Balard
and the research unit **UMR5253**

Specialty: **Chemistry and Physicochemistry of Materials**

Presented by **Iuliia SAVYCH MACIEJASZ**

SYNTHESIS AND CHARACTERISATION OF NANOFIBRE SUPPORTS FOR PLATINUM AS ELECTRODES FOR POLYMER ELECTROLYTE FUEL CELLS

16 July 2014

M. N. ALONSO-VANTE, Professor, University of Poitiers	**Reviewer**
M. P. KULESZA, Professor, University of Warsaw	**Reviewer**
M. J. ROZIÈRE, Professor, UM 2	**Supervisor**
Mme S. CAVALIERE, Lecturer, UM 2	**Co-Supervisor**
Mme D. J. JONES, Research Director, UM 2	**Examiner**
M. J. J. ZAJĄC, Professor, UM 2	**President of the jury**
M. P. KNAUTH, Professor, Aix-Marseille University	**Examiner**
Mme M. L. DI VONA, Professor, University of Rome	**Examiner**

UNIVERSITÉ MONTPELLIER 2
SCIENCES ET TECHNIQUES

À mon mari !
To my husband!
Mojemu mężowi!

ACKNOWLEDGEMENTS

I would like to thank one of my supervisors, Prof. Jacques Rozière for the scientific discussions during my PhD thesis. I am highly impressed by his vast knowledge in the field of fuel cells and original strategies of solving many scientific problems.

I would like to acknowledge my co-supervisor, Dr Sara Cavaliere for her encouragement and her time that she gave very generously to discuss with me scientific issues, and to check my thesis, scientific publications and oral presentations.

My special thanks goes to Dr Deborah Johnes, the director of research, who gave me the opportunity to work on such an interesting topic and to participate in the Marie Curie program. She believed in my ideas and gave me the possibility to work independently. All this helped me to solve research problems and to become self-confident and independent researcher.

I would like to thank all the members of the jury for reading my PhD thesis and being present during my public defense for the Ph.D. degree. In particular, I would like to thank Prof. Kulesza and Prof. Alonso-Vante for their positive reports. Also I would like to thank president of the committee Prof. Zając and the examiners Prof. Knauth and Prof. Di Vona. Last but not lease, I would like to thank the members of my research committee Dr. D. Jones, Prof. J. Rozière and Dr. S. Cavaliere, without whose guidance the completion of this thesis would not be possible.

I would like to say thank you to my colleagues Ganna, Tahra, Vanessa, Rakhi, Kristina, Anna, Christoph, Álvaro, Stefano, Surya, Elia, Paul, Visot, Yannick, Aurélien, Pierre, Najib, Giorgio, Kahlil, Marcus, Adam, Bernard, Laura, Philippe, Marta, Anita, Nikolas, Vincent, Julien, Marie and all the members of the AIME team for their support and good time that I have spent with them.

A special thanks for Marc, Nicolas and Julien for their help with the single fuel cell testing. Also, for David and José for their help with Raman analysis and Didier Cot for his help with obtaining SEM images. I would like also to acknowledge Frédéric for helping me with understanding various electrochemistry problems and Vanessa for English proofreading of my thesis.

Thanks to Cathy and Tatyana for their help with all the administrative issues.

I would like to thank my parents, my sister and whole my family, all my friends and my husband, whom I love a lot, for their love and support.

Contents

List of acronyms

AFC	- Alkaline fuel cell
ATO	- Sb doped tin oxide
BET	- Brunauer–Emmett–Teller
CCM	- Catalyst coated membrane
CCS	- Catalyst coated substrate
CL	- Catalyst layer
CNFs	- Carbon nanofibres
CNTs	- Carbon nanotubes
CVD	- Chemical vapour deposition
DFT	- Density Functional Theory
DMF	- Dimethylformamide
DMFC	- Direct methanol fuel cell
DOE	- Department of Energy
ECSA	- Electrochemical surface area
EDX	- Energy-dispersive X-ray spectroscopy
EOR	- Ethanol oxidation reaction
FC	- Fuel cell
FWHM	- Full width of high maximum
GDE	- Gas diffusion electrode
GDL	- Gas diffusion layer
HT-PEMFC	- High-temperature proton exchange membrane fuel cell
ITO	- Indium tin oxide
LSV	- Linear sweep voltammetry
MCFC	- Molten carbonate fuel cell
MEA	- Membrane electrode assembly
MOR	- Methanol oxidation reaction
MWCNTs	- Multi-wall carbon nanotubes
NSTF	- Nanostructured thin-films
OCV	- Open circuit voltage
OMC	- Ordered mesoporous carbon
ORR	- Oxygen reduction reaction
PAFC	- Phosphoric acid fuel cell

PAN	- Polyacrylonitrile
PBI	- Polybenzimidazole
PCFC	- Protonic Ceramic fuel cell
PEM	- Proton exchange membrane or Polymer electrolyte membrane
PEMFC	- Proton exchange membrane fuel cell or Polymer electrolyte membrane fuel cell
PFSA	- Perfluorosulfonic acid
PTFE	- Polytetrafluoroethylene
PVA	- Polyvinyl alcohol
PVP	- Polyvinyl pyrrolidone
RDE	- Rotating disc electrode
RH	- Relative humidity
RHE	- Reversible hydrogen electrode
RRDE	- Rotating ring disc electrode
SEM	- Scanning electron microscope
SMSI	- Strong metal support interactions
SOFC	- Solid oxide fuel cell
SWCNTs	- Single-wall carbon nanotubes
TGA	- Thermogravimetric analysis
TEM	- Transmission electron microscope
TNFs	- Titania nanofibers
TONT	- Titanium oxide nanotubes
XPS	- X-ray photoelectron spectroscopy
XRF	- X-ray fluorescence

Une Version Abrégée en Français

sur

la thèse

de

SYNTHESE ET CARACTERISATION DE NANOCOMPOSITES PLATINE/NANOFIBRES POUR ELECTRODES DE PILES A COMBUSTIBLE A ELECTROLYTE POLYMERE

CHAPITRE 1: Contexte et motivation

Introduction

L'utilisation de combustibles fossiles (pétrole et gaz) a engendré un impact négatif sur l'environnement comme le réchauffement climatique (en raison de l'émission de dioxyde de carbone) et la pollution (due au monoxyde de carbone et aux oxydes d'azote). Avec la croissance de la population mondiale, la demande d'énergie augmentera également, ce qui entraînera une diminution des réserves de pétrole et de gaz. Par conséquent, l'utilisation de sources d'énergie renouvelable est nécessaire.

Le remplacement des combustibles fossiles par des sources d'énergie renouvelables est très attrayant, mais il y a toujours le problème concernant le stockage de l'énergie produite. L'énergie peut être stockée sous forme d'hydrogène, produit par électrolyse, et ensuite convertie en énergie électrique grâce à la technologie des piles à combustible. Une pile à combustible est une pile qui convertit l'énergie chimique en énergie électrique par l'oxydation du combustible. Il existe plusieurs types de piles à combustible. Parmi eux, les cellules à combustible à membrane électrolyte polymère (PEMFC) offrent plusieurs avantages tels que de fortes densités de courant et le démarrage/arrêt rapide en raison des températures de fonctionnement relativement basses. De plus, elles sont des convertisseurs d'énergie propre, n'émettant pas de dioxyde de carbone. Tous ces atouts rendent l'utilisation des PEMFC idéale pour une variété d'applications telles que le transport, le stationnaire et les appareils électroniques portables.

L'assemblage membrane-électrode (AME) est le cœur de la PEMFC, composé d'une membrane conductrice de protons placée entre deux électrodes. L'hydrogène est fourni du côté anode, où il est décomposé sur la surface de platine en protons et électrons. Les protons migrent à travers la membrane à la cathode, tandis que les électrons se déplacent le long d'un circuit électrique extérieur vers la cathode, où ils réagissent avec l'oxygène. L'eau est le seul produit formé en milieu acide pendant cette réaction. Les couches catalytiques aux électrodes sont constituées de nanoparticules de catalyseur (par exemple platine) déposées sur un support de noir de carbone mélangé avec un ionomère. Un support de catalyseur performant doit fournir une conductivité électrique élevée, une grande surface spécifique et une porosité adéquate pour obtenir une dispersion homogène du catalyseur et une grande résistance à la corrosion. Les noirs de carbone sont actuellement utilisés en tant que supports en raison de leur conductivité élevée et de leur grande surface développée. Cependant, ils se corrodent en particulier en phase de

démarrage et d'arrêt, ce qui se traduit par l'agglomération et la perte des nanoparticules de platine. Le carbone est oxydé à hauts potentiels, et la dissolution des nanoparticules de platine se produit à des potentiels supérieurs à 0,6 V. De plus, la corrosion de carbone à niveau local peut conduire à l'effondrement de la structure de l'électrode poreuse, qui est responsable des pertes de performance. La courte durée de vie de l'AME est l'un des principaux obstacles pour la commercialisation des PEMFC.

Par conséquent, d'autres supports carbonés ayant une meilleure stabilité électrochimique (tel que le noir de carbone graphitisé, les nanofibres et les nanotubes de carbone) sont en cours d'étude. Cependant, la corrosion du carbone ne peut pas être complètement évitée. Par conséquent, des supports céramiques tels que des oxydes, des carbures et nitrures suscitent beaucoup d'attention en tant que supports alternatifs. Selon des calculs thermochimiques et des mesures expérimentales, l'oxyde de titane et l'oxyde d'étain sont stables dans les conditions de fonctionnement de PEMFC. Par conséquent, ce travail est axé sur le développement d'oxyde de titane et d'oxyde d'étain en tant que supports pour nanoparticule de platine dans les PEMFC.

Filage électrostatique

Au cours des dernières décennies, les nanostructures monodimensionnelles ont suscité un grand intérêt en raison de leurs propriétés électriques, optiques, catalytiques et mécaniques exceptionnelles. Il existe plusieurs méthodes pour la fabrication de fibres et de tubes tels que le dépôt chimique en phase vapeur, la synthèse hydrothermale et assistée par les micro-ondes etc. Cependant, elles nécessitent généralement de conditions strictes ou de procédures en plusieurs étapes. En revanche, le filage électrostatique est une méthode simple qui permet d'obtenir des matériaux de différente composition (fibres organiques, céramiques, hybrides et métalliques), et morphologie (nanofibres, nanotubes, fibres creuses à canaux multiples). En outre, il permet de préparer des structures 1D continues avec des diamètres uniformes.

Le système de filage électrostatique se compose d'une source de haute tension, d'un collecteur, d'un pousse-seringue et d'une seringue. Quand une haute tension est appliquée à une goutte de liquide, elle se charge et prend une forme conique en raison de la répulsion électrostatique (ce qu'on appelle le cône de Taylor). Si la force électrostatique dépasse la tension superficielle et la force viscoélastique, un jet liquide se forme à partir d'une solution de polymère. Ce jet liquide est soumis à un processus d'allongement et amincissement, pendant lequel le solvant s'évapore. Enfin, un tissu de fibres est déposé sur le collecteur.

Objectif de la thèse

Dans ce travail, des nanofibres de carbone, TiO_2 et SnO_2 ont été préparées par la technique de filage électrostatique. Afin d'améliorer la conductivité électronique et la surface spécifique de TiO_2 et SnO_2, différents traitements thermiques et le dopage avec un hétéroatome (Nb) ont été mis en œuvre. Les propriétés des supports de catalyseur obtenus ont été caractérisées par la diffraction des rayons X (DRX), la spectroscopie de photoélectrons X (XPS), la spectroscopie Raman, les mesures de surface spécifique, les mesures de conductivité électronique, la microscopie électronique à balayage (MEB) et la microscopie électronique à transmission (MET). Ensuite des nanoparticules de platine ont été obtenues par la méthode polyol assistée par les micro-ondes et déposées sur les fibres et les tubes. L'influence de tels supports sur l'activité catalytique et la stabilité a été évaluée en utilisant une électrode à disque tournant. Le meilleur électrocatalyseur (Pt sur SnO_2 dopé par Nb) a été caractérisé in situ dans une monocellule de pile à combustible à électrolyte polymère.

CHAPITRE 2: Nanofibres de carbone

Nanofibres de carbone

Les nanofibres de carbone graphitisé sont largement étudiées en tant que supports de catalyseur pour PEMFC en raison de leur résistance à la corrosion plus élevée et leur conductivité. Cependant, une graphitisation à des températures très élevées provoque une diminution de la surface spécifique, ce qui ne permet pas d'atteindre la dispersion élevée et la forte interaction avec le catalyseur métallique qui caractérisent les supports conventionnels tels que le noir de carbone.

Dans ce travail, les nanofibres de carbone (CNF) ont été obtenus par filage électrostatique d'une solution de polyacrylonitrile (PAN) (voir la Figure 1). La carbonisation a été réalisée à trois températures différentes (700 - 100 - 1500 °C). Les échantillons obtenus ont été caractérisés par la spectroscopie Raman, les mesures de surface spécifique, les mesures de conductivité électronique et la microscopie électronique à balayage.

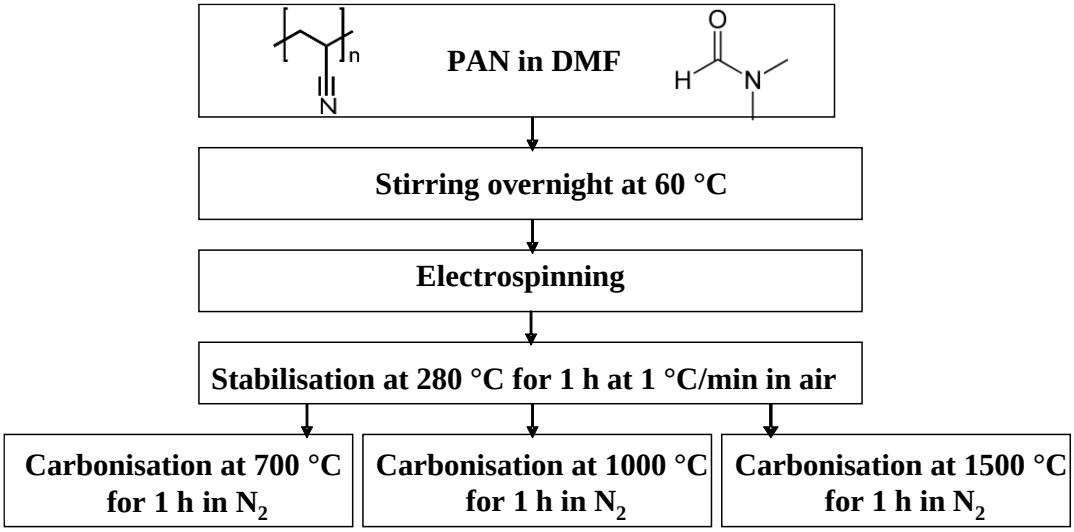

Figure 1 : Représentation schématique du protocole de synthèse des fibres de carbone par filage électrostatique.

Les propriétés des fibres de carbone sont résumées dans le Tableau 1. Le degré de graphitisation et la conductivité électronique augmentent avec la température de carbonisation, tandis que la surface spécifique diminue. CNF_{1000} et CNF_{1500} ont été choisis pour la caractérisation électrochimique en raison de leur conductivité électrique élevée par rapport à celle des CNF_{700}.

Tableau 1 : Rapport bande D / bande G, la conductivité électronique, la surface spécifique des fibres de carbone.

Température de carbonisation	**700 °C**	**1000 °C**	**1500 °C**
Rapport des bandes D/G	2.2	1.7	0.9
Conductivité électronique, S/cm	0.0012	6.2	10
Surface spécifique, m^2/g	262	36	20

Stabilité électrochimique

Le test de corrosion accélérée a été réalisé à 1,4 V vs. *ERH* (électrode réversible à hydrogène) pendant 2 h à 80 °C dans H_2SO_4, 0,5 M, afin d'évaluer la stabilité électrochimique des fibres de carbone. Les courants de corrosion mesurés pour CNF_{1000}, CNF_{1500} et Vulcan XC-72R en fonction du temps sont présentés dans la Figure 2. Les courants de corrosion intégrés pour CNF_{1000}, Vulcan XC-72R et CNF_{1500} ont des valeurs de 5,6 et 3,9 et 1,4 C / mg, respectivement, indiquant une meilleure résistance à la corrosion de CNF_{1500} attribuée à son degré élevé de graphitisation.

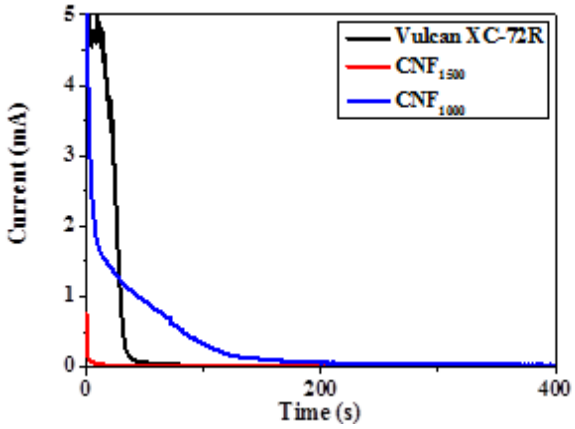

Figure 2 : Courant d'oxydation en fonction du temps pour CNF_{1000}, CNF_{1500} et Vulcan XC-72R à 1,4 V vs. EDH, 80 °C dans une solution de H_2SO_4 0,5 M.

CHAPITRE 3: Dioxyde de titane

Le dioxyde de titane est un matériau prometteur en tant que support en raison de sa stabilité électrochimique élevé et de fortes interactions avec le catalyseur métallique. Cependant, sa faible conductivité électrique est l'une des principales limitations dans son application à la pile à combustible. Ainsi, pour faire face à ce problème, deux stratégies ont été utilisées, le dopage par des ions métalliques d'une part et le traitement à haute température en présence de H_2 d'autre part. Les phases de Magneli obtenues à haute température (≥ 1000 °C) possèdent des conductivités électroniques très élevée. Cependant, en général, elles présentent de très faibles surfaces spécifiques (de l'ordre de 1 m^2 / g), ce qui n'est pas assez élevé pour être utilisé comme support de catalyseur. Par conséquent, une température relativement basse de réduction de 800 °C a été choisie pour obtenir un compromis entre la conductivité élevée et une grande surface spécifique.

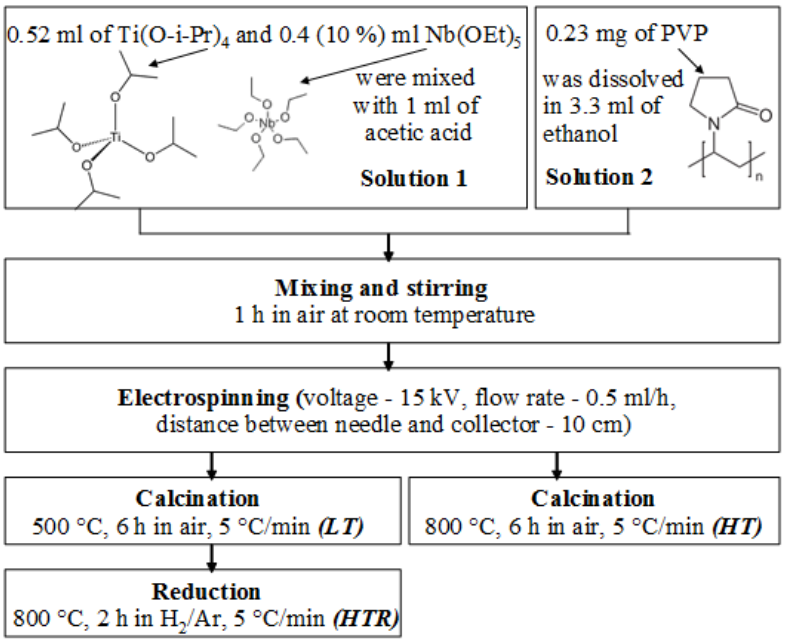

Figure 3 : Etapes de synthèse des nanofibres d'oxyde de titane.

Synthèse et caractérisation de nanofibres d'oxyde de titane

Afin de préparer des fibres d'oxyde de titane, l'isopropoxyde de titane a été mélangé avec la solution de polymère (polyvinylpyrrolidone - PVP) qui a été utilisée pour augmenter la viscosité de la solution. L'acide acétique a été ajouté à la solution pour la stabiliser en empêchant l'hydrolyse totale de l'isopropoxyde de titane avant le filage électrostatique. Les

fibres ainsi préparées ont été calcinés à l'air à 500 °C ou à 800 °C à 5 °C / min pendant 6 heures afin d'éliminer le polymère. Les fibres calcinées à 500 °C et à 800 °C sont indiquées comme LT (basse température) et HT (haute température), respectivement (Figure 3). L'échantillon réduit à 800 °C a été nommé HTR (réduction à haute température). Les nanofibres LT et HT sont blanches, tandis que HTR sont de couleur bleue, ce qui suggère la présence de Ti^{3+}.

Les valeurs de conductivité de pastilles (obtenus par pressage d'échantillons LT) réduites à 800 °C sous atmosphère d'Ar/H_2 sont rassemblées dans le Tableau 2. Après un tel traitement thermique, la conductivité augmente de ~ 10^{-9} S/cm pour LT à ~ 10^{-3} S/cm pour HTR. L'augmentation de conductivité est probablement due à la présence de Ti^{3+} à la surface des nanofibres de TiO_2, détectée par l'analyse XPS.

Enfin, la conductivité de 10^{-5} S/m pour l'échantillon non dopé, atteint ~ 10^{-3} S/m pour l'échantillon HTR dopé par Nb.

Tableau 2 : Valeurs de conductivité électrique des nanofibres de TiO_2 HTR avec différentes concentrations de Nb.

$\%_{at}$ Nb	**0**	**5**	**10**	**20**
σ (S/cm)	$2{\cdot}10^{-5}$	$2{\cdot}10^{-3}$	$5{\cdot}10^{-3}$	$1{\cdot}10^{-3}$

Afin d'estimer la surface spécifique, des isothermes d'adsorption/désorption d'azote ont été établies pour les nanofibres LT, HT et HTR (Figure 4). L'isotherme de l'échantillon LT présente une hystérésis, qui est typique des matériaux mésoporeux (isotherme de type IV). Les isothermes des échantillons préparés à haute température, HT et HTR, ont montré une diminution de l'adsorption de l'azote. En effet, les traitements à haute température conduisent à la disparition des pores et à la diminution de la rugosité de la surface en raison de l'agglomération des grains. Par conséquent, la surface spécifique diminue après réduction à 800 °C de 65 à 16 m^2 / g pour 10 at. % Nb dopé TiO_2 (Figure 4).

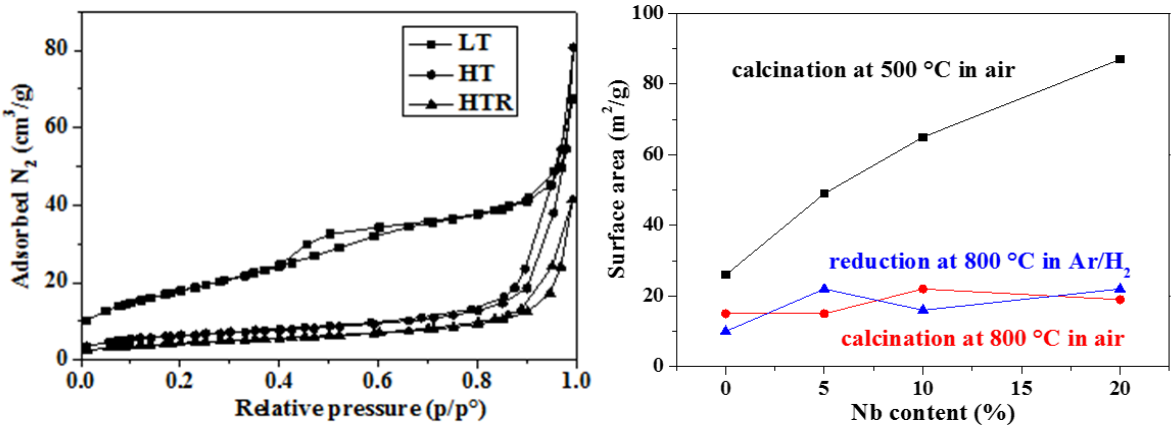

Figure 4 : Isothermes d'adsorption-désorption d'azote obtenues pour les nanofibres LT, HT et HTR (à gauche); Valeurs de surface spécifique en fonction de la teneur en Nb en fibres de TiO_2 (à droite).

Parmi les différents échantillons d'oxyde de titane dopé au niobium, celui réduit à haute température (HTR) et contenant 10 at. % de Nb présente la conductivité électronique la plus élevée. Par conséquent, cet échantillon (nommé nanofibres d'oxyde de titane - TNF) a été sélectionné pour le dépôt de nanoparticules de platine et la caractérisation électrochimique.

Synthèse de Pt/TNF

Les nanoparticules de platine ont été préparées par la méthode polyol assistée par les micro-ondes (Figure 5). Dans ce procédé, l'éthylène glycol joue le rôle de solvant, réducteur et stabilisant des nanoparticules de platines. L'hydroxyde de sodium a été ajouté jusqu'à ce que le pH 11.5, afin d'augmenter la concentration de l'anion glycolate après réduction. Ce dernier peut stabiliser les nanoparticules en formant des complexes chélates à la surface du platine par l'intermédiaire de leurs groupes carboxyliques. Le temps de réaction a été diminué de 2 heures à 6 min à l'aide du réacteur à micro-ondes. L'acide sulfurique a été ajouté aux nanoparticules de platine jusqu'à ce que le pH soit devenu 2, afin d'éviter la répulsion électrostatique entre les nanoparticules de platine et l'oxyde de titane.

Les nanoparticules de platine déposées sur les TNF et le carbone Vulcan XC-72R (support commercial) sont présentées dans la Figure 6. Les particules de platine sont dispersées de façon moins homogène sur les TNF que sur le Vulcan XC-72R. Leur diamètre moyen est de 2,3 nm pour Pt/TNF et 2,4 nm pour Pt/Vulcan XC-72R.

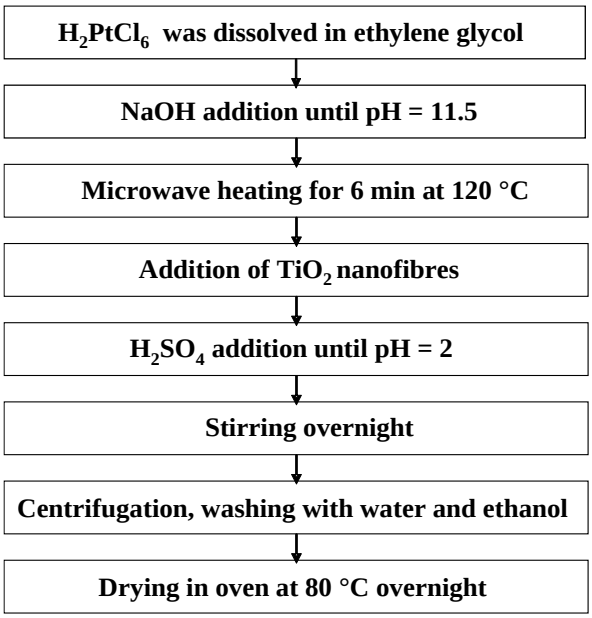

Figure 5 : Schéma du protocole de synthèse des nanoparticules de platine.

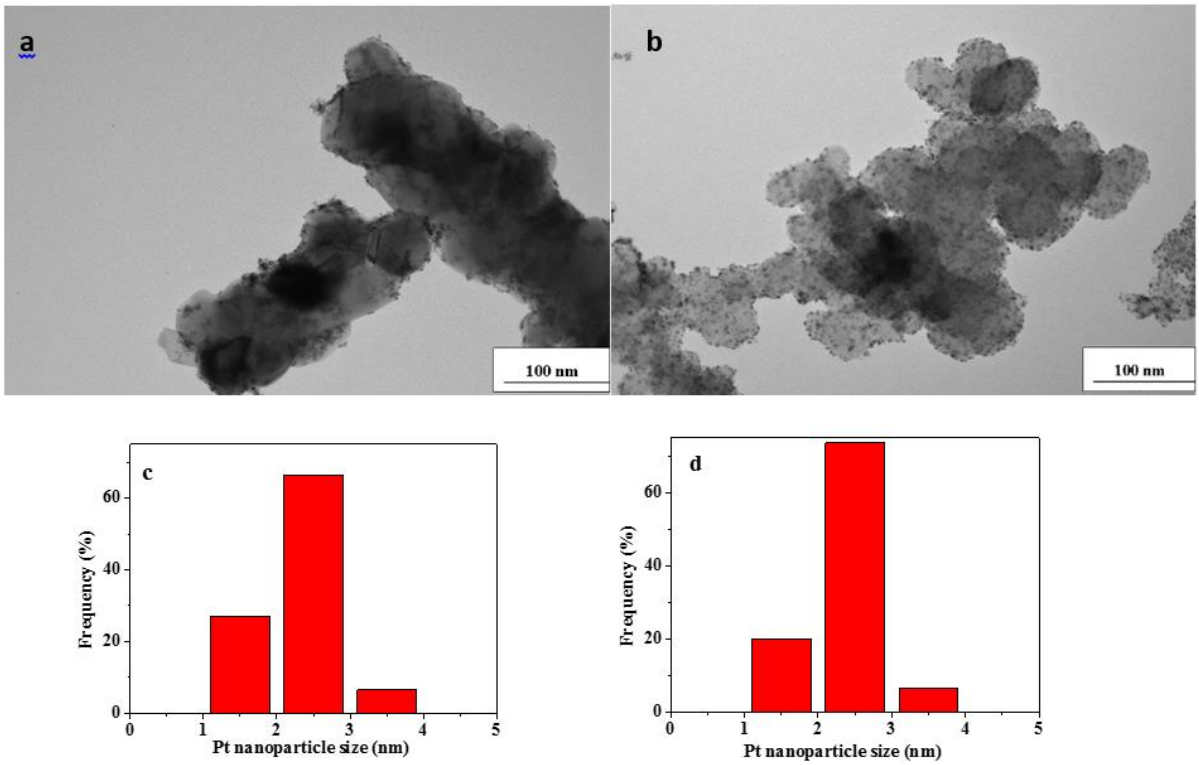

Figure 6 : Image MET de 16% Pt/TNF (a) et 33% Pt/Vulcan XC-72R (b) et histogrammes de distribution de taille des nanoparticules de platine obtenues à partir de mesures des 100 nanoparticules (c, d).

Stabilité électrochimique

La stabilité électrochimique de Pt supporté sur l'oxyde de titane et Vulcan XC-72R a été évalué en effectuant 1000 cycles entre 0,05 et 1,2 V. La perte de surface électrochimique (ECSA) a été calculée après intégration de la zone d'adsorption/désorption d'hydrogène avant et après 1000 cycles (Figure 7). La perte d'ECSA était de 25% pour Pt/TNF, 32% pour le Pt/Vulcain XC-72R et 39% pour catalyser commercial (Pt/C).

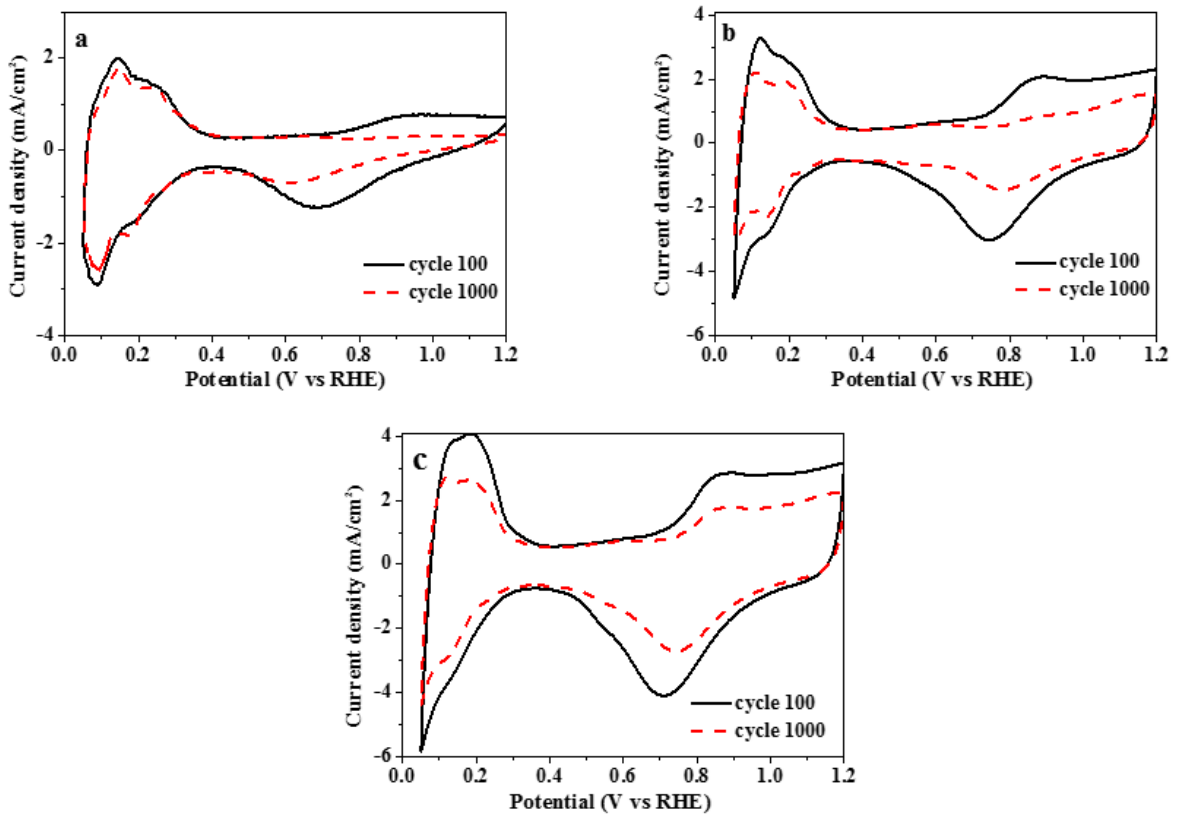

Figure 7 : Voltampérogrammes obtenus après 100 et 1000 cycles pour Pt/TNF (a), Pt/C (b) et Pt/Vulcan XC-72R (c).

Sur la figure 8 sont présentées les activités massiques pour la réaction de réduction de l'oxygène (ORR), calculées à partir des courbes de polarisation, à une vitesse de rotation de 900 tours par minute, avant et après 1000 cycles. Tous les catalyseurs ont présentés des pertes d'activité massique (Tableau 3). Un tel résultat peut être attribué à la formation d'une couche résistive de TiO_2 à la surface des fibres au cours des 1000 cycles.

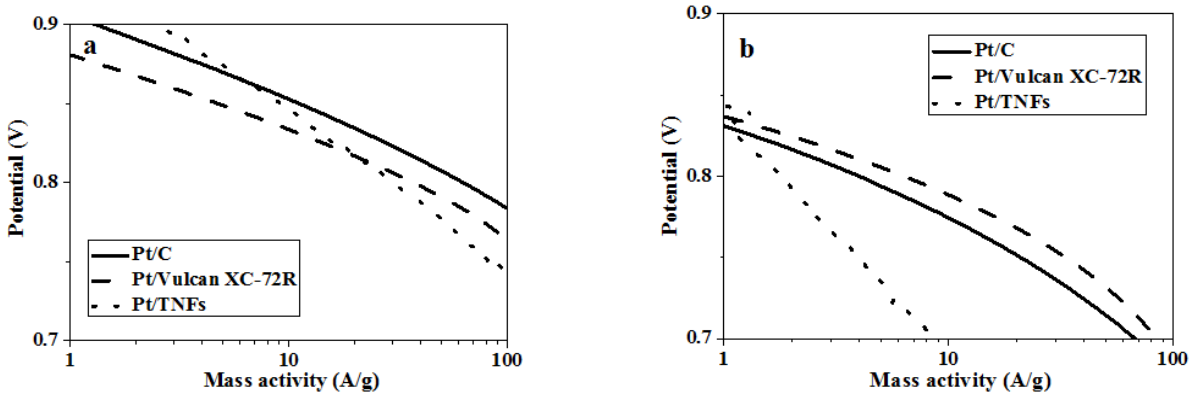

Figure 8 : Activités massiques pour la réduction de l'oxygène avant (a) et après (b) 1000 cycles électrochimiques.

Tableau 3 : Perte d'activité massique pour la réduction de l'oxygène après les 1000 cycles électrochimiques.

Catalyseur	**Pt/C**	**Pt/Vulcan XC-72R**	**Pt/TNFs**
Perte d'activité massique, %	94	81	94

Le catalyser Pt/TNF a conservé 75% de son ECSA initiale après les 1000 cycles, mais a montré une forte perte d'activité massique (Tableau 3), ce qui peut être attribuée à la formation d'une couche d'oxyde résistif sur la surface des nanofibres.

CHAPITRE 4: Oxyde d'étain

Les fibres creuses sont généralement préparées par filage électrostatique en utilisant une aiguille à configuration coaxiale. Cependant, cette technique nécessite un contrôle strict des paramètres de travail, et les paires de solution de précurseur appropriés. Par conséquent, un nouveau procédé a été proposé, qui permet la fabrication de fibres creuses céramique après le traitement thermique sans utilisation de l'aiguille coaxiale.

Synthèse des fibres-dans-tubes d'oxyde d'étain

Afin d'obtenir SnO_2 dopé au Nb, $SnCl_2$ et $NbCl_5$ ont été dissous dans l'éthanol, tandis que polymère de PVP a été dissous dans du DMF (Figure 9). Le mélange obtenu a été agité. Des fibres de PVP/$SnCl_2$ ont été préparées par filage électrostatique et ensuite calcinées à 600 °C afin d'éliminer le polymère et permettre la formation de fibres creuses.

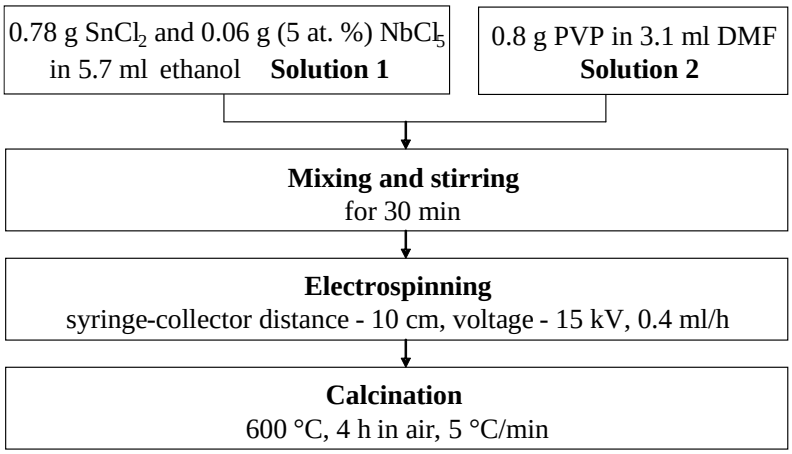

Figure 9 : Représentation schématique du protocole de synthèse de l'oxyde d'étain dopé au niobium.

Une structure des fibres inhabituelles a été obtenue dans le cas d'échantillons dopés au niobium, comme représenté sur la Figure 10. Des grains plus gros forment les parois des tubes externes, tandis que des petits grains forment des fibres situées à l'intérieur des tubes.

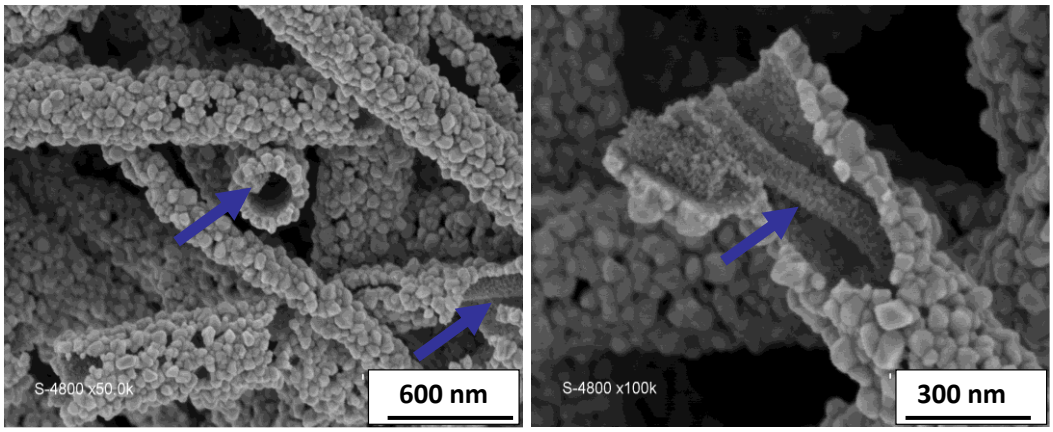

Figure 10 : Images MEB des fibres d'oxyde d'étain dopé au niobium.

Effet des paramètres de synthèse sur la morphologie de l'oxyde d'étain

L'oxyde d'étain dopé avec différent pourcentages atomiques de niobium (0,5, 2, 5 et 10 at. %) a été préparé, afin de comprendre l'influence de la concentration de Nb sur la morphologie des fibres. Les images MET montrent les sections transversales des fibres obtenues (Figure 11). Des fibres creuses ont été observées lorsque la concentration de Nb est comprise entre 5 et 10 at. %, tandis que des fibres denses ont été obtenues lorsque le dopage Nb se situe entre 0,5 et 2 at. %. Par conséquent, on peut conclure que la présence de Nb favorise la formation de la morphologie des fibres creuses.

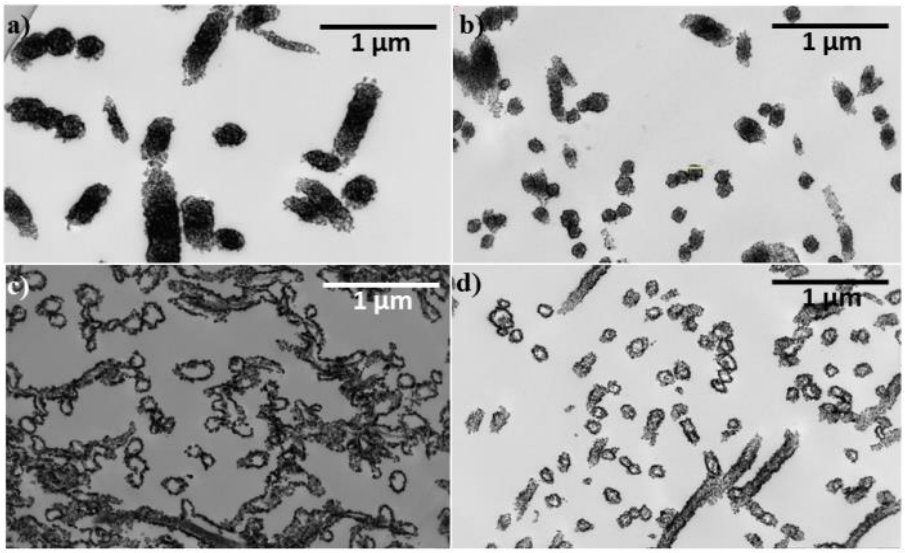

Figure 11 : Images MET de coupes transversales de SnO_2 dopé au 0,5 (a), 2 (b), 5 (c), et 10 at. % Nb (d).

Afin d'évaluer l'effet de la vitesse de chauffage sur la morphologie de la fibre, Nb-SnO_2 a été calciné dans différentes conditions, comme présenté sur la Figure 12. Avec une vitesse de chauffage de 1 °C/min, des fibres denses ont été obtenues, tandis qu'à 5 °C/min et 10 °C/min, des fibres creuses avec un diamètre plus grand ont été observées en raison de l'effet de l'expansion des gaz. Une telle augmentation de la vitesse de chauffage augmente la décomposition du polymère, ce qui conduit à une augmentation de dégagement de dioxyde de carbone et permet ainsi la formation de fibres creuses avec un diamètre supérieur. Par conséquent, les fibres creuses peuvent être obtenues en utilisant des vitesses de chauffage élevées.

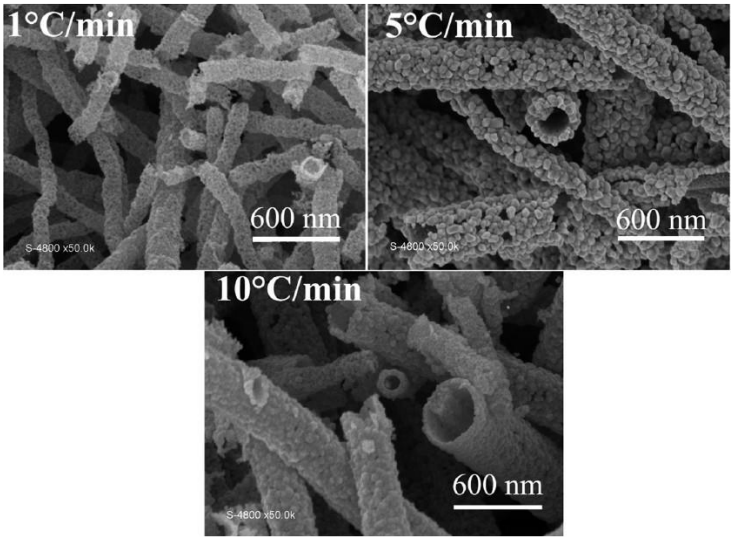

Figure 12 : Tubes de Nb-SnO_2 préparés en utilisant les taux de chauffage de 1, 5 et 10 °C/min.

Effet du dopage sur la conductivité électrique et la surface spécifique de SnO_2

L'addition de Nb conduit à une augmentation de la conductivité électrique de SnO_2 de 0,0011 S/cm à 0,021 S/cm. De plus, le dopage par Nb a un impact significatif sur la morphologie des fibres de SnO_2 comme l'inhibition de la croissance des grains de SnO_2. Cela conduit à une augmentation de la surface spécifique de SnO_2 de 26 à 42 m^2/g.

Synthèse de Pt/Nb-SnO_2

Les nanoparticules de platine ont été préparées comme décrit dans le chapitre précédent. L'image MET montre le catalyseur obtenu avec une teneur de 21% de Pt (Figure 13). La surface intérieure des fibres creuses est également accessible à des particules de platine, ce qui permet une bonne dispersion de Pt. Le diamètre moyen des particules est environ 3 nm, qui est proche de la taille des particules calculée à partir de diffraction des rayons X (4 nm).

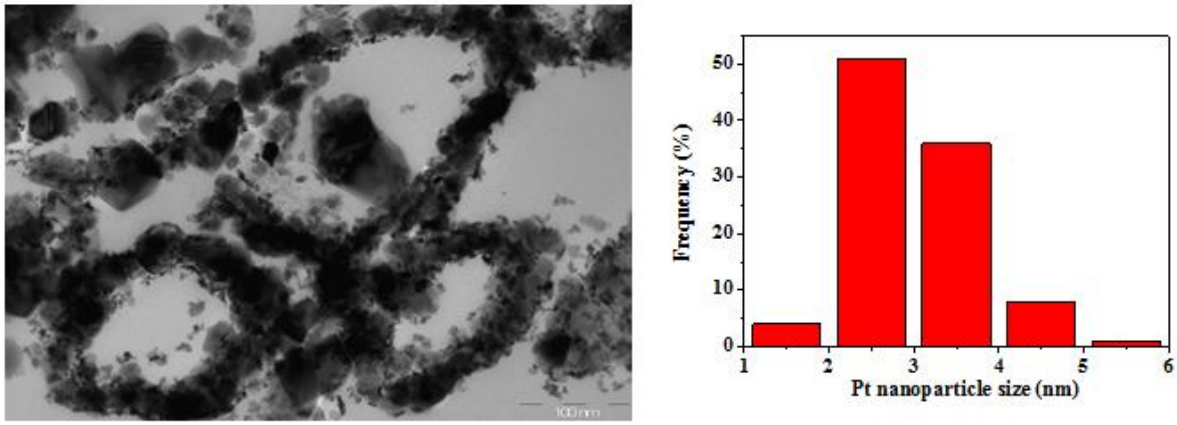

Figure 13 : Images MET de coupes transversales de 21% Pt/Nb-SnO₂ (à gauche) et histogrammes de la distribution de la taille des nanoparticules de platine obtenues à partir de la mesure de 100 nanoparticules (à droite).

Stabilité électrochimique

L'ECSA a été évaluée avant et après 2000 cycles électrochimiques, afin de comparer la stabilité du Pt/Nb-SnO_2 avec un catalyseur conventionnel Pt /C. Sur la figure 14 sont présentés les voltampérogrammes obtenus après 100, 1000 et 2000 cycles pour Pt/Nb-SnO_2 et Pt/C. L'ECSA diminue avec le nombre de cycles pour tous les échantillons. Généralement, ce phénomène est attribué à la dissolution, la migration, l'agglomération et la croissance de nanoparticules Pt. Cependant, Pt/Nb-SnO_2 a subi une perte d'ECSA significativement plus faible (24%) comparée à celle de Pt/C (86%) après 2000 cycles. Ce résultat peut être attribué à une meilleure durabilité électrochimique de Pt/Nb-SnO_2, et suggère une forte interaction entre les nanoparticules de platine et d'oxyde d'étain.

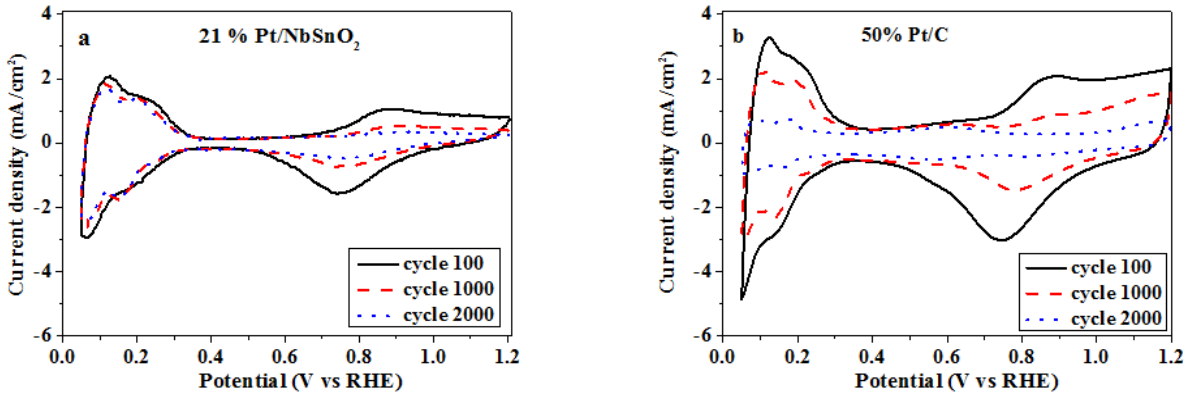

Figure 14 : Voltampérogrammes obtenus après 100, 1000 et 2000 cycles pour Pt/Nb-SnO₂ (a) et Pt/C (b) à une vitesse de balayage de 50 mV/s.

L'activité massique pour la réaction de réduction de l'oxygène a été évaluée avant et après les 2000 cycles (Figure 15). Le catalyseur Pt/Nb-SnO_2 a présenté une perte de 90% de l'activité massique après 2000 cycles, tandis que Pt/C a montré une perte de 99% après le même nombre de cycles, ce qui indique une meilleure stabilité du support Nb-SnO_2. Ce résultat est lié à la diminution d'ECSA observé précédemment.

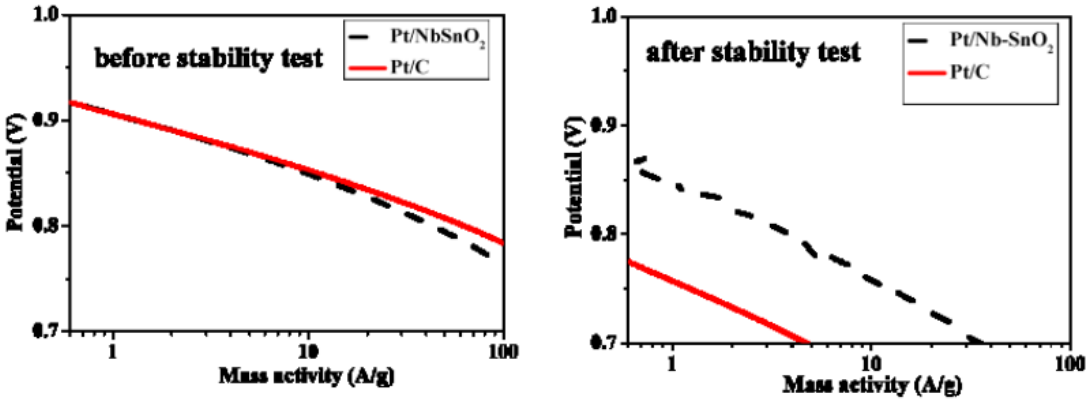

Figure 15 : Activités de masse de mesures à 900 tours par minute pour Pt/Nb-SnO_2 et Pt/C avant (à gauche) et après (à droite) le test de stabilité. Charge de Pt sur les électrodes était ~ 120 µg/cm^2.

Pt/Nb-SnO_2 catalyseur présente une meilleure stabilité électrochimique par rapport à Pt/TNF. Par conséquent, il a été sélectionné pour la caractérisation dans une cellule de PEMFC.

CHAPITRE 5: Caractérisation in situ d'une AME à base de Pt / Nb-SnO_2 dans une cellule de PEMFC

Préparation d'AME

Afin de préparer un assemblage membrane-électrode (AME), Pt/Nb-SnO_2 ou un catalyseur commercial Pt/C ont été dispersés dans l'éthanol et une solution de Nafion®. Les encres catalytiques obtenus ont été pulvérisées sur la couche de diffusion (10 Sigracet BC, 4 cm^2) et ont été séchées à 80 °C sur une plaque chauffante. L'épaisseur des électrodes obtenues était d'environ 10 µm. Le chargement de Pt et la quantité de Nafion® dans l'electrode était 0,5 mg/cm^2.

Performance d'AME à base de Pt/Nb-SnO_2

La Figure 16 montre les courbes de polarisation d'AME contenant Pt/Nb-SnO_2, Pt/Nb-SnO_2-Vulcan et Pt/C à la cathode. L'AME à base de Pt/Nb-SnO_2 fournit une densité de puissance maximale de 0,41 W/cm^2, ce qui est relativement élevé étant donné que l'électrode n'a pas été optimisée en termes de chargement de platine ou ionomère. L'AME à base de Pt/C présente une densité de puissance maximale plus élevée de 0,96 W/cm^2 indiquant une meilleure utilisation de Pt pour le catalyseur commercial.

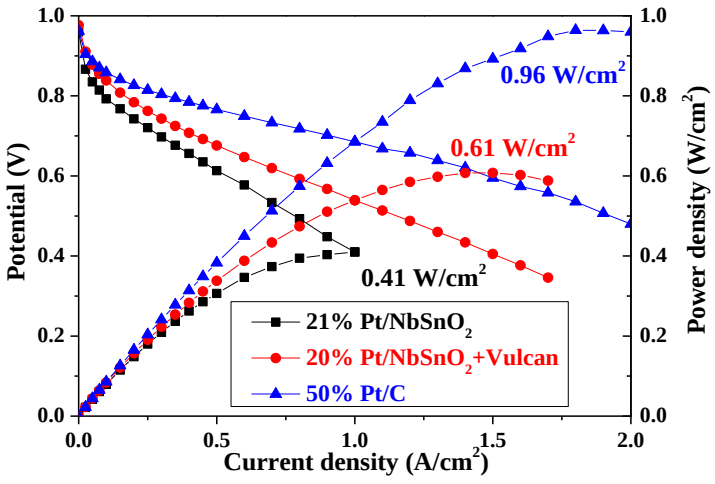

Figure 16 : Courbes de polarisation pour des AME contenant Pt/Nb-SnO_2 (100% RH), Pt/Nb-SnO_2-Vulcan (50% RH à la cathode) et Pt/C (100% RH) à 80 °C sous H_2/O_2 (1,5: 2) et 2 bars (abs).

Afin d'améliorer la conductivité électrique de la cathode, du noir de carbone (Vulcan XC-72R) a été ajouté à l'encre du catalyseur. La teneur obtenue en Vulcan XC-72R était 0,125 mg/cm^2. Ainsi, la densité de puissance maximale a été augmentée de 0,41 W/cm^2 à 0,61 W/cm^2 pour Pt/Nb-SnO_2-Vulcan-AME.

Durabilité d'AME à base de Pt/Nb-SnO_2

Afin d'étudier la stabilité des performances des piles à combustible, un test de vieillissement accéléré a été réalisé. Au cours de chaque cycle, la valeur de potentiel a été variée entre 0,9 et 1,4 V avec un palier de potentiel de 3 s. Les conditions expérimentales du test de stabilité sont indiquées dans le Tableau 4.

Tableau 4 : Conditions du test de stabilité.

T	80 °C
Humidité relative (RH)	100 %
Pression	2 bar (abs)
Gaz stœchiométrie	H_2/O_2 – 1.5/2
Protocole d'un cycle	0.9 V pendant 3 s et ensuite 1.4 V pendant 3 s
Nombre de cycles	1200

Sur la figure 17 sont présentées les courbes de polarisation des AME contenant Pt/Nb-SnO_2 et Pt/C à la cathode avant et après le test de stabilité. Le potentiel de circuit ouvert (OCV) était d'environ 0,96 V pour tous les AME et il est resté pratiquement inchangé après le test de stabilité. La courbe de polarisation de l'AME contenant Pt/Nb-SnO_2 est restée pratiquement inchangée, tandis que pour Pt/C, on constate une augmentation importante des polarisations déjà après 400 cycles.

A haut potentiel (1,4 V), l'oxydation de carbone conduit à une fonctionnalisation de la surface de carbone, ce qui se traduit par une augmentation du caractère hydrophile de la couche de catalyseur et des grandes surtensions de transport de masse. La diminution de la performance de la pile à combustible est également liée à l'amincissement de la couche catalytique en raison du détachement, de la migration et de l'isolement de nanoparticules de platine suite à la corrosion du carbone. Pour l'AME contenant Pt/Nb-SnO_2-Vulcan on constate également une chute de tension importante due à la corrosion du noir de carbone.

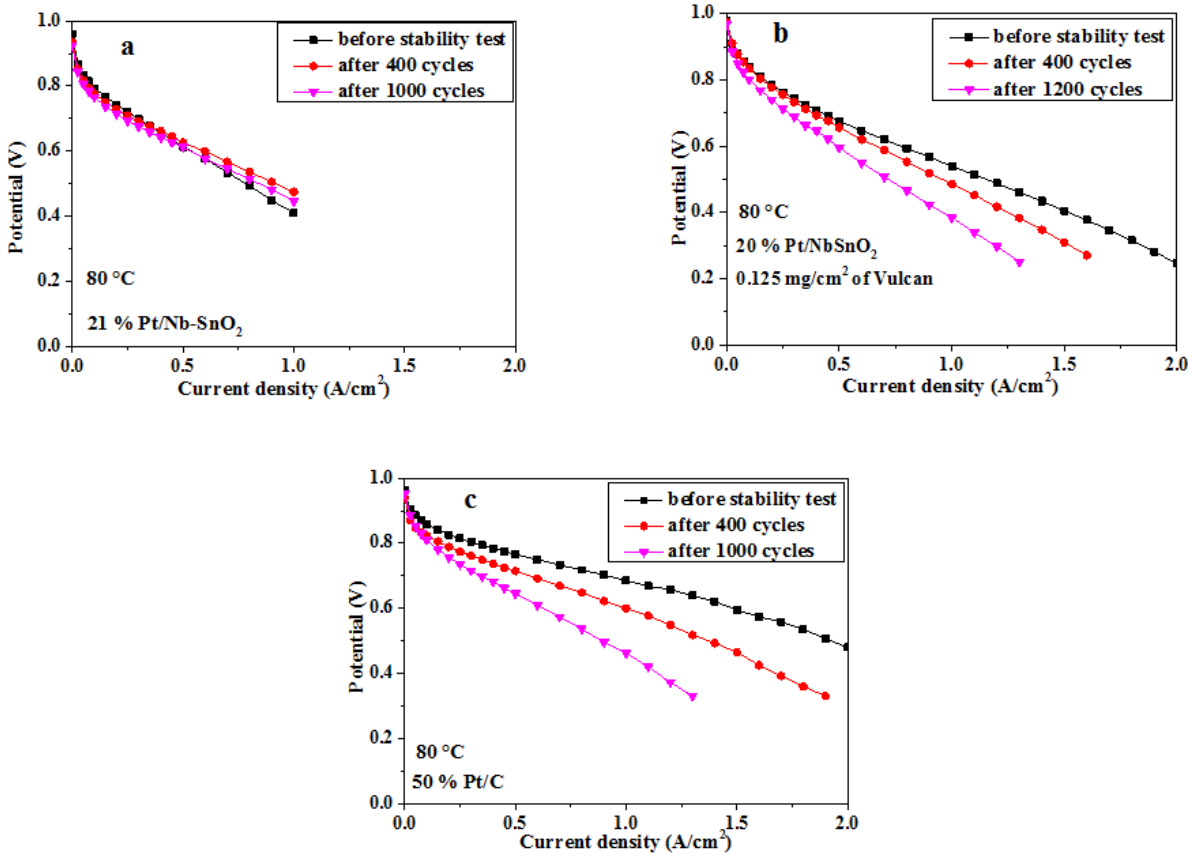

Figure 17 : Courbes de polarisation pour PEMFC contenant Pt/Nb-SnO₂ (a), Pt/Nb-SnO₂-Vulcan (b) et Pt/C (c) à la cathode avant et après le test de stabilité à 80 °C.

La Figure 18 montre des images MEB des AME contenant Pt/Nb-SnO_2, Pt/Nb-SnO_2-Vulcan et Pt/C. La couche catalytique contenant Pt/C présente une agrégation significative des nanoparticules de platine, tandis qu'aucune agrégation particulière du platine ne peut être observée à la cathode contenant Pt/Nb-SnO_2. On observe également que la structure tubulaire d'oxyde d'étain est maintenue pendant le test de stabilité.

Une bande de Pt prononcée peut être observée au milieu de la membrane, dans l'AME contenant Pt/C, qui résulte de la dissolution de Pt à la cathode et la migration des ions à travers la membrane, et la précipitation de particules de platine après réduction par l'hydrogène présent au sein de la membrane. Ce phénomène est moins évident pour l'AME contenant Pt/Nb-SnO_2, ce qui peut être attribué à la plus grande stabilité de l'oxyde d'étain et les interactions fortes entre le Pt et l'oxyde.

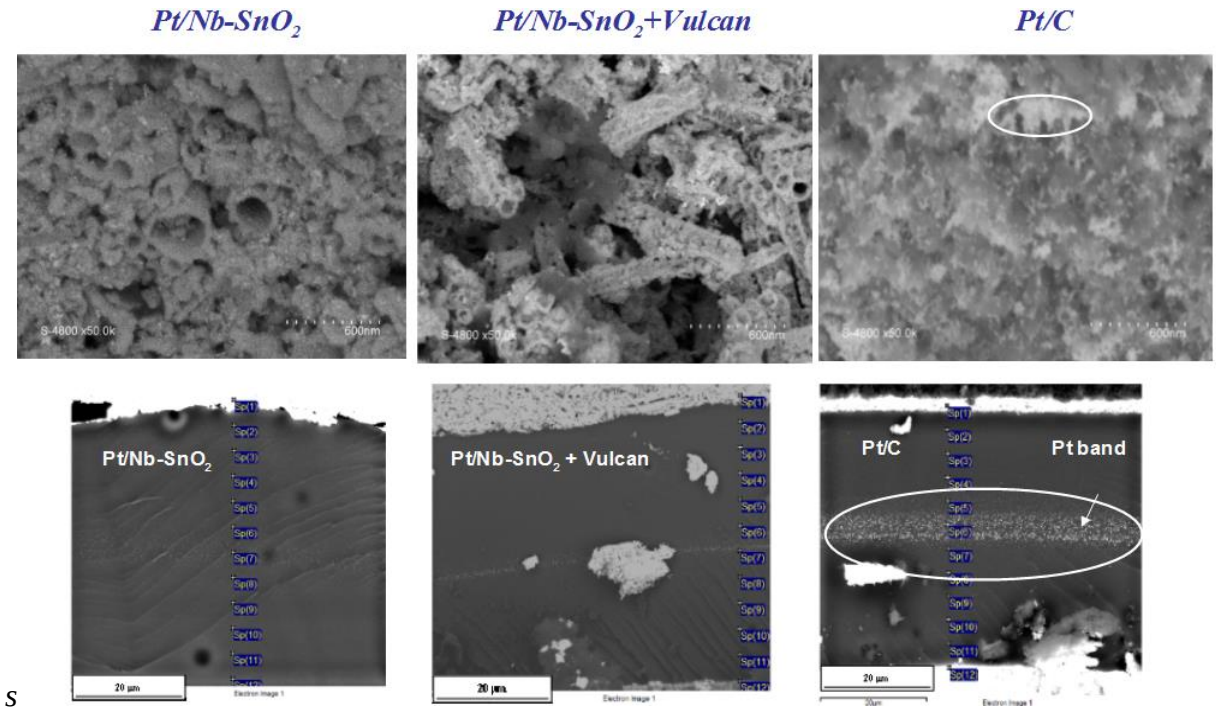

S

Figure 18 : Images MEB des AME contenant Pt/Nb-SnO₂, Pt/Nb-SnO₂-Vulcan et Pt/C après le test de stabilité.

CONCLUSIONS ET PERSPECTIVES

Des nanofibres de carbone ont été préparées par filage électrostatique et calcination à trois différentes températures (700, 1000 et 1500 °C) afin de trouver un compromis entre la stabilité électrochimique et de la surface spécifique. Les CNF_{700} ont présenté une surface spécifique élevée, mais n'étaient pas suffisamment conductrices pour être utilisées en pile. Les échantillons CNF_{1000} et CNF_{1500} ont donné des conductivités bien plus élevées, mais des surfaces spécifiques inférieures à celle de CNF_{700}. CNF_{1500} était plus stable que $CNFs_{1000}$ et support commercial (Vulcan XC-72R).

Pour les futurs travaux, le dopage à l'azote peut être utilisé pour améliorer la stabilité électrochimique, la conductivité et l'interaction entre les nanoparticules de Pt et les CNF. Une activation à la vapeur d'eau pendant l'étape de carbonisation pourrait permettre l'élaboration de CNF avec une surface développée supérieure.

Dans le chapitre 3, nous avons étudié des nanofibres d'oxyde de titane préparés par filage électrostatique. La conductivité électrique de nanofibres de TiO_2 a été améliorée par le dopage par Nb et par un traitement thermique à 800 °C en présence d'hydrogène. De plus, le dopage par Nb inhibe la croissance des grains de TiO_2 conduisant à l'amélioration de la surface spécifique des nanofibres. Cependant, la surface spécifique a diminué de manière significative après une calcination à des températures élevées.

Le catalyseur Pt/TNF a présenté une plus grande stabilité après 1000 cycles électrochimiques que celle de Pt/CNF. Cependant, l'activité massique pour la réaction de réduction de l'oxygène a diminuée de façon dramatique au cours du test de stabilité, probablement en raison de la formation d'une couche résistive de TiO_2 à la surface des TNF. En outre, l'activité de Pt/TNF était inférieure à celle de Pt/C. Ce résultat peut être attribué à la conductivité et la surface spécifique fable des TNF. Par conséquent, la conductivité électrique de ces matériaux pourra être augmentée davantage en utilisant différents dopants (par exemple, Ta et W).

Dans le chapitre suivant, SnO_2 a également été caractérisé comme support de catalyseur pour PEMFC. Ainsi, SnO_2 dopé par Nb a été obtenu en combinant le filage électrostatique avec un traitement thermique spécifique. L'addition de Nb a permis d'améliorer la conductivité électrique et la surface spécifique de SnO_2 et obtenir des fibres creuses.

Pt déposé sur SnO_2 dopé par Nb fourni une stabilité électrochimique plus élevée par rapport à un catalyseur commercial type Pt/C. Par conséquent, il a été choisi pour une caractérisation supplémentaire dans une monocellule de pile à combustible.

Dans la dernière partie de cette étude, Pt/Nb-SnO_2 a été intégré dans l'assemblage membrane-électrode (AME) à la cathode avec une membrane Nafion®. L'AME à base de Pt/Nb-SnO_2 a montré une plus faible densité de puissance maximale, mais une plus grande stabilité que celle de l'AME contenant Pt/C à la cathode. Dans le cas de l'AME à base de Pt/C, une bande de Pt a été observée dans la membrane après le test de stabilité, indiquant la dissolution de ce métal à la cathode, sa migration et sa précipitation au milieu de la membrane. Afin d'augmenter la conductivité de la couche de catalyseur, le carbone Vulcan XC-72R a été ajouté à l'encre catalytique contenant Pt/Nb-SnO_2. Cela s'est traduit par une amélioration des performances de la pile à combustible. Cependant, cette AME présente une stabilité inférieure à celle sans Vulcan XC-72R indiquant la corrosion du carbone.

Afin d'améliorer les performances de l'AME contenant l'oxyde d'étain l'optimisation de la structure de la couche catalytique à la cathode (épaisseur, porosité) et les techniques de préparation des électrodes (conditions de pressage à chaud) devra être abordée. De plus, la teneur en catalyseur et ionomère doivent également être optimisés.

CHAPTER 1:

Context and motivation

General introduction

The use of fossil fuels (oil, gas and coal) has engendered a negative impact on the environment such as global warming (due to carbon dioxide emission) and environmental pollution (due to carbon monoxide, nitrogen oxides and unburned hydrocarbons emissions). With the growth of the world population, the demand for energy will also increase, which will cause a depletion of the oil and gas reserve. According to the BP Statistical Review of World of Energy 2012, the world primary energy consumption has grown by 1.8 % in 2012 and the oil reserves are sufficient to meet the demand for only 52.9 years of global production [1]. Therefore, the use of alternative sources of energy [2] is required.

Renewable energy sources such as solar and wind power offer such possibility. These environmentally clean technologies are expected to replace the conventional fossil fuels in the future. In 2012, Denmark has signed an energy agreement where at least 50 % of the electricity will be provided by wind power by 2020 and 100 % by renewable energy by 2050. The federal Government of Germany has decided to close down all nuclear plants facilities by 2022 due to nuclear waste problems and risk of nuclear meltdown, as occurred in Fukushima in 2011 and in Chernobyl in 1986.

Even though the replacement of fossil fuels by renewable power sources is quite appealing, there is still the problem concerning the storage of the energy produced. The issue can be resolved by coupling the system with batteries, a pumped hydro or hydrogen storage [3],[4]. For instance, in Lolland (Denmark), in Unst (Scotland) and in other countries [5], the excess of renewable power is stored in the form of hydrogen. This hydrogen is produced by electrolysis and can be converted into electrical power through fuel cell technology. The proton exchange membrane fuel cell (also known as polymer electrolyte membrane fuel cell, PEMFC) is one of the most efficient fuel cells, which can be used in transport, portable and stationary applications. However, low life time and high cost of the PEMFC are two main barriers to its commercialisation. In particular, carbon supported Pt electrocatalyst provides poor durability. In order to overcome the problem of support corrosion, carbon should be replaced with more stable materials. Therefore, this work is focused on development of alternative catalyst supports for PEMFC.

1. Fuel cells

1.1 Introduction

Christian Friedrich Schönbein discovered the principle of fuel cell in 1838 [6] followed by the pioneering work of Sir William Grove in 1839, who built up the first fuel cell called "a gaseous Voltaic battery" [7],[8]. Porous platinum was used as the electrodes and diluted sulfuric acid was the electrolyte. Mond and Langer improved the Grove's fuel cell using porous matrix to hold the liquid electrolyte and platinum black as a catalyst [9]. After 100 years since discovery of the first fuel cell, Francis Thomas Bacon developed the first alkaline 40-cell stack with a power of 5 kW. A similar type of alkaline fuel cell was used by the NASA for the space missions in 1960s (Apollo in 1968).

A fuel cell is a device that converts chemical energy into electrical energy through the oxidation of the fuel. The system consists of two electrodes in contact with an electrolyte, which conducts only ionic species. At the anode, fuel is decomposed into ions and electrons. Depending on the type of the fuel cell the ionic species travel from anode to cathode or vice versa, while electrons travel along an external circuit to the cathode, where reduction of oxygen takes place.

There are many advantages of using fuel cells over conventional energy conversion devices such as [10]:

- Efficiency of fuel cells is not limited by the Carnot cycle. Therefore, they show higher theoretical and practical efficiency than combustion engines (the theoretical efficiency of a fuel cell at 25 °C using hydrogen is around 83 %).
- Scalable power. Small fuel cells can be almost as efficient as large ones compared to other technologies such as gas turbines that can be 50 % less efficient when scaled down to a smaller size.
- Possibility to connect individual fuel cells in a series (fuel cell stack).
- Zero CO_2 emission, when hydrogen produced by electrolysis is used as fuel. Water is the only product of the reactions in PEMFC.
- Absence of moving parts in the fuel cells what makes them quiet.
- Furthermore, fuel cells generate the electricity as long as the oxidant and fuel are supplied. This is an important advantage over conventional batteries, which often require long recharge time.

Types of fuel cells

There are seven main types of fuel cells: the solid oxide FC (SOFC), the proton ceramic FC (PCFC), the molten carbonate FC (MCFC), the phosphoric acid FC (PAFC), the alkaline FC (AFC), the direct alcohol fuel cells (such as the direct methanol FC, DMFC) and the polymer electrolyte membrane FC (PEMFC). Molten carbonate, protonic ceramic and solid oxide fuel cells are known as ***high temperature fuel cells***, where the working conditions vary between 650 °C and 1000 °C. They are suitable for stationary and combined heat and power applications. Non-noble catalysts and different fuels are used in high temperature fuel cells.

Low temperature fuel cells

Alkaline fuel cells were developed for the Apollo space programme in the 1960s. The oxygen reduction reaction is much faster in KOH than in the acid electrolyte. Therefore, alkaline fuel cell is one of the most efficient fuel cells (reaching an efficiency of 70 %). It is also one of the cheapest to manufacture as non-platinum catalysts such as Raney nickel and silver are used, but these fuel cells work well only with very pure gases as they are quite sensitive to CO_2 impurities. One of the main challenges for AFCs is the conductivity and durability of the membranes.

Direct alcohol fuel cell is another type of low temperature fuel cell where the hydrogen is replaced by e.g. methanol or ethanol. These fuels can be easily obtained from biomass thus making such technologies very attractive. The positive aspect of such a system is that a liquid fuel is easier to handle than hydrogen, thereby offering the possibility to commercialise the direct methanol (DMFC) for portable applications (for example cell phones). However, methanol cross-over is one of the main hurdle of this type of fuel cell.

Phosphoric acid fuel cells are another type of fuel cells that use concentrated phosphoric acid as the electrolyte. They were the first to be commercialised in the 1960s. The electrolyte used is absorbed into a porous ceramic material. The working temperature of such device is around 200 °C. In consequence, better oxygen reduction kinetics, faster gas transport and increased tolerance towards CO poisoning can be achieved. High temperature proton exchange membrane fuel cells are based upon a polymer/phosphoric acid membrane system and operate at a cell temperatures between 130 – 200 °C, generally 160 °C.

Characteristics of different types of fuel cells as well as their applications, efficiency and advantages are listed in Table 1.

Table 1: Comparison of fuel cell types

FC	Electrolyte	Mobile Ion	T, °C	Electrical Efficiency	Applications	Advantages
Polymer Electrolyte Membrane (PEMFC)	Poly-perfluoro-sulfonic acid	H^+	80	60 % transportation 35 % stationary	• Backup power • Portable power • Distributed generation • Transportation	• Solid electrolyte reduced corrosion • Quick start-up • Low temperature
Direct methanol (DMFC)	Poly-perfluoro-sulfonic acid	H^+	0-80	40 %	• Portable • Combined heat and power (CHP)	• Liquid fuel • Quick start-up • Low temperature
Alkaline (AFC)	Solution of KOH soaked in a matrix	OH^-	90-200	60 %	• Military • Space	• Cathode reaction is faster • Variety of catalysts
Phosphoric acid (PAFC)	Phosphoric acid soaked in a matrix	H^+	150-200	40 %	• Distributed generation	• High efficiency with CHP • Increased tolerance to fuel impurities
Molten Carbonate (MCFC)	Solution of lithium, sodium or potassium carbonates soaked in a matrix	CO_3^{2-}	600-700	45 – 50 %	• Distributed generation • Electric utility	• High efficiency • Fuel flexibility • Variety of catalysts • Suitable for CHP
Protonic Ceramic (PCFC)	Perovskite-type ceramic membrane	H^+	600-700	-	• Power station • Micro-cogeneration	• Fossil fuel can be used • Solid electrolyte
Solid oxide (SOFC)	Yttria stabilized zirconia	O^{2-}	700-1000	60%	• Auxiliary power • Electric utility • Distributed generation	• High efficiency • Fuel flexibility • Variety of catalysts • Solid electrolyte

1.2 Polymer Electrolyte Membrane Fuel Cells (PEMFC)

1.2.1 Introduction and principle

The first PEM fuel cell was developed by Willard Thomas Grubb and Leonard Niedrach in the early 1960s. A huge progress in PEMFC performance was achieved in 1966, when the sulfonated polystyrene membrane was replaced by Nafion® membrane (DuPont) [11]. In 1960s and early 1970s the utilisation of carbon black supported Pt allowed an increase of the Pt surface area from 25 m^2/g for Pt black to 100 m^2/g for Pt/C and decrease of the Pt sintering rate. In 1983 the decrease in a thickness of the Nafion® membrane from 175 to 50 µm resulted in a significant enhancement of PEMFC performance [12]. Furthermore, a new short side chain perfluorosulfonic acid (PFSA) membrane was developed by DOW in this period, with lower equivalent weight and high conductivity. Finally, the addition of dispersed Nafion® into the electrode layer ensured proton transport, which leads to more efficient catalyst utilisation and hence high fuel cell performance. For example, in 1988 Srinivasan et al. [13] worked on optimisation of the ionomer content in the catalyst layer and used high Pt loading to obtain thin electrodes, which allowed achieving enhanced fuel cell performance.

Currently, Nafion® is still the most used PEMFC membrane due to its high proton conductivity and durability, while carbon black supported Pt and Pt alloys are still the most used electrocatalysts.

PEMFCs provide several advantages such as high power densities and fast start-up and shutdown due to the low operating temperatures. Moreover, they are environmentally friendly due to the zero emission of greenhouse gases. All these positive attributes make PEMFCs ideal for a variety of applications such as transport, small-stationary and portable electronics. However, further hurdles remain to be overcome to make such system attractive for worldwide commercialisation. For instance, reduction of the precious metal used, improvement of the lifetime of the device, reduction of the catalyst poisoning (by CO, sulphur species, and ammonia) as well as improvement in the water management.

The membrane electrode assembly (MEA) in the core structure of PEMFC consists of a polymer electrolyte membrane (PEM), a cathode and an anode, as shown in Figure 1.

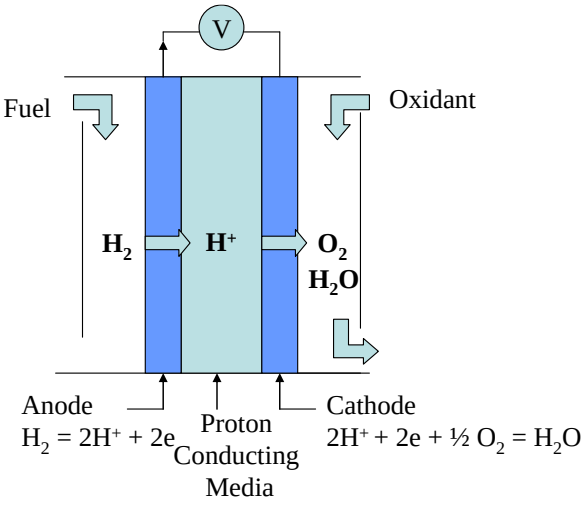

Figure 1: Schematic structure of a fuel cell membrane electrode assembly (MEA)

Hydrogen gas is supplied to the anode side, where it is decomposed on the Pt surface into protons and electrons as followed:

$$H_2 \rightarrow 2H^+ + 2e^- \qquad E^0_{H^+/H_2} = 0 \text{ V at } 25\ ^\circ\text{C}$$

The formed protons then migrate through the PEM to the cathode, while the electrons travel along an external electrical circuit towards the cathode as well, where both of them react with oxygen. Water is the only product formed in acid medium in this reaction:

$$O_2 + 4H^+ + 4e^- \rightarrow 2H_2O \qquad E^0_{O_2/H_2O} = 1.23 \text{ V at } 25\ ^\circ\text{C}$$

The change of the Gibbs free energy for a reaction under standard conditions is defined as follows:

$$\Delta G^\circ = - nF\Delta E^0,$$

where n is the number of the electrons transferred in the electrochemical reaction, F is the Faraday constant (1 F = 96500 C) and ΔE^0 is the cell voltage for thermodynamic equilibrium at standard conditions. The Gibbs free energy change for the reaction described below can be estimated by using thermodynamic data for each component. For the reaction between H_2 and O_2 in a PEMFC, the ΔG° of the reaction is -237 kJ/mol at room temperature.

$$H_2 + ½\ O_2 \rightarrow H_2O,\ \Delta G^\circ = -237 \text{ kJ/mol at } 25\ ^\circ\text{C}$$

The equilibrium cell voltage can be calculated from the following equation:

$$\Delta E^\circ = -\Delta G^\circ / nF = 1.23\ V$$

The cell voltage ΔE° is defined as the difference of the equilibrium electrode potentials between the cathode and anode:

$$\Delta E^\circ = E^\circ_{Cathode} - E^\circ_{Anode}$$

Mechanism of the hydrogen oxidation reaction (HOR)

There are two main pathways for HOR namely Tafel-Volmer and Heyrovski-Volmer [14]. The first mechanism involves adsorption of hydrogen onto the catalyst surface and dissociation of H_2 molecules into the atoms (Tafel reaction), while during the second one, dissociation into proton and hydrogen atom takes place (Heyrovski reaction), followed by fast charge-transfer step (Volmer reaction):

$$\text{Tafel reaction: } H_2 \rightarrow H_{ad} + H_{ad}$$

$$\text{Heyrovsky reaction: } H_2 \rightarrow H_{ad} + H^+ + e^-$$

$$\text{Volmer reaction: } H_{ad} \rightarrow H^+ + e^-$$

The HOR in fuel cells on the Pt surface was considered to occur via Tafel-Volmer mechanism. However, more recent studies have shown that HOR on Pt surface occurs via the Tafel-Volmer mechanism at low overpotentials, whereas the contribution of Heyrovsky-Volmer pathway increases with the overpotential [15],[16].

The HOR kinetics is ca 10^6 times faster compared with that of ORR. Therefore, substantial efforts have been made for the development of efficient ORR electrocatalyst [17],[18].

Mechanism of the oxygen reduction reaction (ORR)

Oxygen reduction reaction in acid medium is a sluggish reaction, which limits the performance of a PEMFC. There are two pathways of ORR, the first one is a 2 electrons reduction via hydrogen peroxide formation followed by another 2 electrons reduction to water, while the second way is the direct 4 electrons reduction. The amount of H_2O_2 produced in ORR and detected using rotating ring disc electrode (RRDE) is usually below 1 % for Pt/C electrocatalyst in the potential range between 0.6 and 1.0 V_{RHE} [19]. Presence of H_2O_2 leads to the degradation of membrane and carbon support due to the formation of $HO^{\bullet}$ radicals. Therefore, the $4e^-$ pathway is preferred. Both mechanisms are shown in Figure 2.

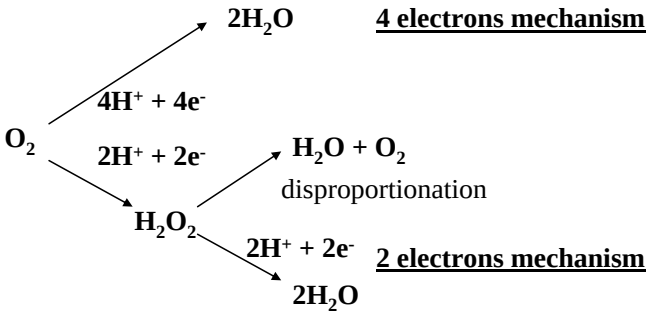

Figure 2: Schematic pathways for the ORR in acidic solution [20].

Using density functional theory (DFT) calculations, the dissociative and the associative mechanisms of oxygen reduction on Pt surface have been proposed [21],[22]. In the dissociative mechanism (detailed form of 4-electron pathway), oxygen adsorption breaks directly the O-O bond and the formed atomic O* (where * is a site on the Pt surface) is reduced to OH* and to H_2O without H_2O_2 formation:

$$½\ O_2 + * \rightarrow O*$$

$$O* + H^+ + e \rightarrow OH*$$

$$OH* + H^+ + e \rightarrow H_2O$$

The associative mechanism becomes dominant with increasing current density. In this mechanism, the O-O bond is not broken during adsorption step, making possible the H_2O_2 formation.

$$O_2 + * \rightarrow O_2*$$

$$O_2* + H^+ + e \rightarrow HO_2*$$

$$HO_2* + H^+ + e \rightarrow H_2O + O*$$

$$O* + H^+ + e \rightarrow OH*$$

$$OH* + H^+ + e \rightarrow H_2O + *$$

There are three models for oxygen adsorption on the Pt surface, namely Griffiths, Bridge and Pauling models [23]:

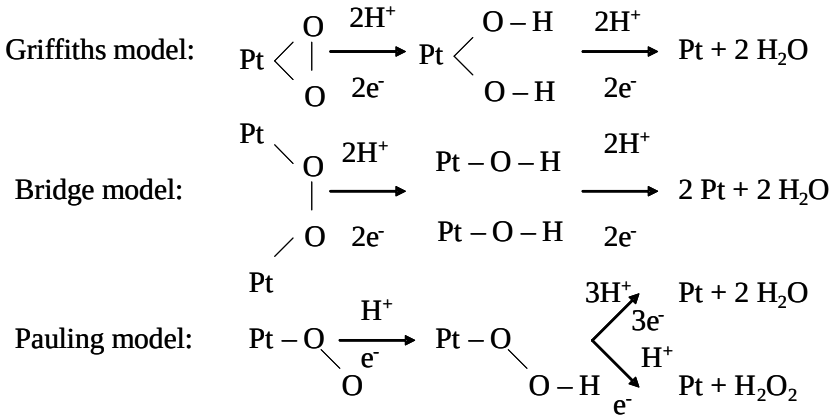

Figure 3 shows the activities of metals plotted as a function of the oxygen binding energies (the so-called volcano plot) and as a function of both the O and the OH binding energy. According to both plots, Pt is the most active ORR catalyst with optimum binding energies of the oxygenated species. For Ag and Au, the low oxygen adsorption becomes rate-determining step. In contrast, for metals located on the left side of the volcano plot, too strong oxygen adsorption results in slow desorption of the oxygenated species [24].

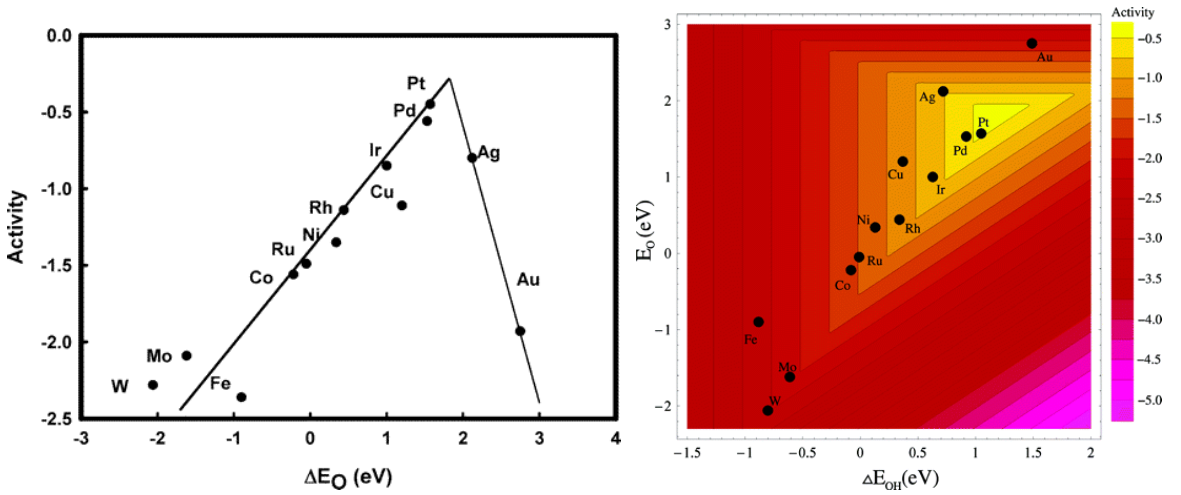

Figure 3: Trends in oxygen reduction activity plotted as a function of the oxygen binding energy (left) and as a function of both the O and the OH binding energy (right) [25]**.**

Particle size effect

The ORR kinetics is sensitive to changes of Pt nanoparticles size. For example, Kinoshita [26] reported that ORR specific activity (A/cm^2_{Pt}) decreases with decreasing particle size (so called "negative size effect"), while mass activity (A/g_{Pt}) reaches the maximum for particles with diameter of ca 3 - 4 nm. In contrast, HOR specific activity increases with decreasing particle size (positive size effect) [19]. Such particle size effect can be attributed to an increased amount of low-coordinated sites, which leads to the stronger adsorption of oxygenated species on the surface of small Pt particles (1 - 5 nm) compared with Pt bulk [24]. In particular in acid electrolytes, particle size effect on ORR plays important role due to the strong adsorption of anions, such as phosphate and sulphate [27].

Butler-Volmer Equation

At low overpotential the reaction kinetics can be described by Butler-Volmer equation:

$$j = j_0\{exp(\alpha_A F\eta/RT)-exp(-\alpha_C F\eta/RT)\}$$

where j is current density, j_0 is the exchange current density, α_A and α_C are the anodic and cathodic transfer coefficients (usually close to 0.5), F is the Faraday constant, η is the overpotential, R is the gas constant and T is the temperature.

At higher overpotential one of the terms of the Butler-Volmer equation becomes much smaller than the other one. Therefore, this equation can be simplified to the Tafel equation:

$$log\ j = log\ j_0 + \alpha F\eta/2.3RT$$

The plot of $log\ j$ versus η is shown in Figure 4. The slope of this plot is known as the Tafel slope. For ORR on platinum surface in acid medium, two linear regions are observed with the

slopes of 60 mV/dec at low overpotentials (Pt is covered by oxygenated species) and of 120 mV/dec at high overpotentials [21],[20].

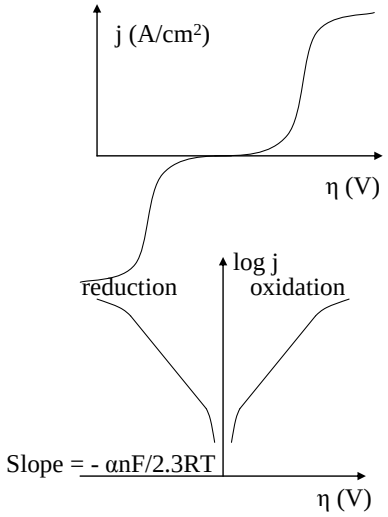

Figure 4: Current-potential curves and corresponding Tafel plots.

1.2.2 Polarisation curve

The plot of cell voltage versus current density is known as the polarisation curve (Figure 5), which is one of the most important characteristics of the fuel cell performance. The polarisation curve can be divided into three domains. In the low current density region the cell voltage decreases with increasing current density due to activation overpotential. In the middle and the high current density regions the potential decreases due to the ohmic polarisation and mass-transport limitations, respectively [12]. Therefore, the cell voltage can be written as follows:

$$E_{cell} = E^0 - \eta_{activation} - \eta_{ohmic} - \eta_{concentration}$$

where E_{cell} is the voltage for a certain operating condition, E^0 is the theoretical cell voltage, $\eta_{activation}$ is the overpotential, which corresponds to the activation at the cathode and anode, η_{ohmic} is the overpotential associated with the conduction of protons and electrons and $\eta_{concentration}$ is the overpotential resulting from the decrease in concentration of the reacting gases [21].

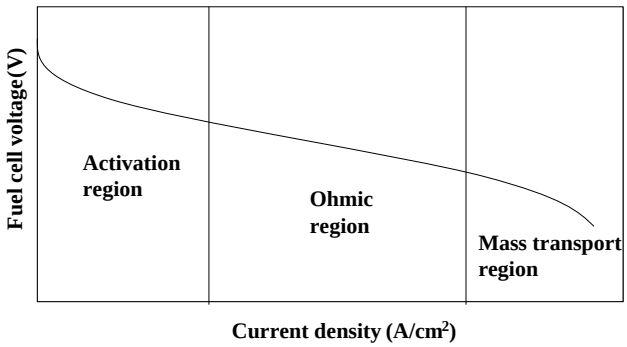

Figure 5: Ideal polarisation curve with losses and corresponding regions.

- ***Activation losses (activation polarisation)***

The cell performance drops significantly in the low current densities as displayed in the polarisation curve due to the slow kinetics of the oxygen reduction reaction. Activation overpotential is defined as the energy that is necessary to apply to the system to initiate the reaction. The relation between the current density and activation overpotential can be described using the Tafel equation:

$$\eta_{activation} = a + b\ log(j)$$

- ***Ohmic losses (ohmic polarisation)***

In the second region of the polarisation curve, the cell potential decreases linearly with current density according to Ohm's law:

$$\eta_{ohmic} = j\ R$$

Ohmic losses are caused by the resistance of the different cell components such as the electrode, the bipolar plate and the main contribution comes from the membrane which is used to transfer protons.

- ***Concentration losses (concentration polarisation)***

At high current densities the potential drops dramatically due to mass-transport limitations. In this region the gas diffusion is slower than the electron transfer and thereby becomes the rate-determining step. The concentration polarisation can be described as:

$$\eta_{concentration} = R\ T / n\ F\ (ln(1 - j/j_l))$$

where j_l is limiting current density.

However, theoretical cell voltage (E^0) is never observed under real experimental conditions due to the fuel crossover and internal currents (j_n). To model this phenomenon previous equations can be modified:

$$\eta_{activation} = a + b\ log(j+j_n)$$

$$\eta_{ohmic} = (j+j_n)\ R$$

$$\eta_{concentration} = R\ T / n\ F\ (ln(1 - (j+j_n)/j_l))$$

1.2.3 PEMFC components

The PEMFC consists of several components such as the membrane electrode assembly (MEA), the gaskets, the bipolar plates and the current-collectors, as shown in Figure 6.

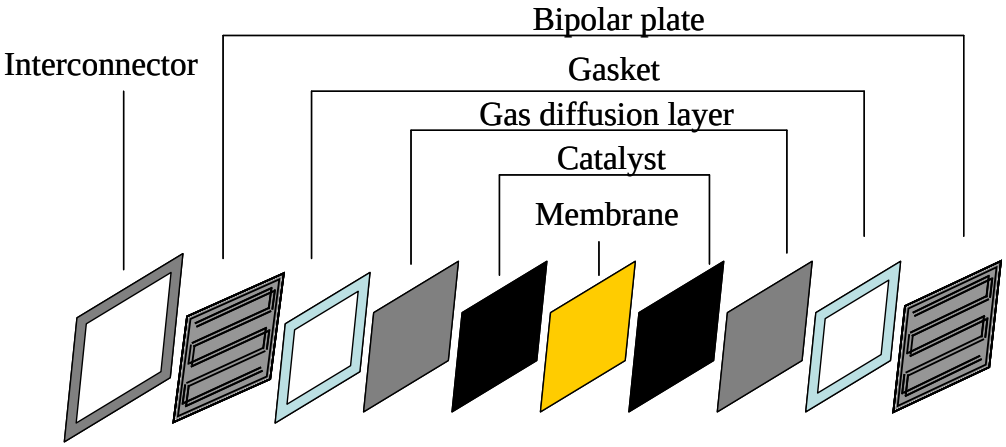

Figure 6: Schematic structure of PEMFC components in a stack.

Bipolar plates

Bipolar plates should provide electrical connection between the MEAs in the stack, transport the fuel and oxidant uniformly via flow channels to the electrodes and remove the water produced at the cathode side. Therefore, the requirements of bipolar plates include high electrical and thermal conductivity, impermeability for gases, high chemical stability, corrosion resistance, low weight and volume as well as low cost. Bipolar plates are usually made of graphite or metals such as stainless steel, titanium and aluminium.

Membrane electrode assembly (MEA)

The MEA is the core of the fuel cell, which is composed by a membrane sandwiched between two electrodes. There are two main methods to prepare MEA such as Catalyst Coated Membrane (CCM) method, where the catalyst is directly applied onto the membrane, and Catalyst Coated Substrate (CCS) method, in which the catalyst is applied on the Gas diffusion layer (GDL). In order to solve the problem of membrane swelling during CCM method, the Decal Transfer Method (DTM) can be used. In this method the catalyst ink is applied on the temporary substrate, hot pressed onto the membrane and then the substrate is peeled off. The components of the MEA are described in the following paragraph.

Polymer Electrolyte Membrane (PEM)

The main functions of PEM are transport of protons as well as separation of fuel and oxidant. Thus, the PEM should posses the following properties [28],[29]:

- High protonic conductivity to transport protons from the anode to the cathode due to the presence of the fixed ionic groups under the influence of a potential gradient. Low membrane thickness leads to improved proton conductivity. However, thick membranes show better physical stability and lower fuel crossover.
- Impermeability to gases to separate hydrogen and oxygen (low crossover);
- High chemical and mechanical stability under fuel cell conditions;
- High electronic resistance;
- Low cost and availability.

Nafion® produced by the DuPont Company is the most characterised and the most used PFSA membrane for PEMFCs. It provides high protonic conductivity in the range from 0.1 mS/cm at 20 % relative humidity (RH) to 100 mS/cm at 100 % RH at 45 - 80 °C [12] as well as high chemical and thermo-mechanical stability due to the combination of sulfonate fixed ionic groups with the polytetrafluoroethylene (PTFE) backbone, as shown in Figure 7.

$$- (CF_2 - CF_2)_x - (CF_2 - \underset{\displaystyle (O - CF_2 - \underset{\displaystyle CF_3}{\underset{|}{CF}})_m - O - (CF_2)_n - SO_3H}{\underset{|}{CF}})_y -$$

Nafion® (m > 1, n = 2, x = 5 – 13.5, y = 1000)

Figure 7: Chemical structure of Nafion®.

The PFSA membranes need to be hydrated in order to conduct the protons. Therefore, Nafion®-based membranes are not able to work at temperatures above 100 °C, unless the fuel cell is pressurised. However, high operating temperatures are desirable to improve ORR kinetics, water management and tolerance of the platinum electrocatalyst toward CO poisoning. In addition, slow kinetics of alcohol oxidation in DAFC may also be improved at high temperature.

High-temperature membranes

In order to improve water-retaining capacity of PFSA and increase its operation temperatures, hydroscopic particles such as oxides and zirconium phosphate can be embedded

in the polymer matrix [30]. Another strategy is to replace water with low volatile solvents using polymer with basic groups that can adsorb acid. For example, polybenzimidazole (PBI) membrane developed by Savinell et al. [31] is a promising candidate for high temperature PEMFC (HT-PEMFC) that can adsorb acid via acid-base interaction. Such phosphoric acid doped PBI membrane provides high conductivity of >0.04 S/cm at 190 °C at 10 % RH as well as good mechanic properties and thermal stability. Highly acid doped PBI membranes under development in the laboratory at ICGM-AIME provide conductivity >150 mS/cm at 140 °C. The proton transfer occurs via a Grotthuss (hopping) mechanism in anhydrous conditions and depends on acid doping level. However, phosphate anion strongly adsorbs on the Pt surface leading to the slow kinetics of ORR. Another disadvantages of this system are phosphoric acid leaching and oligomerisation of phosphoric acid which results in decrease of proton conductivity [32]. Finally, carbon corrosion rate increases with the temperature. Thus, more durable alternative catalyst support materials should be developed.

Electrodes

Electrodes are composed of catalyst layer and gas diffusion layer (GDL), as shown in Figure 8.

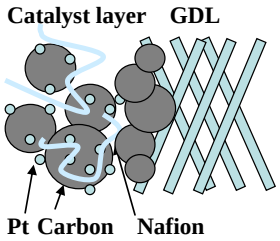

Figure 8: Schematic structure of the PEMFC electrode.

a. Gas diffusion layer (GDL)

The gas diffusion layer is placed between the catalyst layer and the bipolar plate. The main functions of GDL are gas distribution, current and heat conduction, as well as water removal [12]. Therefore, the requirements for a GDL are:

- High porosity to transport reactants and to remove water;
- High electronic and thermal conductivity;
- Good mechanical strength.

There are two layers within the GDL, a thin microporous and a thick macroporous layer (diffusion layer), as shown in Figure 9. Microporous layer consists of carbon black powder or graphite particles mixed with a hydrophobic binder (usually PTFE). It possesses a pore size

between 100 and 500 nm and suitable hydrophobicity to remove water [33]. Furthermore, it provides electrical contact between catalyst and macroporous layer of GDL. Macroporous layer consists of carbon fibres in the form of paper or cloth and have a pore size between 10 and 30 µm [34]. Polyacrylonitrile (PAN) and heavy fractions of petroleum or coal (pitch-precursor-carbon) are mainly used as the precursors for carbon fibres.

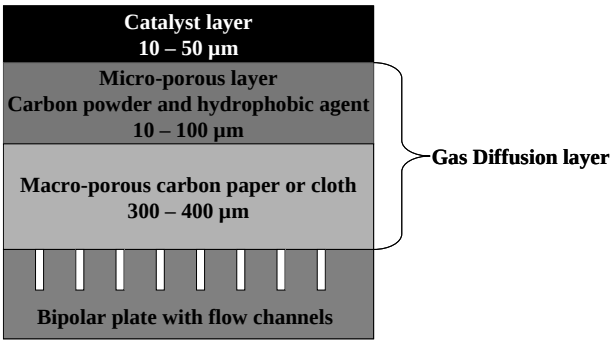

Figure 9: Schematic structure of PEMFC electrode [21].

b. Catalyst layer (CL)

CL is composed of catalyst (e.g. platinum) nanoparticles on carbon black support mixed with PFSA ionomer and PTFE, which provides hydrophobicity leading to improved water management. Good CL has to provide [28],[12]:

- The three-phase boundary sites, where electrolyte, reactants and catalyst are in contact, as shown in Figure 10 [35];
- High active surface area per catalyst mass;
- Hydrophobic pathways to transport reactants to the catalyst;
- Hydrophilic pathways for efficient water removal;
- High electronic conductivity.

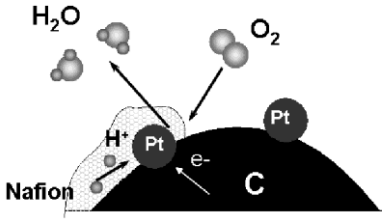

Figure 10: Schematic diagram of a three-phase boundary [21].

The presence of the Nafion® ionomer in the catalyst layer provides a pathway for protons transport and plays the role of a binder that holds the catalyst particles together. Improved ionic conductivity of the CL results in the increased number of catalyst active sites and better platinum utilisation. However, very high ionomer loading can hinder the gas transport to the reactive sites and leads to the mass transport losses. Therefore, the optimisation of the

ionomer content in the CL is one of the main challenges for the catalyst layer design. The optimum ionomer loading depends on the surface area and density of the support and should be ca 30 wt. %, when carbon black, such as Vulcan, is used as a catalyst support [12].

Moreover, porosity and thickness of the catalyst layer also have to be optimised. On the one hand high catalyst layer porosity leads to the increase of the mass transfer rates, but on the other hand, it results in a decrease of electron and proton transport rates. Porosity is usually in the range from 30 to 60 % for PEMFC electrodes. The thickness of the catalyst layer may be reduced by using high Pt loadings. For example, catalyst layer with 10 μm thickness for 0.4 mg/cm^2 Pt loading can be prepared with 50 wt. % Pt/C electrocatalyst, which allows to reduce ionic and mass-transfer resistance [12].

Pt is the state of the art catalyst for both HOR and ORR. The sluggish ORR kinetics can be improved by using Pt alloys. In particular, so-called Pt skin structure with a pure Pt atomic layer on the surface of the alloys has shown high ORR activity [36]. For example, $Pt_3Ni_1(111)$ skin provided two orders of magnitude higher ORR activity compared with commercial Pt/C [37],[38]. However, the main disadvantage of Pt-based catalysts is their high cost. Therefore, non-precious metal catalysts have attracted great attention [39]. Already in 1964 Jasinski et al. [40] investigated activity of Co phthalocyanine as a fuel cell cathode catalyst. Dodelet's group has achieved high ORR activity increase by mixing carbon support with iron and nitrogen precursors, followed by ball-milling and pyrolysis. Such Fe-based catalysts contain Fe cations coordinated by pyridinic nitrogen (active sites) in the graphitic sheets within the micropores [41]. Research is performed on non-noble metal catalysts in the Laboratory.

Catalyst supports play an important role in the improvement of fuel cell performance and durability. They are used in order to increase the surface area of catalyst per unit of mass as well as to prevent the agglomeration of the catalyst nanoparticles. The catalyst support should possess the following properties:

- High electronic conductivity;
- High surface area to enhance catalyst dispersion;
- High amount of mesopores to provide an accessibility of the reactants to the catalytic sites and removal of the water;
- High stability in acidic environment and at high potentials under fuel cell operation.

Performance, durability and cost of CL are main aspects to be considered for the commercialisation of PEMFC. According to the United States Department of Energy (DOE)

2017 targets, the MEA with platinum group metals loading of 0.125 mg/cm^2 should provide power densities of 8.0 kW/g_{Pt} [17]. Furthermore, electrocatalyst has to maintain 90 % of its initial performance after 5000 h of operation [42].

1.2.4 Degradation of MEA components

One of the fundamental drawbacks of PEMFC is its poor durability overtime. Therefore, it is important to understand the mechanisms of catalyst and membrane degradation in order to improve their stability.

1.2.4.1 PEM degradation

The PEM degradation can be physical (cracks and creep) or chemical due to peroxide radical formation during PEMFC operation. Operating conditions, such as relative humidity (RH), temperature, cell voltage and current density have a great influence on both types of degradation. In particular, fast degradation occurs under open circuit voltage (OCV) conditions.

Chemical degradation

According to the LaConti mechanism, oxygen crossover through the membrane to the anode results in H_2O_2 formation [43]:

$$H_2 + Pt \rightarrow Pt\text{-}H \text{ (anode)}$$

$$Pt\text{-}H + O_2 \text{ (diffused through PEM to anode)} \rightarrow \bullet OOH$$

$$\bullet OOH + Pt\text{-}H \rightarrow H_2O_2$$

Hydrogen peroxide formation is accelerated at the anode side at potentials below 0.2 V, where the hydrogen adsorption occurs on the Pt surface [44]. The presence of impurities such as Fe^{2+} and Cu^{2+} enhances the membrane degradation [45],[46] due to the formation of hydroxyl and hydroperoxyl radicals in the reaction with H_2O_2 (Fenton reaction):

$$Fe^{2+} + H_2O_2 \rightarrow Fe^{3+} + \bullet OH + OH^-$$

$$\bullet OH + H_2O_2 \rightarrow + \bullet OOH + H_2O$$

Furthermore, at high potential Pt nanoparticles dissolution from the cathode and re-precipitate in the membrane takes place [47]. Such Pt ions can generate free radicals inside the membrane [48]. Formed radicals tend to attack the end groups of the polymer, which results in fast polymer decomposition leading to the thinning of the membrane and loss of fluorine [49]:

$$R\text{-}CF_2COOH + \bullet OH \rightarrow R\text{-}CF_2\bullet + CO_2 + H_2O$$

$$R\text{-}CF_2\bullet + \bullet OH \rightarrow R\text{-}CF_2OH + R\text{-}COF + HF$$

$$R\text{-}COF + H_2O \rightarrow R\text{-}COOH + HF$$

The main strategies to extend membrane lifetime include reduction of metal ion contaminations, avoiding oxygen permeability and increasing membrane humidification [50]. Furthermore, new polymer composites with improved chemical stability have been developed [51]. Finally, chemical cross-linking and the use of radical-trapping metal ions are effective approaches for improving PFSA membrane stability. For example, Ce^{3+} and Mn^{2+} ions known as radical scavengers or inhibitors can prevent membrane degradation [52],[53]. However, presence of such ions can decrease membrane conductivity by blocking the cation exchange sites. Therefore, a good compromise between high durability and high performance of PEM should be found [54]. Novel approaches to the integration of radical scavengers in MEAs are being developed in the Laboratory.

Physical degradation

Although PFSA-based membranes are considered as stable, the physical degradation is still observed in particular for thin membranes (<50 µm). Such physical degradation can be caused by various phenomena such as swelling, local drying under low-humidity conditions, contact pressure, high local current density, changes in temperature and catalyst penetration into the membrane. The mechanical properties of PFSA can be improved by using chemical cross-linking or physical reinforcement. Especially, the latter one has been explored to great extent due to the easy fabrication by using inorganic nanoparticles such as oxides and zirconium phosphate or porous electrospun fibre mat as reinforcing matrix [30].

1.2.4.2 Electrode degradation

Electrode durability is one of the main issues concerning PEMFC technology. There are two main mechanisms of electrode degradation such as carbon corrosion and platinum nanoparticles dissolution and agglomeration. Each of them has an influence on each other [55].

a Carbon corrosion

It has been suggested that at potentials above 0.2 V, carbon can undergo corrosion, as shown in the following reaction [56]:

$$C + 2H_2O \rightarrow CO_2 + 4H^+ + 4e^- \qquad (E^0 = 0.206\ V_{RHE})$$

However, at potentials encountered in normal PEMFC operation (0.6 – 0.9 V_{RHE}) kinetics of carbon corrosion is slow. It is generally accepted that elevated potentials greater than 1.2 V_{RHE} lead to the corrosion of carbon at a significantly high reaction rate.

Different factors influence the kinetics of carbon corrosion:

- Structure of the carbon particles. Carbon black composed of an amorphous core and graphitic surface are generally less stable compared to graphitised carbon.
- Presence of Pt accelerates formation of highly reactive OH and OOH radicals, which can attack carbon surface [57].
- Carbon functionalisation with various groups such as phenols, carbonyls, carboxylic acids, ethers, quinones, and lactones, might play the role of protective layer. However, the presence of water results in further oxidation of the surface oxide layer to CO_2 [58]:

$$\text{R-C-H} \rightarrow \text{R-C-OH} \rightarrow \text{R-C=O} \rightarrow \text{R-COOH} \rightarrow \text{R-H} + CO_2$$

Carbon functionalisation leads to an increase in the hydrophilicity of the catalyst layer, which results in flooding and mass-transport overpotentials.

- Some PEMFC operating conditions such as start-up and shutdown lead to local fuel starvation, when H_2 and O_2 are coexisting in the anode side. Thus, oxygen reduction occurs at the anode side. Protons for this reaction can be obtained from carbon oxidation or oxygen evolution reaction at the cathode side, as shown in Figure 11. Consequently, a reverse current is established, which forces the cathode to very high potentials up to 1.44 V leading to carbon corrosion in a short period of time [59]. Therefore, local hydrogen starvation is one of the main reasons for catalyst layer degradation on the cathode side.

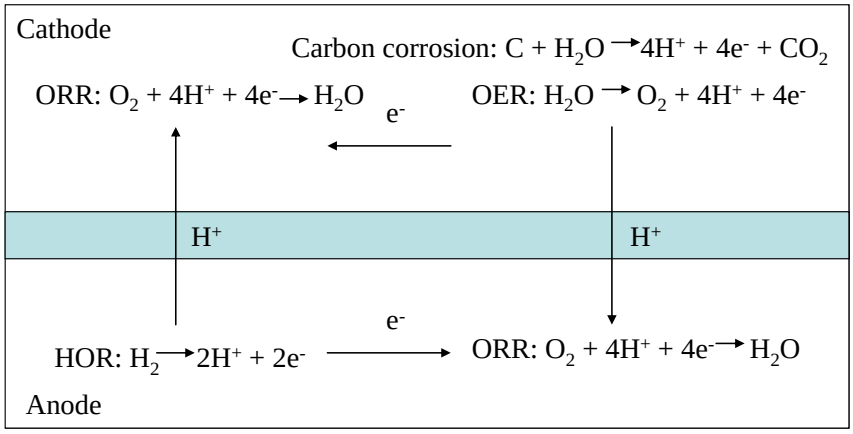

Figure 11: A schematic illustration of electrode reactions occurring during start/stop conditions [56]**.**

Maas et al. [60] and Mathias et al. [61] reported that carbon degradation depends on potential, temperature and humidity. The mechanism of carbon corrosion consists of the following steps [62]:

- oxidation of the carbon lattice, $C \rightarrow C^{+} + e^{-}$
- hydrolysis, $C + 1/2H_2O \rightarrow CO + H^{+}$ ($E^0 = 0.518\ V_{RHE}$)
- carbon dioxide formation, $CO + H_2O \rightarrow CO_2(g) + 2H^{+} + 2e^{-}$ ($E^0 = -0.103\ V_{RHE}$)

Carbon corrosion results in detachment of catalyst nanoparticles and thinning of cathode catalyst layer leading to PEMFC performance losses.

b Platinum dissolution and agglomeration

The Pourbaix diagram shown in Figure 12 presents stability region for Pt, PtO, PtO_2 and PtO_3 as a function of electrolyte pH and electrode potential at 25 °C [63]. Pt is thermodynamically unstable at pH lower than 0 and potential higher than 1.0 V_{RHE}. Furthermore, Pt dissolution increases with the increasing potential and temperature.

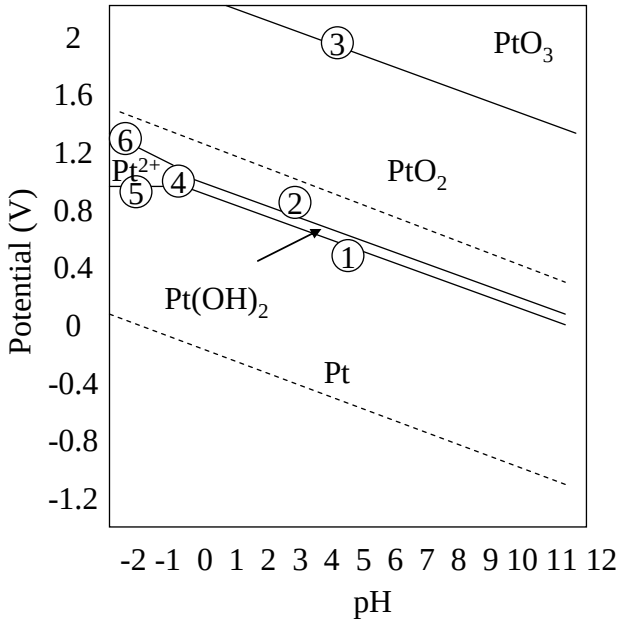

Figure 12: Regions of stability for platinum vs potential and pH at 25 °C and the corresponding reactions:

1. **$Pt + 2H_2O \rightarrow Pt(OH)_2 + 2H+ + 2e^{-}$;**
2. **$Pt(HO)_2 \rightarrow PtO_2 + 2H^{+} + 2e^{-}$;**
3. **$PtO_2 + H_2O \rightarrow PtO_3 + 2H^{+} + 2e^{-}$;**
4. **$Pt^{2+} + 2H_2O \rightarrow Pt(OH)_2 + 2H^{+}$;**
5. **$Pt \rightarrow Pt^{2+} + 2e^{-}$;**
6. **$Pt^{2+} + 2H_2O \rightarrow PtO_2 + 4H^{+}\ 2e^{-}$.**

Darling and Meyers described a three-step model, which explains the oxidation and dissolution of platinum in a PEMFC [64],[65]:

Platinum dissolution: $Pt \rightarrow Pt^{2+} + 2e^{-}$;

Platinum oxide formation: $Pt + H_2O \rightarrow PtO + 2H^{+} + 2e^{-}$;

Platinum oxide dissolution: $PtO + 2H^{+} \rightarrow Pt^{2+} + H_2O$.

Whereas Shao-Horn et al. proposed four mechanisms explaining the decrease of electrochemical surface area (ECSA) especially after potential cycling operations [66]:

- **Ostwald ripening** involves Pt dissolution from small size particles and re-deposition (reduction) onto large particles, which results in the growth of larger particles at the expense of small ones [67].
- **Pt crystal migration and coalescence** on the carbon support without Pt dissolution by thermal motion (sintering).
- **Dissolution and re-precipitation of Pt single crystals in the membrane** involves the dissolution of Pt in the first step followed by migration into the membrane and finally deposition of Pt metal in a reducing atmosphere. This leads to Pt loss from the catalyst layer. Platinum band is usually observed in aged MEA [68].
- **Detachment of Pt nanoparticles** occurs due to carbon corrosion. Such isolated Pt particles are not able to participate in the electrochemical reactions.

Poisoning of the Pt surface with contaminates from the fuel and the air (such as CH_4, CO, CO_2, H_2S, NH_3, NO, NO_2, SO_2, SO_3, and O_3) also leads to the loss of catalyst activity and fuel cell performance. For example, adsorbed CO blocks the access of H_2 to the Pt catalytic active sites and thereby decreases the activity of the catalyst [69].

2 State of the art for PEMFC electrocatalyst supports

2.1 Carbon-based catalyst supports

The properties of catalyst support play important role for PEMFC performance and durability. For example, electrode thickness, catalyst activity and stability can be influenced by the choice of the support. Therefore, various carbon-based materials such as carbon blacks, mesoporous carbon, carbon nanofibres and nanotubes were developed.

2.1.1 Carbon blacks

Carbon blacks are conventionally used as catalyst support due to their high electrical (>1 S/cm) and thermal conductivity, high surface area (1500 m^2/g for Black Pearls) and the ability to form porous CL. They are cheap and available in large quantities. Carbon blacks consist of porous particles of around 20 - 50 nm in diameter. Two main types of carbon blacks are usually used in PEMFC [28]:

- furnace blacks (e.g., Vulcan XC-72R with surface area of ca 230 m^2/g) made by pyrolysis from heavy oils;
- extra conductive blacks (e.g. Ketjen Black with surface area of ca 800 m^2/g), a by-product of heavy oil cracking.

Carbon blacks with a hydrophobic agent (PTFE) are also used as the microporous layer in the GDL. However, the electrochemical and thermal stability of these materials need to be improved. Especially, amorphous core of carbon particles is susceptible to corrosion. Other disadvantages of the carbon black are microporous structure and impurities formed during synthesis.

2.1.2 Mesoporous carbon

Mesoporous carbon [70],[71] can be divided into ordered (OMC) with regular pore structure and disordered (DOMC) carbon. Both provide high surface area with pore size between 2 and 50 nm. OMCs are usually prepared by using mesoporous templates. Yu et al. [72] investigated the effect of the catalyst support pore size on DMFC performance. They demonstrated that mesoporous carbon with a pore diameter of 25 nm showed the highest performance due to its high surface area and large pore volume. In comparison with Vulcan XC-72R, mesoporous carbons possess less micropores and deep cracks, which hinder triple-phase boundary formation. Thus, high surface area and interconnected mesopores system can facilitate the transport of reactants and products. However, the cost of mesoporous carbon is much higher than that of conventional carbon blacks.

The durability of both carbon blacks and mesoporous carbons needs to be improved. Therefore, graphitised carbons were developed. For example, Shao et al. obtained a highly graphitised mesoporous carbon (GMPC) supported Pt, which exhibited an improved activity and durability compared to the commercial Pt/C [73].

2.1.3 Graphitised and nitrogen doped carbons

Graphitised carbons can be obtained by heat-treatment at high temperatures. High graphitic content leads to stronger delocalised π-bond (sp^2-hybridised carbon) on the carbon surface, which are important for the strong metal–support interaction (SMSI) [74]. Moreover, graphitisation enhances stability and conductivity of the carbon, but decreases its surface area. As a consequence, catalyst nanoparticles dispersion is usually reduced. Furthermore, graphitisation does not eliminate corrosion completely; it only slows down the reaction kinetics.

Nitrogen-doped carbons as support showed enhanced catalytic activity and durability towards oxygen reduction and methanol oxidation due to a better interaction between Pt nanoparticles and the support [75].

a. Carbon nanotubes (CNTs)

Since the first reports of CNTs in 1991 by Iijima et al. [76], they have attracted huge interest in the field of nanotechnology. CNTs are also used as catalyst support for PEMFC [77],[78]. They consist of graphene sheets rolled into a cylinder. There are two types of CNTs, namely, single-wall (SWCNTs) and multi-wall (MWCNTs) with diameter of ca 10-50 nm, as shown in Figure 13.

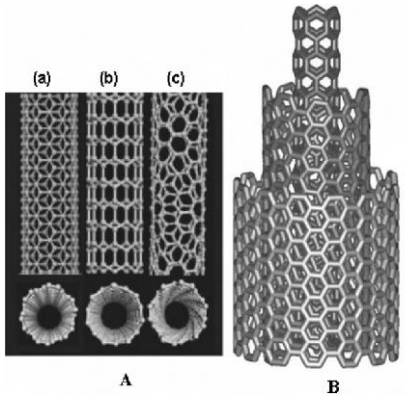

Figure 13: A: Schematic illustrations of the structures of (a) armchair, (b) zigzag, and (c) chiral SWCNTs. B: Structure of a MWCNT [79]**.**

There are three main synthesis methods of CNTs namely arc discharge, laser ablation and chemical vapour deposition (CVD) via catalytic deposition of carbon precursors [79]. CVD method allows control of morphology of the CNTs and their orientation on the substrate.

CNTs provide many advantages such as high electrical conductivity, high corrosion resistance [80], high surface area (200 – 400 m^2/g for MWCNTs and 400 – 900 m^2/g for SWCNTs) and strong interaction with the Pt nanoparticles (due to the delocalised π electrons of CNTs), resulting in increased catalytic activity of the Pt supported on CNTs. Moreover, CNTs possess improved mesoporosity, fewer organosulfur impurities (poisoning for Pt) as well as higher mechanical and thermal stability compared to carbon blacks [81]. Unlike carbon blacks, CNTs are free from deep cracks, which can be the cause of catalyst activity losses [82],[83]. However, CNTs are chemically inert thus making it difficult to deposit Pt nanoparticles. Functionalisation of the CNTs with strong acids (HNO_3 and H_2SO_4) introduces surface groups such as hydroxyl and carboxyl acid groups, which can improve the dispersion of catalyst nanoparticles. Nevertheless, CNTs supported catalysts have received great attention due to their enhanced activity and durability [84],[85],[86]. Saha and co-workers [87] developed MWCNTs grown on a carbon paper supported Pt nanoparticles. Such electrodes have provided higher single-cell performance in a H_2/O_2 fuel cell than Pt/C-based electrodes. However, the high cost of production and the risk for the health [88] have hindered the commercialisation of CNTs.

b. Graphite-based carbon nanofibres (CNF)

Graphitised CNFs are cyclindric nanostructures with high aspect ratio, which consist of graphene sheets. There are three main types of CNFs namely stacked platelet (graphene layer perpendicular to the growth axis), tubular (graphene layer parallel to the growth axis) or fishbone type (with an angel of 45° to the growth axis), as shown in Figure 14 [78].

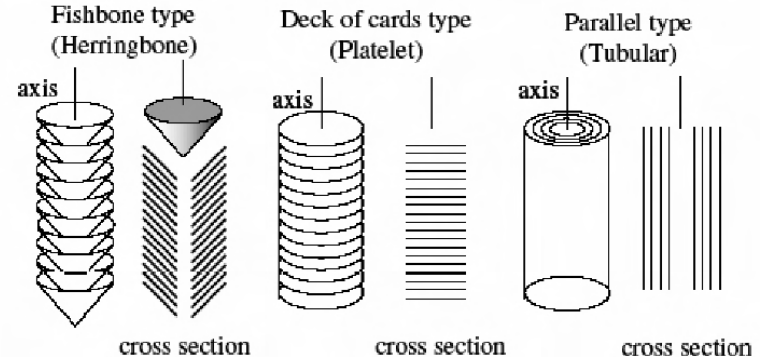

Figure 14: Schematic representation of three types of CNFs [79].

The diameter of CNFs is much higher than that of CNTs and can reach up to 500 nm. CNF are usually produced by CVD or by electrospinning of polymer solutions (see Paragraph 3) followed by a thermal-treatment [89]. As CNTs, CNFs are promising catalyst supports for PEMFC due to their high electrical conductivity, high corrosion resistance and strong interaction between catalyst and support [90]. In addition, they provide crystalline structure and high conductivity at a lower cost compared with CNTs [91].

CNFs supported catalysts have received great attention in particular for DMFC. For instance, Bessel et al. [92] demonstrated that platinum supported on "platelet" and "ribbon" type graphite showed improved performance for methanol oxidation compared to Vulcan XC-72R. Park et al. [93] also reported that a graphite carbon nanofibres (G-CNFs) supported PtRu catalysts showed higher catalytic activity towards methanol oxidation than the Vulcan XC-72R supported catalyst due to the strong interactions between the metal particles and the G-CNFs. Furthermore, Knupp et al. [94] observed that the electrochemical surface area (ECSA) of Pt/CNFs (64.8 m^2/g) was higher than that of commercial Pt/C catalyst (50.6 m^2/g).

Li et al. [95] deposited Pt nanoparticles of 2 - 4 nm on stacked-cup carbon nanofibres (SC-CNFs obtained by CVD) via a modified ethylene glycol method. The Pt/SC-CNFs-based MEA demonstrates higher Pt utilisation than carbon black-based MEA due to the formation of continuous conductive networks in the ionomer matrix.

2.1.4 Conductive diamonds

Diamond is a promising catalyst support for PEMFC owing to its very wide potential window, mechanical stability and corrosion resistance under oxidative conditions. Electrical conductivity of non-conducting diamond can be improved by using p-type (boron) or n-type (nitrogen) doping. For instance, boron doped diamond (BDD) developed by Wang and Swain, exhibit no activity loss even after 2000 potential cycles [96]. Generally, BDD possesses low surface area, which should be improved in order to make this material more promising for PEMFC applications [97],[82].

2.2 Alternative supports materials

Another approach to overcome the problem of support corrosion is replacement of carbon by alternative materials. Thus, metal oxides, carbides, borides, nitrides and organic whiskers have been developed in order to meet the durability targets for PEMFC [70],[98],[99].

Moreover, the presence of strong metal support interactions (SMSI) [100] can increase ORR activity, stability, CO-tolerance of the catalyst and even enhance charge-transfer

properties [101]. For instance, a decrease in Pt 4f binding energy observed for $Pt/TiO_2/C$ compared to Pt/C using XPS was attributed to increased electron density on the Pt surface atoms, which can explain enhanced ORR activity of TiO_2 supported Pt [102]. Also, Pt/SnO_2-C showed improved ORR activity, CO-tolerance and stability compared to Pt/C due to SMSI [103].

2.2.1 Carbides

Metal carbides are very attractive support materials due to their stability in acidic solutions at anodic potentials, unique resistance to poisons (carbon monoxide, hydrocarbons, and hydrogen sulfides) and high electrical conductivity. Tungsten carbide is the most studied among other carbides due to its high electrical conductivity and commercial availability. Chhina et al. demonstrated that Pt supported on WC provides lower ORR activity, but higher durability than conventional Pt/C catalyst [104],[105]. Bernard d'Arbigny et al. developed Pt supported on hollow carbon microspheres with a tungsten carbide kernel, which demonstrated high specific surface area, electrical conductivity and high ECSA retention after prolonged cycles [106]. Furthermore, Nie et al. reported much higher ORR activity for Pt-WC/C than for Pt/C [107]. However, thermodynamic instability in oxidative environments is one of the main disadvantages of carbides [98].

2.2.2 Metal oxides

Conducting oxides are promising candidates that may replace commercial carbon in PEM fuel cells due to their high electrochemical stability and SMSI, which could promote electrocatalysis and favour the anchoring of catalyst nanoparticles in the oxide surface [82],[108]. According to thermochemical calculations reported by Sasaki et al. [109], Sn, Ti, Nb, Ta, W, and Sb are stable as oxides under PEMFC conditions such as 80 °C, 1.0 V_{SHE} and pH = 0. This calculations are in agreement with the experimental data [110], [111]. Furthermore, transition metal oxides (CeO_2, SnO_2 and TiO_2) are known to accelerate alcohol electrooxidation and enhance CO-tolerance of Pt [112], consequently, they are widely used in DMFCs anodes [113]. Finally, oxides with good proton conductivity can improve transfer of protons in the catalyst layer [114].

Pt supported on various oxides such as TiO_x, SnO_x, WO_x, CeO_2, MoO_x, RuO_x and Ta_2O_5 have been already explored as electrocatalyst for PEMFC and DMFC [98],[114]. For instance, Pt immobilised in a tungsten oxide matrix exhibited enhanced activity of methanol oxidation

reaction [115],[116],[117]. In this paragraph, progress in development of titanium and tin oxides is reviewed.

a. Titanium oxide as catalyst support

Titanium oxide is commonly applied in pigments, coatings and sunscreens [118]. Since discovery of photocatalytic water splitting on TiO_2 by Fujishina and Honda [119] in 1972, TiO_2 is widely explored for energy-related applications [120], such as photocatalysis, dye-sensitised solar cells, Li-ion batteries, supercapacitors and fuel cells. Titania is very stable under PEMFC conditions, non-toxic, cheap and available. All these advantages make titanium oxide a promising support material, but its poor electrical conductivity (10^{-13} S/cm) has to be improved. Indeed, TiO_2 is a semiconductor with a band gap of 3.2 eV for anatase and of 3.0 eV for rutile. Its electrical conductivity can be increased by doping (with Nb, V, Ta and Ru) or by reduction at high temperatures to form sub-stoichiometric oxides. For instance, Pt supported on Ru doped TiO_2 was investigated by Haas et al. [121] and Wang et al. [122].

Nb is the most used n-type dopant [123] due to the similarity of the ionic radius of Ti^{3+} (0.68 Å) and Nb^{5+} (0.7 Å) as well as the possibility of solid solution formation in a wide concentration range [124]. The charge compensation for substitution of Ti^{4+} by Nb^{5+} can be reached via the creation of one Ti^{4+} vacancy per four Nb atoms or via reduction of one Ti^{4+} to Ti^{3+} per Nb atom [125].

Recently, Wang et al. prepared Pt [126] and PtPd [127] nanoparticles supported on 6 at. % Nb doped TiO_2. Such Pt-Pd alloy supported on Pd-composited $Nb_{0.06}Ti_{0.94}O_2$ electrocatalyst showed higher mass activity than Pt/C.

Another approach to create conductive oxide is the formation of sub-stoichiometric oxide by heating TiO_2 in the presences of H_2 or with metallic titanium under an inert atmosphere [128]:

$$nTiO_2 + H_2 \rightarrow Ti_nO_{2n-1} + H_2O$$

$$1/2Ti+(n-1/2)TiO \rightarrow Ti_nO_{2n-1}$$

Such titanium suboxides Ti_nO_{2n-1} where $3 < n < 10$ (Magneli phases) are commercially available under the Ebonex® (Altraverde) trade name. In general, titanium suboxides exhibit high conductivity (1000 S/cm for Ti_4O_7 at RT [82]), but low specific surface area [129], which may lead to poor catalyst dispersion. Chen et al. [128] compared stability of different conductive oxide supports such as Ebonex®, and Ti_4O_7 and $Nb_{0.1}Ti_{0.9}O_2$. They all showed high electrical conductivity, but poor surface area between 1 and 2 m^2/g. Ebonex® and Ti_4O_7 microparticles could be thermally oxidised in air at temperature above 400 °C to non-

conductive TiO_2, unlike $Nb_{0.1}Ti_{0.9}O_2$, which was thermally and electrochemically stable. Ioroi et al. [130] also prepared Ti_4O_7 microparticles, which were more oxidation-resistant than Vulcan XC-72R. However, the mass activity of Pt/Ti_4O_7 was lower than that of conventional Pt/C, what was attributed to low ECSA of Pt/Ti_4O_7. Recently, Ioroi et al. [131],[132],[133] obtained Magneli phase TiO_x with improved surface area of more than 20 m^2/g using a pulsed UV laser irradiation method. Pt supported on such nano-submicron TiO_x particles provided high ORR activity and retained their initial ECSA even after 10000 voltage cycles between 0.05 and 1.2 V vs RHE at 100 mV/s, while Pt/Vulcan XC-72R lost 30 – 50 % of its ECSA. Ti-alloyed Pt/TiO_x catalysts demonstrated higher specific activity than conventional Pt/Vulcan XC-72R due to the formation of Pt-Ti alloy.

Both approaches Nb doping and high-temperature reduction can be applied in order to enhance electrical conductivity. For example, Park et al. [134] developed Nb-TiO_2 nanoparticles (reduced at 400 °C) supported Pt that showed better ORR activity than commercial Pt/C, which was explained by SMSI. In contrast, Chhina et al. [135] obtained Nb-TiO_2 (reduced at 700 °C) supported Pt, which was less active, but more stable than Pt/C. However, Nb-TiO_2 (reduced at 700 °C) supported Pt obtained by Popov group [136] exhibited improved conductivity, activity, as well as high durability. The properties of recently developed TiO_x supported catalyst are summarised in Table 2.

Titanium oxide nanotubes (TONT) are attractive catalyst supports due to their high surface area and mesoporosity [137]. Wang et al. [138] and Macak et al. [139] reported that TONT supported catalyst showed high methanol oxidation activity. Kang et al. developed TONT supported PtNi [140] and PtCo [141] electrocatalysts. PtNi/TONT showed very poor ORR activity (due to the OH adsorption), which was significantly improved after reduction in H_2 at 400 °C. $Pt_{70}Co_{30}$/TONT electrocatalyst showed much higher ORR activity compared to $Pt_{70}Co_{30}$ on compact TiO_2 films due to the high surface area, accessibility of the inner wall and porous structure of the TONT. Recently, Zhang et al. [142] developed ternary tin-palladium-platinum catalysts supported on hydrogenated TiO_2 nanotube arrays [143].

Such electrocatalyst exhibits much higher activity and excellent longer-term electrochemical durability compared to the commercial 20 % Pt/C.

Table 2: Properties of TiO_2 as catalyst support for PEMFC.

Ref.	Electro-catalyst	Synthesis of the support	T, °C gas	Sur-face area, m^2/g	Conducti-vity of the support, S/cm	ECSA, m^2/g (Pt-NP size)	ORR activity or max power density	Catalyst was more stable than Pt/C after the following test
Park 2007 [134]	Pt/Nb-TiO_x	hydro-thermal	400 H_2	-	0.1	- (3 nm)	higher than that for Pt/C	-
Chhina 2009 [135]	Pt/Nb-TiO_x	hydrolysis	700 H_2	13	$6.1\ 10^{-4}$	-	lower than that for Pt/C	60 h at 1.4 V
Huang 2009 [144]	Pt/TiO_2	template-assisted	-	250	-	13.8 (6.2 nm)	0.94 W/cm^2	200 h at 1.2 V
Huang 2010 [136]	Pt/Nb-TiO_x	template-assisted	700 H_2	10	1.11	-	0.72 W/cm^2	2500 cycles (0 - 1.2 V)
Huang 2011 [145]	Pt/TiO_2	template-assisted	-	266		31.2 (5.1 nm)	2.3 mA/cm^2 at 0.85 V 1.01 W/cm^2	2500 cycles (0.6 -1.4 V)
Ioroi 2011 [132]	Pt/TiO_x	pulsed UV laser irradiation	900 H_2	-	10^{-3}	(5-10 nm)	-	10000 cycles (1.0 -1.5 V)
Huang 2012 [146]	PtPd/ TiO_2	template-assisted	300 N_2	186	$1.47\ 10^{-6}$	(3-5 nm)	3 mA/cm^2 at 0.85 V 1.15 W/cm^2	1500 cycles (0.6 -1.4 V)
Bauer 2012 [149]	Pt/Nb-TiO_2	sPEEK template	500 air	120	-	25 (5 nm)	3.9 A/g_{Pt} at 0.9 V	1000 cycles (0.05 -1.2 V)
Chevallier 2012 [150]	Pt/Nb-TiO_2	sPEEK template	500 air	120 -150	$1\ 10^{-4}$	30	5.3 A/g_{Pt} at 0.9 V	1000 cycles (0.05 -1.2 V)
Zhang 2013 [143]	NiPt/ TiO_2 tubes	Electro-chemical anodic oxidation	-	104	$1.42\ 10^{-4}$	(30 nm)	0.557 W/cm^2	600 cycles (0 -1.2 V)
Wang 2012 [126]	Pt/$Nb_{0.06}$-$Ti_{0.94}O_2$	acid-catalysed sol-gel	400 H_2	63- 48	$2\ 10^{-5}$	11 - 27	6-32 A/g_{Pt} at 0.9 V	19 % mass activity loss 1000 cycles (0 -1.2 V)
Wang 2013 [127]	PtPd/ $Nb_{0.06}$-$Ti_{0.94}O_2$	acid-catalysed sol-gel	700 H_2	4.5	$4.45\ 10^{-3}$	22.2	130 mA/mg_{Pt} at 0.9 V	Mass activity losses are 31 – 74 % 1000 cycles (0 -1.2 V)
Siracusano 2013 [147]	Pt/TiO_x (amorph) $TiTaO_x$ (amorph) $TiTaO_x$ TiO_2 $TiTaO_x$	complexation complexation complexation sulphite route sulphite route	300 – 600 air	117.7 253 66 279 175	0.38 Ohm cm^2/mg 0.04 0.39 0.12 0.09	-	Pt/$TiTaO_x$ (Sulphite route) showed the best PEMFC performance	-
Stassi 2013 [148]	PtCo/Ta-TiO_2	sulphite route	400 O_2	150	-	12.1 (2.9 nm)	lower performance than PtCo/C	Holding at 1.4 V for 150 min
Cerri 2013 [151]	Pt/Nb-TiO_2	physical vapor deposition (PVD)	450 – 600 O_2	-	~0.1 Ohm cm	(2 nm)	Pt/6.1% Nb-TiO_2 has the best ORR activity	-

Popov et al. developed a high surface area (186 - 266 m^2/g) mesoporous TiO_2 (calcined at 300 °C) supported catalyst [144],[145],[146] that showed high ORR activity as well as high electrochemical stability. However, large catalyst loading (~60 wt. %) and ultrathin catalyst layer (~ 1 µm) were used to overcome the problem of low support conductivity. Recently, Arico et al. investigated Pt [147] and PtCo [148] supported on Ta doped TiO_2. Such PtCo/oxide showed a lower ECSA and larger ohmic resistance, but higher durability compared to Pt_3Co_1/C.

High surface amorphous titania calcined at low temperature is usually non-conductive, but it can provide high catalyst dispersion even at large metal loadings, which are required to improve the resistance of the catalyst layer. However, amorphous titania showed low stability in strong acidic environment [143]. In contrast, sub-oxides are highly conductive, but generally they have poor surface area. Doped TiO_2 is usually more stable than sub-oxide. Consequently doping is preferred. Synthesis of highly conductive Ti oxide with large surface area and mesoporous structure is still a challenge. Therefore, a compromise between conductivity, surface area, crystalline properties and stability needs to be found.

b. Tin oxide as catalyst support

Tin oxide is widely used in solar cells, microelectronics, displays, gas sensors, oxidation catalyst and transparent conductor [152]. Table 3 summarises the properties of SnO_2 and Pt/SnO_2. As shown in the last column of the Table 3, SnO_2 as support can withstand high cyclability under high applied potential. Tseung and Dhara were the first to investigate the activity of Pt supported on tin oxide for the reduction of oxygen. They demonstrated that the doped electrocatalyst was more stable than Pt black at 150 °C in 85% H_3PO_4 [153]. Watanabe et al. also developed conductive tin oxide supported Pt for ORR [154]. Enhanced oxygen reduction activity on tin oxide supported Au was attributed to the metal support interactions [155]. Recently, Pt supported on high surface area mesoporous tin oxide demonstrated good activity for ORR and better stability in cycling test than commercial Pt/C catalyst [156].

Adsorption of OH species on SnO_2 promotes the oxidation of CO and alcohols on the Pt surface and thus leads to enhanced tolerance of the catalyst towards CO poisoning. Therefore, SnO_2 supported catalysts were successfully used for formic acid [157], methanol and ethanol oxidation reactions (MOR and EOR) [158],[159],[160]. Okanishi et al. demonstrated that the degradation of Pt/SnO_2 with 100 ppm CO was much smaller than that of Pt/C due to the strong interactions between Pt and SnO_2 [161].

Tin oxide is an n-type semiconductor with rutile structure and band gap of 3.6 eV. Its electrical resistivity varies in the range from 10 to 10^6 Ω cm, depending on the oxide stoichiometry. However, electrical conductivity of SnO_2 can be improved by using either a donor (Sb^{5+}, Nb^{5+}) or acceptor (Al^{3+}) doping [110]. For example, electrical conductivity of SnO_2 was increased dramatically by doping it with Sb [162]. Pt supported on Sb doped SnO_2 (Pt/ATO) showed not only higher activities for MOR and EOR, but also higher stability than commercial Pt/C [163]. Furthermore, Pt/ATO electrocatalyst showed improved activity for the ORR in comparison to Pt black [164]. Recently, Yin et al. [165] also synthesised ATO support with improved electrical conductivity (1.13 S/cm at 130 °C). Pt on such ATO/carbon composite support showed enhanced ORR activity and durability, which was attributed to modified electronic structure of Pt by the ATO. Ru-SnO_2 supported Pt possesses good catalytic activity towards MOR as well as improved durability [166],[167]. However, Elezovic et al. [168] recently demonstrated that Pt/Ru-SnO_2 was less stable than Pt/Sb-SnO_2.

Takasaki et al. [110] showed that Nb doping leads to an improvement in the electronic conductivity and specific surface area of tin oxide. Pt supported on such Nb doped tin oxide demonstrated excellent stability towards potential cycling. Recently, the same group developed Nb doped SnO_2 cathode using pulse laser deposition in order to reduce contact resistance between the particles of SnO_2. Such $Sn_{0.98}Nb_{0.02}O_2$ supported Pt electrocatalyst provided improved PEMFC performance while keeping the high durability [169].

One-dimensional structures (high-aspect-ratio supports) such as nanofibres and nanotubes are known to have unique electrical properties and high specific surface area [78]. Saha et al. developed catalyst supported on SnO_2 nanowires grown directly on the carbon paper by a thermal evaporation method, which exhibited higher activity for ORR and MOR than a commercial Pt/C [170],[171]. Authors attributed such high activity mainly to the unique 3D structure of the nanowires support and strong interaction between Pt and SnO_2.

Recently, Dou et al. reported that Pt supported on SnO_2 nanoclusters demonstrated comparable performance to Pt/C as anode electrocatalyst, but exhibited superior stability [172]. Zhang et al. [156] obtained Pt supported on high surface area mesoporous tin oxide (205 m^2/g), which demonstrated good activity for ORR and better stability towards potential cycling than commercial Pt/C catalyst. Gurrola et al. [173] obtained mesoropous ATO with the highest until now reported surface area of 217 m^2/g. Such ATO supported Pt electrocatalyst showed significant stability compared with Pt/Vulcan XC-72R. Sasaki et al. [174] reported that Pt/SnO_2 shows the best performance in terms of both

electrochemical activity, and stability compared to Pt supported on MoO_3, SnO_2, Nb_2O_5, Ta_2O_5, TiO_2, and WO_3.

All these advantages demonstrate that SnO_2 can be a promising candidate that might replace commercial carbon in PEMFCs due to its high electrochemical stability, reasonable electronic conductivity and metal support interactions that could promote electrocatalysis [161].

Table 3: Properties of SnO_2 as catalyst support for PEMFC.

Ref.	Pt on tin oxide	Synthesis	T, °C	Conductivity, S/cm	Surface area, m^2/g	ORR activity or PEMFC performance	Catalyst was more stable than Pt/C after
Saha 2007 [170]	SnO_2 nano-wires	Thermal evaporation method	-	-	-	high	-
Lee 2008 [163]	Sb-SnO_2	Hydrolysis	400	-	99.7	Methanol oxidation	1000 cycles (0.05-1.2V)
Masao 2009 [175]	SnO_2	Co-precipitation	600	-	less than 20	lower than for Pt/C	10000 cycles (0.6 -1.3 V)
Takasaki 2009 [176]	SnO_2 $NbSnO_2$ $AlSnO_2$	Co-precipitation	600	-	less than 30	lower than for Pt/C	10000 cycles 0.9 V (30 s) -1.3 V (30 s)
Zhang 2010 [156]	SnO_2	Neutral surfactant template-assisted method	400	-	205	13 A/g at 0.85 V	1600 cycles (0-1.2 V)
Kakinuma 2011 [177]	$Sb_{0.04}$-$Sn_{0.96}O_{2-\delta}$	Flame combustion method	-	1.2	125	1.2 mA/cm^2 at 0.8 V	5000 cycles (0.9-1.3V)
Takasaki 2011 [110]	SnO_2 Nb-SnO_2 Al-SnO_2 Sb-SnO_2	Co-precipitation	600	10^{-4}	less than 50	lower than for Pt/C	60000 cycles 0.9 V (30 s) -1.3 V (30 s)
Higashi 2013 [169]	$Nb_{0.04}$ $Sn_{0.96}O_2$	Pulse laser deposition	-	-	-	lower than for Pt/C	60000 cycles (1.0-1.5V)
Dou 2013 [172]	SnO_2 nano-cluster	Mesoporous silica as a hard template	700	-	128	anode catalyst	0 h at 1.6 V
Kakinuma 2013 [178]	Nb-$SnO_{2-\delta}$ Sb-$SnO_{2-\delta}$	Flame combustion method	800	1) 0.7 2) 40	1) 37 2) 33	1) 608 A/g at 0.85 V 2) 515 A/g at 0.85 V	10^5 cycles 0.9 V (30 s) -1.3 V (30 s)
Rabis 2013 [179]	SnO_2 thin films	Magnetron sputtering	-	-	3.5	43 μA/cm^2_{Pt} at 0.9 V	-
Gurrola 2013 [173]	Sb-SnO_2	Sol-gel	500	0.202	216.7	-	100 cycles (0 – 1.7 V)
Elezovic 2013 [168]	Sb-SnO_2 Ru-SnO_2	Hydrazine reduction method	400	-	1) 115 2) 141	1) 94 mA/mg 2) 107 mA/mg at 0.85 V	Pt/Sb-SnO_2 is more stable than Pt/Ru-SnO_2
Yin 2014 [165]	Sb-SnO_2 (ATO)	Hydrolysis	600	0.09 – 0.83	21 – 57	Pt/C-ATO showed lower activity than Pt/C	3000 cycles (0.35 -0.85 V)

2.2.3 Nonconductive whiskers

Debe et al. from 3M [180],[181] developed nanostructured thin-films (NSTF), which consist of oriented nonconductive crystalline whiskers obtained by thermal sublimation and annealing of a perylene red organic pigment. These organic whiskers are insoluble in strong acids, chemically and thermally very stable. The thickness of the NSTF can be controlled by changing the length of the whiskers. Such NSTF was sputter-coated by continues Pt layer, which ensures electron transport. Ultrathin electrode layer (10 - 30 times thinner than conventional Pt/C electrode layer) provides lower ionic resistivity even without additional ionomer as well as better access to all Pt surface area. Unlike conventional electrodes, Pt-coated whiskers showed 100 % catalyst utilisation with a reduction in the mass-transport losses at high current densities. Also, such catalyst exhibits much higher stability than Pt/C catalyst towards potential cycling under fuel cell conditions. Recently, PtNi alloy supported NSTF electrocatalyst showed extremely high ORR activities [182],[183].

3 The electrospinning technique

3.1 Introduction and principle

In the last few decades, one-dimensional structures attracted great interest due to their unusual electrical, optical, catalytic and mechanical properties. There are several methods for the fabrication of fibres and tubes such as chemical vapour deposition (CVD), hard and soft templating, hydrothermal, microwave-assisted routes and others [184]. However, they usually require strict synthesis conditions and multi-step procedures.

Electrospinning is a facile method that allows obtaining various materials such as organic, ceramic, hybrid and even metallic fibres, as well as different morphologies such as hollow fibres, core-shell structures and multichannel tubes [185],[186]. Furthermore, it allows preparation of extremely long 1D structures with uniform diameters ranging from tens of nanometres to several micrometres.

In 1902 and 1903 the spraying of liquid by using electrical charges was patented by Cooley and Moore [187]. In 1914 Zeleny observed the spinning behaviour of conducting polymer solution in an electric field [188]. In 1934 Formhals wrote the first patent about electrospinning and its set-up [189]. This method did not receive much attention until the 1990s, when Doshi et al. and other researchers demonstrated that various organic polymers can be electrospun into fibres [190]. Since then, the amount of publications about electrospinning increased dramatically up to 3699 publications in 2013 (from SciFinder).

Electrospinning system consists of a source of high voltage, a grounded collector (usually aluminum plate or rotating drum) a pump and a spinneret (a needle), as shown in Figure 15. Electrospinning setup is usually placed in a closed box in order to control the humidity. The syringe is filled with the polymer solution or the melt. When a high voltage is applied to a drop of fluid polymer on the tip of the syringe needle, the drop becomes charged and elongated into a conical shape due to electrostatic repulsion (this shape is known as Taylor cone). If the electrostatic force overcomes the surface tension and viscoelastic force, a jet of polymer solution forms from the tip of Taylor cone. The liquid jet undergoes an elongation and thinning process, during which the solvent evaporates. This leads to the deposition of the non-woven fibrous mat on the collector.

Several parameters influence fibre diameter and morphology, namely molecular weight and concentration of the polymer, solution properties (viscosity, conductivity and surface tension), process parameters (applied potential, flow rate, distance between the capillary and collector) and ambient parameters (room temperature and humidity). In particular, the

polymer concentration has a very important influence on the fibres morphology and diameter. When the concentration is low, the liquid jet can breakup, what results in the electrospraying of drops. If the concentration is increased, beads and fibres can be obtained. When it is high enough, fibres without beads are obtained. The diameter of the fibres increases with precursor concentration [192].

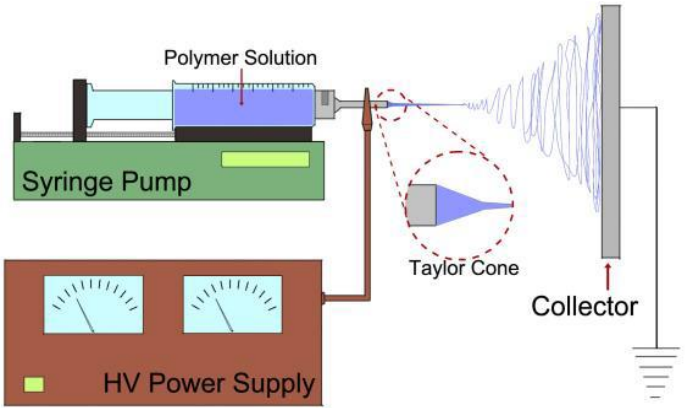

Figure 15: Scheme of the electrospinning set-up [191]**.**

There are various applications of electrospinning [193],[194], such as filtration [195], medical (tissue engineering, wound dressing and drug delivery) [196], sensors [197] and energy related applications [191]. Electrospun fibres and fibre mats are widely used as electrode or membranes in energy conversion and storage devices such as solar cells, fuel cells, lithium ion batteries and supercapacitors due to its high porosity and surface area [198],[199].

Despite the huge progress in electrospinning during the last few decades, the fabrication of fibres without beads and with diameter smaller than 50 nm is still challenging. Another problem is the fragility of the ceramic films, which are easily destroyed after calcination and could not be handled as a self-standing mat.

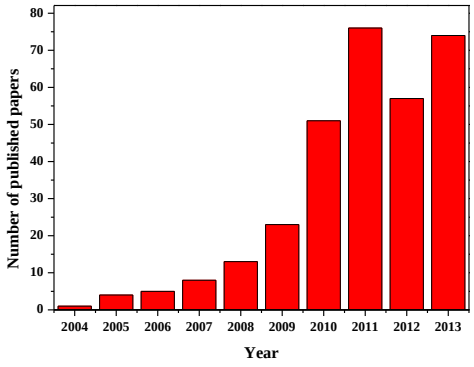

Figure 16: Research articles published on the use of electrospun nanofibres in the field of fuel cell (from SciFinder using keywords: "electrospinning" and "fuel cell").

3.2 Electrospun fibres as electrocatalyst support

In the last years, significant attention has been gained by electrospun fibres for fuel cell applications. The number of publications increased from 1 in 2004 to 74 in 2013, as shown in Figure 16. In particular, carbon and ceramic fibres described in this paragraph have been explored as support to disperse the Pt nanoparticles [191].

3.2.1 Carbon nanofibres

Several polymers can be electrospun and carbonised such as polyacrylonitrile (PAN), polybenzimidazole (PBI), poly(vinyl alcohol) (PVA), poly(amic acid) (PAA), polyimide (PI), pitch and others [200],[201]. PAN is the most widely used precursor for production of carbon fibres due to the high carbon yield [202]. PAN-based CNFs [203],[204] found application in energy conversion devices such as PEM fuel cells, supercapacitors and lithium ion batteries [191],[198].

Thermal treatment of PAN nanofibres consists of three steps: stabilisation, carbonisation and graphitisation [205],[206]. The first step is stabilisation in air between 180 °C and 300 °C, which allows the cyclisation of the nitrile groups (Figure 17). Stabilisation is usually performed at a low heating rate to prevent melting or fusing of the fibres. During the stabilisation process, two reactions take place, which are: cyclisation and dehydrogenation. The PAN-based fibres change colour from white to dark brown. The second step is carbonisation in a nitrogen or argon atmosphere between 600 °C and 1300 °C to keep out non-carbon atoms. The third step is graphitisation at 1500 – 3000 °C, which leads to an increase in graphite content. During heat treatment, the PAN fibre is stretched and shrinks in diameter.

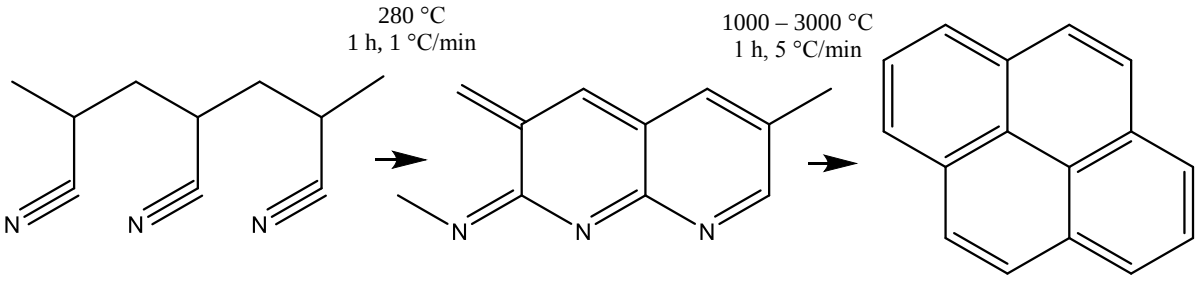

Figure 17: Mechanism of CNF formation

One of the advantages of the 1 D structure is the increased conductivity along the axis of the fibres. The electrical conductivity of single CNF carbonised at 1000 °C was 275 S/cm [207]. Agend et al. measured even higher electrical conductivity of around 600 S/cm for a CNF mat carbonised at 1100 °C [208].

CNF supported catalyst exhibit a good performance towards the electrocatalytic oxidation of formic acid [209] and methanol (MOR) [210]. Lin et al. used soft 1-aminopyrene-functionalisation methods to activate CNFs before catalyst deposition. Obtained Pt/CNFs electrocatalyst exhibit improved ECSA and performance for the MOR compared to the catalyst deposited by traditional harsh oxidising functionalisation using HNO_3 and H_2SO_4 acids [211]. Li et al. developed catalyst supported on electrospun fibrous mats (CFM), which provides with high electrical conductivity and increased activity towards MOR [212],[213],[214],[215]. Park et al. [216] observed high PEMFC performance with Pt/CNFs electrocatalyst, which was attributed to higher electrical conductivity (9.9 S/cm) and larger surface area (307 m^2/g) of CNFs compared to the commercial Vulcan XC-72R support (4.5 S/cm and 235 m^2/g). Recently, Padmavathi et al. [217] demonstrated that fuctionalisation treatments of CNFs with acids resulted in an enhanced PEMFC performance. Properties of CNFs supported catalyst are listed in Table 4.

3.2.2 Electrospun metal oxides

Originally electrospinning was used to obtain polymer fibres. However, combination of electrospinning and appropriate thermal treatment allows fabrication of inorganic fibres. Electrospinning solution consists of a carrier polymer (usually poly(vinyl pyrlidone) (PVP), polyacrylonitrile (PAN) or poly(vinyl acetate) (PVA)), metal salt precursor and solvent (water, ethanol and dimethylformamide (DMF)), which evaporates during the electrospinning procedure. The polymer is added to increase the viscosity of the solution and make it spinnable. After electrospinning of such solution calcination is necessary in order to remove all organic components. In some cases viscous solution could be used without addition of polymer [220]. The metal alkoxide are usually used as precursors for oxide-based fibres [185],[221].

It is also possible to obtain porous and hollow ceramic fibres. For example, titania tubes can be prepared by co-spinning of two solutions such as $Ti(O\textit{i}Pr)_4$/PVP and heavy mineral oil. In this case, the spinneret consists of two coaxial capillaries, which allow the generation of core-shell fibres. Mineral oil can be removed by extraction with n-hexane followed by calcination in air [222],[223]. Even titania tube with channel number from two to five can be

prepared via multifluidic coaxial electrospinning [224]. Furthermore, high surface area (199 m^2/g) mesoporous fibres have been obtained using surfactant and low calcination temperature of 400 °C [225].

Table 4: PAN-based electrospun nanofibres for fuel cell electrodes application

Ref.	Material	Fibre diameter, nm	Conductivity of CNF, S/cm	Surface area of CNF, m^2/g	Catalyst size, nm	ECSA, m^2/g	Advantages	FC type
Park [216]	Pt/CNFs	250	9.9	307	2.6	30.8	High FC performance	H_2-PEM
Li [212]	Pt/CFM	150	50	7	50-200	-	Improved performance	DMFC
Li [213]	Pt/C-CFM	150	55	-	-	-	High activity and stability	DMFC
Li [218]	Pt/C-CFM	150	42	-	5	-	High performance	DMFC
Liu [214]	Pt/AuCFM	740	10^4	-	4.2-7.5	39.8	High activity	DMFC
Chang [215]	Pt/Graphene-CFMs	150	65	-	5-10	34.8	Improved stability	DMFC
Lin [210]	Pt/CNFs	200-300	-	-	20	187 µC	High performance	DMFC
Lin [211]	PtRu/1-AP-CNFs	100-300	-	-	3.1	32.7	Improved ECSA and performence	DMFC
Huang [209]	PtAu/CNFs	700	-	-	118	-	Higher activity than that of Pt/C	FAFC
Padma-vanthi [217]	Pt/CNFs	300	-	107.9-237.54	3.9-5.2	17.16-35.34	High activity and stability	H_2-PEM
An [219]	Pt/CNFs Pt/CNFs-Ru core-shell	197-250	-	-	1-3	-	Higher activity than that of Pt/C	DMFC

3.2.3 Electrospun titania

TiO_2 has been explored as alternative support for PEMFC as already seen in paragraph 2.2.2. Electrospun titanium oxide fibres are used for lithium ion batteries [226], dye-sensitised solar cells [227], H_2-PEMFC and DMFC [191]. Indeed, electrospun TiO_2 supported Pt prepared by microwave irradiation showed higher activity towards methanol oxidation than commercial Pt/C [228].

In collaborative research between the Laboratory and the Institute for Fuel Cell Innovation (Vancouver, Canada), electrospun Nb-TiO_2 supported Pt demonstrated higher stability compared to that of the commercially available Pt/C catalyst [149]. Pt supported on Nb-TiO_2 and on reduced TiO_x showed improved ORR activity compared to Pt/TiO_2 due to their enhanced electrical conductivity [229].

Recently, Du et al. [230] deposited Pt nanoparticles on the electrospun Nb-TiO_2 membrane using atomic layer deposition (ALD). 10 at. % Nb doped TiO_2 supported Pt exhibited ~20-fold higher ORR activity compared to the Pt/TiO_2. Only 10 % loss in ORR activity was observed after stability test.

In order to increase the conductivity of TiO_2, Senevirathne et al. [231] reduced titania nanofibres at 1050 °C. However, the obtained Ti_4O_7 supported Pt electrocatalyst showed poor ORR mass activity after prolonged cycles due to the progressive formation of a TiO_2 insulating layer.

Another approach to increase both electrical conductivity and surface area of TiO_2-based support is the use of carbon-TiO_2 composite materials. For instance, the PtRu supported on the carbon-TiO_2 composite electrospun nanofibre support showed a significant increase in the MOR activity and durability compared to RtRu supported on Vulcan [232]. The use of the carbon-TiO_2 support leads to decreased CO poisoning keeping the high conductivity and high surface area of the carbon support. Synthesis conditions and properties of Pt supported on TiO_2-based electrospun nanofibres are listed in Table 5.

a. Electrospun tin oxide

Electrospun tin oxide is used for gas sensors [235], lithium ion batteries [236], dye-sensitised solar cells [237] and fuel cells. For instance, Kim et al. [238] added electrospun Sb doped SnO_2 nanowires to the commercial Pt/C electrocatalyst. Obtained hybrid Pt/C-ATO catalyst exhibited enhanced alcohol oxidation activity and durability.

Recently, Ogi [239],[240] has proposed to use electrospun Pt/SnO_2 nanofibres (with ECSA of 81 m^2/g) as anode electrocatalyst due to its ORR-blocking properties, which can prevent cathode degradation during start-up and shutdown of FC (see reverse-current mechanism paragraph 1.2.4.2). ORR inhibition effect of Pt/SnO_2 was attributed to the presence of organic nitrile-group molecules (from the carrier polymer, PAN), which are easily adsorbed by hydroxyl molecules. It is well known that high hydroxyl coverage on Pt inhibits oxygen reduction [241].

Table 5: TiO_2-based electrospun nanofibres for PEMFC electrodes application

Ref.	**Electro-catalyst**	**Calcination T, °C, gas**	**Pt deposition method**	**Support surface area, m^2/g**	**ECSA, m^2/g (Pt particle size)**	**Activity**	**Catalyst was more stable than Pt/C after the following test**
Bauer 2010 [229]	1) Pt/ $NbTiO_2$, 2) Pt/ TiO_x	500 air, 650 H_2	Polyol method	-	1.3-5 (5 nm)	ORR activity was lower than that for Pt/C	1000 cycles (0.05 - 1.3 V)
Senevi-rathne 2012 [231]	Pt/Ti_4O_7	1050 H_2/N_2 (1:1)	$NaBH_4$ reduction	6	~ 6	ORR mass activity: 11 mA/mg_{Pt}	Non-conductive TiO_2 layer formation
Bauer 2012 [149]	$Pt/NbTiO_2$	500 air	Polyol method	72	22 (5 nm)	ORR mass activity: 3.2 A/g_{Pt} at 0.9 V	1000 cycles (0.05 - 1.2 V)
Du 2014 [230]	$Pt/NbTiO_2$	500 air	ALD 500 °C 5% H_2/Ar	14.74	(14 nm)	ORR mass activity: 0.28 mA/g_{Pt} at 0.9 V	10 % ORR activity loss 30000 cycles (0.6 – 1.0 V)
Long 2010 [228]	Pt/TiO_2	500 air	Microwave assisted polyol method	-	-	Methanol electro-oxidation	-
Formo 2008 [233] [234]	Pt/TiO_2	510 air	Polyol method	-	16 - 56	Methanol electro-oxidation	-
Abdel-kareem 2012 [232]	PtRu/C-TiO_2	1000 N_2, 850 steam	$NaBH_4$ reduction	207	(9.6 nm)	Methanol electro-oxidation	Showed higher stability than PtRu/Vulcan

4 Principle of the synthesis and deposition of Pt nanoparticles

There are many methods that can be used for the deposition of metal catalyst on the support, for example impregnation, colloidal methods (so-called Bönnemann method, see below, microemulsion and polyol [242]), electrodeposition, vapour deposition and others [21].

4.1 Impregnation

In the impregnation method, the Pt salt (for example H_2PtCl_6) is reduced either under a flow of H_2 at around 300 °C or by using a reducing agent [243]. It is a very simple method, which allows the obtaining of a good dispersion on the support with very small Pt nanoparticle size of around 2 nm. One of the advantages of this method is the deposition of the Pt nanoparticles within the pore structure of the support. The disadvantage of this method is the very poor Pt loading, between 1 and 10 wt. %, which is too low for PEMFC cathode application. The attempt to increase the metal loading on the carbon support leads to a less homogeneous distribution of the particle size. This method does not provide the control of Pt particle size and distribution. In order to overcome this problem, Coutanceau et al. [244] used a colloid method.

4.2 Colloid methods

In this particular method, the reduction of platinum salt in the solution is followed by the adsorption of the Pt ions on the support. The use of a stabilising agents such as polyvinyl pyrrolidone (PVP) and surfactants allows an efficient control of the metal nanoparticle size and also prevents the agglomeration of the Pt nanoparticles [245]. But it can be difficult to remove these surfactant molecules from the surface of the catalyst after the synthesis. This problem was resolved by using ethylene glycol as the stabilising agent due to its easy removal by heat treatment below 160 °C. Another disadvantage of the colloidal methods is the high dilution of the colloidal particles, which involve a big amount of solvent; therefor this method is not the best solution for large scale production.

- ***Bönnemann method***

In this method, tetraalkylammonium salt acts as both the reducing agent and the stabilising agent for Pt and Pt alloys in tetrahydrofuran. Small nanoparticles of PtRu and Pt_3Sn below 2 nm diameter with a very narrow particle size distribution were obtained by this

method, but the surfactant needs to be removed by calcination at 300 °C [246]. However, such high temperature can cause changes in the catalyst structure.

- ***Microemulsion method***

In this system water droplets with metal salts (nanoreactors) are dispersed in a nonpolar solvent. The surfactant acts as the separator between the two phases. The reduction of the metal salts and grain growth take place in a surfactant stabilised microdroplets, as described by Boutonnet et al. [247]. This method allows the synthesis of monodispersed particles with a very narrow size distribution. But the use of surfactant with long washing steps is not economical in terms of scale-up [242].

- ***Polyol method***

Fievet et al. [248], [249] proposed the reduction of metal-containing salt by using poly(ethylene glycol)s. In the so-called polyol method ethylene glycol plays the role of the solvent, reducing agent and stabilising agent for metal particles. Unlike other stabilising agents, it can be easily removed at low temperatures.

The ethylene glycol can be oxidised in the reaction with a metal salt to aldehydes and then to glycolic and oxalic acids. At high pH, the glycolic acid dissociates and is present in the form of glycolate anion, which stabilizes the Pt nanoparticles by forming a chelate-type complex via carboxyl groups [250]. The metal particle size depends strongly on the concentration of the glycolate anion in the solution. Therefore, the size of the Pt nanoparticle can be controlled by changing the pH of the solution and precursor concentration. The higher is the pH of the initial solution, the smaller is the particles size of the Pt [251].

- ***Microwave-assisted polyol method***

Microwave heating have many advantages namely rapid and homogeneous heating, high reaction rate and chemical yield. Such system results in uniform nucleation, leading to formation of monodispersed small nanoparticles, with narrow particle size distribution [252]. Ethylene glycol is a very efficient solvent for microwave rapid heating due to its high dielectric constant ($\varepsilon = 41.2$).

Motivation of the PhD thesis

The main aim of the research described in this thesis was to overcome the problem of carbon corrosion by using alternative catalyst supports, which may increase the lifetime of PEMFC. In this work, carbon, TiO_2 and SnO_2 nanofibres were prepared via the electrospinning technique. In order to enhance electronic conductivity and surface area of TiO_2 and SnO_2 various thermal treatments and doping (Nb or Sb) were applied. The structural, surface and electrical properties of obtained catalyst supports were characterised by various methods including scanning electron microscopy (SEM), transmission electron microscopy (TEM), X-ray diffraction (XRD), X-ray photoelectron spectroscopy (XPS), Raman spectroscopy, Brunauer–Emmett–Teller (BET) analysis and electronic conductivity measurements. Afterward Pt nanoparticles were deposited on the selected electrospun fibres by modified microwave-assisted polyol method. The influence of such carbon-based and oxide-based supports on the catalyst activity and stability was evaluated *ex situ* on rotating disk electrode (RDE). The support with best electrochemical prosperities was then chosen for *in situ* characterisation in a single PEMFC test bench.

Second, third and fourth chapters describe synthesis and characterisations of electrospun carbon, TiO_2 and SnO_2 nanofibres, respectively. The effect of doping on the conductivity, surface area and morphology of TiO_2 and SnO_2 is also investigated. The fifth chapter describes the characterisation of the obtained SnO_2 supported Pt in a single fuel cell with Nafion® and polybenzimidazole membranes. The general conclusions and future perspectives are presented in the last chapter.

The thesis presented in this manuscript was carried out in the group of ICGM-AIME (Institute Charles Gerhardt of Montpellier; research group: Aggregates, Interfaces and Materials for Energy) under the supervision of Prof. Jacques Rozière and Dr. Sara Cavaliere.
The various aspects of the research described in this thesis were financed by:

- QuasiDry (QUASI-anhydrous and DRY membranes for next generation fuel cells) is an European Framework Programme 7 project (2011);
- Marie Curie Initial Training Network SUSHGEN (Sustainable Hydrogen Generation) is an European Framework Programme 7 project (2012);
- SURICAT (SUpports Robustes et Innovants pour CATalyseurs de PEMFC) is a project of National Research Agency (2013 - 2014).

References

[1] "BP Statistical Review of World Energy About this review Contents," June, 2013.

[2] Q. Schiermeier, J. Tollefson, T. Scully, A. Witze, and M. Oliver, "Energy alternatives: Electricity without carbon," *Nature*, vol. 454, pp. 816–823, 2008.

[3] F. Díaz-González, A. Sumper, O. Gomis-Bellmunt, and R. Villafáfila-Robles, "A review of energy storage technologies for wind power applications," *Renewable and Sustainable Energy Reviews*, vol. 16, no. 4, pp. 2154–2171, May 2012.

[4] F. T. Wagner, B. Lakshmanan, and M. F. Mathias, "Electrochemistry and the Future of the Automobile," *The Journal of Physical Chemistry Letters*, vol. 1, no. 14, pp. 2204–2219, Jul. 2010.

[5] G. Gahleitner, "Hydrogen from renewable electricity: An international review of power-to-gas pilot plants for stationary applications," *International Journal of Hydrogen Energy*, vol. 38, no. 5, pp. 2039–2061, Feb. 2013.

[6] C. F. Schönbein, "On the Voltaic Polarization of Certain Solid and Fluid Substances," *The London and Edinburgh Philosophical Magazine and Journal of Science*, vol. XIV, pp. 42–45, 1839.

[7] W. R. Grove, "On a Gaseous Voltaic Battery," *Philosophical Magazine and Journal of Science*, vol. XXI, pp. 417–420, 1842.

[8] U. Bossel, *The Birth of the Fuel Cell 1835-1845*. 2000.

[9] L. Mond and C. Langer, "A new form of gas battery," *Proceedings of the Royal Society of London*, vol. 46, p. 296, 1889.

[10] A. Dicks, *Fuel Cell Systems Explained*. 2003, p. 23.

[11] "Proton exchange membrane fuel cell," *http://en.wikipedia.org/wiki/Proton_exchange_membrane_fuel_cell#cite_note-11.* .

[12] S. S. Kocha, "Volum 3. Fuel Cell Technology and Applications Part1," in in *Hand book of Fuel Cells*, First., W. Vielstich, A. Lamm, and H. A. Gasteiger, Eds. Chichester: John Wiley and Sons, 2003, pp. 538–560.

[13] S. Srinivasan, E. A. Ticianellii, R. Derouin, and A. Redondo, "Advances in solid polymer electrolyte technology with low platinum loading," *Journal of Power Sources,*, vol. 22, pp. 359–375, 1988.

[14] N. M. Markovic, B. N. Grgur, and P. N. Ross, "Temperature-Dependent Hydrogen Electrochemistry on Platinum Low-Index Single-Crystal Surfaces in Acid Solutions," *The Journal of Physical Chemistry B*, vol. 101, pp. 5405–5413, 1997.

[15] P. M. Quaino, J. L. Fernández, M. R. Gennero de Chialvo, and a. C. Chialvo, "Hydrogen oxidation reaction on microelectrodes: Analysis of the contribution of the kinetic routes," *Journal of Molecular Catalysis A: Chemical*, vol. 252, no. 1–2, pp. 156–162, Jun. 2006.

[16] J. X. Wang, T. E. Springer, and R. R. Adzic, "Dual-Pathway Kinetic Equation for the Hydrogen Oxidation Reaction on Pt Electrodes," *Journal of The Electrochemical Society*, vol. 153, no. 9, p. A1732, 2006.

[17] M. K. Debe, "Electrocatalyst approaches and challenges for automotive fuel cells.," *Nature*, vol. 486, no. 7401, pp. 43–51, Jun. 2012.

[18] H. a Gasteiger and N. M. Marković, "Just a dream-or future reality?," *Science*, vol. 324, no. 5923, pp. 48–9, Apr. 2009.

[19] F. Maillard, S. Pronkin, and E. R. Savinova, "Volum 5. Advances in Electrocatalysis, Materials, Diagnostics and Durability: Part 1," in in *Hand book of Fuel Cells*, W. Vielstich, H. Yokokawa, and H. A. Gasteiger, Eds. Chichester: John Wiley and Sons, 2003, pp. 91–112.

[20] P. Derek, Ed., *A First Course in Electrode Processes*. Cambridge: RSC Publishing, 2009, p. 211.

[21] H. Zhang, X. Wang, J. Zhang, and J. Zhang, "PEM Fuel Cell Electrocatalysts and Catalyst Layers. Conventional Catalyst Ink, Catalyst Layer and MEA Preparation," J. Zhang, Ed. London: Springer-Verlag, 2008, pp. 1 – 1137.

[22] V. Zhdanov and B. Kasemo, "Kinetics of electrochemical O_2 reduction on Pt," *Electrochemistry Communications*, vol. 8, no. 7, pp. 1132–1136, Jul. 2006.

[23] E. Yeager, "Dioxygen electrocatalysis: mechanisms in relation to catalyst structure," *Journal of Molecular Catalysis*, vol. 38, pp. 5–25, 1986.

[24] I. Katsounaros, S. Cherevko, A. R. Zeradjanin, and K. J. J. Mayrhofer, "Oxygen electrochemistry as a cornerstone for sustainable energy conversion," *Angewandte Chemie*, vol. 53, no. 1, pp. 102–21, Jan. 2014.

[25] J. K. Nørskov, J. Rossmeisl, A. Logadottir, L. Lindqvist, D.- Lyngby, and H. Jo, "Origin of the Overpotential for Oxygen Reduction at a Fuel-Cell Cathode," *J. Phys. Chem. B*, vol. 108, pp. 17886–17892, 2004.

[26] K. Kinoshita, "Particle Size Effects for Oxygen Reduction on Highly Dispersed Platinum in Acid Electrolytes," *Journal of The Electrochemical Society*, vol. 137, no. 3, p. 845, 1990.

[27] M. Peuckert, T. Yoneda, R. A. D. Betta, and M. Boudart, "Oxygen Reduction on Small Supported Platinum Particles," *J. Electrochem. Soc.*, vol. 133, p. 944, 1986.
[28] D. P. Wilkinson, J. Zhang, R. Hui, J. Fergus, and X. Li, Eds., *Proton exchange membrane fuel cells*. Boca Raton: CRC Press, 2010, pp. 1 – 446.
[29] S. J. Peighambardoust, S. Rowshanzamir, and M. Amjadi, "Review of the proton exchange membranes for fuel cell applications," *International Journal of Hydrogen Energy*, vol. 35, no. 17, pp. 9349–9384, Sep. 2010.
[30] S. Subianto, M. Pica, M. Casciola, P. Cojocaru, L. Merlo, G. Hards, and D. J. Jones, "Physical and chemical modification routes leading to improved mechanical properties of perfluorosulfonic acid membranes for PEM fuel cells," *Journal of Power Sources*, vol. 233, pp. 216–230, Jul. 2013.
[31] J. S. Wainright, J. Wang, D. Weng, R. F. Savinell, and M. Litt, "Acid-Doped Polybenzimidazoles: A New Polymer Electrolyte," *J. Electrochem. Soc.*, vol. 142, no. 7, pp. 121–123, 1995.
[32] J. S. Wainright, M. H. Litt, and R. F. Savinell, "Volum 3. Fuel Cell Technology and Applications Part1," in in *Hand book of Fuel Cells*, W. Vielstich, A. Lamm, and H. A. Gasteiger, Eds. Chichester: John Wiley and Sons, 2003, pp. 349–356.
[33] M. F. Mathias, J. Roth, J. Fleming, and W. Lehnert, "Volum 3. Fuel Cell Technology and Applications Part1," in in *Hand book of Fuel Cells*, W. Vielstich, A. Lamm, and H. A. Gasteiger, Eds. Chichester: John Wiley and Sons, 2003, pp. 517–537.
[34] S. Park, J.-W. Lee, and B. N. Popov, "A review of gas diffusion layer in PEM fuel cells: Materials and designs," *International Journal of Hydrogen Energy*, vol. 37, no. 7, pp. 5850–5865, Apr. 2012.
[35] R. O'Hayre, D. M. Barnett, and F. B. Prinz, "The Triple Phase Boundary," *Journal of The Electrochemical Society*, vol. 152, no. 2, p. A439, 2005.
[36] J. Greeley, I. E. L. Stephens, a S. Bondarenko, T. P. Johansson, H. a Hansen, T. F. Jaramillo, J. Rossmeisl, I. Chorkendorff, and J. K. Nørskov, "Alloys of platinum and early transition metals as oxygen reduction electrocatalysts.," *Nature chemistry*, vol. 1, no. 7, pp. 552–6, Oct. 2009.
[37] V. R. Stamenkovic, B. Fowler, B. S. Mun, G. Wang, P. N. Ross, C. a Lucas, and N. M. Marković, "Improved oxygen reduction activity on $Pt_3Ni(111)$ via increased surface site availability.," *Science*, vol. 315, no. 5811, pp. 493–7, Jan. 2007.
[38] V. R. Stamenkovic, B. S. Mun, K. J. J. Mayrhofer, P. N. Ross, and N. M. Markovic, "Effect of surface composition on electronic structure, stability, and electrocatalytic properties of Pt-transition metal alloys: Pt-skin versus Pt-skeleton surfaces.," *Journal of the American Chemical Society*, vol. 128, no. 27, pp. 8813–9, Jul. 2006.
[39] F. Jaouen, E. Proietti, M. Lefèvre, R. Chenitz, J.-P. Dodelet, G. Wu, H. T. Chung, C. M. Johnston, and P. Zelenay, "Recent advances in non-precious metal catalysis for oxygen-reduction reaction in polymer electrolyte fuel cells," *Energy & Environmental Science*, vol. 4, no. 1, p. 114, 2011.
[40] R. Jasinski, "A New Fuel Cell Cathode Catalyst," *Nature*, vol. 201, pp. 1212–1213, 1964.
[41] M. Lefèvre, E. Proietti, F. Jaouen, and J.-P. Dodelet, "Iron-based catalysts with improved oxygen reduction activity in polymer electrolyte fuel cells.," *Science*, vol. 324, no. 5923, pp. 71–4, Apr. 2009.
[42] "US Department of Energy (DOE). Fuel cell technologies office multi-year research, development and demonstration plan— Technical Plan: Fuel Cells," *http://www1.eere.energy.gov/hydrogenandfuelcells/mypp/*, 2012. .
[43] R. Borup, J. Meyers, B. Pivovar, Y. S. Kim, R. Mukundan, N. Garland, D. Myers, M. Wilson, F. Garzon, D. Wood, P. Zelenay, K. More, K. Stroh, T. Zawodzinski, J. Boncella, J. E. McGrath, M. Inaba, K. Miyatake, M. Hori, K. Ota, Z. Ogumi, S. Miyata, A. Nishikata, Z. Siroma, Y. Uchimoto, K. Yasuda, K.-I. Kimijima, and N. Iwashita, "Scientific aspects of polymer electrolyte fuel cell durability and degradation.," *Chemical reviews*, vol. 107, no. 10, pp. 3904–51, Oct. 2007.
[44] N. M. Markovic, H. A. Gasteiger, and P. N. Ross, "Oxygen Reduction on Platinum Low-Index Single-Crystal Surfaces in Sulfuric Acid Solution: Rotating Ring Pt(hkl) Disk Studies," *Journal of Physical Chemistry*, vol. 99, no. 11, pp. 3411–3415, 1995.
[45] T. Kinumoto, M. Inaba, Y. Nakayama, K. Ogata, R. Umebayashi, A. Tasaka, Y. Iriyama, T. Abe, and Z. Ogumi, "Durability of perfluorinated ionomer membrane against hydrogen peroxide," *Journal of Power Sources*, vol. 158, pp. 1222–1228, 2006.
[46] A. Pozio, R. F. Sil, M. De Francesco, and L. Giorgi, "Nafion degradation in PEFCs from end plate iron contamination," *Electrochimica Acta*, vol. 48, pp. 1543–1549, 2003.
[47] J. Peron, Y. Nedellec, D. Jones, and J. Roziere, "The effect of dissolution, migration and precipitation of platinum in Nafion®-based membrane electrode assemblies during fuel cell operation at high potential," *Journal of Power Sources*, vol. 185, no. 2, pp. 1209–1217, Dec. 2008.
[48] A. Ohma, S. Suga, S. Yamamoto, and K. Shinohara, "Phenomenon Analysis of PEFC for Automotive Use (1): Membrane Degradation Behavior During OCV Hold Test," *ECS Transactions*, vol. 3, no. 1, pp. 519–529, 2006.

[49] D. E. Curtin, R. D. Lousenberg, T. J. Henry, P. C. Tangeman, and M. E. Tisack, "Advanced materials for improved PEMFC performance and life," *Journal of Power Sources*, vol. 131, no. 1–2, pp. 41–48, May 2004.

[50] A. B. LaConti, M. Hamdan, and R. C. McDonald, "Volum 3. Fuel Cell Technology and Applications Part1," in in *Hand book of Fuel Cells*, 1st ed., W. Vielstich, A. Lamm, and H. A. Gasteiger, Eds. Chichester: John Wiley and Sons, 2003, pp. 647–662.

[51] E. Endoh, "Highly Durable MEA for PEMFC Under High Temperature and Low Humidity Conditions Eiji Endoh," *ECS Transactions*, vol. 3, no. 1, pp. 9–18, 2006.

[52] B. P. Pearman, N. Mohajeri, D. K. Slattery, M. D. Hampton, S. Seal, and D. a. Cullen, "The chemical behavior and degradation mitigation effect of cerium oxide nanoparticles in perfluorosulfonic acid polymer electrolyte membranes," *Polymer Degradation and Stability*, vol. 98, no. 9, pp. 1766–1772, Sep. 2013.

[53] B. P. Pearman, N. Mohajeri, R. P. Brooker, M. P. Rodgers, D. K. Slattery, M. D. Hampton, D. A. Cullen, and S. Seal, "The degradation mitigation effect of cerium oxide in polymer electrolyte membranes in extended fuel cell durability tests," *Journal of Power Sources*, vol. 225, pp. 75–83, Mar. 2013.

[54] M. P. Rodgers, L. J. Bonville, H. R. Kunz, D. K. Slattery, and J. M. Fenton, "Fuel cell perfluorinated sulfonic acid membrane degradation correlating accelerated stress testing and lifetime.," *Chemical reviews*, vol. 112, no. 11, pp. 6075–103, Nov. 2012.

[55] Y. Yu, H. Li, H. Wang, X.-Z. Yuan, G. Wang, and M. Pan, "A review on performance degradation of proton exchange membrane fuel cells during startup and shutdown processes: Causes, consequences, and mitigation strategies," *Journal of Power Sources*, vol. 205, pp. 10–23, May 2012.

[56] F. N. Büchi, M. Inanba, and T. J. Schmidt, Eds., *Polymer Electrolyte Fuel Cell Durability*. New York: Springer-Verlag, 2009, pp. 1–69.

[57] M. Cai, M. S. Ruthkosky, B. Merzougui, S. Swathirajan, M. P. Balogh, and S. H. Oh, "Investigation of thermal and electrochemical degradation of fuel cell catalysts," *Journal of Power Sources*, vol. 160, no. 2, pp. 977–986, Oct. 2006.

[58] Y. Yang and Z. G. Lin, "In situ FTIR characterization of the electrooxidation of glassy carbon electrodes," *Journal of Applied Electrochemistry*, vol. 25, no. 3, pp. 259–266, Mar. 1995.

[59] C. A. Reiser, L. Bregoli, T. W. Patterson, J. S. Yi, J. D. Yang, M. L. Perry, and T. D. Jarvi, "A Reverse-Current Decay Mechanism for Fuel Cells," *Electrochemical and Solid-State Letters*, vol. 8, no. 6, p. A273, 2005.

[60] S. Maass, F. Finsterwalder, G. Frank, R. Hartmann, and C. Merten, "Carbon support oxidation in PEM fuel cell cathodes," *Journal of Power Sources*, vol. 176, no. 2, pp. 444–451, Feb. 2008.

[61] M. F. Mathias, R. Makharia, H. A. Gasteiger, J. J. Conley, T. J. Fuller, C. J. Gittleman, S. S. Kocha, D. P. Miller, C. K. Mittelsteadt, T. Xie, S. G. Yan, P. T. Yu, U. S, and H. Hoover, "Two Fuel Cell Cars In Every Garage?," *The Electrochemical Society Interface*, vol. 14, no. 3, p. 24, 2005.

[62] K. H. Kangasniemi, D. a. Condit, and T. D. Jarvi, "Characterization of Vulcan Electrochemically Oxidized under Simulated PEM Fuel Cell Conditions," *Journal of The Electrochemical Society*, vol. 151, no. 4, p. E125, 2004.

[63] B. M. J. N. Pourbaix, J. Van Muylder, and N. De Zoubov, "Electrochemical Properties of the Platinum Metals," *Platinum Metals Rev.*, vol. 3, no. 2, pp. 47–53, 1959.

[64] R. M. Darling and J. P. Meyers, "Kinetic Model of Platinum Dissolution in PEMFCs," *Journal of The Electrochemical Society*, vol. 150, no. 11, p. A1523, 2003.

[65] S. Zhang, X.-Z. Yuan, J. N. C. Hin, H. Wang, K. A. Friedrich, and M. Schulze, "A review of platinum-based catalyst layer degradation in proton exchange membrane fuel cells," *Journal of Power Sources*, vol. 194, no. 2, pp. 588–600, Dec. 2009.

[66] Y. Shao-Horn, W. C. Sheng, S. Chen, P. J. Ferreira, E. F. Holby, and D. Morgan, "Instability of Supported Platinum Nanoparticles in Low-Temperature Fuel Cells," *Topics in Catalysis*, vol. 46, no. 3–4, pp. 285–305, Nov. 2007.

[67] P. J. Ferreira, G. J. la O', Y. Shao-Horn, D. Morgan, R. Makharia, S. Kocha, and H. A. Gasteiger, "Instability of Pt/C Electrocatalysts in Proton Exchange Membrane Fuel Cells," *Journal of The Electrochemical Society*, vol. 152, no. 11, p. A2256, 2005.

[68] K. G. Gallagher, R. M. Darling, and T. F. Fuller, "Volum 6. Advances in Electrocatalysis, Material, Diagnostics and Durability: Part 2," in in *Hand book of Fuel Cells*, W. Vielstich, H. Yokokawa, and H. A. Gasteiger, Eds. Chichester: John Wiley and Sons, 2003, pp. 819–829.

[69] O. Yamazaki, Y. Oomori, H. Shintaku, and T. Tabata, "Study on Degradation of the Pt-Ru Anode of PEFC for Residential Application (2) Analyses of the MEAs Degrad ed in the Anode Performance," *ECS Transactions*, vol. 11, no. 1, pp. 287–295, 2007.

[70] S. Sharma and B. G. Pollet, "Support materials for PEMFC and DMFC electrocatalysts—A review," *Journal of Power Sources*, vol. 208, pp. 96–119, Jun. 2012.

[71] E. Antolini, "Carbon supports for low-temperature fuel cell catalysts," *Applied Catalysis B: Environmental*, vol. 88, no. 1–2, pp. 1–24, Apr. 2009.
[72] G. S. Chai, S. B. Yoon, J.-S. Yu, J.-H. Choi, and Y.-E. Sung, "Ordered Porous Carbons with Tunable Pore Sizes as Catalyst Supports in Direct Methanol Fuel Cell," *The Journal of Physical Chemistry B*, vol. 108, no. 22, pp. 7074–7079, Jun. 2004.
[73] Y. Shao, S. Zhang, R. Kou, X. Wang, C. Wang, S. Dai, V. Viswanathan, J. Liu, Y. Wang, and Y. Lin, "Noncovalently functionalized graphitic mesoporous carbon as a stable support of Pt nanoparticles for oxygen reduction," *Journal of Power Sources*, vol. 195, no. 7, pp. 1805–1811, Apr. 2010.
[74] F. Coloma and J. L. G. Fierro, "Preparation of Platinum Supported on Pregraphitized Carbon Blacks," *Langmuir*, vol. 10, no. 3, pp. 750–755, 1994.
[75] Y. Shao, J. Sui, G. Yin, and Y. Gao, "Nitrogen-doped carbon nanostructures and their composites as catalytic materials for proton exchange membrane fuel cell," *Applied Catalysis B: Environmental*, vol. 79, no. 1, pp. 89–99, Feb. 2008.
[76] S. Iijima and T. Ichlhashi, "Single-shell carbon nanotubes of 1-nm diameter," *Nature*, vol. 363, pp. 603–605, 1993.
[77] K. Lee, J. Zhang, H. Wang, and D. P. Wilkinson, "Progress in the synthesis of carbon nanotube- and nanofiber-supported Pt electrocatalysts for PEM fuel cell catalysis," *Journal of Applied Electrochemistry*, vol. 36, no. 5, pp. 507–522, Mar. 2006.
[78] M. S. Saha, V. Neburchilov, D. Ghosh, and J. Zhang, "Nanomaterials-supported Pt catalysts for proton exchange membrane fuel cells," *Wiley Interdisciplinary Reviews: Energy and Environment*, vol. 2, no. 1, pp. 31–51, Jan. 2013.
[79] X. Sun and M. S. Saha, "Nanotubes, Nanofibres and Nanowires as Supports for Catalysts," in *PEM Fuel Cell Electrocatalysts and Catalyst Layers. Conventional Catalyst Ink, Catalyst Layer and MEA Preparation*, H. Zhang, X. Wang, J. Zhang, and J. Zhang, Eds. London: Springer-Verlag, 2008, pp. 655–703.
[80] X. Wang, W. Li, Z. Chen, M. Waje, and Y. Yan, "Durability investigation of carbon nanotube as catalyst support for proton exchange membrane fuel cell," *Journal of Power Sources*, vol. 158, no. 1, pp. 154–159, Jul. 2006.
[81] F. Hu and P. K. Shen, "Adwances of the Nanostructured Carbon-Based Catalyst for Low-Temperature Fuel Cells," in in *Nanostructured and Advanced Materials for Fuel Cells*, S. P. Jiang and P. K. Shen, Eds. Boca Raton: CRC Press, 2014, pp. 223–248.
[82] Y. Shao, J. Liu, Y. Wang, and Y. Lin, "Novel catalyst support materials for PEM fuel cells: current status and future prospects," *Journal of Materials Chemistry*, vol. 19, no. 1, p. 46, 2009.
[83] S. Zhang, Y. Shao, G. Yin, and Y. Lin, "Recent progress in nanostructured electrocatalysts for PEM fuel cells," *Journal of Materials Chemistry A*, pp. 4631–4641, 2013.
[84] S. Park, Y. Shao, R. Kou, V. V. Viswanathan, S. a. Towne, P. C. Rieke, J. Liu, Y. Lin, and Y. Wang, "Polarization Losses under Accelerated Stress Test Using Multiwalled Carbon Nanotube Supported Pt Catalyst in PEM Fuel Cells," *Journal of The Electrochemical Society*, vol. 158, no. 3, pp. B297–B302, 2011.
[85] S. Wang, S. P. Jiang, T. J. White, and X. Wang, "Synthesis of Pt and Pd nanosheaths on multi-walled carbon nanotubes as potential electrocatalysts of low temperature fuel cells," *Electrochimica Acta*, vol. 55, no. 26, pp. 7652–7658, Nov. 2010.
[86] X. Wang, M. Waje, and Y. Yan, "CNT-Based Electrodes with High Efficiency for PEMFCs," *Electrochemical and Solid-State Letters*, vol. 8, no. 1, p. A42, 2005.
[87] M. S. Saha, R. Li, and X. Sun, "High loading and monodispersed Pt nanoparticles on multiwalled carbon nanotubes for high performance proton exchange membrane fuel cells," *Journal of Power Sources*, vol. 177, no. 2, pp. 314–322, Mar. 2008.
[88] M. Pacurari, V. Castranova, and V. Vallyathan, "Single- and multi-wall carbon nanotubes versus asbestos: are the carbon nanotubes a new health risk to humans?," *Journal of toxicology and environmental health. Part A*, vol. 73, no. 5, pp. 378–95, Jan. 2010.
[89] F. R. Colom, A. Sepulvedaescribano, "Heat-treated carbons-blacks as supports for platinum catalysts," *Journal of Catalysis*, vol. 154, no. 2, pp. 299–305, 1995.
[90] Y. Shao, G. Yin, and Y. Gao, "Understanding and approaches for the durability issues of Pt-based catalysts for PEM fuel cell," *Journal of Power Sources*, vol. 171, no. 2, pp. 558–566, Sep. 2007.
[91] D. Sebastián, M. J. Lázaro, I. Suelves, R. Moliner, V. Baglio, a. Stassi, and a. S. Aricò, "The influence of carbon nanofiber support properties on the oxygen reduction behavior in proton conducting electrolyte-based direct methanol fuel cells," *International Journal of Hydrogen Energy*, vol. 37, no. 7, pp. 6253–6260, Apr. 2012.

[92] C. a. Bessel, K. Laubernds, N. M. Rodriguez, and R. T. K. Baker, "Graphite Nanofibers as an Electrode for Fuel Cell Applications," *The Journal of Physical Chemistry B*, vol. 105, no. 6, pp. 1115–1118, Feb. 2001.

[93] I.-S. Park, K.-W. Park, J.-H. Choi, C. R. Park, and Y.-E. Sung, "Electrocatalytic enhancement of methanol oxidation by graphite nanofibers with a high loading of PtRu alloy nanoparticles," *Carbon*, vol. 45, no. 1, pp. 28–33, Jan. 2007.

[94] S. L. Knupp, W. Li, O. Paschos, T. M. Murray, J. Snyder, and P. Haldar, "The effect of experimental parameters on the synthesis of carbon nanotube/nanofiber supported platinum by polyol processing techniques," *Carbon*, vol. 46, no. 10, pp. 1276–1284, Aug. 2008.

[95] W. Li, M. Waje, Z. Chen, P. Larsen, and Y. Yan, "Platinum nanopaticles supported on stacked-cup carbon nanofibers as electrocatalysts for proton exchange membrane fuel cell," *Carbon*, vol. 48, no. 4, pp. 995–1003, Apr. 2010.

[96] J. Wang and G. M. Swain, "Fabrication and Evaluation of Platinum/Diamond Composite Electrodes for Electrocatalysis," *Journal of The Electrochemical Society*, vol. 150, no. 1, p. E24, 2003.

[97] A. E. Fischer and G. M. Swain, "Preparation and Characterization of Boron-Doped Diamond Powder," *Journal of The Electrochemical Society*, vol. 152, no. 9, p. B369, 2005.

[98] A. Rabis, P. Rodriguez, and T. J. Schmidt, "Electrocatalysis for Polymer Electrolyte Fuel Cells: Recent Achievements and Future Challenges," *ACS Catalysis*, vol. 2, no. 5, pp. 864–890, May 2012.

[99] E. Antolini and E. R. Gonzalez, "Ceramic materials as supports for low-temperature fuel cell catalysts," *Solid State Ionics*, vol. 180, no. 9–10, pp. 746–763, May 2009.

[100] S. J. Tauster, "Strong metal-support interactions," *Accounts of Chemical Research*, vol. 20, no. 11, pp. 389–394, Nov. 1987.

[101] J. Ma, A. Habrioux, and N. Alonso-Vante, "The Effect of Substrates at Cathodes in Low-temperature Fuel Cells," *ChemElectroChem*, vol. 1, no. 1, pp. 37–46, Jan. 2014.

[102] A. Lewera, L. Timperman, A. Roguska, and N. Alonso-vante, "Metal-Support Interactions between Nanosized Pt and Metal Oxides (WO_3 and TiO_2) Studied Using X-ray Photoelectron Spectroscopy," *The Journal of Physical Chemistry C*, vol. 115, pp. 20153–20159, 2011.

[103] B. Ruiz Camacho, C. Morais, M. A. Valenzuela, and N. Alonso-Vante, "Enhancing oxygen reduction reaction activity and stability of platinum via oxide-carbon composites," *Catalysis Today*, vol. 202, pp. 36–43, Mar. 2013.

[104] H. Chhina, S. Campbell, and O. Kesler, "Thermal and electrochemical stability of tungsten carbide catalyst supports," *Journal of Power Sources*, vol. 164, no. 2, pp. 431–440, Feb. 2007.

[105] H. Chhina, S. Campbell, and O. Kesler, "High surface area synthesis, electrochemical activity, and stability of tungsten carbide supported Pt during oxygen reduction in proton exchange membrane fuel cells," *Journal of Power Sources*, vol. 179, no. 1, pp. 50–59, Apr. 2008.

[106] J. Bernard d'Arbigny, G. Taillades, M. Marrony, D. J. Jones, and J. Rozière, "Hollow microspheres with a tungsten carbide kernel for PEMFC application," *Chemical communications*, vol. 47, no. 28, pp. 7950–2, Jul. 2011.

[107] M. Nie, P. K. Shen, M. Wu, Z. Wei, and H. Meng, "A study of oxygen reduction on improved Pt-WC/C electrocatalysts," *Journal of Power Sources*, vol. 162, no. 1, pp. 173–176, Nov. 2006.

[108] J. Ma, A. Habrioux, and N. Alonso-Vante, "The Effect of Substrates at Cathodes in Low-temperature Fuel Cells," *ChemElectroChem*, vol. 1, no. 1, pp. 37–46, Jan. 2014.

[109] K. Sasaki, F. Takasaki, and Z. Noda, "Alternative Electrocatalyst Support Materials for Polymer Electrolyte Fuel Cells Thermochemical stability of support materials," *ECS Transactions*, vol. 33, no. 1, pp. 473–482, 2010.

[110] F. Takasaki, S. Matsuie, Y. Takabatake, Z. Noda, A. Hayashi, Y. Shiratori, K. Ito, and K. Sasaki, "Carbon-Free Pt Electrocatalysts Supported on SnO_2 for Polymer Electrolyte Fuel Cells: Electrocatalytic Activity and Durability," *Journal of The Electrochemical Society*, vol. 158, no. 10, p. B1270, 2011.

[111] K. Kanda, Z. Noda, Y. Nagamatsu, T. Higashi, S. Taniguchi, S. M. Lyth, a. Hayashi, and K. Sasaki, "Negligible Start-Stop-Cycle Degradation in a PEFC Utilizing Platinum-Decorated Tin Oxide Electrocatalyst Layers with Carbon Fiber Filler," *ECS Electrochemistry Letters*, vol. 3, no. 4, pp. F15–F18, Feb. 2014.

[112] J. Xi, J. Wang, L. Yu, X. Qiu, and L. Chen, "Facile approach to enhance the Pt utilization and CO-tolerance of Pt/C catalysts by physically mixing with transition-metal oxide nanoparticles.," *Chemical communications*, no. 16, pp. 1656–8, May 2007.

[113] J.-K. Oh, Y.-W. Lee, S.-B. Han, A.-R. Ko, D.-Y. Kim, H.-S. Kim, S.-J. Kim, B. Roh, I. Hwang, and K.-W. Park, "3-Dimensional TiO_2 nanostructure supports and their improved electrochemical properties in methanol electrooxidation," *Catalysis Science & Technology*, vol. 1, no. 3, p. 394, 2011.

[114] Z. Zhang, J. Liu, J. Gu, L. Su, and L. Cheng, "An Overview on Metal Oxide Materials as Electrocatalysts and Supports for Polymer Electrolyte Fuel Cells," *Energy & Environmental Science*, pp. 1–95, 2014.

[115] P. J. Kulesza and B. Grzybowska, "Tungsten Oxides as Active Supports for Highly Dispersed Platinum Microcenters: Electrocatalytic Reactivity Toward Reduction of Hydrogen Peroxide and Oxygen," *J. Electrochem. Soc.*, vol. 144, no. 6, p. 1911, 1997.

[116] P. J. Kulesza and L. R. Faulkner, "Electrodeposition and Characterization of Three-Dimensional Tungsten(VI, V)-Oxide Films Containing Spherical Pt Microparticles," *J. Electrochem. Soc.*, vol. 136, no. 3, p. 707, 1989.

[117] P. J. Kulesza, B. Grzybowska, M. a Malik, M. Chojak, and K. Miecznikowski, "Oxidation of methanol at an electrocatalytic film containing platinum and polynuclear oxocyanoruthenium microcenters dispersed within tungsten oxide matrix," *Journal of Electroanalytical Chemistry*, vol. 512, no. 1–2, pp. 110–118, Oct. 2001.

[118] X. Chen and S. S. Mao, "Titanium dioxide nanomaterials: synthesis, properties, modifications, and applications.," *Chemical reviews*, vol. 107, no. 7, pp. 2891–959, Jul. 2007.

[119] A. Fujishima and K. Honda, "Electrochemical Photolysis of Water at a Semiconductor Electrode," *Nature*, vol. 238, pp. 37–38, 1972.

[120] Z. Weng, H. Guo, X. Liu, S. Wu, K. W. K. Yeung, and P. K. Chu, "Nanostructured TiO_2 for energy conversion and storage," *RSC Advances*, vol. 3, no. 47, p. 24758, 2013.

[121] O. E. Haas, S. T. Briskeby, O. E. Kongstein, M. Tsypkin, and R. Tunold, "Synthesis and Characterisation of $Ru_xTi_{x-1}O_2$ as a Catalyst Support for Polymer Electrolyte Fuel Cell," *Journal of New Materials for Elect rochemical Systems*, vol. 11, pp. 9–14, 2008.

[122] A. Wang, H. Xu, Y. Lu, J. Hu, X. Kong, B. Tian, and H. Dong, "Synthesis and Characterization of Ruthenium-Titanium Composite Oxide and a Platinum Catalyst Supported on It," *Chinese Journal of Catalysis*, vol. 30, no. 3, pp. 179–181, Mar. 2009.

[123] E. Valenzuela, V. Ramos-Sanchez, A. Adolfo, L. Arista, and O. Savadogo, "Nanostructured TiO_2 Doped with Nb as a Novel Support for PEMFC," *Journal of Materials*, vol. 2013, pp. 1–7, 2013.

[124] K. A. Michalow, D. Flak, A. Heel, M. Parlinska-Wojtan, M. Rekas, and T. Graule, "Effect of Nb doping on structural, optical and photocatalytic properties of flame-made TiO_2 nanopowder," *Environmental Science and Pollution Research*, vol. 19, no. 9, pp. 3696–3708, 2012.

[125] A. M. Ruiz, G. Dezanneau, J. Arbiol, A. Cornet, and J. R. Morante, "Insights into the Structural and Chemical Modifications of Nb Additive on TiO_2 Nanoparticles," *Chemistry of Materials*, vol. 16, no. 17, pp. 862–871, 2004.

[126] Y.-J. Wang, D. P. Wilkinson, and J. Zhang, "Synthesis of conductive rutile-phased $Nb_{0.06}Ti_{0.94}O_2$ and its supported Pt electrocatalysts ($Pt/Nb_{0.06}Ti_{0.94}O_2$) for the oxygen reduction reaction," *Dalton transactions*, vol. 41, no. 4, pp. 1187–94, Jan. 2012.

[127] Y.-J. Wang, D. P. Wilkinson, A. Guest, V. Neburchilov, R. Baker, F. Nan, G. a. Botton, and J. Zhang, "Synthesis of Pd and Nb–doped TiO_2 composite supports and their corresponding Pt–Pd alloy catalysts by a two-step procedure for the oxygen reduction reaction," *Journal of Power Sources*, vol. 221, pp. 232–241, Jan. 2013.

[128] G. Chen, S. R. Bare, and T. E. Mallouk, "Development of Supported Bifunctional Electrocatalysts for Unitized Regenerative Fuel Cells," *Journal of The Electrochemical Society*, vol. 149, no. 8, p. A1092, 2002.

[129] F. C. Walsh and R. G. a. Wills, "The continuing development of Magnéli phase titanium sub-oxides and Ebonex® electrodes," *Electrochimica Acta*, vol. 55, no. 22, pp. 6342–6351, Sep. 2010.

[130] T. Ioroi, Z. Siroma, N. Fujiwara, S. Yamazaki, and K. Yasuda, "Sub-stoichiometric titanium oxide-supported platinum electrocatalyst for polymer electrolyte fuel cells," *Electrochemistry Communications*, vol. 7, no. 2, pp. 183–188, Feb. 2005.

[131] T. Ioroi, H. Kageyama, T. Akita, and K. Yasuda, "Formation of electro-conductive titanium oxide fine particles by pulsed UV laser irradiation.," *Physical chemistry chemical physics: PCCP*, vol. 12, no. 27, pp. 7529–35, Jul. 2010.

[132] T. Ioroi, T. Akita, S. Yamazaki, Z. Siroma, N. Fujiwara, and K. Yasuda, "Corrosion-Resistant PEMFC Cathode Catalysts Based on a Magnéli-Phase Titanium Oxide Support Synthesized by Pulsed UV Laser Irradiation," *Journal of The Electrochemical Society*, vol. 158, no. 10, p. C329, 2011.

[133] T. Ioroi, T. Akita, M. Asahi, S. Yamazaki, Z. Siroma, N. Fujiwara, and K. Yasuda, "Platinum–titanium alloy catalysts on a Magnéli-phase titanium oxide support for improved durability in Polymer Electrolyte Fuel Cells," *Journal of Power Sources*, vol. 223, pp. 183–189, Feb. 2013.

[134] K.-W. Park and K.-S. Seol, "Nb-TiO_2 supported Pt cathode catalyst for polymer electrolyte membrane fuel cells," *Electrochemistry Communications*, vol. 9, no. 9, pp. 2256–2260, Sep. 2007.

[135] H. Chhina, S. Campbell, and O. Kesler, "Ex Situ and In Situ Stability of Platinum Supported on Niobium-Doped Titania for PEMFCs," *Journal of The Electrochemical Society*, vol. 156, no. 10, p. B1232, 2009.

[136] S.-Y. Huang, P. Ganesan, and B. N. Popov, "Electrocatalytic activity and stability of niobium-doped titanium oxide supported platinum catalyst for polymer electrolyte membrane fuel cells," *Applied Catalysis B: Environmental*, vol. 96, no. 1–2, pp. 224–231, Apr. 2010.

[137] D. V. Bavykin, J. M. Friedrich, and F. C. Walsh, "Protonated Titanates and TiO_2 Nanostructured Materials: Synthesis, Properties, and Applications," *Advanced Materials*, vol. 18, no. 21, pp. 2807–2824, Nov. 2006.

[138] M. Wang, D. Guo, and H. Li, "High activity of novel Pd/TiO2 nanotube catalysts for methanol electro-oxidation," *Journal of Solid State Chemistry*, vol. 178, no. 6, pp. 1996–2000, Jun. 2005.

[139] J. M. Macak, P. J. Barczuk, H. Tsuchiya, M. Z. Nowakowska, a. Ghicov, M. Chojak, S. Bauer, S. Virtanen, P. J. Kulesza, and P. Schmuki, "Self-organized nanotubular TiO_2 matrix as support for dispersed Pt/Ru nanoparticles: Enhancement of the electrocatalytic oxidation of methanol," *Electrochemistry Communications*, vol. 7, no. 12, pp. 1417–1422, Dec. 2005.

[140] S. H. Kang, T.-Y. Jeon, H.-S. Kim, Y.-E. Sung, and W. H. Smyrl, "Effect of Annealing PtNi Nanophases on Extended TiO_2 Nanotubes for the Electrochemical Oxygen Reduction Reaction," *Journal of The Electrochemical Society*, vol. 155, no. 10, p. B1058, 2008.

[141] S. H. Kang, Y.-E. Sung, and W. H. Smyrl, "The Effectiveness of Sputtered PtCo Catalysts on TiO_2 Nanotube Arrays for the Oxygen Reduction Reaction," *Journal of The Electrochemical Society*, vol. 155, no. 11, p. B1128, 2008.

[142] C. Zhang, H. Yu, Y. Li, L. Fu, Y. Gao, W. Song, Z. Shao, and B. Yi, "Highly stable ternary tin-palladium-platinum catalysts supported on hydrogenated TiO_2 nanotube arrays for fuel cells.," *Nanoscale*, vol. 5, no. 15, pp. 6834–41, Aug. 2013.

[143] C. Zhang, H. Yu, Y. Li, W. Song, B. Yi, and Z. Shao, "Preparation of Pt catalysts decorated TiO_2 nanotube arrays by redox replacement of Ni precursors for proton exchange membrane fuel cells," *Electrochimica Acta*, vol. 80, pp. 1–6, Oct. 2012.

[144] S.-Y. Huang, P. Ganesan, and B. N. Popov, "Development of Novel Metal Oxide Supported Pt catalysts for Polymer Electrolyte Membrane and Unitized Regenerative Fuel Cells Applications," *ECS Transactions*, vol. 25, no. 1, pp. 1893–1902, 2009.

[145] S.-Y. Huang, P. Ganesan, and B. N. Popov, "Titania supported platinum catalyst with high electrocatalytic activity and stability for polymer electrolyte membrane fuel cell," *Applied Catalysis B: Environmental*, vol. 102, no. 1–2, pp. 71–77, Feb. 2011.

[146] S.-Y. Huang, P. Ganesan, and B. N. Popov, "Electrocatalytic Activity and Stability of Titania-Supported Platinum–Palladium Electrocatalysts for Polymer Electrolyte Membrane Fuel Cell," *ACS Catalysis*, vol. 2, no. 5, pp. 825–831, May 2012.

[147] S. Siracusano, a. Stassi, E. Modica, V. Baglio, and a. S. Aricò, "Preparation and characterisation of Ti oxide based catalyst supports for low temperature fuel cells," *International Journal of Hydrogen Energy*, vol. 38, no. 26, pp. 11600–11608, Aug. 2013.

[148] A. Stassi, I. Gatto, V. Baglio, E. Passalacqua, and A. S. Aricò, "Oxide-supported PtCo alloy catalyst for intermediate temperature polymer electrolyte fuel cells," *Applied Catalysis B: Environmental*, vol. 142–143, pp. 15–24, Oct. 2013.

[149] A. Bauer, L. Chevallier, R. Hui, S. Cavaliere, J. Zhang, D. Jones, and J. Rozière, "Synthesis and characterization of Nb-TiO_2 mesoporous microsphere and nanofiber supported Pt catalysts for high temperature PEM fuel cells," *Electrochimica Acta*, vol. 77, pp. 1–7, Aug. 2012.

[150] L. Chevallier, A. Bauer, S. Cavaliere, R. Hui, J. Rozière, and D. J. Jones, "Mesoporous nanostructured Nb-doped titanium dioxide microsphere catalyst supports for PEM fuel cell electrodes.," *ACS applied materials & interfaces*, vol. 4, no. 3, pp. 1752–9, Mar. 2012.

[151] I. Cerri, T. Nagami, J. Davies, C. Mormiche, A. Vecoven, and B. Hayden, "Innovative catalyst supports to address fuel cell stack durability," *International Journal of Hydrogen Energy*, vol. 38, no. 1, pp. 640–645, Jan. 2013.

[152] M. Batzill and U. Diebold, "The surface and materials science of tin oxide," *Progress in Surface Science*, vol. 79, no. 2–4, pp. 47–154, 2005.

[153] A. C. Tseung and S. C. Dhara, "Loss of surface area by platinum and supported platinum black electrocatalyst," *Electrochimica Acta*, vol. 20, no. 9, pp. 681–683, 1975.

[154] M. Watanabe, S. Venkatesan, and H. A. Laitinen, "Preparation of Dispersed Platinum on Conductive Tin Oxide and Its Catalytic Activity for Oxygen Reduction," *Journal of Electrochemical Society*, vol. 130, no. 1, pp. 59–64, 1983.

[155] W. S. Baker, J. J. Pietron, M. E. Teliska, P. J. Bouwman, D. E. Ramaker, and K. E. Swider-Lyons, "Enhanced Oxygen Reduction Activity in Acid by Tin-Oxide Supported Au Nanoparticle Catalysts," *Journal of The Electrochemical Society*, vol. 153, no. 9, p. A1702, 2006.

[156] P. Zhang, S.-Y. Huang, and B. N. Popov, "Mesoporous Tin Oxide as an Oxidation-Resistant Catalyst Support for Proton Exchange Membrane Fuel Cells," *Journal of The Electrochemical Society*, vol. 157, no. 8, p. B1163, 2010.

[157] H. Lu, Y. Fan, P. Huang, and D. Xu, "SnO_2 nanospheres supported Pd catalyst with enhanced performance for formic acid oxidation," *Journal of Power Sources*, vol. 215, pp. 48–52, Oct. 2012.

[158] L. A. Frolova, Y. A. Dobrovolsky, and N. G. Bukun, "Oxide supported platinum electrocatalysts for hydrogen and alcohol fuel cells," *Russian Journal of Electrochemistry*, vol. 47, no. 6, pp. 697–708, Jun. 2011.

[159] Y. Fan, J. Liu, H. Lu, P. Huang, and D. Xu, "Hierarchical structure SnO_2 supported Pt nanoparticles as enhanced electrocatalyst for methanol oxidation," *Electrochimica Acta*, vol. 76, pp. 475–479, Aug. 2012.

[160] H. Zhang, C. Hu, X. He, L. Hong, G. Du, and Y. Zhang, "Pt support of multidimensional active sites and radial channels formed by SnO_2 flower-like crystals for methanol and ethanol oxidation," *Journal of Power Sources*, vol. 196, no. 10, pp. 4499–4505, May 2011.

[161] T. Okanishi, T. Matsui, T. Takeguchi, R. Kikuchi, and K. Eguchi, "Chemical interaction between Pt and SnO and influence on adsorptive properties of carbon monoxide," *Applied Catalysis A: General*, vol. 298, pp. 181–187, Jan. 2006.

[162] I. Saadeddin, B. Pecquenard, J. P. Manaud, R. Decourt, C. Labrugère, T. Buffeteau, and G. Campet, "Synthesis and characterization of single- and co-doped SnO_2 thin films for optoelectronic applications," *Applied Surface Science*, vol. 253, no. 12, pp. 5240–5249, Apr. 2007.

[163] K. Lee, I. Park, Y. Cho, D. Jung, N. Jung, H. Park, and Y. Sung, "Electrocatalytic activity and stability of Pt supported on Sb-doped SnO_2 nanoparticles for direct alcohol fuel cells," *Journal of Catalysis*, vol. 258, no. 1, pp. 143–152, Aug. 2008.

[164] D. J. You, K. Kwon, C. Pak, and H. Chang, "Platinum–antimony tin oxide nanoparticle as cathode catalyst for direct methanol fuel cell," *Catalysis Today*, vol. 146, no. 1–2, pp. 15–19, Aug. 2009.

[165] M. Yin, J. Xu, Q. Li, J. O. Jensen, Y. Huang, L. N. Cleemann, N. J. Bjerrum, and W. Xing, "Highly active and stable Pt electrocatalysts promoted by antimony-doped SnO_2 supports for oxygen reduction reactions," *Applied Catalysis B: Environmental*, vol. 144, pp. 112–120, Jan. 2014.

[166] J.-M. Lee, S.-B. Han, Y.-W. Lee, Y.-J. Song, J.-Y. Kim, and K.-W. Park, "RuO_2–SnO_2 nanocomposite electrodes for methanol electrooxidation," *Journal of Alloys and Compounds*, vol. 506, no. 1, pp. 57–62, Sep. 2010.

[167] H. L. Pang, X. H. Zhang, X. X. Zhong, B. Liu, X. G. Wei, Y. F. Kuang, and J. H. Chen, "Preparation of Ru-doped SnO_2-supported Pt catalysts and their electrocatalytic properties for methanol oxidation.," *Journal of colloid and interface science*, vol. 319, no. 1, pp. 193–8, Mar. 2008.

[168] N. R. Elezovic, B. M. Babic, V. R. Radmilovic, and N. V. Krstajic, "Synthesis and Characterization of Pt Catalysts on SnO_2 Based Supports for Oxygen Reduction Reaction," *Journal of the Electrochemical Society*, vol. 160, no. 10, pp. F1151–F1158, Sep. 2013.

[169] T. Higashi, Z. Noda, A. Hayashi, and K. Sasaki, "Pulse Laser Deposition and Sputtering of Carbon-free Pt/SnO_2 Electrocatalysts for PEFC," *ECS Transactions*, vol. 58, no. 1, pp. 1293–1299, 2013.

[170] M. Saha, Sudan, R. Li, M. Cai, and X. Sun, "High Electrocatalytic Activity of Platinum Nanoparticles on SnO_2 Nanowire-Based Electrodes," *Electrochemical and Solid-State Letters*, vol. 10, no. 8, p. B130, 2007.

[171] M. S. Saha, R. Li, and X. Sun, "Composite of Pt–Ru supported SnO_2 nanowires grown on carbon paper for electrocatalytic oxidation of methanol," *Electrochemistry Communications*, vol. 9, no. 9, pp. 2229–2234, Sep. 2007.

[172] M. Dou, M. Hou, D. Liang, W. Lu, Z. Shao, and B. Yi, "SnO_2 nanocluster supported Pt catalyst with high stability for proton exchange membrane fuel cells," *Electrochimica Acta*, vol. 92, pp. 468–473, Mar. 2013.

[173] M. P. Gurrola, M. Guerra-Balcázar, L. Álvarez-Contreras, R. Nava, J. Ledesma-García, and L. G. Arriaga, "High surface electrochemical support based on Sb-doped SnO_2," *Journal of Power Sources*, vol. 243, pp. 826–830, Dec. 2013.

[174] Y. Takabatake, Z. Noda, S. M. Lyth, a. Hayashi, and K. Sasaki, "Cycle durability of metal oxide supports for PEFC electrocatalysts," *International Journal of Hydrogen Energy*, pp. 1–9, Feb. 2014.

[175] A. Masao, S. Noda, F. Takasaki, K. Ito, and K. Sasaki, "Carbon-Free Pt Electrocatalysts Supported on SnO_2 for Polymer Electrolyte Fuel Cells," *Electrochemical and Solid-State Letters*, vol. 12, no. 9, p. B119, 2009.

[176] F. Takasaki, Z. Noda, A. Masao, Y. Shiratori, K. Ito, and K. Sasaki, "Carbon-free Pt Electrocatalysts Supported on Doped SnO_2 for Polymer Electrolyte Fuel Cells," *ECS Transactions*, vol. 25, no. 1, pp. 831–837, 2009.

[177] K. Kakinuma, M. Uchida, T. Kamino, H. Uchida, and M. Watanabe, "Synthesis and electrochemical characterization of Pt catalyst supported on $Sn_{0.96}Sb_{0.04}O_{2-\delta}$ with a network structure," *Electrochimica Acta*, vol. 56, no. 7, pp. 2881–2887, Feb. 2011.

[178] K. Kakinuma, Y. Chino, Y. Senoo, M. Uchida, T. Kamino, H. Uchida, S. Deki, and M. Watanabe, "Characterization of Pt catalysts on Nb-doped and Sb-doped $SnO_{2-\delta}$ support materials with aggregated structure by rotating disk electrode and fuel cell measurements," *Electrochimica Acta*, vol. 110, pp. 316–324, Nov. 2013.

[179] A. Rabis, E. Fabbri, A. Foelske, M. Horisberger, R. Kötz, and T. J. Schmidt, "Durable Oxide-based Catalysts for Application as Cathode Materials in Polymer Electrolyte Fuel Cells (PEFCs) A. Rabis," *ECS Transactions*, vol. 50, no. 36, pp. 9–17, 2013.

[180] M. K. Debe, A. K. Schmoeckel, S. M. Hendricks, G. D. Vernstrom, G. M. Haugen, R. T. Atanasoski, and R. T., "Durability Aspects of Nanostructured Thin Film," *ECS Transactions*, vol. 1, no. 8, pp. 51–66, 2006.

[181] M. K. Debe, A. K. Schmoeckel, G. D. Vernstrom, and R. Atanasoski, "High voltage stability of nanostructured thin film catalysts for PEM fuel cells," *Journal of Power Sources*, vol. 161, no. 2, pp. 1002–1011, Oct. 2006.

[182] M. K. Debe, A. J. Steinbach, G. D. Vernstrom, S. M. Hendricks, M. J. Kurkowski, R. T. Atanasoski, P. Kadera, D. A. Stevens, R. J. Sanderson, E. Marvel, and J. R. Dahn, "Extraordinary Oxygen Reduction Activity of Pt_3Ni_7," *Journal of The Electrochemical Society*, vol. 158, no. 8, p. B910, 2011.

[183] M. K. Debe, "Nanostructured Thin Film Electrocatalysts for PEM Fuel Cells – A Tutorial on the Fundamental Characteristics and Prac tical Properties of NSTF Catalysts," *ECS Transactions*, vol. 45, no. 2, pp. 47–68, 2012.

[184] G. Shen, P.-C. Chen, K. Ryu, and C. Zhou, "Devices and chemical sensing applications of metal oxide nanowires," *Journal of Materials Chemistry*, vol. 19, no. 7, p. 828, 2009.

[185] D. Li, J. T. McCann, Y. Xia, and M. Marquez, "Electrospinning: A Simple and Versatile Technique for Producing Ceramic Nanofibers and Nanotubes," *Journal of the American Ceramic Society*, vol. 89, no. 6, pp. 1861–1869, Jun. 2006.

[186] W.-E. Teo, R. Inai, and S. Ramakrishna, "Technological advances in electrospinning of nanofibers," *Science and Technology of Advanced Materials*, vol. 12, no. 1, p. 013002, Feb. 2011.

[187] J. F. Cooley, "Apparatus for electrically dispersing fluids," 1902.

[188] J. Zeleny, "The Electrical Discharge from Liquid Points, and a Hydrostatic Method of Measuring the Electric Intensity at their Surfaces," *Physical Review*, vol. 3, pp. 69–91, 1914.

[189] A. Formhals, "Process and apparatus for preparing artificial threads," 1934.

[190] J. Doshi and D. H. Reneker, "Electrospinning Process and Applications of Electrospun Fibers," *Journal of Electrostatics*, vol. 35, pp. 151–160, 1995.

[191] S. Cavaliere, S. Subianto, I. Savych, D. J. Jones, and J. Rozière, "Electrospinning: designed architectures for energy conversion and storage devices," *Energy & Environmental Science*, vol. 4, pp. 4761–4785, 2011.

[192] H. Fong, I. Chun, and D. H. Reneker, "Beaded nanofibers formed during electrospinning," *Polymer*, vol. 40, no. 16, pp. 4585–4592, Jul. 1999.

[193] J. H. Wendorff, S. Agarwal, and A. Greiner, Eds., *Electrospinning. Materials, Processing and Applications*. Weinheim: John Wiley and Sons, 2012, pp. 1 – 241.

[194] S. Ramakrishna, K. Fujihara, W.-E. Teo, T.-C. Lim, and Z. Ma, Eds., *An Introduction to Electrospinning and Nanofibers*. Singapore: World Scientific Publishing, 2005, pp. 1 – 380.

[195] R. Barhate and S. Ramakrishna, "Nanofibrous filtering media: Filtration problems and solutions from tiny materials," *Journal of Membrane Science*, vol. 296, no. 1–2, pp. 1–8, Jun. 2007.

[196] W. Cui, Y. Zhou, and J. Chang, "Electrospun nanofibrous materials for tissue engineering and drug delivery," *Science and Technology of Advanced Materials*, vol. 11, no. 1, p. 014108, Feb. 2010.

[197] Y. Ding, Y. Wang, L. Zhang, H. Zhang, C. M. Li, and Y. Lei, "Preparation of TiO_2-Pt hybrid nanofibers and their application for sensitive hydrazine detection.," *Nanoscale*, vol. 3, no. 3, pp. 1149–57, Mar. 2011.

[198] Z. Dong, S. J. Kennedy, and Y. Wu, "Electrospinning materials for energy-related applications and devices," *Journal of Power Sources*, vol. 196, no. 11, pp. 4886–4904, Jun. 2011.

[199] V. Thavasi, G. Singh, and S. Ramakrishna, "Electrospun nanofibers in energy and environmental applications," *Energy & Environmental Science*, vol. 1, no. 2, p. 205, 2008.

[200] C.-K. Liu, K. Lai, W. Liu, M. Yao, and R.-J. Sun, "Preparation of carbon nanofibres through electrospinning and thermal treatment," *Polymer International*, vol. 58, no. 12, pp. 1341–1349, Dec. 2009.
[201] M. Inagaki, Y. Yang, and F. Kang, "Carbon nanofibers prepared via electrospinning.," *Advanced materials*, vol. 24, no. 19, pp. 2547–66, May 2012.
[202] S. K. Nataraj, K. S. Yang, and T. M. Aminabhavi, "Polyacrylonitrile-based nanofibers—A state-of-the-art review," *Progress in Polymer Science*, vol. 37, no. 3, pp. 487–513, Mar. 2012.
[203] I. S. Chronakis, "Novel nanocomposites and nanoceramics based on polymer nanofibers using electrospinning process—A review," *Journal of Materials Processing Technology*, vol. 167, no. 2–3, pp. 283–293, Aug. 2005.
[204] L. Zhang, A. Aboagye, A. Kelkar, C. Lai, and H. Fong, "A review: carbon nanofibers from electrospun polyacrylonitrile and their applications," *Journal of Materials Science*, vol. 49, no. 2, pp. 463–480, Sep. 2014.
[205] N. Yusof and a. F. Ismail, "Post spinning and pyrolysis processes of polyacrylonitrile (PAN)-based carbon fiber and activated carbon fiber: A review," *Journal of Analytical and Applied Pyrolysis*, vol. 93, pp. 1–13, Jan. 2012.
[206] M. S. a. Rahaman, a. F. Ismail, and a. Mustafa, "A review of heat treatment on polyacrylonitrile fiber," *Polymer Degradation and Stability*, vol. 92, no. 8, pp. 1421–1432, Aug. 2007.
[207] Y. Wang and J. J. Santiago-aviles, "Magnetoconductance , carrier concentration and mobility measurement in electrospun carbon nanofibers," *Carbon*, vol. 41, pp. 2665–2667, 2003.
[208] F. Agend, N. Naderi, and R. Fareghi-alamdari, "Fabrication and Electrical Characterization of Electrospun Polyacrylonitrile-Derived Carbon Nanofibers," *Journal of Applied Polymer Science*, vol. 106, pp. 255–259, 2007.
[209] J. Huang, H. Hou, and T. You, "Highly efficient electrocatalytic oxidation of formic acid by electrospun carbon nanofiber-supported Pt_xAu_{100-x} bimetallic electrocatalyst," *Electrochemistry Communications*, vol. 11, no. 6, pp. 1281–1284, Jun. 2009.
[210] Z. Lin, L. Ji, and X. Zhang, "Electrocatalytic properties of Pt/carbon composite nanofibers," *Electrochimica Acta*, vol. 54, no. 27, pp. 7042–7047, Nov. 2009.
[211] Z. Lin, L. Ji, W. E. Krause, and X. Zhang, "Synthesis and electrocatalysis of 1-aminopyrene-functionalized carbon nanofiber-supported platinum–ruthenium nanoparticles," *Journal of Power Sources*, vol. 195, no. 17, pp. 5520–5526, Sep. 2010.
[212] M. Li, G. Han, and B. Yang, "Fabrication of the catalytic electrodes for methanol oxidation on electrospinning-derived carbon fibrous mats," *Electrochemistry Communications*, vol. 10, no. 6, pp. 880–883, Jun. 2008.
[213] M. Li, S. Zhao, G. Han, and B. Yang, "Electrospinning-derived carbon fibrous mats improving the performance of commercial Pt/C for methanol oxidation," *Journal of Power Sources*, vol. 191, no. 2, pp. 351–356, Jun. 2009.
[214] X. Liu, M. Li, G. Han, and J. Dong, "The catalysts supported on metallized electrospun polyacrylonitrile fibrous mats for methanol oxidation," *Electrochimica Acta*, vol. 55, no. 8, pp. 2983–2990, Mar. 2010.
[215] Y. Chang, G. Han, M. Li, and F. Gao, "Graphene-modified carbon fiber mats used to improve the activity and stability of Pt catalyst for methanol electrochemical oxidation," *Carbon*, vol. 49, no. 15, pp. 5158–5165, Dec. 2011.
[216] J.-H. Park, Y.-W. Ju, S.-H. Park, H.-R. Jung, K.-S. Yang, and W.-J. Lee, "Effects of electrospun polyacrylonitrile-based carbon nanofibers as catalyst support in PEMFC," *Journal of Applied Electrochemistry*, vol. 39, no. 8, pp. 1229–1236, Jan. 2009.
[217] R. Padmavathi and D. Sangeetha, "Synthesis and characterization of electrospun carbon nanofiber supported Pt catalyst for fuel cells," *Electrochimica Acta*, vol. 112, pp. 1–13, Dec. 2013.
[218] M. Li, Y. Chang, G. Han, and B. Yang, "Platinum nanoparticles supported on electrospinning-derived carbon fibrous mats by using formaldehyde vapor as reducer for methanol electrooxidation," *Journal of Power Sources*, vol. 196, no. 19, pp. 7973–7978, Oct. 2011.
[219] G.-H. An and H.-J. Ahn, "Pt electrocatalyst-loaded carbon nanofibre–Ru core–shell supports for improved methanol electrooxidation," *Journal of Electroanalytical Chemistry*, vol. 707, pp. 74–77, Oct. 2013.
[220] G. Zhang, W. Kataphinan, R. Teye-Mensah, P. Katta, L. Khatri, E. a. Evans, G. G. Chase, R. D. Ramsier, and D. H. Reneker, "Electrospun nanofibers for potential space-based applications," *Materials Science and Engineering: B*, vol. 116, no. 3, pp. 353–358, Feb. 2005.
[221] H. Wu, W. Pan, D. Lin, and H. Li, "Electrospinning of ceramic nanofibers: Fabrication, assembly and applications," *Journal of Advanced Ceramics*, vol. 1, no. 1, pp. 2–23, Jun. 2012.
[222] D. Li and Y. Xia, "Direct Fabrication of Composite and Ceramic Hollow Nanofibers by Electrospinning," *Nano Letters*, vol. 4, no. 5, pp. 933–938, May 2004.

[223] J. T. McCann, D. Li, and Y. Xia, "Electrospinning of nanofibers with core-sheath, hollow, or porous structures," *Journal of Materials Chemistry*, vol. 15, no. 7, p. 735, 2005.
[224] Y. Zhao, X. Cao, and L. Jiang, "Bio-mimic multichannel microtubes by a facile method.," *Journal of the American Chemical Society*, vol. 129, no. 4, pp. 764–5, Jan. 2007.
[225] S. Madhugiri, B. Sun, P. G. Smirniotis, J. P. Ferraris, and K. J. Balkus, "Electrospun mesoporous titanium dioxide fibers," *Microporous and Mesoporous Materials*, vol. 69, no. 1–2, pp. 77–83, Apr. 2004.
[226] M. Fehse, S. Cavaliere, P. E. Lippens, I. Savych, A. Iadecola, L. Monconduit, D. J. Jones, J. Rozie, F. Fischer, C. Tessier, L. Stievano, D. De Recherche, and B. A. Daney, "Nb-Doped TiO_2 Nanofibers for Lithium Ion Batteries," *J. Phys. Chem. C*, vol. 117, p. 13827 − 13835, 2013.
[227] T. G. Deepak, A. Gs, S. Thomas, A. T. A, S. V Nair, and S. Nair, "A Review on Materials for Light Scattering in Dye-sensitized Solar Cells," *RSC Advances*, vol. 4, pp. 17615–17638, 2014.
[228] Q. Long, M. Cai, J. Li, H. Rong, and L. Jiang, "Improving the electrical catalytic activity of Pt/TiO_2 nanocomposites by a combination of electrospinning and microwave irradiation," *Journal of Nanoparticle Research*, vol. 13, no. 4, pp. 1655–1662, Apr. 2010.
[229] A. Bauer, K. Lee, C. Song, Y. Xie, J. Zhang, and R. Hui, "Pt nanoparticles deposited on TiO_2 based nanofibers: Electrochemical stability and oxygen reduction activity," *Journal of Power Sources*, vol. 195, no. 10, pp. 3105–3110, May 2010.
[230] Q. Du, J. Wu, and H. Yang, "Pt@Nb-TiO_2 Catalyst Membranes Fabricated by Electrospinning and Atomic Layer Deposition," *ACS Catalysis*, vol. 4, pp. 144–151, 2014.
[231] K. Senevirathne, R. Hui, S. Campbell, S. Ye, and J. Zhang, "Electrocatalytic activity and durability of Pt/NbO_2 and Pt/Ti_4O_7 nanofibers for PEM fuel cell oxygen reduction reaction," *Electrochimica Acta*, vol. 59, pp. 538–547, Jan. 2012.
[232] M. A. Abdelkareem, Y. Ito, T. Tsujiguchi, and N. Nakagawa, "Carbon-TiO_2 Composite Nanofibers as a Promising Support for PtRu Anode Catalyst of DMFC," *ECS Transactions*, vol. 50, no. 2, pp. 1959–1967, 2012.
[233] E. Formo, Z. Peng, E. Lee, X. Lu, H. Yang, and Y. Xia, "Direct Oxidation of Methanol on Pt Nanostructures Supported on Electrospun Nanofibers of Anatase," *The Journal of Physical Chemistry C*, vol. 112, no. 27, pp. 9970–9975, Jul. 2008.
[234] E. Formo, E. Lee, D. Campbell, Y. Xia, B. Engineering, W. U. V, and S. Louis, "Functionalization of Electrospun TiO_2 Nanofibers with Pt Nanoparticles and Nanowires for Catalytic Applications," *Nano letters*, vol. 8, pp. 668–672, 2008.
[235] J. Wu, D. Zeng, and S. Zhang, "Mesoporous Al-doped SnO_2 nanotubes with enhanced gas-sensing properties fabricated by electrospinning," in *AMA Conferences - Sensor Materials*, 2013, pp. 257–262.
[236] L. Li, X. Yin, S. Liu, Y. Wang, L. Chen, and T. Wang, "Electrospun porous SnO_2 nanotubes as high capacity anode materials for lithium ion batteries," *Electrochemistry Communications*, vol. 12, no. 10, pp. 1383–1386, Oct. 2010.
[237] C. Gao, X. Li, B. Lu, L. Chen, Y. Wang, F. Teng, J. Wang, Z. Zhang, X. Pan, and E. Xie, "A facile method to prepare SnO_2 nanotubes for use in efficient SnO_2-TiO_2 core-shell dye-sensitized solar cells," *Nanoscale*, vol. 4, no. 11, pp. 3475–81, Jun. 2012.
[238] Y. S. Kim, H. S. Jang, and W. B. Kim, "An efficient composite hybrid catalyst fashioned from Pt nanoparticles and Sb-doped SnO_2 nanowires for alcohol electro-oxidation," *Journal of Materials Chemistry*, vol. 20, no. 36, p. 7859, 2010.
[239] A. B. Suryamas, G. M. Anilkumar, S. Sago, T. Ogi, and K. Okuyama, "Electrospun Pt/SnO_2 nanofibers as an excellent electrocatalysts for hydrogen oxidation reaction with ORR-blocking characteristic," *Catalysis Communications*, vol. 33, pp. 11–14, Mar. 2013.
[240] S. Sago, A. B. Suryamas, G. M. Anilkumar, T. Ogi, and K. Okuyama, "In situ growth of Pt nanoparticles on electrospun SnO_2 fibers for anode electrocatalyst application," *Materials Letters*, vol. 105, pp. 202–205, Aug. 2013.
[241] J. Zhang, M. B. Vukmirovic, K. Sasaki, A. U. Nilekar, M. Mavrikakis, and R. R. Adzic, "Mixed-metal pt monolayer electrocatalysts for enhanced oxygen reduction kinetics.," *Journal of the American Chemical Society*, vol. 127, no. 36, pp. 12480–1, Sep. 2005.
[242] K.-Y. Chan, J. Ding, J. Ren, S. Cheng, and K. Y. Tsang, "Supported mixed metal nanoparticles as electrocatalysts in low temperature fuel cells," *Journal of Materials Chemistry*, vol. 14, no. 4, p. 505, 2004.
[243] E. Antolini, "Formation , microstructural characteristics and stability of carbon supported platinum catalysts for low temperature fuel cells," *Journal of Materials Science*, vol. 38, pp. 2995–3005, 2003.
[244] C. Coutanceau, S. Brimaud, C. Lamy, J.-M. Léger, L. Dubau, S. Rousseau, and F. Vigier, "Review of different methods for developing nanoelectrocatalysts for the oxidation of organic compounds," *Electrochimica Acta*, vol. 53, no. 23, pp. 6865–6880, Oct. 2008.

[245] A. Esmaeilifar, S. Rowshanzamir, M. H. Eikani, and E. Ghazanfari, "Synthesis methods of low-Pt-loading electrocatalysts for proton exchange membrane fuel cell systems," *Energy*, vol. 35, no. 9, pp. 3941–3957, Sep. 2010.

[246] H. Bönnemann, R. Brinkmann, P. Britz, U. Endruschat, R. Mörtel, U. A. Paulus, T. J. Schmidt, H. A. Gasteiger, and R. J. Behm, "Nanoscopic Pt-bimetal colloids as precursors for PEM fuel cell catalysts," *Journal of New Materials for Electrochemical Systems*, vol. 206, pp. 199–206, 2000.

[247] P. Boutonnet, M; Kizling, J; Stenius, "The preparation of monodisperse colloidal metal particles from microemulions," *Colloids and Surfaces*, vol. 5, no. 3, pp. 209–225, 1982.

[248] F. Fievet, J. P. Lagier, and B. Blin, "Homogeneous and heterogeneous nucleations in the polyol process for the preparation of micron and submicron size metal particles," *Solid State Ionics*, vol. 32–33, no. Part 1, pp. 195–205, 1989.

[249] G. Viau, P. Toneguzzo, A. Pierrard, O. Acher, and F. Fie, "Heterogeneuos Nucleation and Growth of Metalnanoparticles in Polyols," *Scripta materialia*, vol. 44, pp. 2263–2267, 2001.

[250] C. Bock, C. Paquet, M. Couillard, G. a Botton, and B. R. MacDougall, "Size-selected synthesis of PtRu nano-catalysts: reaction and size control mechanism," *Journal of the American Chemical Society*, vol. 126, no. 25, pp. 8028–37, Jun. 2004.

[251] H.-S. Oh, J.-G. Oh, Y.-G. Hong, and H. Kim, "Investigation of carbon-supported Pt nanocatalyst preparation by the polyol process for fuel cell applications," *Electrochimica Acta*, vol. 52, no. 25, pp. 7278–7285, Sep. 2007.

[252] M. Tsuji, M. Hashimoto, Y. Nishizawa, M. Kubokawa, and T. Tsuji, "Microwave-assisted synthesis of metallic nanostructures in solution," *Chemistry a Eurorean Journal*, vol. 11, no. 2, pp. 440–52, Jan. 2005.

CHAPTER 2:

Carbon nanofibres as electrocatalyst support

1 Synthesis and characterisation of carbon nanofibres

Graphitised CNFs are widely explored as catalyst supports for H_2-PEMFC and DMFC due to their higher corrosion resistance, enhanced conductivity and SMSI compared to that of traditional carbon black supports (see Chapter 1). However, graphitisation at high temperatures usually induces a decrease of the specific surface area, which is essential for high catalyst dispersion on the support. Therefore in this chapter, electrospun CNFs were carbonised at three temperatures (700, 1000 and 1500 °C) in order to find a good compromise between high electrical conductivity and high specific surface area for the support. The obtained samples were characterised by scanning electron microscopy (SEM), Raman, N_2 adsorption/desorption, conductivity measurement and finally accelerated corrosion tests. Afterwards Pt nanoparticles were prepared using microwave-assisted polyol method and deposited on CNFs. Electrochemical characterisation of the obtained Pt/CNFs electrocatalyst was performed using RDE.

Results described in this chapter have been partially published in [1]:

I. Savych, J. Bernard d'Arbigny, S. Subianto, S. Cavaliere, D. J. Jones, and J. Rozière, On the Effect of Non-Carbon Nanostructured Supports on the Stability of Pt Nanoparticles during Voltage Cycling: a Study of TiO_2 Nanofibres, *Journal of Power Sources* (2014) 257, 147-155.

1.1 Synthesis of carbon nanofibres

The synthesis steps for the preparation of carbon nanofibres (CNFs) from a polymer precursor are depicted in Figure 1. A 7.5 wt. % polyacrylonitrile (PAN, M_w ~ 150,000 g/mol, Sigma-Aldrich) solution in N,N-dimethylformamide (DMF, 98 %, Sigma-Aldrich) was stirred at 60 °C overnight, in order to obtain a homogeneous solution and thus electrospun fibres with uniform diameter. The fibre diameter increases with the polymer concentration [2]. Therefore, the concentration of 7.5 wt. % PAN was chosen in order to achieve small fibre diameter and avoid beads formation, which takes place at low concentration of the polymer. The solution was electrospun under 10 kV. The distance between the needle tip and aluminium collector was 10 cm and the flow rate was 0.5 ml/h. The electrospun nanofibrous mat was stabilised in air at 280 °C for 1 h. The heating rate (1 °C/min) was relatively low in order to prevent release of large amount of heat leading to the fusing of the polymer [2]. After cooling down to room temperature (RT), the fibres were carbonised at 700 °C, 1000 °C or 1500 °C (called from now on as CNF_{700}, CNF_{1000} and CNF_{1500}) for 1 h in an inert atmosphere (heating rate was 5 °C/min).

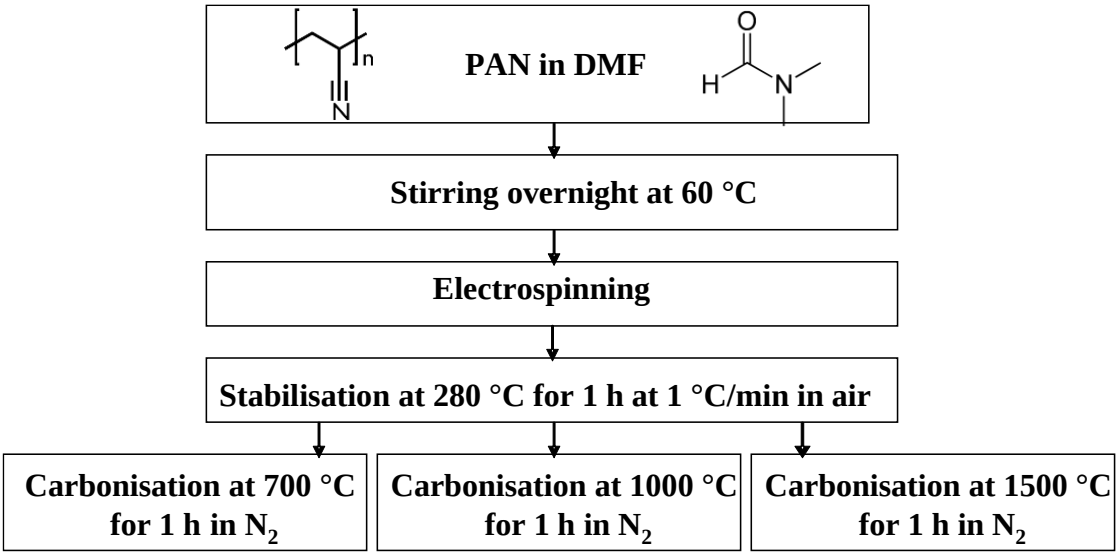

Figure 1: Schema of CNFs synthesis protocol by electrospinning of PAN.

1.2 Morphological characterisation of carbon nanofibres

1.2.1 SEM analysis

Figure 2 shows as-spun (a), stabilised at 280 °C (b), carbonised at 700 °C (e) and 1000 °C (f) CNFs with an average diameter of 447, 411, 273 and 224 nm, respectively. It can be observed that the carbon fibres diameter decreases with increasing carbonisation temperature. This behaviour is attributed to weight loss and gas evolution (CO, CO_2, etc). A decrease in fibre diameter at temperatures higher than 1000 °C is related to the densification caused by the liberation of heteroatoms [3]. After the stabilisation, the white nanofibrous mat became brown, and after carbonisation it became black, with a mass loss of about 46 % of the initial weight.

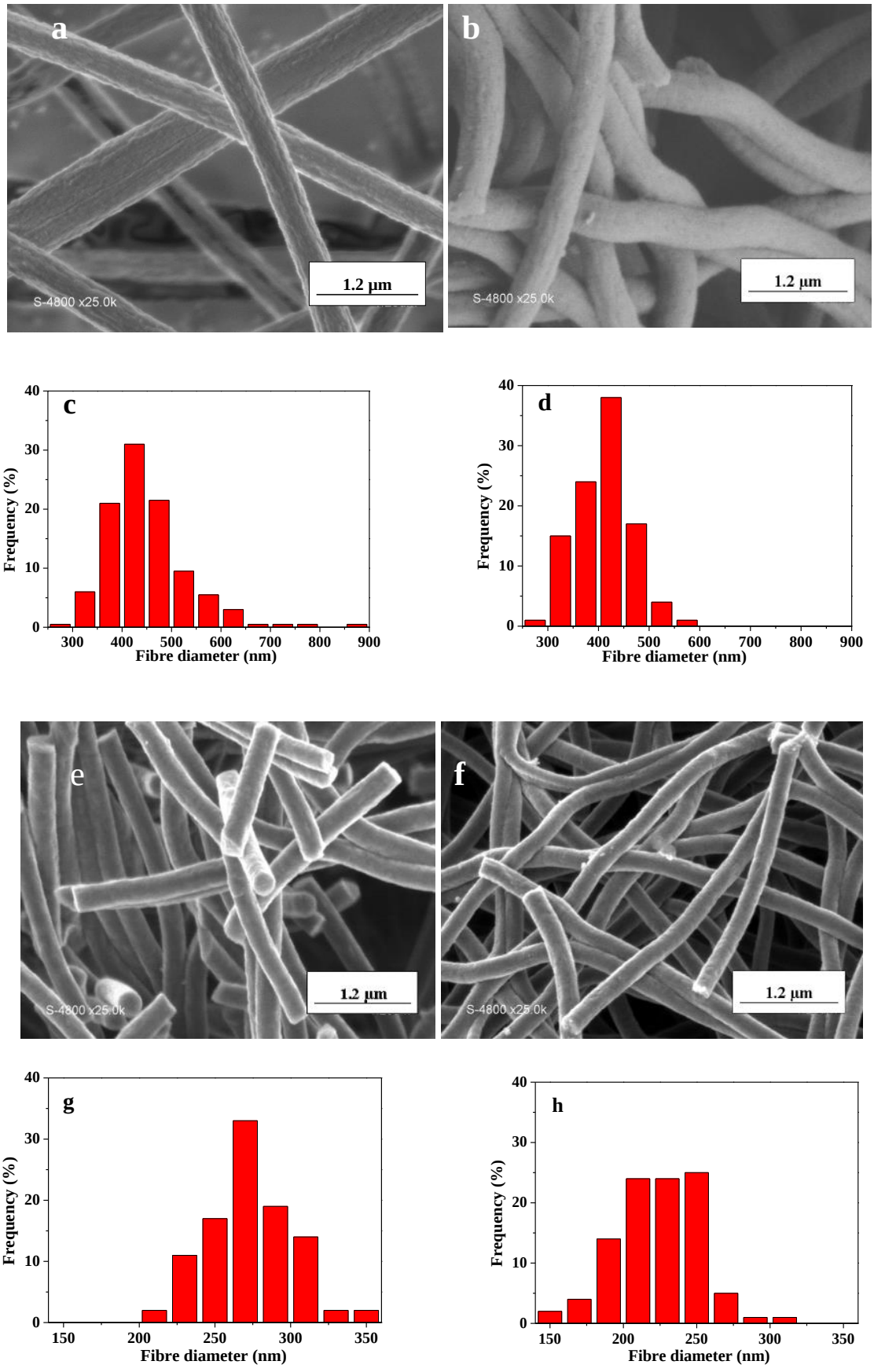

Figure 2: SEM images of as-spun (a), stabilised at 280 °C (b) and carbonised at 700 °C (e), at 1000 °C (f) CNFs and corresponding fibres diameter distribution histograms obtained from measurements of 100 CNFs (c, d, g and h).

1.2.2 Specific surface area measurements

High surface area is one of the most important characteristics of the support, which allows high catalyst dispersion. In order to determine the specific surface area of CNFs, N_2 adsorption/desorption analysis was carried out. The nitrogen adsorption/desorption isotherms of CNF_{700}, CNF_{1000} and CNF_{1500} are depicted in Figure 3. The adsorption was completed at low relative pressure approximately at 0.05 (type I isotherm [4]), which is typical for microporous materials. However, CNF_{1000} and CNF_{1500} provided very low amount of micropores compared to CNF_{700} sample, which showed the highest BET surface area of 262 m^2/g. CNF_{1500} showed the smallest surface area of 20 m^2/g, as calculated by the Brunauer–Emmett–Teller (BET) method. Specific surface area of CNFs decreased with the increasing carbonisation temperature due to the unification of micropores at high temperatures [2].

The specific surface area of CNF_{1000} (36 m^2/g) obtained in this work was lower than that of electrospun CNFs carbonised at 1000 °C obtained by Padmavathi et al. (107.9 m^2/g) [5]. This difference in surface area can be attributed to the high heating rate (10 °C/min) used by Padmavathi et al. However, our CNF_{1500} sample provided slightly higher surface area (20 m^2/g) compared to that of electrospun carbon nanofibrous mats (CFMs) carbonised at 1200 °C for 1 h (7 m^2/g) [6]. Specific surface area of CNFs can be enhanced using steam activation at 800 °C and 30 vol. % steam [4].

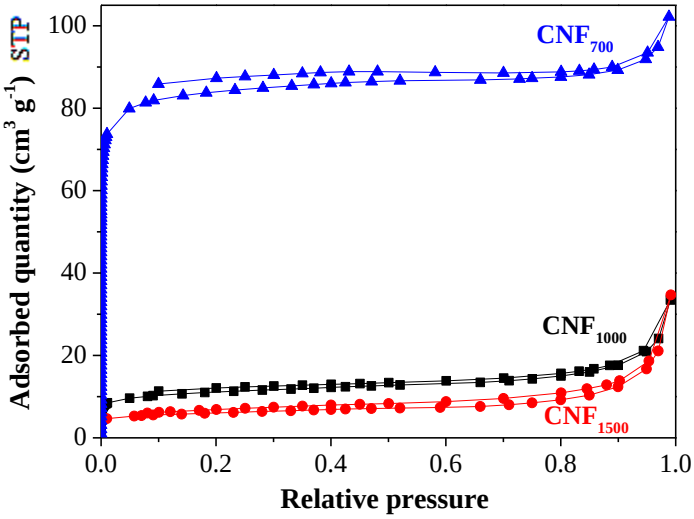

Figure 3: Nitrogen adsorption/desorption isotherms of CNF_{700}, CNF_{1000} and CNF_{1500}.

1.3 Structural characterisation of carbon nanofibres

1.3.1 Raman analysis

Raman spectroscopy was performed in order to determine the degree of graphitisation of the carbons carbonised at different temperatures.

Raman spectra of CNF_{700}, CNF_{1000} and CNF_{1500} are shown in Figure 4. D and G-bands [7] are observed at 1360 and 1590 cm^{-1}, respectively. The D-band corresponds to disordered structures and G-band is attributed to the E_{2g} (C=C stretching vibrations) in the sp^2-hybridised graphitic structures [8]. The intensity of G-band increases, while its full width at half maximum (FWHM) decreases with increasing carbonisation temperature. It is well known that the relative intensity ratio I_D/I_G of the D-band and G-band depends on the degree of graphitisation and arrangement of graphitic planes. This I_D/I_G ratio has decreased from 2.2 for CNF_{700} to 1.7 for CNF_{1000} and 0.9 for CNF_{1500}. Kim et al. [9] observed similar I_D/I_G ratios of 2.7 and 1.4 for electrospun carbon nanofibres carbonised at 700 °C and 1000 °C, respectively. This decrease in I_D/I_G ratios with increasing carbonisation temperature is attributed to conversion of disordered carbon into more ordered graphitic structure. Carbons with high graphitisation degree show the advantage of improved resistivity to corrosion, but the deposition of catalyst can be more difficult due to the decreased number of active sites on the carbon surface [10].

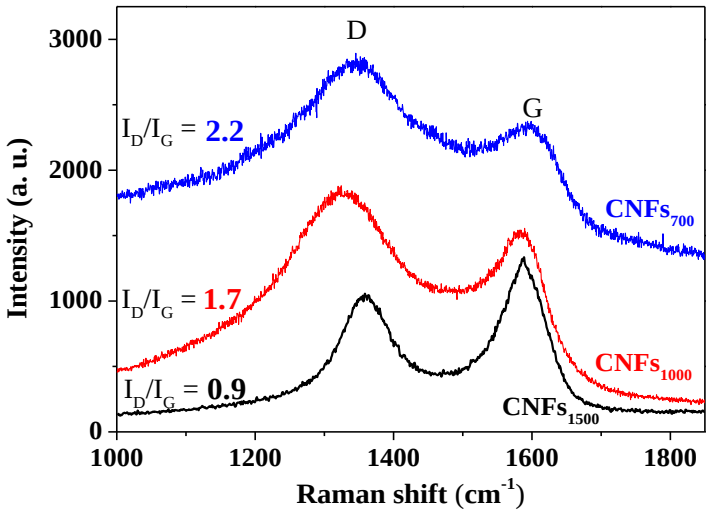

Figure 4*:* Raman spectra of carbon fibres carbonised at 700 °C, 1000 °C and 1500 °C.

1.3.2 XRD analysis

X-ray diffraction patterns of CNF_{1000} are shown in the Figure 5. The reflection at 2 θ = 25° was attributed to the (002) crystallographic plane of graphite structure [9]. A small broad peak at 2 θ = 43° is assigned to the graphite basal plane (100) [11],[12].

The large width of both peaks indicates the amorphous structure of the CNF support. The average crystallite size of 1.4 nm were calculated from the (002) plane using the Scherrer formula, which was smaller than the one obtained by Kim et al, where they found an average size of 2.15 nm [9] for CNFs calcinated at 1000 °C:

$$L= (K \lambda)/((\beta_{obs} - \beta_{instrm}) \cos(\theta)),$$

where: L = Cristallite size (nm), λ = wavelength of the radiation (1.54 Å Kα1 of Cu), K = Sherrer constant (usually 0.87 < K < 1), β_{obs} = observed full width at half maximum (FWHM) (radian), β_{instrm} = instrumental broadening.

FWHM was measured using the XFit program. The instrumental broadening was calculated using the following formula:

$$\beta_{instrm} = A + B_1 \text{ x } (2\ \theta) + B_2 \text{ x } (2\ \theta)^2 ,$$

where: $A = 8.11\ 10^{-2}$ is polynomial constant, $B_1 = -8.36\ 10^{-4}$ and $B_2 = 9.29\ 10^{-6}$ are polynomial factors.

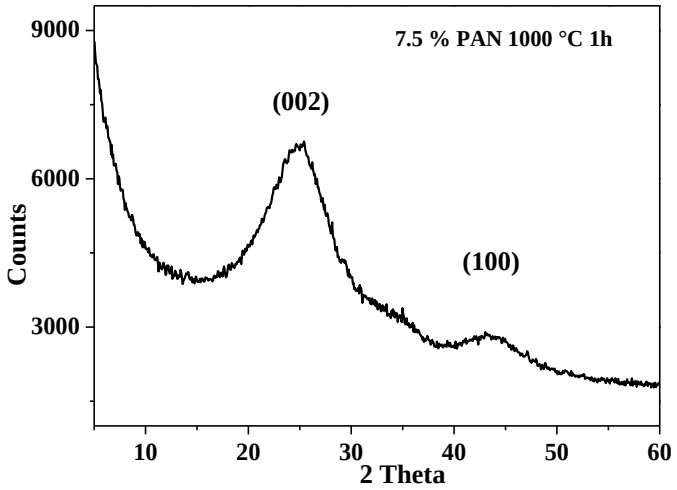

Figure 5: X-ray diffraction patterns of CNF_{1000}.

1.4 Electrical characterisation of carbon nanofibres

1.4.1 Electrical conductivity measurements

Electrical conductivity is a crucial property of the electrode materials. The Van der Pauw method was used to observe the trends in resistivity of carbon-based supports using thin and flat pellets with similar porosity and uniform thickness.

An in-house developed conductivity cell consists of a Teflon body, ceramic heating element and four small area electrodes positioned, as shown in Figure 6. The temperature was controlled using a thermocouple. The four electrodes (A, B, C and D) were coated with Pt and placed on the boundary of the pellet. A current was passed through two electrodes (for instance, I_{AB}) and the voltage was measured through the other two electrodes (for instance, U_{CD}). The resistance can be calculated via Ohm's law:

$$R_{AB,CD} = U_{CD}/I_{AB} \text{ and } R_{BC,DA} = U_{DA}/I_{BC}$$

Van der Pauw showed that the sheet resistance can be measured from these two resistances using the equation [13]:

$$\exp(-\pi\, t\, R_{AB,CD}/\rho) + \exp(-\pi\, t\, R_{AC,BD}/\rho) = 1,$$

where: t is the thickness of the sample and ρ is the specific resistance of the material. This equation can be solved for ρ as:

$$\rho = (\pi\, t / \ln 2)\, F\, (R_{AB,CD} + R_{AC,BD})/2,$$

where: F is the "correction function" of the ratio $R_{AB,CD}/R_{AC,BD}$ defined by Van der Pauw [13]. When the sample has an axis of symmetry ($R_{AB,CD} = R_{AC,BD}$) the sheet resistance can be calculated as:

$$\rho = \pi\, t\, R_{AB,CD}/\ln 2$$

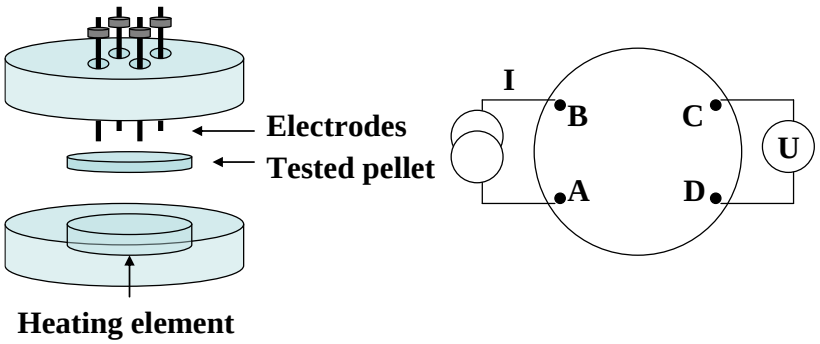

Figure 6: Schema of the in-house developed conductivity cell.

Figure 7 shows the electrical conductivities of the carbon nanofibres measured as a function of temperature between 20 and 250 °C with a few minutes stabilisation for each point. The electrical conductivity values increased with increasing final carbonisation temperature of PAN fibres. The electrical conductivity of $CNF_{700°C}$ (10^{-3} S/cm) at RT was about three orders of magnitude lower than that of CNF_{1000} (6.2 S/cm), CNF_{1500} (10.0 S/cm) and Vulcan XC-72R (5.3 S/cm). Similar increase of the conductivity with carbonisation temperature of PAN was observed by Kim et al. (6.8 10^{-3} S/cm for CNF_{700}, 1.96 S/cm for CNF_{1000} [9] and 14.86 S/cm for CNF_{1500} [3]). These results can be attributed to the increase in graphitisation degree with increasing carbonisation temperature. The commercial Vulcan XC-72R and CNF_{1500} show metallic behaviour. Their electrical conductivity decreases with the increase of temperature, while the conductivity of CNF_{1000} remains almost unchanged. The CNF_{700} sample shows semiconductor behaviour, its conductivity increases with increasing temperature.

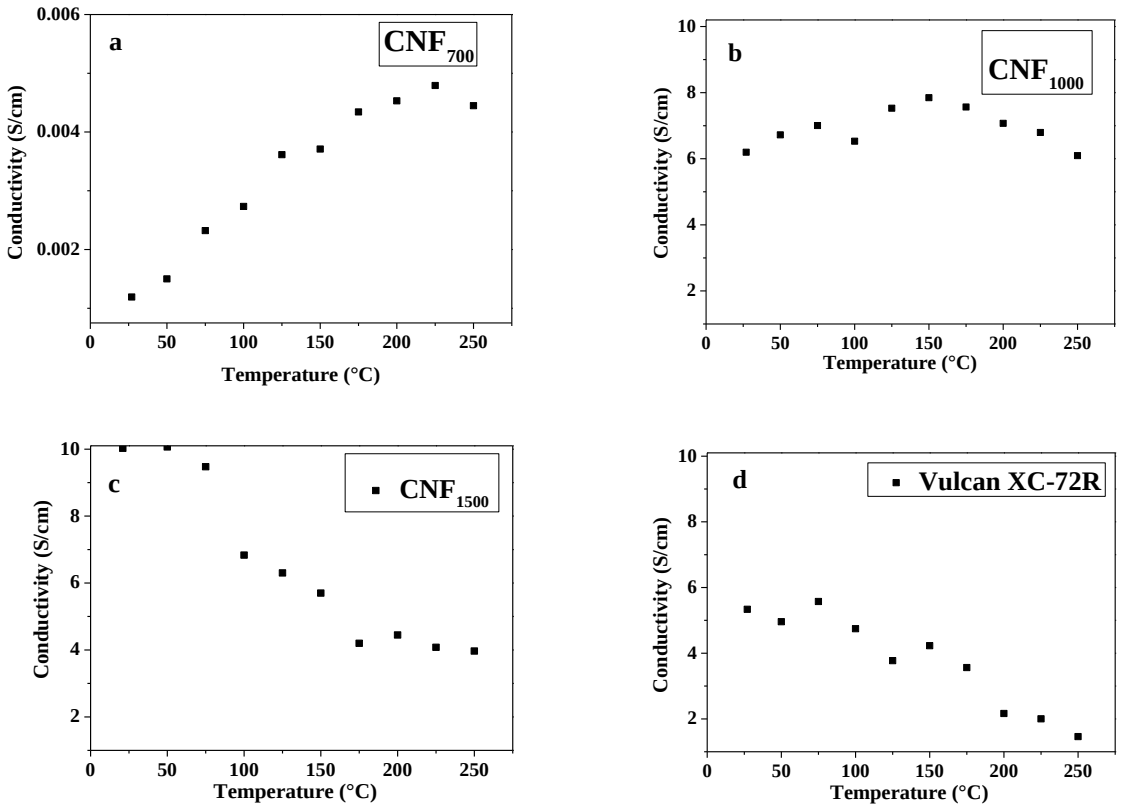

Figure 7: Electrical conductivity of CNF_{700} (a), CNF_{1000} (b), CNF_{1500} (c) and Vulcan XC-72R (d) as a function of the temperature.

The properties of the synthesised CNFs are summarised in Table 1. The degree of graphitisation and electrical conductivity of carbon fibres increase with carbonisation temperature, however the specific surface area decreases. CNF_{1000} and CNF_{1500} sample were chosen for further characterisation due to their high conductivity compared to that of CNF_{700}.

Table 1: Ratio of D-band /G-band, conductivity and surface area of CNF_{700}, CNF_{1000} and CNF_{1500}.

Carbonisation temperature	700 °C	1000 °C	1500 °C
Ratio of D-band /G-band	2.2	1.7	0.9
Electrical conductivity, S/cm	0.0012	6.2	10
Specific surface area, m^2/g	262	36	20

1.4.2 Electrochemical stability of the support

The accelerated stress test [14],[15] was carried out at 1.4 V RHE for 2 h at 80 °C in 0.5 M H_2SO_4, in order to evaluate and compare electrochemical stability of CNFs at high potentials. Corrosion currents measured for CNF_{1000}, CNF_{1500} and Vulcan XC-72R are shown in Figure 8a. The integrated corrosion-oxidation charges for CNF_{1000}, Vulcan XC-72R and CNF_{1500} were 5.6 and 3.9 and 1.4 C/mg, respectively, indicating higher corrosion resistance of CNF_{1500} attributed to its high graphitic degree. Commercial Ketjenblack support showed higher oxidation charge (17.44 C/mg) [14]. This result may be related to the high surface area of Ketjenblack (850 m^2/g). Oxidation currents in logarithmic scale show comparable slopes for all samples indicating similar degradation mechanisms (Figure 8b).

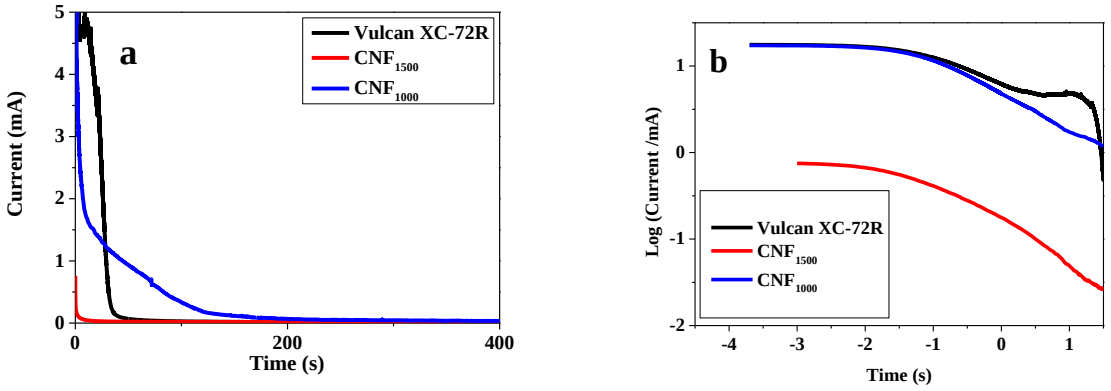

Figure 8: Oxidation currents in linear (a) and logarithmic (b) scales for CNF_{1000}, CNF_{1500} and Vulcan XC-72R at 1.4 V_{RHE}, 80 °C in 0.5 M H_2SO_4 solution.

CNF_{1500} has shown the best electrochemical stability among the tested samples. However, due to the technical limitations of our laboratory (tubular oven cannot be heated at 1500 °C) it was provided by external laboratory. Unfortunately, it was not possible to obtain higher amount of this material, which was necessary for further characterisation. Therefore, only the CNF_{1000} sample was characterised as Pt nanoparticles support, as described in the following paragraphs.

2 Synthesis and characterisation of Pt supported on CNFs

In this work, Pt nanoparticles were synthesised by microwave-assisted polyol method (see section 4 of Chapter 1) and deposited on commercial Vulcan XC-72R support and CNFs, in order to investigate the effect of support on the catalyst activity and stability. Briefly, Pt precursor was dissolved in ethylene glycol, which plays the role of the solvent, as well as reducing and stabilising agent for Pt nanoparticles. NaOH solution in ethylene glycol was added, in order to increase concentration of glycolate ions, which can stabilise Pt particles by forming chelate-type complexes via their carboxyl groups [16]. The obtained solution was heated in microwave reactor at 120 °C for 6 min. More details on the preparation procedure are provided in the experimental part (Annex A).

2.1 Synthesis and physico-chemical characterisation of Pt/CNFs

Zeta potential measurements

Oh et al. have modified the polyol method by changing the pH after the reduction of Pt, in order to increase the Pt loading on the carbon support and minimise the loss of Pt [16]. In our work, Zeta potential measurement were also performed, in order to find the optimum pH value for the Pt adsorption onto the CNFs surface. Figure 9 shows the zeta potential measured as a function of pH for Pt colloid on different supports. As observed in the Figure, the zeta potential of Pt colloid was negative for the whole pH range from 2 to 10, while the zeta potential for the carbon (Vulcan XC-72R) became positive when the pH of the solution changed from alkaline to acidic. Oh et al. also reported that zeta potential of the carbon support was positive at pH < 4 [17]. The zeta potential of CNFs was positive when the pH was ca 2. To avoid the electrostatic repulsive force and allow adsorption of Pt on the CNFs surface, the pH of the solution was changed from 11 to 2 after the polyol synthesis.

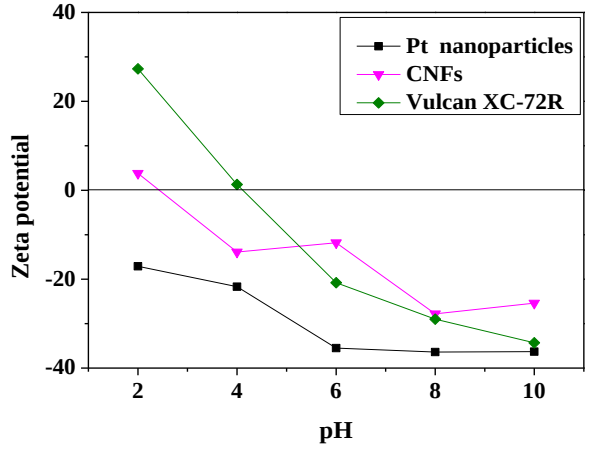

Figure 9: Zeta potential as a function of pH for Pt colloid and different supports.

Morphological characterisation

Figure 10 shows TEM images of the obtained Pt nanoparticles on CNFs and Vulcan XC-72R supports. The Pt nanoparticles diameter was 2.3 nm for Pt on CNFs and 2.4 nm for Pt on Vulcan XC-72R. The Pt nanoparticles were less homogeneously dispersed on the surface of CNFs than on the Vulcan XC-72R.

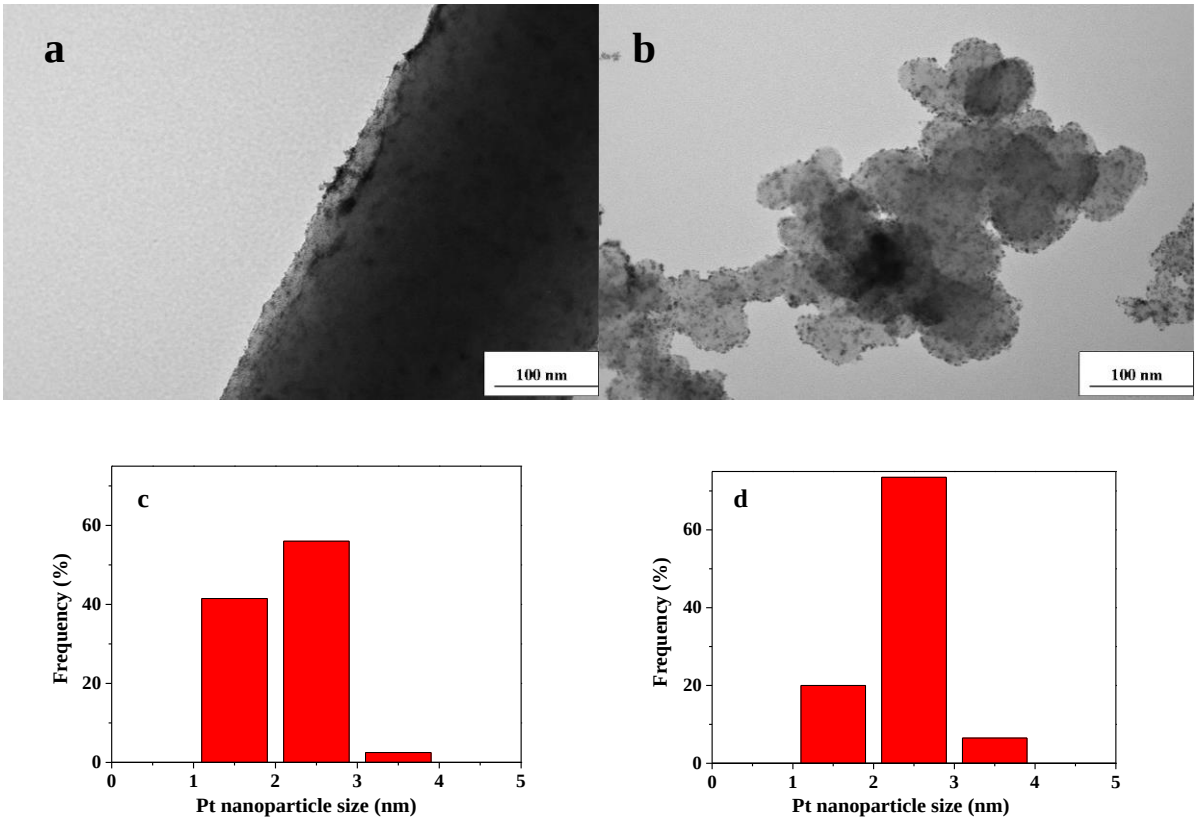

Figure 10: TEM micrographs of Pt/CNFs (a) and Pt/Vulcan XC-72R (b) and corresponding Pt nanoparticle size distribution histograms (c and d).

Determination of the Pt loading

Pt loading on the carbon-based supports was measured by thermogravimetric analysis (TGA). Pt/CNFs and Pt/Vulcan XC-72R were heated up to 800 °C at a heating rate of 10 °C/min in air in order to decompose the carbon and to obtain pure Pt. The measured Pt loading were 18 wt. % for Pt/CNFs and 33 wt. % for Pt/Vulcan XC-72R, respectively. Higher Pt adsorption on the Vulcan XC-72R may be attributed to high specific surface area of the commercial support.

Surface analysis

In order to determine the surface oxidation states of the deposited Pt nanoparticles, XPS analysis of Pt/CNFs and Pt/Vulcan XC-72R was performed. The investigated regions were the

C 1s of the support and the Pt 4f of the deposited electrocatalyst for the two carbon-based samples (Figure 11). The C 1s spectrum was fitted with two peaks for the Pt/CNFs and with three peaks for Pt/Vulcan XC-72R. The most intense peak at 284.7 eV is assigned to graphitic carbon. The higher binding energy peak at 286 eV corresponds well to the published value for –CO like species [19]. The small peak at 288.8 eV of the Pt/Vulcan XC-72R can be attributed to the functional groups with high oxygen contents (for example -COOH).

After fitting the Pt 4f signal, it can be observed that there are two peaks underneath each of the peaks of the doublet. The intense doublet (at 71.4 eV for Pt/CNFs and 71.5 eV for Pt/Vulcan XC-72R) corresponds to metallic Pt. The slight shift of this doublet to higher binding energies is typical for small Pt particles [20]. The small doublet at 72.3 eV for Pt/CNFs and for Pt/Vulcan can be attributed to the PtO and $Pt(OH)_2$ [21].

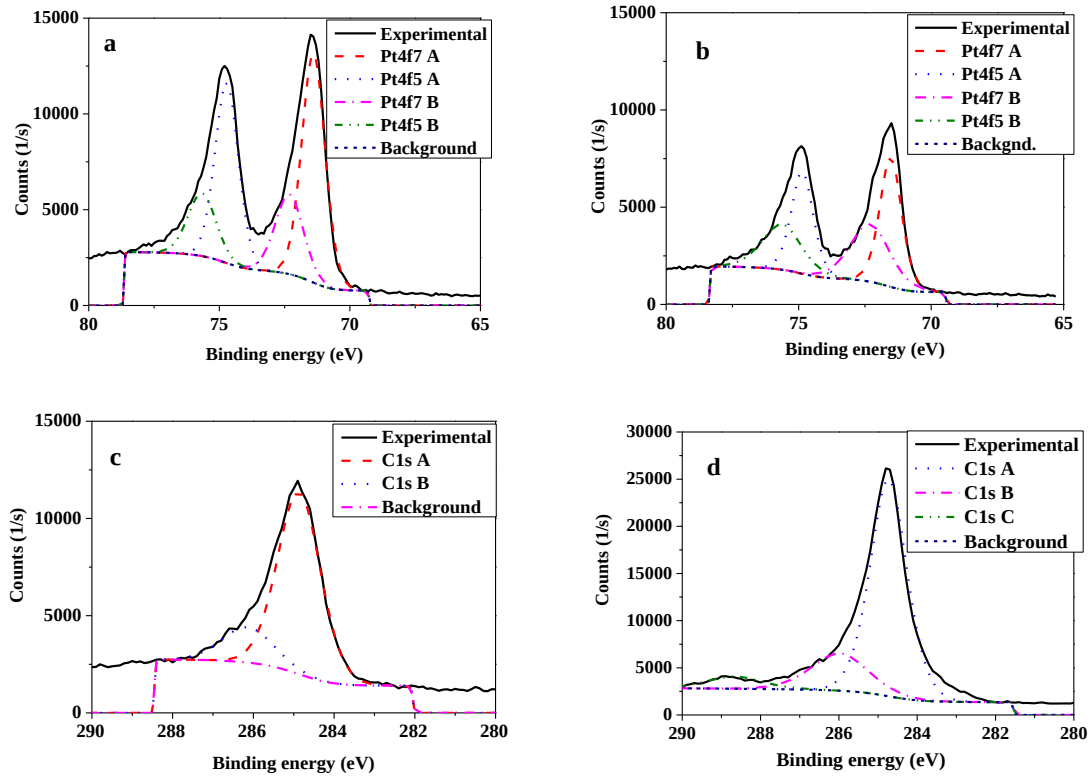

Figure 11: The C 1s and Pt 4f regions of the XPS spectrum of the Pt (a) on CNFs (c) and Pt (b) on Vulcan XC-72R (d) electrocatalysts.

2.2 Electrochemical characterisation of Pt/CNFs

The electrochemical surface area (ECSA) and stability of the obtained electrocatalysts and commercial Pt/C was evaluated by cycling voltammetry in three-electrode cell. Furthermore, ORR activity measurements and TEM observations were carried out before and after stability test, in order to compare degradation of different carbon-based supports.

2.2.1 Measurements in three-electrode cell

Principle

The electrochemical characterisation was carried out in a three-electrode set up consisting of a working electrode, a reference electrode and a counter electrode (Figure 12). During cycling voltammetry and linear sweep voltammetry the current was measured while the applied voltage was varied. The working electrode is used to apply the desired potential in a controlled way. A rotating disc electrode (working electrode) consisted of a glassy carbon disc with a surface area of 0.196 cm^2 surrounded by a Teflon sheath. A saturated calomel reference electrode (Hg / Hg_2Cl_2 / Cl^-) was used as the reference electrode to control the applied potential. The standard potential of this electrode is +0.241 V versus standard hydrogen electrode (RHE) at 25 °C in acidic medium. The main disadvantage of this electrode is the diffusion of Cl^- ions from the electrode to the Pt surface. Such ions can be adsorbed on the Pt, thereby blocking its active sites. In order to solve this problem, the reference electrode with a double liquid junction was used. The secondary salt bridge should be filled with a reference electrolyte solution which does not contain Cl^- ions (for example KNO_3). Pt wire was used as the counter electrode. The electrochemical characterisation was performed in N_2 saturated 0.1 M $HClO_4$. This acid was chosen in order to avoid the poisoning effect of sulphate adsorption onto the Pt surface in H_2SO_4 solution [22].

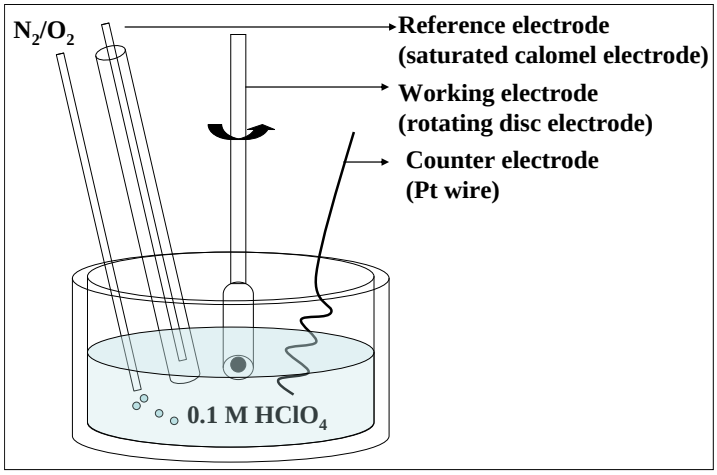

Figure 12: Schema of the three-electrode cell

2.2.2 Determination of the electrochemical surface area (ECSA)

Principle

Cyclic voltammetry was performed to determine the ECSA of the composite electrodes prepared in this thesis. The electrode was cycled in the potential range from 0.05 to 1.2 V vs. RHE at a scan rate of 50 mV/s in an electrolyte solution containing 0.1 M $HClO_4$.

Figure 13 shows typical cyclic voltammogram of a Pt/C catalyst. Three distinct zones may be observed in the voltammogram of Pt in the acid solution, namely: the hydrogen region, the double layer region and the oxygen region. In the double-layer region only the capacitive processes take place. Pt oxide is formed in the potential region from 0.8 to 1.2 V (oxygen region). The obtained PtO layer is desorbed in the reverse sweep from 1.2 to 0.6 V (hydrogen region). Hydrogen adsorption/desorption region in the potential range of 0.05 to 0.4 V is usually used to estimate the electrochemical surface area (ECSA) by integrating the hydrogen adsorption peak after subtracting the effect of the double layer region using the following equation:

$$ECSA = Q_{ads} / \Gamma\, m_{Pt} \text{ [23]},$$

where: $Q_{ads} = \int Idt$ is charge density obtained after the integration of the hydrogen desorption peak, $\Gamma = 210\ \mu C/cm^2$ [24] is the charge required to reduce a monolayer of protons onto the Pt surface and m_{Pt} is mass of Pt on the electrode. Γ is a charge equivalent for 1 cm^2 of Pt, it can be calculated according to the following equation:

$$\Gamma = e \times d = (1.602 \times 10^{-19}\ C) \times (1.31 \times 10^{15}\ cm^2) = 210\ \mu C/cm^2 \text{ [23]},$$

where: e is the electron charge and d is diameter of the Pt atom, in the case when Miller index planes (100), (110), and (111) predominate, in a proportion of 33 % for each one.

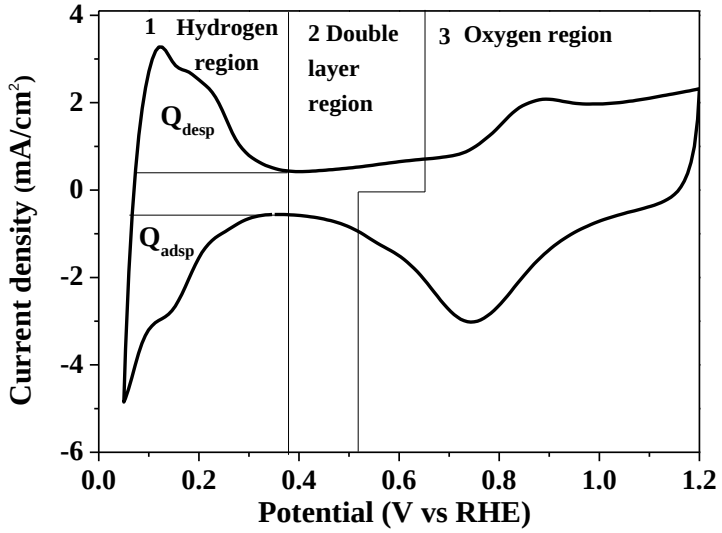

Figure 13: Cyclic voltammogram for a 50 % Pt/C (JM) in N_2 saturated 0.1 M $HClO_4$ with a scan rate of 50 mV/s.

Results and discussion

Cyclic voltammograms of Pt/C, Pt/Vulcan XC-72R and Pt/CNFs are shown in Figure 14. The ECSA for Pt/C, Pt/Vulcan XC-72R and Pt/CNFs was calculated to be 33 m^2/g, 47 m^2/g and 24 m^2/g respectively. The ECSA calculated for Pt/C (33 m^2/g) is smaller compared to that of Pt/Vulcan XC-72R (47 m^2/g). This result may be attributed to the larger Pt nanoparticles size of 3.8 nm (obtained from TEM observations) for Pt/C sample compared to particle size of 2.4 nm for Pt/Vulcan XC-72R. The smallest ECSA (24 m^2/g) was obtained for Pt supported on CNFs, which can be related to the small specific surface area of the CNFs (36 m^2/g). This can lead to poor Pt dispersion and formation of bigger aggregates of the Pt nanoparticles. The ECSA obtained in this thesis is higher than that of 20 wt. % Pt/CNFs (17.16 m^2/g) obtained by Padmavathi et al. [5], probably due to the difference in Pt nanoparticles size (2.4 and 5.2 nm).

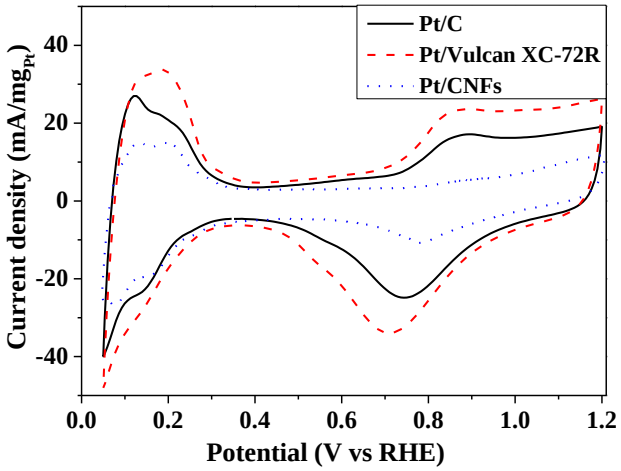

Figure 14: Cyclic voltammograms obtained for Pt/CNFs, Pt/C and Pt/Vulcan XC-72R in N_2 saturated 0.1 M $HClO_4$ solution.

2.2.3 Determination of kinetics of oxygen reduction reaction activity

Principle

An electrochemical reaction usually consists of two main steps, the electron transfer process and mass transfer process. The velocity of the reaction is determined by the slowest step called the rate-determining step. Three distinctive regions can be observed on the polarisation curves of the oxygen reduction reaction: the electron-transfer, mixed and mass transport controlled regions (Figure 15). In the electron-transfer controlled regime, the current density varies with the potential, but it is independent of the rotation rate of the RDE. When the mass transfer becomes the rate-determining step, the current density is independent of potential, but depends strongly on the rotation rate of the RDE.

ORR mass activities were calculated from the polarisation curves at a rotation speed of 900 rpm before and after the stability test using the Koutecky-Levich equation [25]:

$$1/J = 1/J_k + 1/J_d,\ J_k = J_d\ J/(J_d - J)$$

where: J_k is the kinetic current density (ORR activity), J_d is a diffusion-limited current density (obtained from the diffusion-limited region at 0.3 V) and J is the measured current density.

The number of electrons involved in the reaction can be approximately estimated using following formula:

$$1/J_d = 1/n\ B\ \omega^{1/2} \text{ in which } B = 0.2\ F\ D_{0_2}^{2/3}\ \nu^{-1/6}\ C_{0_2},$$

where: n is the number of electrons involved in the reaction, J is the experimentally obtained current density, F the Faraday constant (96485.34 C/mol), ω the rotation speed of the RDE, C_{0_2} the bulk O_2-solubility (1.26 10^{-3} mol/L), D_{0_2} the diffusion coefficient of O_2 in the $HClO_4$ solution (1.93 10^{-5} cm^2/s) and ν the kinematic viscosity of the electrolyte (1.009 10^{-2} cm^2/s) [26].

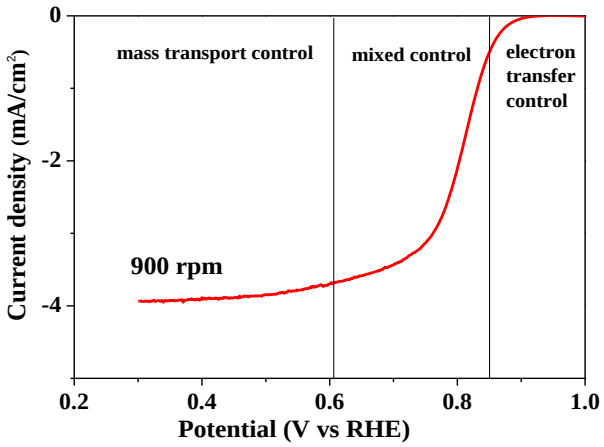

Figure 15: Oxygen reduction reaction polarization curves obtained on Pt/Vulcan XC-72R.

Results and discussion

The linear sweep voltammograms recorded for Pt/C, Pt/Vulcan and Pt/CNFs are shown in Figure 16. The current density is reported as current per geometric electrode area of the RDE. The polarisation curves show an onset potential at ca 0.9 V. In the region from 0.95 to 0.60 V, the ORR curves of Pt/C and Pt/Vulcan XC-72R were under mixed kinetic and diffusion control. The mixed kinetic-diffusion controlled region of Pt/CNFs was shifted slightly to a lower potential, ranging from 0.85 to 0.50 V. The $E_{1/2}$ is the point half-way between the diffusion limited current and the zero current and it is usually used to indicate the ORR activity of the electrocatalyst. The $E_{1/2}$ of Pt/CNFs, Pt/C and Pt/Vulcan XC-72R was 0.75, 0.82 and

0.81, respectively at 900 rpm, indicating lower ORR activity of Pt/CNFs compared to that of Pt/C and Pt/Vulcan XC-72R.

Linear plots were obtained for Pt/CNFs, Pt/C and Pt/Vulcan XC-72R by using the Levich-Koutecky equation at 0.3 V (Figure 16d). The number of electrons involved in the reaction was ca 3.4, 3.6 and 3.7 for Pt/CNFs, Pt/Vulcan XC-72R and Pt/C, respectively, indicating that oxygen reduction occurs mostly via a 4 electron mechanism (see Chapter 1).

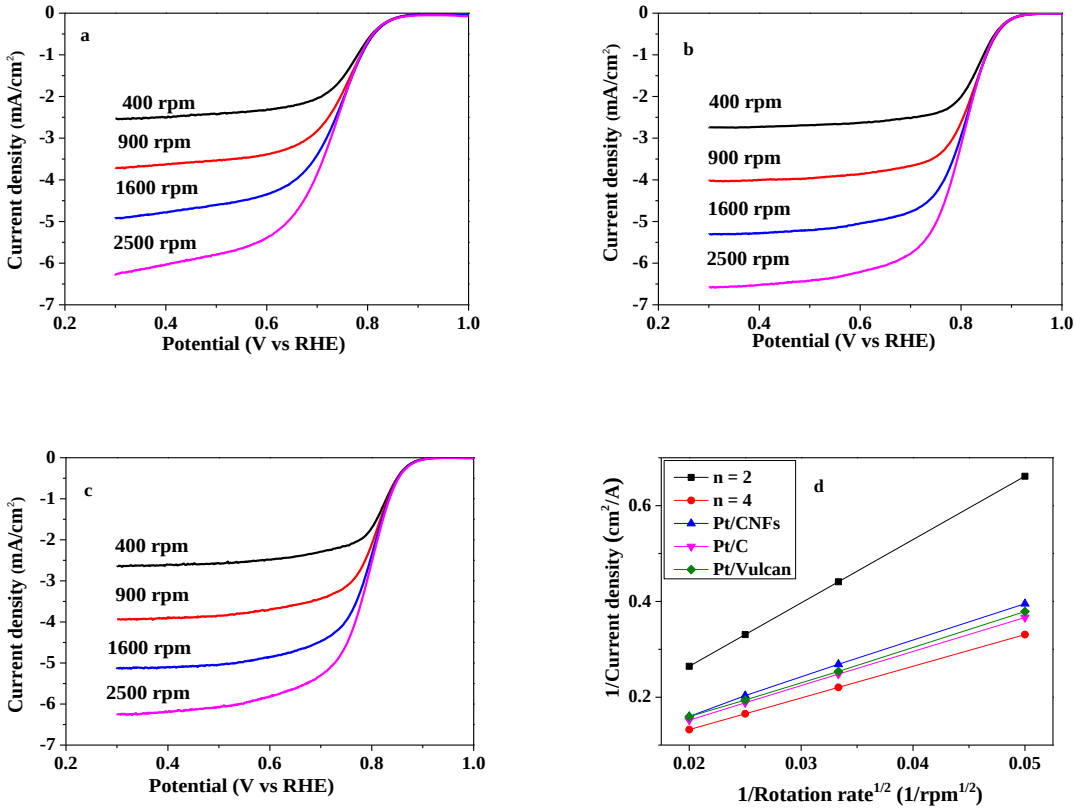

Figure 16: Oxygen reduction reaction polarization curves obtained on Pt/CNFs (a), Pt/C (b) and Pt/Vulcan XC-72R (c) and the inverse current densities as a function of the inverse of the square root of the rotation rate (d).

Figure 17 shows potential plotted as a function of kinetic current density in logarithmic scale, known as Tafel plot. Similar values of Tafel slope (Table 2) for Pt/C and Pt/Vulcan XC-72R indicate the same mechanism of the ORR reaction for both electrocatalysts. However, Pt/CNFs shows higher Tafel slope, what may be attributed to slightly different mechanism of oxygen reduction.

Furthermore, Pt/CNFs shows the lowest ORR mass activity at 0.8 V_{RHE} (Table 2). This result may be attributed to smaller specific surface area of the CNFs (36 m^2/g) compared to the commercial Vulcan XC-72R (250 m^2/g) as well as to difference in ECSA of these electrocatalysts.

Table 2: Comparison of ORR mass activities and Tafel slopes for ORR on different catalysts.

Electrocatalyst	Pt/C	Pt/Vulcan XC-72R	Pt/CNFs
ORR mass activity at 0.8 V, A/g_{Pt}	61.4	36.5	7.6
Tafel slope, mV/dec	-55	-52	-75

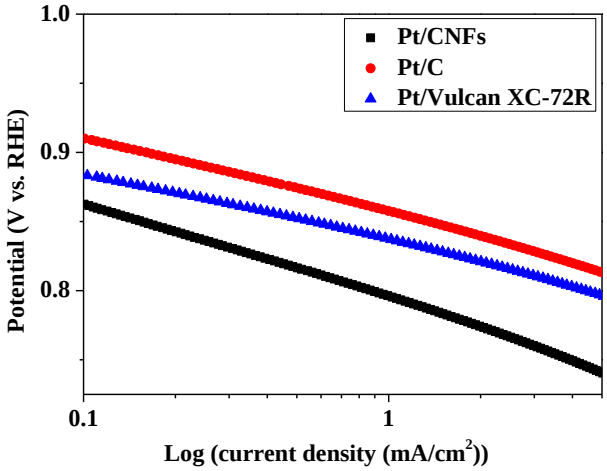

Figure 17: Tafel plots for ORR of different catalysts at 900 rpm in 0.1 M $HClO_4$.

2.2.4 Evaluation of the electrochemical stability

Cyclic voltammograms of Pt/C, Pt/Vulcan XC-72R and Pt/CNFs before and after the stability test are shown in Figure 18. For all samples, a decrease in the Pt ECSA was observed with increasing cycle number due to the Pt nanoparticles sintering (see TEM, page 94). The electrochemical surface area decreased dramatically from 24 to 2 m^2/g for Pt/CNFs (Table 3). The other two electrocatalysts showed a similar trend, but their ECSA decreased less rapidly from 33 to 20 m^2/g for Pt/C and from 47 to 32 m^2/g for Pt/Vulcan XC-72R. It can be concluded that the CNFs support is less stable compared to the conventional carbon materials. This result is in agreement with the results obtained from the potential hold test (see paragraph 1.4.2). Poor Pt dispersion can be also a reason for low Pt/CNFs durability. Furthermore, it can be noticed that there is an increase in the capacitance in the double layer region for Pt/CNFs after prolonged cycling, which may indicate the oxidation of the CNFs and the formation of surface functional groups such as -OH and -COOH [27].

Table 3: ECSA of Pt/CNFs, Pt/C and Pt/Vulcan XC-72R before and after the 1000 cycle stability test.

Number of cycles	Cycle 20	Cycle 100	Cycle 1000
Pt/CNFs	24	16	2
Pt/C	33	33	20
Pt/Vulcan XC-72R	47	40	32

Figure 18 also shows a decrease in the intensity and a shift of the oxygen reduction peak between 0.7 and 0.9 V for Pt/C and Pt/Vulcan. In the case of Pt/CNFs this peak has almost disappeared, which indicates a poor ORR activity after the stability test [22].

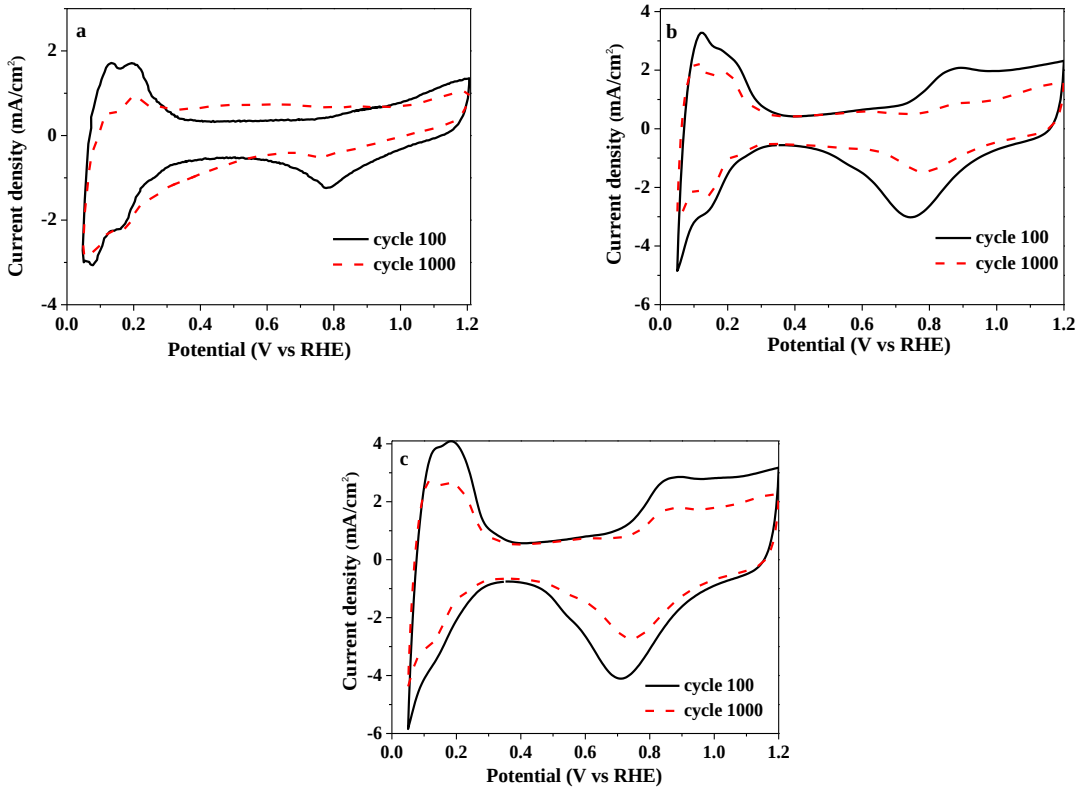

Figure 18: Cyclic voltammograms obtained after 100 and 1000 cycles for Pt/CNFs (a), Pt/C (b) and Pt/Vulcan XC-72R (c).

ORR activity evaluation after stability test

Figure 19 shows the ORR mass activities calculated from the polarisation curves at a rotation speed of 900 rpm before and after the stability test. The mass activities at 0.8 V were much higher for Pt/C and Pt/Vulcan XC-72R than for Pt/CNFs, as shown in Table 4. The smaller ORR activity of Pt/Vulcan XC-72R compared to the commercial Pt/C can be related to smaller nanoparticle size of the Pt supported on Vulcan XC-72R [28].

After the stability test, all the catalysts showed very poor mass activity, especially the Pt/CNFs catalyst (Table 4). This result indicates the lower stability of the CNFs compared to the commercial supports and is consistent with the rapid ECSA loss of Pt/CNFs.

Table 4: ORR mass activities before and after the stability test at 0.8 V_{RHE}.

Electrocatalyst	Pt/C	Pt/Vulcan XC-72R	Pt/CNFs
Before 1000 cycles	61.4	36.5	7.6
After 1000 cycles	3.9	5.5	0.8

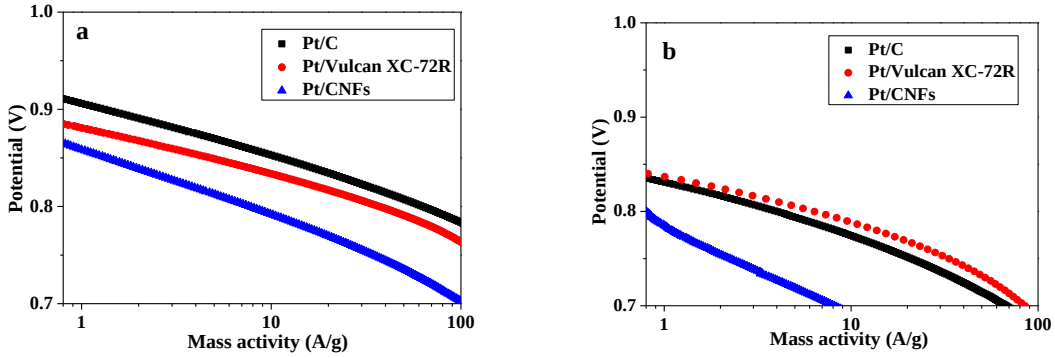

Figure 19 : Mass activities of ORR measurements before (a) and after (b) the stability test.

Transmission electron micrographs before and after the stability test

TEM images show that the particle size of all catalysts increased after the stability tests which results in the reduction of the ECSA and the ORR activity loss. The average particle size increased from 2.3 to 7.0 nm with a great dispersion in size up to 15 nm for Pt/CNFs, from 2.4 to 5.0 nm for Pt/Vulcan XC-72R and from 3.8 to 5.3 nm for Pt/C (Figure 20, Figure 21 and Figure 22, respectively). This result is in agreement with the huge loss of ECSA for Pt/CNFs (see Figure 18) and can be explained by the corrosion of the carbon-based support during the potential cycling experiment. Chang et al. [29] also observed the growth of Pt agglomeration up to 50 nm on the carbon fibre mat (CFM) surface after the stability test.

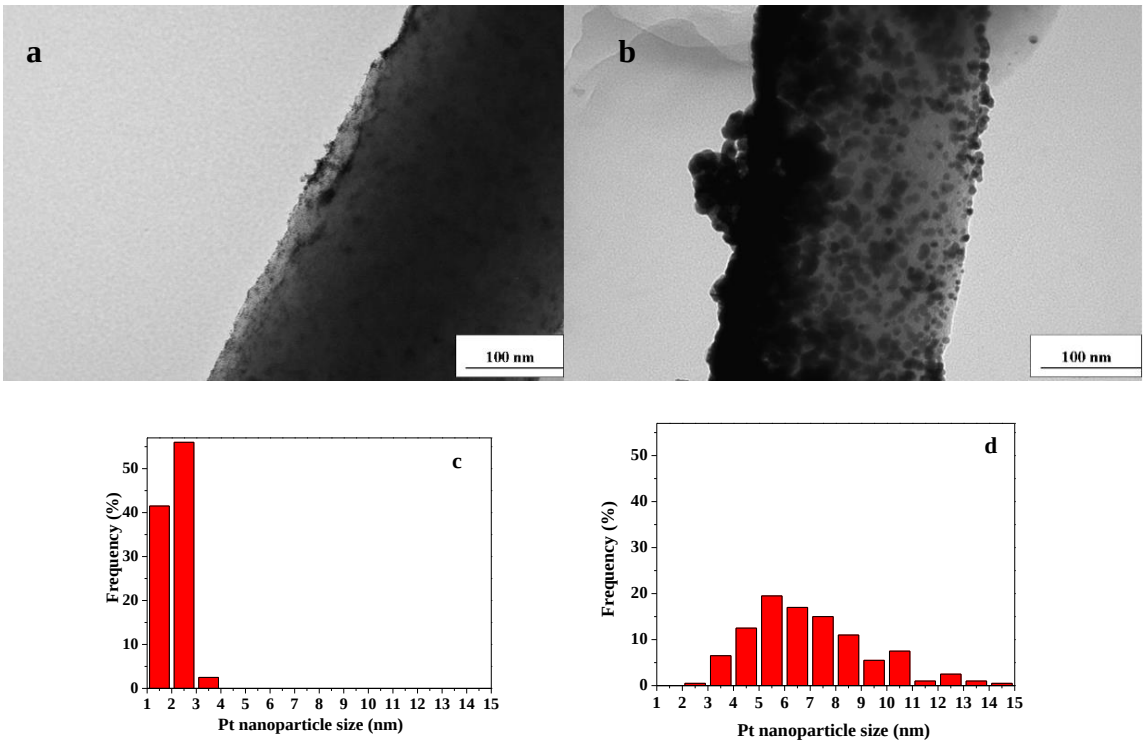

Figure 20: TEM micrographs of Pt/CNFs before (a) and after voltammetric cycling (b) and corresponding Pt nanoparticle size distribution histograms (c and d), respectively.

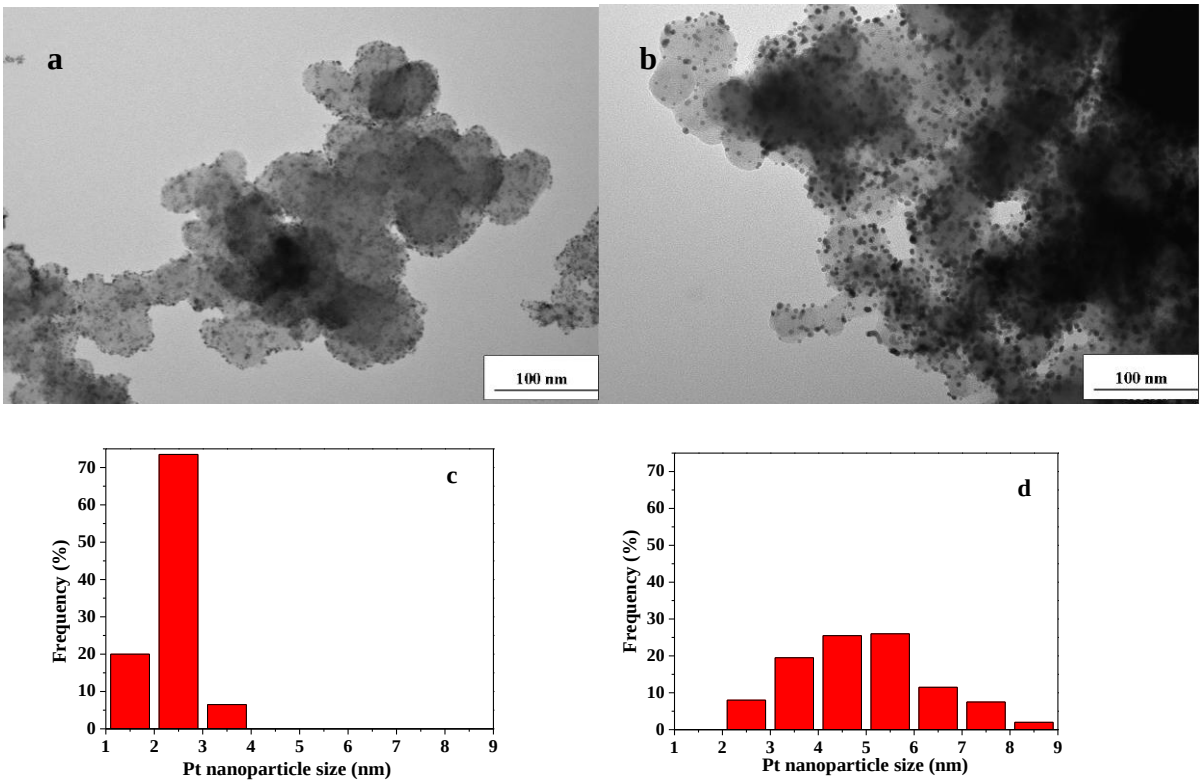

Figure 21: TEM micrographs of Pt/Vulcan XC-72R before (a) and after potential cycling (b) and corresponding Pt nanoparticle size distribution histograms (c and d), respectively.

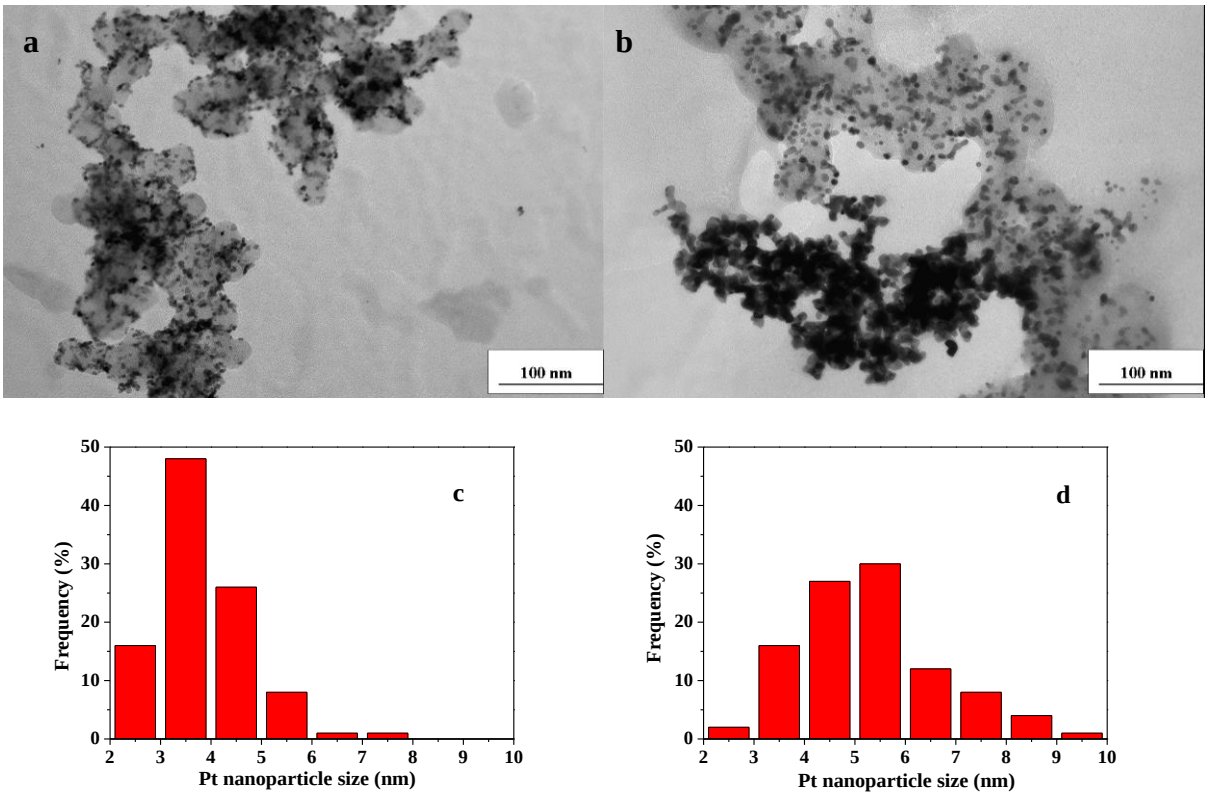

Figure 22: TEM micrographs of Pt/C before (a) and after potential cycling (b) and corresponding Pt nanoparticle size distribution histograms (c and d), respectively.

Conclusions and perspectives

CNFs were obtained by electrospinning and calcined at different temperatures in order to find a good compromise between surface area, electrical conductivity and electrochemical stability. CNF_{700} showed high surface area, but lower conductivity compared to CNF_{1000} and CNF_{1500}. Furthermore, CNF_{1500} was more stable than $CNFs_{1000}$ and commercial support (Vulcan XC-72R). However, it could not be further prepared in our laboratory for technical issues. Therefore, CNF_{1000} were selected for further deposition of Pt nanoparticles, which were prepared using microwave-assisted polyol method. The obtained Pt/CNFs electrocatalyst provided lower ECSA and ORR activity compared to that of Pt/Vulcan XC-72R and commercial Pt/C, probably due to poor surface area of CNFs support. Furthermore, Pt/CNFs electrocatalyst showed lower ECSA and ORR activity after accelerated stress test caused by the Pt nanoparticles agglomeration and poor corrosion resistance of the support.

In order to increase the stability of the Pt/CNFs, CNFs should be graphitised at temperatures higher than 1000 °C. Another approach to avoid carbon corrosion is to replace carbon-based materials with a more stable support such as doped TiO_x or SnO_2 (see Chapters 3 and 4).

References

[1] I. Savych, J. Bernard d'Arbigny, S. Subianto, S. Cavaliere, D. J. Jones, and J. Rozière, "On the Effect of Non-Carbon Nanostructured Supports on the Stability of Pt Nanoparticles during Voltage Cycling: a Study of TiO_2 Nanofibres," *Journal of Power Sources*, vol. 257, pp. 147–155, Feb. 2014.

[2] C.-K. Liu, K. Lai, W. Liu, M. Yao, and R.-J. Sun, "Preparation of carbon nanofibres through electrospinning and thermal treatment," *Polymer International*, vol. 58, no. 12, pp. 1341–1349, Dec. 2009.

[3] C. Kim, K. S. Yang, M. Kojima, K. Yoshida, Y. J. Kim, Y. a. Kim, and M. Endo, "Fabrication of Electrospinning-Derived Carbon Nanofiber Webs for the Anode Material of Lithium-Ion Secondary Batteries," *Advanced Functional Materials*, vol. 16, no. 18, pp. 2393–2397, Dec. 2006.

[4] C. Kim, K.-S. Yang, and W.-J. Lee, "The Use of Carbon Nanofiber Electrodes Prepared by Electrospinning for Electrochemical Supercapacitors," *Electrochemical and Solid-State Letters*, vol. 7, no. 11, p. A397, 2004.

[5] R. Padmavathi and D. Sangeetha, "Synthesis and characterization of electrospun carbon nanofiber supported Pt catalyst for fuel cells," *Electrochimica Acta*, vol. 112, pp. 1–13, Dec. 2013.

[6] M. Li, G. Han, and B. Yang, "Fabrication of the catalytic electrodes for methanol oxidation on electrospinning-derived carbon fibrous mats," *Electrochemistry Communications*, vol. 10, no. 6, pp. 880–883, Jun. 2008.

[7] Y. Wang, S. Serrano, and J. J. Santiago-avile, "Raman characterization of carbon nanofibers prepared using electrospinning," *Synthetic Metals*, vol. 138, pp. 423–427, 2003.

[8] T. Jawhari, A. Roid, and J. Casado, "Raman Spectroscopic Characterization of some Commercially Available Carbon Black Materials," *Carbon*, vol. 33, no. 11, pp. 1561–1565, 1995.

[9] C. Kim, S.-H. Park, J.-I. Cho, D.-Y. Lee, T.-J. Park, W.-J. Lee, and K.-S. Yang, "Raman spectroscopic evaluation of polyacrylonitrile-based carbon nanofibers prepared by electrospinning," *Journal of Raman Spectroscopy*, vol. 35, no. 11, pp. 928–933, Nov. 2004.

[10] Y. Shao, G. Yin, and Y. Gao, "Understanding and approaches for the durability issues of Pt-based catalysts for PEM fuel cell," *Journal of Power Sources*, vol. 171, no. 2, pp. 558–566, Sep. 2007.

[11] C. Wang, H. Gao, H. Li, Y. Zhang, B. Huang, J. Zhao, Y. Zhu, W. Z. Yuan, and Y. Zhang, "Graphene nanoribbons hybridized carbon nanofibers: remarkably enhanced graphitization and conductivity, and excellent performance as support material for fuel cell catalysts.," *Nanoscale*, vol. 6, no. 3, pp. 1377–83, Jan. 2014.

[12] G. Wang, C. Pan, L. Wang, Q. Dong, C. Yu, Z. Zhao, and J. Qiu, "Activated carbon nanofiber webs made by electrospinning for capacitive deionization," *Electrochimica Acta*, vol. 69, pp. 65–70, May 2012.

[13] L. J. van der Pauw, "A method of measuring specific resistivity and Hall effect of discs of arbitrary shape," *Philips Research Reports*, vol. 13, no. 1, pp. 1–9, 1958.

[14] S. Siracusano, a. Stassi, E. Modica, V. Baglio, and a. S. Aricò, "Preparation and characterisation of Ti oxide based catalyst supports for low temperature fuel cells," *International Journal of Hydrogen Energy*, vol. 38, no. 26, pp. 11600–11608, Aug. 2013.

[15] M. Wesselmark and C. Lagergren, "Degradation Studies of PEMFC Cathodes Based on Different Types of Carbon," *ECS Transactions*, vol. 25, no. 1, pp. 1241–1250, 2009.

[16] H.-S. Oh, J.-G. Oh, Y.-G. Hong, and H. Kim, "Investigation of carbon-supported Pt nanocatalyst preparation by the polyol process for fuel cell applications," *Electrochimica Acta*, vol. 52, no. 25, pp. 7278–7285, Sep. 2007.

[17] H.-S. Oh, J.-G. Oh, and H. Kim, "Modification of polyol process for synthesis of highly platinum loaded platinum–carbon catalysts for fuel cells," *Journal of Power Sources*, vol. 183, no. 2, pp. 600–603, Sep. 2008.

[18] H. Chhina, "Oxidation-resistatnt catalyst supports for Proton exchnge membrane fuel cells," 2009.

[19] Z. Liu, L. M. Gan, L. Hong, W. Chen, and J. Y. Lee, "Carbon-supported Pt nanoparticles as catalysts for proton exchange membrane fuel cells," *Journal of Power Sources*, vol. 139, no. 1–2, pp. 73–78, Jan. 2005.

[20] C. Roth, M. Goetz, and H. Fuess, "Synthesis and characterization of carbon-supported Pt-Ru-WOx catalysts by spectroscopic and diffraction methods," *Journal of Applied Electrochemistry*, vol. 31, pp. 793–798, 2001.

[21] A. K. Shukla, M. K. Ravikumar, A. Roy, S. R. Barman, and D. D. Sarma, "Electro-oxidation of Methanol in Sulfuric Acid Electrolyte on Platinized-Carbon Electrodes with Several Functional-Group Characteristics," *Journal of Electrochemical Society*, vol. 141, no. 6, pp. 463–467, 1994.

[22] A. Stassi, E. Modica, V. Antonucci, and a. S. Aricò, "A Half Cell Study of Performance and Degradation of Oxygen Reduction Catalysts for Application in Low Temperature Fuel Cells," *Fuel Cells*, vol. 9, no. 3, pp. 201–208, Jun. 2009.

[23] J. M. Doña Rodríguez, J. A. Herrera Melián, and J. Pérez Peña, "Determination of the Real Surface Area of Pt Electrodes by Hydrogen Adsorption Using Cyclic Voltammetry," *Journal of Chemical Education*, vol. 77, no. 9, p. 1195, Sep. 2000.

[24] B. E. Conway and H. Angerstein-Kozlowska, "The electrochemical study of multiple-state adsorption in monolayers," *Accounts of Chemical Research*, vol. 14, no. 2, pp. 49–56, Feb. 1981.

[25] S. L. Gojkovic, S. K. Zecevic, and R. F. Savinell, "O_2 Reduction on an Ink-Type Rotating Disk Electrode Using Pt Supported on High-Area Carbons," *Journal of Electrochemical Society*, vol. 145, no. 11, pp. 3713–3720, 1998.

[26] D.-S. Kim, T.-J. Kim, J.-H. Kim, E. F. A. Zeid, and Y.-T. Kim, "Fine Structure Effect of PdCo electrocatalyst for Oxygen Reduction Reaction Activity: Based on X-ray Absorption Spectroscopy Studies with Synchrotron Beam," *Journal of Electrochemical Science and Technology*, vol. 1, no. 1, pp. 31–38, Sep. 2010.

[27] M. Dou, M. Hou, D. Liang, W. Lu, Z. Shao, and B. Yi, "SnO_2 nanocluster supported Pt catalyst with high stability for proton exchange membrane fuel cells," *Electrochimica Acta*, vol. 92, pp. 468–473, Mar. 2013.

[28] A. Sarapuu, A. Kasikov, T. Laaksonen, K. Kontturi, and K. Tammeveski, "Electrochemical reduction of oxygen on thin-film Pt electrodes in acid solutions," *Electrochimica Acta*, vol. 53, no. 20, pp. 5873–5880, Aug. 2008.

[29] Y. Chang, G. Han, M. Li, and F. Gao, "Graphene-modified carbon fiber mats used to improve the activity and stability of Pt catalyst for methanol electrochemical oxidation," *Carbon*, vol. 49, no. 15, pp. 5158–5165, Dec. 2011.

CHAPTER 3:

Titanium dioxide as electrocatalyst support

1 Synthesis and characterisation of electrospun titanium dioxide

Titanium dioxide is a promising material as a PEMFC support due to its high electrochemical stability and strong metal support interactions (see Chapter 1) [1]. However, its low electrical conductivity is one of the main limitations for its fuel cell application. Thus, in order to deal with this problem, two strategies have been used, namely doping with aliovalent metal ions (to modify the band gap) and treatment at high temperature in the presence of H_2 (to obtain a conductive suboxide). Magneli phase (obtained by reduction at temperature higher than 1000 °C) is highly conductive, but usually it has low surface area. Therefore, relatively low reduction temperature of 800 °C was chosen in order to prevent TiO_2 particles from sintering and thus to maintain high surface area of the corresponding nanofibres. Niobium doping was used to enhance the electronic conductivity of TiO_2. Moreover, niobium inhibits TiO_2 grain growth, which is expected to result in an enhanced surface area of Nb doped TiO_2 nanofibres.

Various methods have been used to prepare 1 D TiO_2 nanostructures including solution-based (hydrothermal, sol-gel, microwave, etc.), vapour-based (CVD, ALD, etc.), template growth and top-down approaches [2]. However, most of these methods are relatively complex, expensive and require a specific protocol. In contrast, electrospinning is a simple, cost-effective and versatile technique, which allows fabrication of nanofibres and tubes with desired diameters and high aspect ratio.

In this study, TiO_2 nanofibres with 5, 10 and 20 at. % Nb, calcined at 500 °C, 800 °C, and reduced at 800 °C were characterised using XRD, XPS, SEM, TEM, Raman spectroscopy, nitrogen adsorption/desorption analysis and electronic conductivity measurements.

10 at. % Nb doped TiO_2 reduced at high temperature was chosen for further Pt deposition due to its high conductivity. Catalyst nanoparticles were synthesised via microwave-assisted polyol method. ORR activity and stability of the obtained electrocatalyst were evaluated using a rotating disc electrode and compared with that of the commercial Pt/C.

The results described in this chapter have been partially published in [3]:
I. Savych, J. Bernard d'Arbigny, S. Subianto, S. Cavaliere, D. J. Jones, and J. Rozière, On the Effect of Non-Carbon Nanostructured Supports on the Stability of Pt Nanoparticles during Voltage Cycling: a Study of TiO_2 Nanofibres, *Journal of Power Sources* (2014) 257, 147-155.

1.1 Synthesis and morphological characterisation of titania nanofibres

Titania nanofibres were obtained by single-needle electrospinning, whereas hollow fibres were obtained by coaxial electrospinning. It was expected that TiO_2 nanotubes would have higher surface area compared to titania nanofibres.

1.1.1 Synthesis of titania nanofibres via single-needle electrospinning

For the preparation of titanium dioxide fibres, a procedure similar to that described in [4] was used. Carrier polymer was added to increase viscosity of the solution and make it spinnable. PVP is usually used to prepare titania nanofibres due to its good solubility in alcohols and compatibility with titania and niobium precursors [5]. The fibre diameter can be controlled by changing polymer and precursor concentration [6]. Acetic acid was added to stabilise the solution by preventing total hydrolysis of alkoxide to titanium oxide:

$$Ti\{OCH(CH_3)_2\}_4 + 2\ H_2O \rightarrow TiO_2 + 4\ (CH_3)_2CHOH$$

The as-prepared fibres were calcined in air at 500 °C or 800 °C at 5 °C/min for 6 h in order to remove the carrier polymer and to allow nucleation and growth of TiO_2 particles. The fibres calcined at 500 and 800 °C were labelled as low temperature (LT) and high temperature (HT), respectively. Part of the fibres calcined at 500 °C were further heat treated at 800 °C under 5 % H_2/Ar atmosphere for 2 h at 5 °C/min. This sample was labelled as high temperature reduction (HTR) nanofibres. The LT and HT nanofibres were white, whereas the HTR ones were blue in colour. Blue colour of HTR suggests the presence of suboxide. Figure 1 presents the synthesis steps for LT, HT and HTR samples.

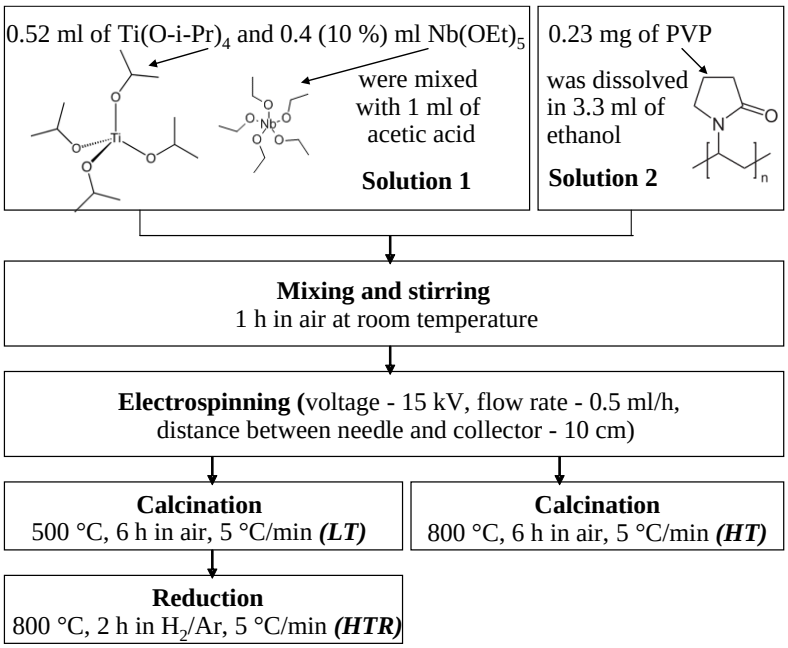

Figure 1: Schema of the synthesis protocol for titania nanofibres.

LT fibres morphology

TEM micrographs of non-doped and 10 at. % doped titania LT fibres are shown in Figure 2. The average fibre diameter was slightly higher for the undoped titania (62 nm) than for the doped sample (47 nm), probably due to smaller particle size of the latter. Nb doping inhibits the grain growth of TiO_2, which was confirmed by grain size calculations (see paragraph 1.2.1).

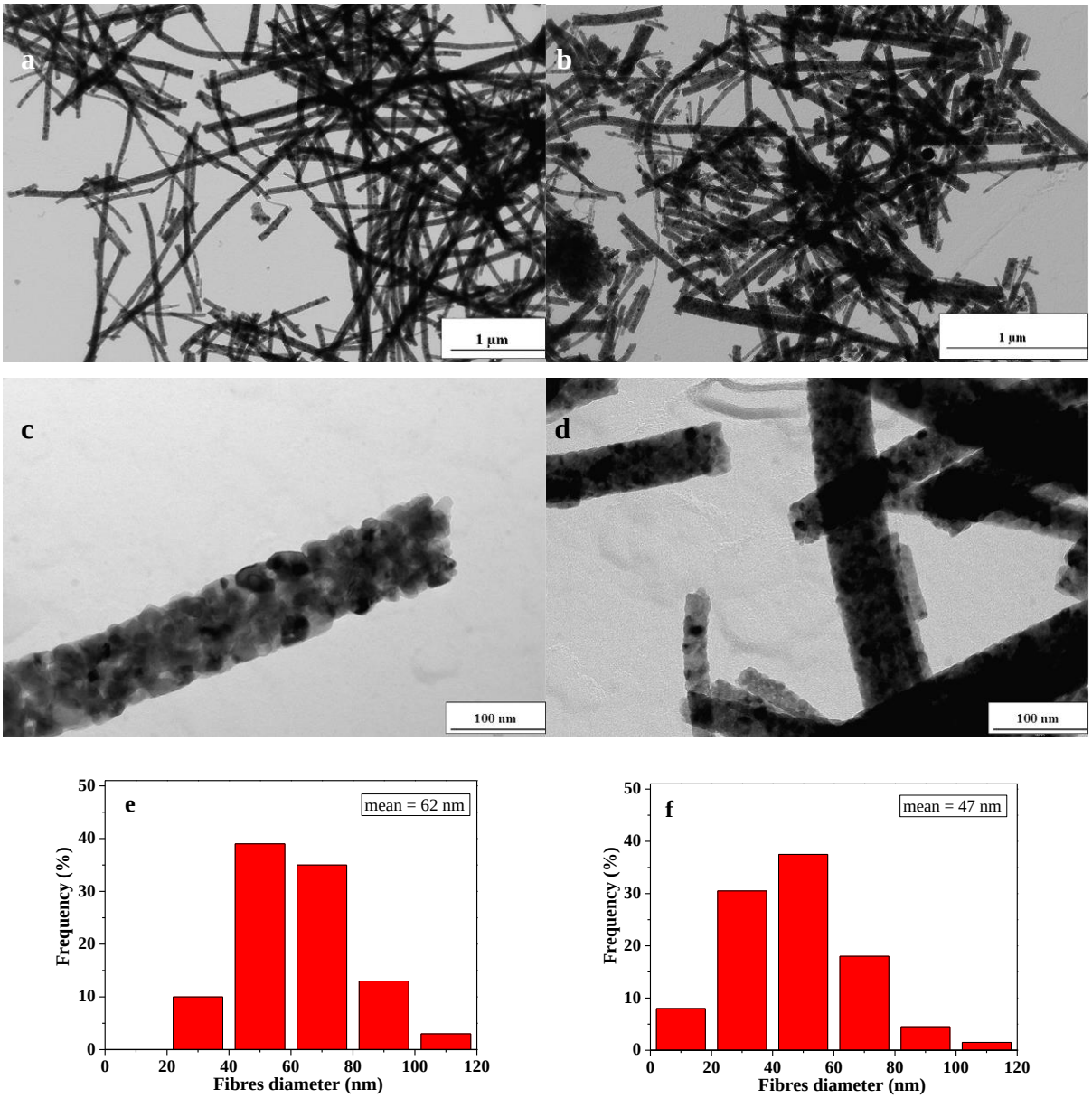

Figure 2: TEM images of non-doped (a, c) and 10 at. % Nb doped (b, d) LT fibres and corresponding size distribution histograms obtained from measurements of 100 nanofibres (e and f), respectively.

Comparison of LT and HTR fibres morphologies

HT and HTR fibres thermal-treated at 800 °C provide similar morphology. Therefore, only LT and HTR samples morphology were compared using SEM and TEM microscopy. The obtained results are shown in Figure 3. The average fibre diameters of the 10 at. % doped LT and HTR fibres were 47 and 57 nm, respectively. Fibre diameter increases after the reductive treatment at high temperature, probably due to particle sintering at 800 °C. The LT sample has a more porous structure with smaller grains of around 10 nm diameter, whereas HTR fibres consist of bigger grains of ca 60 nm diameters.

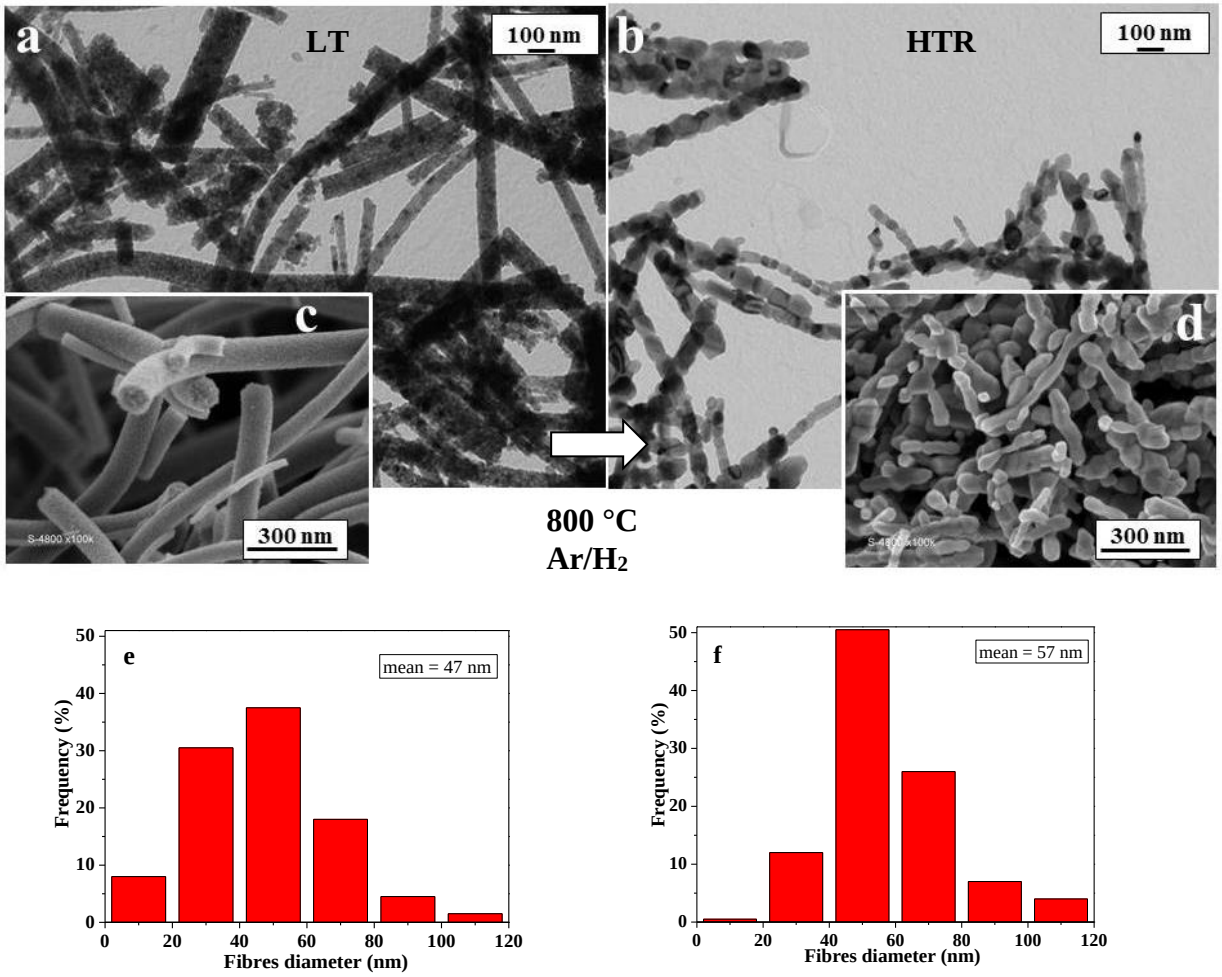

Figure 3: TEM (a, b) and SEM (c, d) images and corresponding size distribution histograms obtained from measurements of 100 nanofibres (e, f) of 10 at. % Nb doped TiO_2 LT and HTR fibres, respectively.

1.1.2 Specific surface area of titania nanofibres

In order to estimate the specific surface area, nitrogen adsorption/desorption isotherms of LT, HT and HTR nanofibres were carried out (Figure 4). The isotherm of the LT sample shows a hysteresis at medium relative pressure, which is typical of mesoporous materials (type IV isotherm). The isotherms of the samples prepared at high temperature, HT and HTR,

showed decreased nitrogen adsorption. Thermal treatment at high temperature leads to the disappearance of pores and surface smoothing due to the grain sintering. Therefore, surface area decreases after reduction at 800 °C from 87 to 22 m^2/g for 20 at. % Nb doped TiO_2, as shown in Table 1. Senevirathne et al. [9] reported a similar decrease from 51 to 6 m^2/g after reduction of electrospun titania at 1050 °C. Also, Huang et al. [10] and Chhina et al. [11] observed the same effect on titanium oxide morphology after high-temperature reduction. However, the BET surface area obtained here for the Nb doped HTR samples (16 - 22 m^2/g) is slightly higher than those reported by Wang et al. [12] (4.5 m^2/g), Huang et al. (10 m^2/g) and Chhina et al. (13.5 m^2/g) for Nb doped titania reduced at 700 °C. This difference can be explained by different preparation method (electrospinning) used in our work.

Table 1: BET surface area (m^2/g) of titania nanofibres with different Nb contents and treated at different temperatures (LT – 500 °C in air, HT – 800 °C in air and HTR – 500 °C in air and then 800 °C in H_2/Ar).

at. % Nb	0	5	10	20
LT	26	49	65	87
HT	15	15	22	19
HTR	10	22	16	22

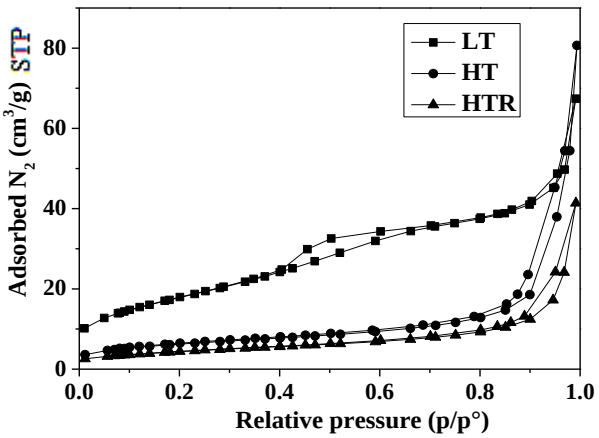

Figure 4: Nitrogen adsorption-desorption isotherms of 10 at. % Nb nanofibres.

The BET surface area of the LT samples increased from 49 m^2/g for 5 at. % Nb-TiO_2 to 87 m^2/g for 20 at. % Nb-TiO_2 (Table 1) with increasing Nb concentration. Similar result was obtained by Michalow et al. (66.7 m^2/g for 5 at. % Nb-TiO_2 and 90.0 m^2/g for 15 at. % Nb-TiO_2) [13]. The observed result may be attributed to the inhibition of the grain growth in the presence of Nb, as reported previously [14]. This is in agreement with the particle size decrease with increasing Nb concentration (see discussion in paragraph 1.2.1 and Table 2).

1.1.3 Synthesis of hollow titania fibres via coaxial electrospinning

Li and Xia demonstrated that coaxial electrospinning could be used to obtain hollow TiO_2 fibres [7]. In our work, similar approach (Figure 5) was used to obtain titania tubes. Our setup was composed of two coaxial needles with diameters of 0.8 and 1.83 mm. The inner needle was connected to a syringe with mineral oil, whereas the outer one was connected to a syringe with titania precursor solution. The as-spun fibres were immersed in n-hexane overnight in order to extract the oil phase and then calcined at 500 °C for 6 h (LT) and afterward reduced at 800 °C for 2 h in 5 % H_2/Ar (HTR). Figure 5 presents the synthesis steps for LT and HTR hollow fibres. More details are provided in the experimental part (Annex A).

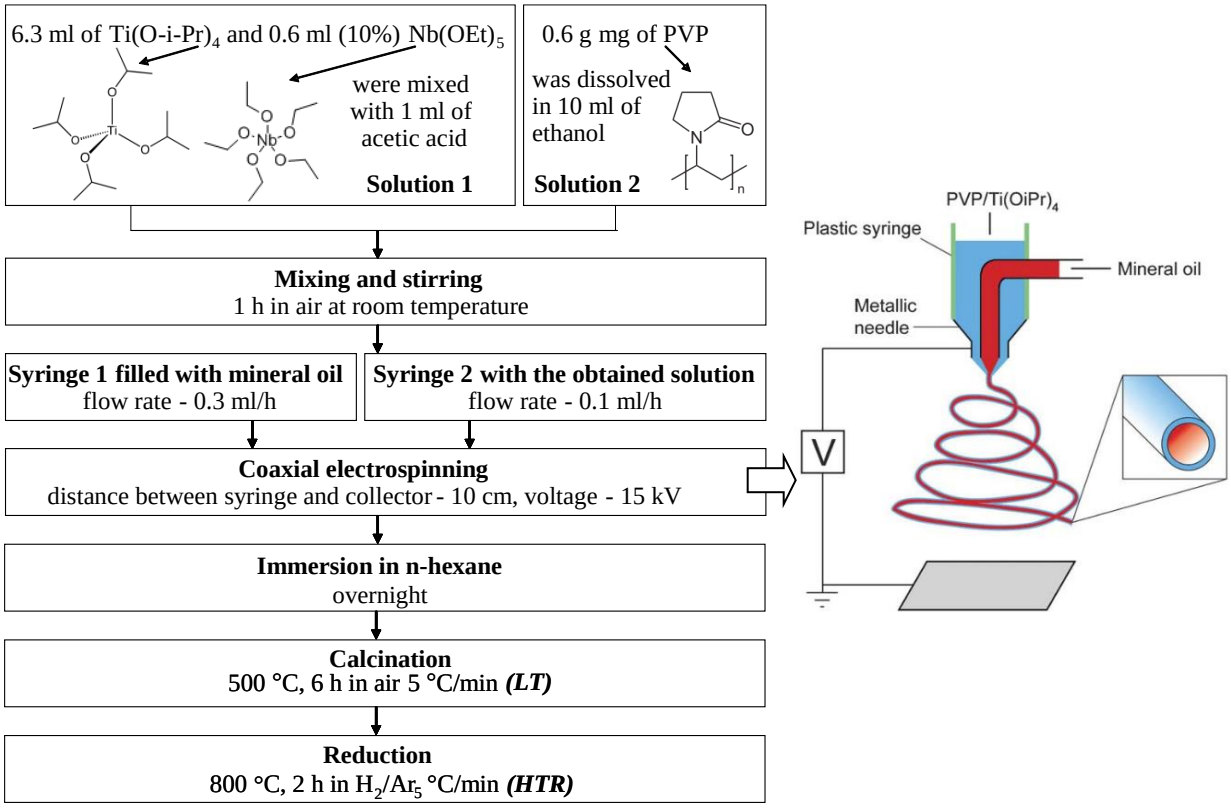

Figure 5: Schema of the synthesis protocol for titania hollow nanofibres (left) and schematic illustration of the setup of coaxial electrospinning (right) [8].

SEM images of Nb doped LT and HTR hollow fibres are shown in Figure 6. The average diameter of the LT and HTR were 173 and 153 nm, respectively. It can be observed that LT hollow fibres consist of smaller grains than HTR fibres. After reduction at 800 °C, the integrity of hollow fibres deteriorated due to the grain growth of Nb doped TiO_2. The wall thickness was between 50 and 100 nm for both LT and HTR samples.

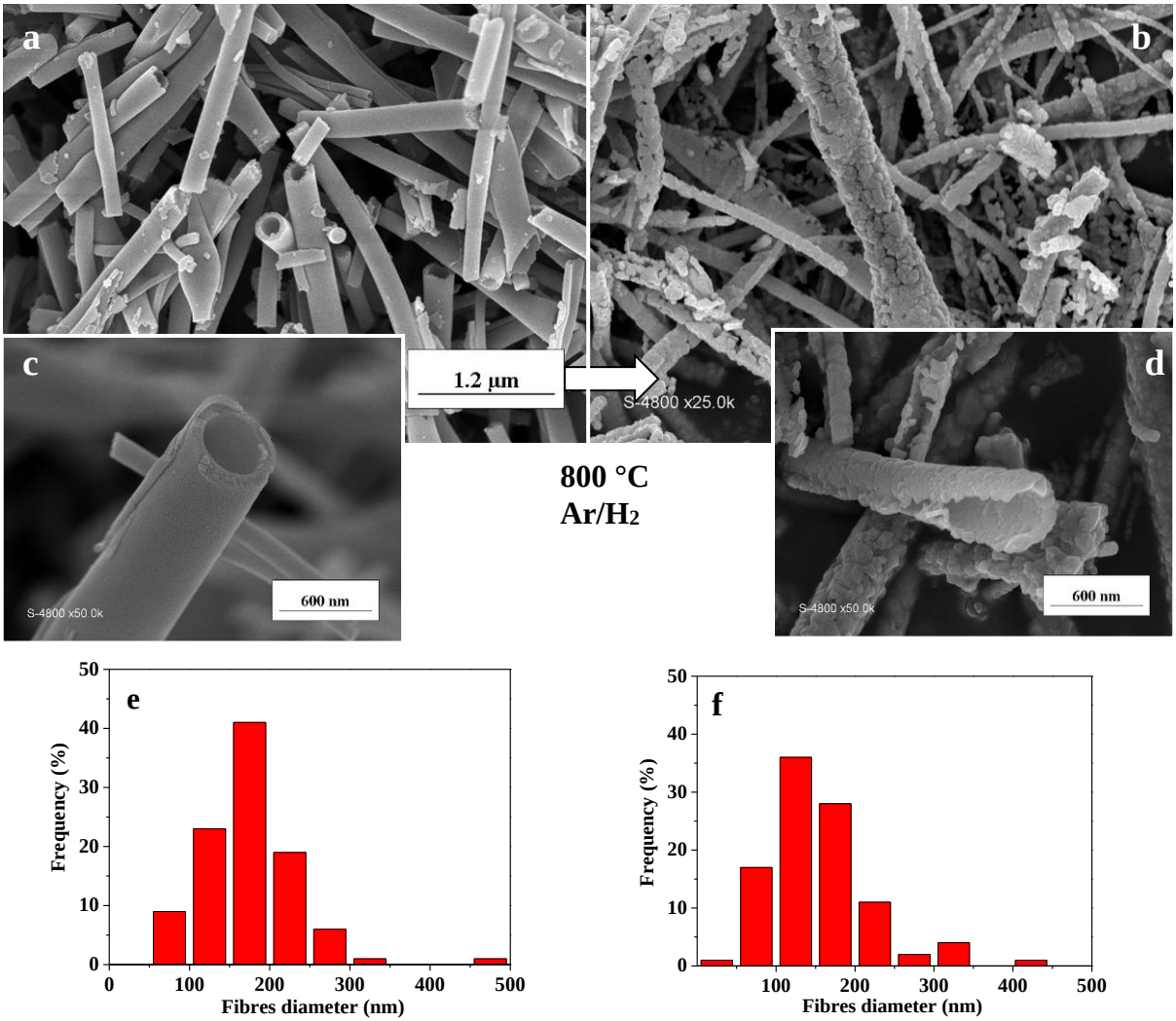

Figure 6: SEM images of 10 at. % Nb doped TiO_2 hollow fibres calcined at 500 °C in air for 1 h (a, c) and reduced at 800 °C in Ar/H_2 for 2 h (b, d) and corresponding size distribution histograms obtained from measurements of 100 nanofibres (e, f).

1.1.4 Specific surface area of hollow titania fibres

The nitrogen adsorption/desorption isotherms of Nb doped LT and HTR hollow fibres are shown in Figure 7. Similarly as for solid nanofibres, the surface area decreases significantly after reduction from 48 m^2/g for LT to 8 m^2/g for HTR hollow fibres. Shao et al. reported similar surface area of 44.5 m^2/g for undoped TiO_2 hollow fibres prepared by coaxial electrospinning and then calcined at 500 °C for 1 h [15].

The surface area of the nanofibres (16 m^2/g) is twice that of hollow fibres (8 m^2/g) with the same Nb amount of 10 at. %, which can be attributed to the larger wall thickness of titania tubes compared to nanofibres diameter. Therefore, titania nanofibres were chosen for further characterisation.

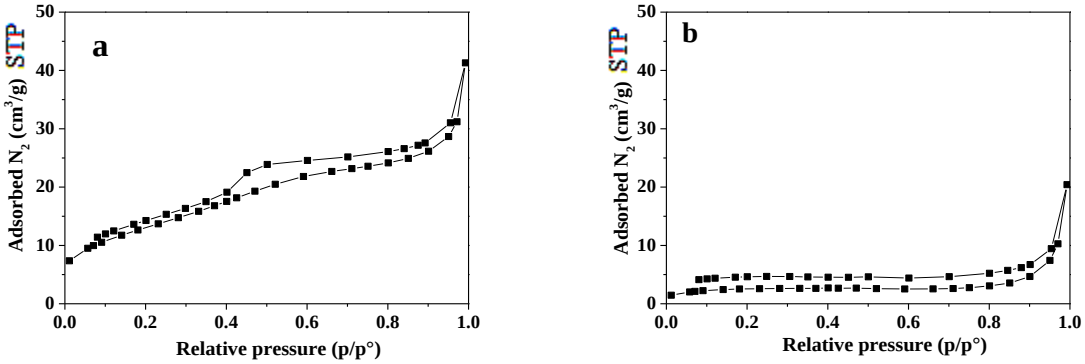

Figure 7: Nitrogen adsorption-desorption isotherms of 10 at. % Nb doped LT (a) and HTR (b) hollow fibres.

1.2 Structural characterisation of titania nanofibres

1.2.1 XRD analysis

Usually, fine titania powders of high purity show phase transformation from kinetically stabilised anatase to thermodynamically stable rutile in the temperature range between 600 and 700 °C [16]. The presence of a dopant can affect this phase transition. In order to understand the effect of Nb on the phase transformation, undoped and Nb doped electrospun TiO_2/PVP fibres were heated from 25 to 900 °C with a heating rate of 1 °C/min. XRD patterns of undoped and Nb doped titania calcined at 550 °C, 640 °C, 760 °C and 900 °C are shown in Figure 8. Already at 550 °C, a weak diffraction line at 27.5° 2θ can be observed in XRD pattern of titania, which indicates the presence of the rutile phase. The diffraction lines corresponding to the rutile phase grow much faster in the case of the undoped sample than for the Nb doped one. Therefore, it can be concluded that the Nb doping inhibits the anatase-to-rutile phase transition. Such an effect of Nb was also observed by different groups [17],[18],[19],[14]. In contrast to the above conclusion, Wang et al. observed that Nb doping facilitates the anatase-to-rutile phase transition of sol-gel TiO_2 thin films [20].

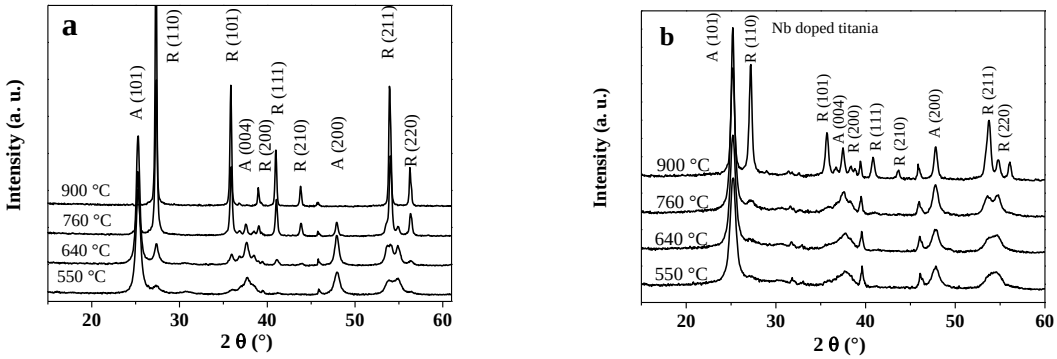

Figure 8: XRD diffractogramms of non-doped (a) and 10 at. % Nb doped (b) titania during heat treatment with a rate 1 °C/min from 550 °C to 900 °C.

The TiO_2/PVP fibres were converted into anatase (JCPDS: 01-084-1285) on heating at a temperature of 500 °C for 6 h, and into the rutile phase after calcination or reduction at 800 °C (Figure 9). The LT sample is mainly in anatase form, with a very little amount of the rutile phase. A weak diffraction line at 25.7 ° 2θ corresponds to the most intense diffraction peak of the rutile structure (110). The broadening of the diffraction peaks of the anatase phase implies the formation of very fine crystalline size of LT sample.

After heat treatment at 800 °C, the HT and HTR samples are mainly in rutile form (JCPDS: 01-078-1510). A weak diffraction line corresponding to the anatase phase can be observed at 25.3 °, which is much more intense in the case of 20 at. % Nb-TiO_2 compared to the other samples due to the inhibition of the anatase-to-rutile phase transition in the presence of Nb (Figure 8).

NbO_2 or Nb_2O_5 phases were not found in any of the samples, indicating that Nb^{5+} was incorporated into the lattice structure of titania. Only titanium niobium oxide $2TiO_2$ $5Nb_2O_5$ (JCPDS: 00-040-0039) was present in the HT sample with 20 at. % Nb loading (Figure 9d). This result may be attributed to the lower solubility limit of Nb in titania for the rutile phase (6 at. % Nb) than for the anatase phase (> 10 at. % Nb) [14].

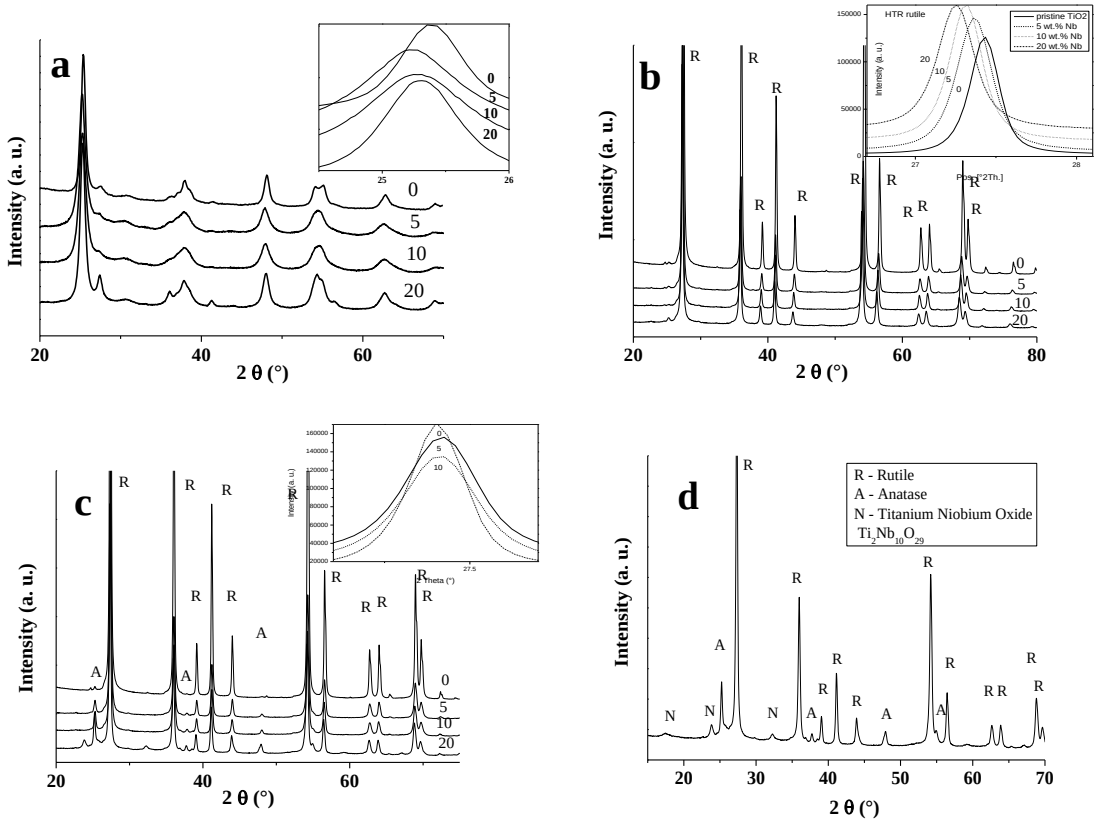

Figure 9: XRD diffractogramms of undoped and 5, 10 and 20 at. % Nb doped LT (a), HT (b), HTR (c) and 20 at. % Nb doped HT sample (d).

The shift of the 101 peak for doped anatase and 110 peak for doped rutile (Figure 9) to lower diffraction angles indicates an enlargement of the unit cell due to the larger ionic radius of Nb^{5+} (0.62 Å) compared to that of Ti^{4+} (0.56 Å) [21]. This result infers the effective incorporation of Nb^{5+} into the titania lattice structure [22],[21].

No suboxide phase was detected in the blue HTR samples, probably due to the small amount of suboxide on the fibres surface, below the detection limit of XRD.

Table 2 shows the coherence length of LT samples estimated from the XRD patterns (Figure 9a) using the Scherrer equation based on the full-width-half-maximum of the TiO_2 diffraction peak given by the (101) plane. This value is similar to the average particle size of 12 nm for electrospun TiO_2 fibres obtained by Kumar et al. [23].

The coherence length from XRD decreases with an increase in the Nb concentration from 15 nm for the non-doped sample to 8 nm for the 10 at. % Nb doping (Table 2). This result is consistent with an increase in BET surface area with increasing Nb concentration (as discussed before). Archana et al. also reported that electrospun Nb doped TiO_2 fibres were constituted by grains of lower diameter compared to pure titania indicating that the doping reduced the TiO_2 grain growth [24].

Table 2 shows that the growth inhibition is effective until Nb concentration is ca 10 at. %. Above this concentration, the crystallites have similar size. Ruiz et al. [14] also observed similar trend. When the Nb concentration exceeded the value of 6 at. % the crystallites of Nb doped TiO_2 had approximately the same size at a given calcination temperature.

Table 2: Crystallite size calculated from XRD patterns of Nb doped anatase nanofibres.

% at. Nb	**0**	**5**	**10**	**20**
Crystallite size (nm)	15	12	8	9

1.2.2 Raman spectroscopy analysis

There are six modes for the anatase phase that can be seen in the Raman spectrum which are A_{1g}, two B_{1g} and three E_g; and four Raman-active modes for the rutile phase, namely the E_g, B_{1g}, A_{1g} and B_{2g}. Figure 10a shows the Raman spectrum of 10 at. % Nb doped titania calcined at 500 °C. The signals at 144, 197, 393, 517 and 639 1/cm may be attributed to anatase modes E_g, E_g, B_{1g}, A_{1g} superimposed with mode B_{1g} and E_g respectively [25]. No peaks for rutile were detected, due to the small amount of rutile phase in the sample and lower detection limit of the Raman analysis compared to XRD. Figure 10b shows the Raman spectrum of 10 at. % Nb doped titania calcined at 500 °C and then reduced at 800 °C. The peaks at 142, 414 and 602 1/cm can be identified as B_{1g}, E_g and A_{1g} respectively. These

results are consistent with XRD results showing that the LT sample is in anatase phase, while the HTR is in rutile phase.

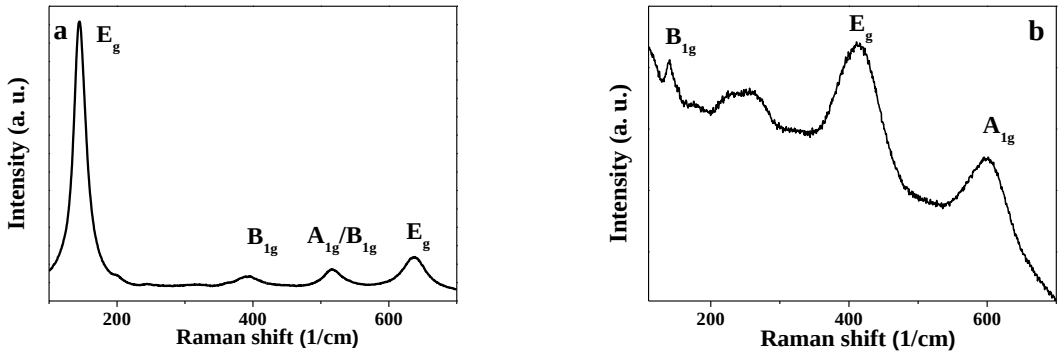

Figure 10: Raman spectra of LT (a) and HTR (b) TiO_2 samples.

1.2.3 Surface analysis by X-ray photoelectron spectroscopy

XPS analysis was performed in order to determine the oxidation state of niobium and titanium in the LT and HTR samples. The high resolution XPS spectra of titanium and niobium for 10 at. % Nb doped LT and HTR samples are shown in Figure 11. The Nb 3d spectrum recorded for the LT sample shows a doublet at 207.2 and 209.9 eV, which can be attributed to the Nb^{5+} oxidation state (Figure 11c). The extra charge of Nb^{5+} can be compensated either by introduction of one Ti^{4+} vacancy per four Nb^{5+} incorporations or by reduction of one Ti^{4+} to Ti^{3+} per one Nb^{5+} incorporation [14],[24]. However, no peaks attributed to Ti^{3+} were observed in the spectrum of the LT sample (Figure 11a). Therefore, it can be concluded that the charge compensation of Nb^{5+} was achieved not by reduction of Ti^{4+} to Ti^{3+}, but by creation of one Ti vacancy per four Nb^{5+} introduced.

Reduction of Ti^{4+} to Ti^{3+} would, however, predominate for reductive conditions and high Nb^{5+} concentrations [14].

The Ti 2p and Nb 3d spectra recorded for the HTR fibres show broader peaks than those recorded on the LT sample. The peak position of the Ti $2p_{3/2}$A at 459.2 eV corresponds to the oxidation state of Ti^{4+}, which was expected for TiO_2 and agrees with the literature for LT Nb-doped titania fibres [4]. In contrast, for the HTR sample, an additional signal is observed at 457.8 eV (Ti $2p_{3/2}$ B) after curve fitting, which is attributed to titanium in the oxidation state of +3 [26]. The relative intensity indicates that ca. 60 % titanium on the surface of the HTR sample is in oxidation state +3, and its presence may explain the improved electrical conductivity and the blue colouration of the HTR sample.

After curve fitting of the niobium spectrum of HTR sample (Figure 11d), two more signals were identified at 206.2 and 208.9 eV, which can be attributed to Nb^{4+} [14]. The amount of Nb^{4+} was about 57 %, indicating that a part of the Nb^{5+} on the surface of the HTR sample has been reduced to Nb^{4+}.

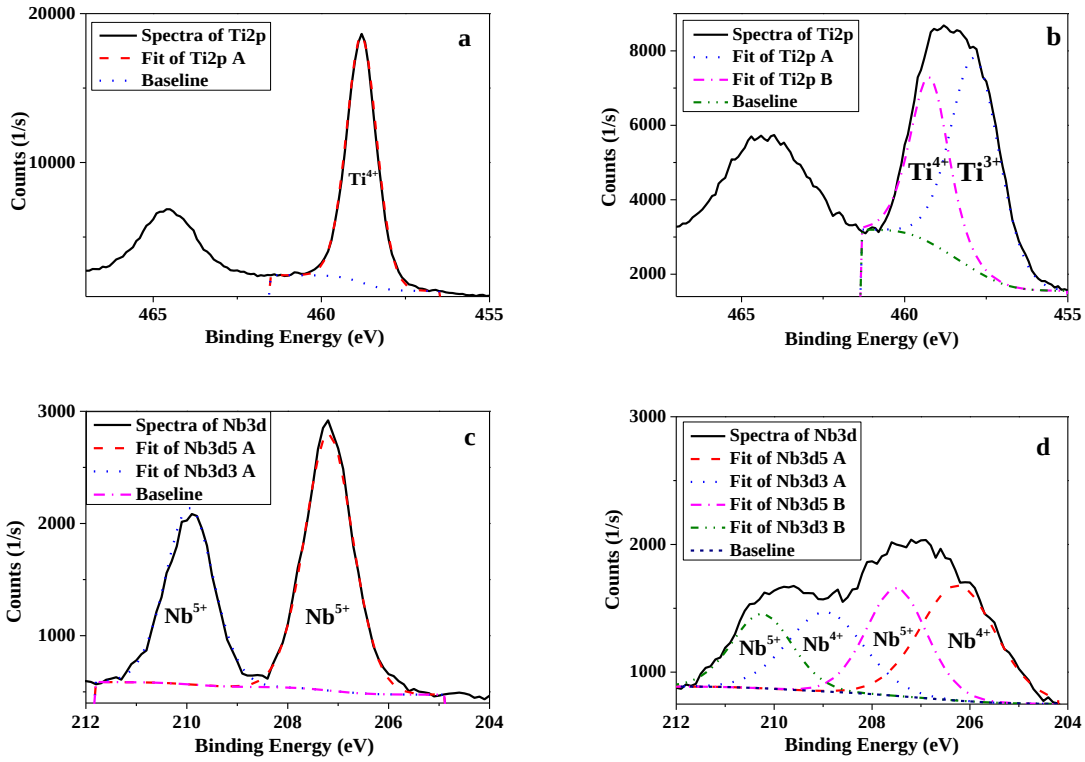

Figure 11: High resolution XPS spectra of Ti for 10 at. % Nb doped LT (a) and HTR (b) and of Nb for 10 at. % Nb doped LT (c) and HTR (d) fibres.

1.3 Electrical and electrochemical characterisation of titania nanofibres

1.3.1 Conductivity measurements

The electrical conductivity of titania nanofibres was estimated using an in-house developed cell equipped with four electrodes. Samples were analysed as pellets prepared by pressing of the powders at 370 MPa for 10 min. The thickness of obtained pellets was between 600 and 900 µm. The electronic conductivity values were calculated by Van der Pauw method as described in Chapter 2 and listed in Table 3.

The conductivity increases from ~10^{-9} S/cm for the undoped LT sample to ~10^{-7} S/cm for 5 at. % Nb doped LT nanofibres. This is indirect proof for the incorporation of Nb into titania lattice structure. HT (rutile phase) and LT (anatase phase) samples show comparable electronic conductivity values.

Table 3: Electronic conductivity (S/cm) of LT and HT TiO_2 nanofibres with different Nb concentrations at RT.

$\%_{at}$ Nb	**0**	**5**	**10**	**20**
LT	$4 \cdot 10^{-9}$	$2 \cdot 10^{-7}$	$7 \cdot 10^{-8}$	$8 \cdot 10^{-8}$
HT	$6 \cdot 10^{-8}$	$2 \cdot 10^{-7}$	$2 \cdot 10^{-7}$	$9 \cdot 10^{-7}$

Electrical conductivity values for pellets (obtained by pressing of LT samples) reduced at 800 °C in Ar/H_2 are listed in Table 4. After such thermal treatment, the conductivity increases from ~10^{-9} S/cm for LT to ~10^{-3} S/cm for HTR samples. The increased conductivity is probably due to the presence of Ti^{3+} on the surface of TiO_2 nanofibres. Chhina et al. reported comparable conductivity for Nb doped titania reduced at 700 °C (6.1 10^{-4} S/cm) and 900 °C (~1.4 10^{-3} S/cm), but lower surface area of 13 and 5 m^2/g, respectively [27]. Difference in electrical conductivity can be attributed to different porosity and thickness of the pellets. Finally, conductivity increases from ~10^{-5} S/m for undoped HTR sample to ~10^{-3} S/m for Nb doped HTR samples.

Table 4: Electrical conductivity of HTR TiO_2 nanofibres with different Nb concentrations at RT.

$\%_{at}$ Nb	**0**	**5**	**10**	**20**
σ (S/cm)	$2 \cdot 10^{-5}$	$2 \cdot 10^{-3}$	$5 \cdot 10^{-3}$	$1 \cdot 10^{-3}$

10 at. % Nb doped HTR sample provides the highest conductivity compared to the other samples. Electrical conductivity of this sample reaches 0.01 S/cm at 100 °C and 0.02 S/cm at 150 °C (operating temperature of HT-PEMFC). Its conductivity increases with increasing temperature indicating semiconducting behaviour of the TiO_2 nanofibres (Figure 12).

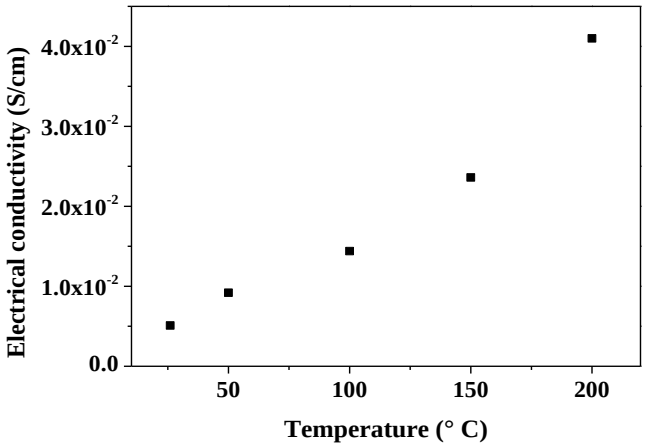

Figure 12: Electrical conductivity of 10 at. % Nb doped HTR titania nanofibres as a function of the temperature.

1.3.2 Electrochemical characterisation

The resistance to electrochemical corrosion of LT and HTR samples was evaluated and compared to that of a conventional carbon support (Vulcan XC-72R). This chronoamperometric test was performed at a potential of 1.4 V vs. RHE for 2 h at 80 °C in 0.5 M sulphuric acid [28]. Such conditions were chosen to simulate conditions in a PEMFC cathode during start-up and shut down, when the potential difference rises up to 1.44 V [29]. The obtained oxidation currents of LT, HTR and Vulcan XC-72R are shown in Figure 13. Vulcan XC-72R begins with a high current peak (oxidation wave) attributed to the oxidation of the amorphous carbon [30]. LT and HTR samples provide similar response to each other. The electrochemical degradation was estimated from the integration of those curves. The integrated charges for HTR, LT fibres and Vulcan XC-72R are 1.04, 0.96 and 3.90 C/mg, respectively. Both rutile and anatase nanofibres show lower corrosion charge and thus higher electrochemical stability than the carbon support. Siracusano et al. obtained comparable oxidation charges for Ti oxide based catalyst supports, which were lower compared to the commercial carbon support [31].

The logarithmic plots of oxidation currents are depicted in Figure 13b. LT and HTR samples provide similar slopes which may indicate similar degradation mechanisms.

Among the various niobium-doped titania nanofibre samples, 10 at. % Nb doped HTR provided the highest electronic conductivity. Therefore, it (labelled as titania nanofibres (TNFs)) was selected for Pt nanoparticle deposition and further characterisation of obtained Pt/TNF.

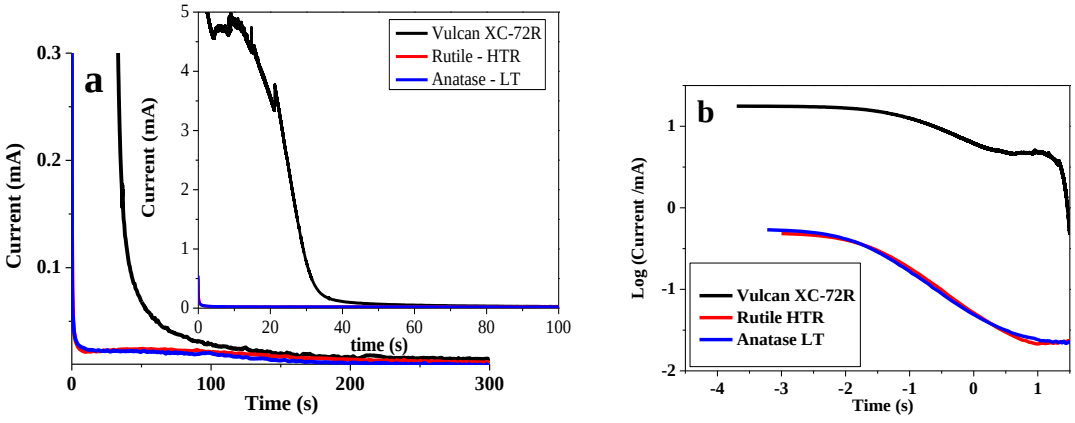

Figure 13: Oxidation currents in linear (a) and logarithmic (b) scales for LT, HTR samples and Vulcan XC-72R at 1.4 V_{RHE}, 80 °C in 0.5 M H_2SO_4 solution.

2 Synthesis and characterisation of Pt supported on Nb doped titania nanofibres

Pt nanoparticles were prepared using a modified microwave-assisted polyol method (Figure 14). Briefly, Pt precursor was dissolved in ethylene glycol, which plays the role of the solvent, as well as reducing and stabilising agent for Pt nanoparticles. NaOH solution in ethylene glycol was added until pH 11.5 was obtained, in order to increase concentration of glycolate ions, which can stabilise Pt particles by forming chelate-type complexes via their carboxyl groups [32]. The obtained solution was heated at 120 °C for 6 min in microwave reactor to allow reduction of Pt salt. Afterwards H_2SO_4 acid solution was added until pH 2 was obtained (as described in the paragraph 2.1) and the mixture was stirred for 24 h to allow Pt adsorption onto the oxide surface. More details on the preparation procedure are provided in the experimental part (Annex A).

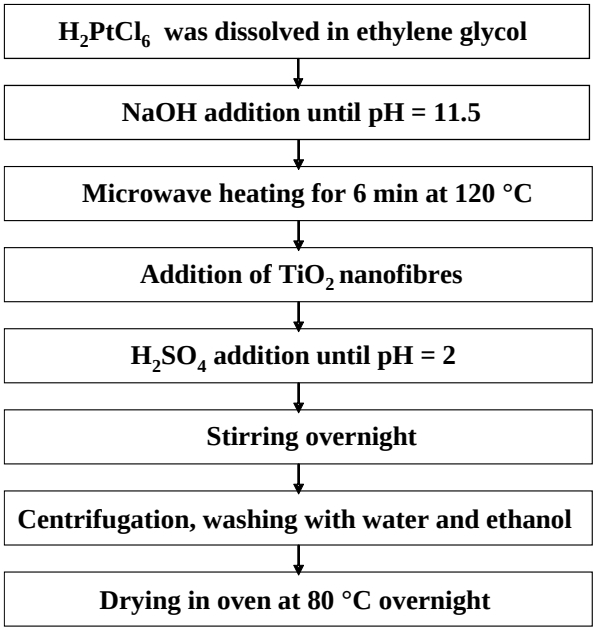

Figure 14 : Schema of the synthesis protocol for titania nanofibres supported Pt.

2.1 Pt deposition and physico-chemical characterisation of obtained Pt/TNFs

Zeta potential measurements

The zeta potential on the surface of TNFs was measured as described in Chapter 2. As shown in Figure 15, it was positive when pH was lower than 3 for TNFs, while it was negative in the whole range of pH for Pt nanoparticles. Therefore, after mixing of synthesised Pt nanoparticles with TNFs, acid was added dropwise until the pH was brought down to 2, in order to avoid the electrostatic repulsion between Pt nanoparticles and TNFs. Such procedure allows adsorption of Pt nanoparticles on the oxide surface and increases Pt loading.

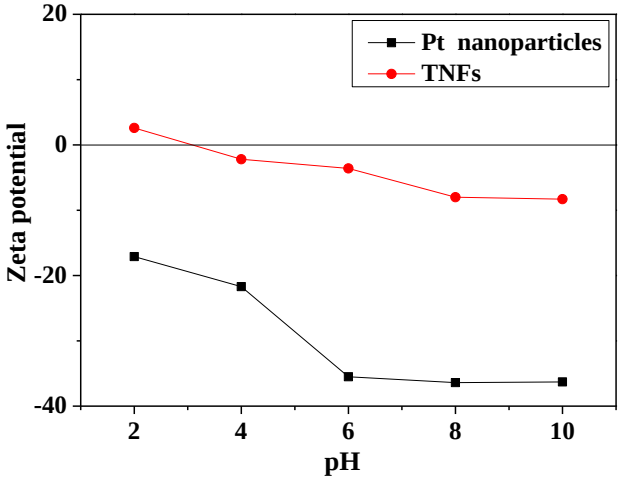

Figure 15: Zeta potential as a function of pH for Pt colloid and TNFs.

Determination of Pt loading on the supports

In order to obtain a similar dispersion of Pt on Nb doped TiO_2 and on carbon black supports (which have different surface area and density), Chhina et al. deposited 10 wt. % Pt on Nb–TiO_2 and 40 wt. % Pt on carbon [33]. Following his example, we have calculated that 14 wt. % Pt/TNF (surface area of TNF ~16 m^2/g) and 27 wt. % Pt/CNF (~36 m^2/g) should provide similar catalyst dispersion to 50 wt. % Pt/C (~100 m^2/g [11]), for Pt nanoparticles with diameter of ~3 nm. Therefore, the target loading of Pt was 14 and 27 wt. % for TNF and CNF supports, respectively.

The obtained Pt loading on TNFs (16 wt. %) was determined by X-ray fluorescence measurements (XRF), while Pt amount on Vulcan XC-72R (33 wt. %) was determine by TGA, as described in the experimental part (Annex A). In order to calibrate the XRF signal, standard samples with 5, 10, 15 and 20 wt. % Pt were prepared by mixing Pt black (Alfa Aesar) with CNF support, as described in the experimental part (Annex A).

Morphological characterisation

The obtained TNFs and Vulcan XC-72R supported Pt nanoparticles are shown in Figure 16. Platinum is less homogeneously dispersed on the TNFs than on the Vulcan XC-72R support. This result may be attributed to the more porous structure and higher surface area of the Vulcan XC-72R compared to that of TNFs. The average diameter of Pt nanoparticles is 2.3 nm for Pt/TNFs and 2.4 nm for Pt/Vulcan XC-72R.

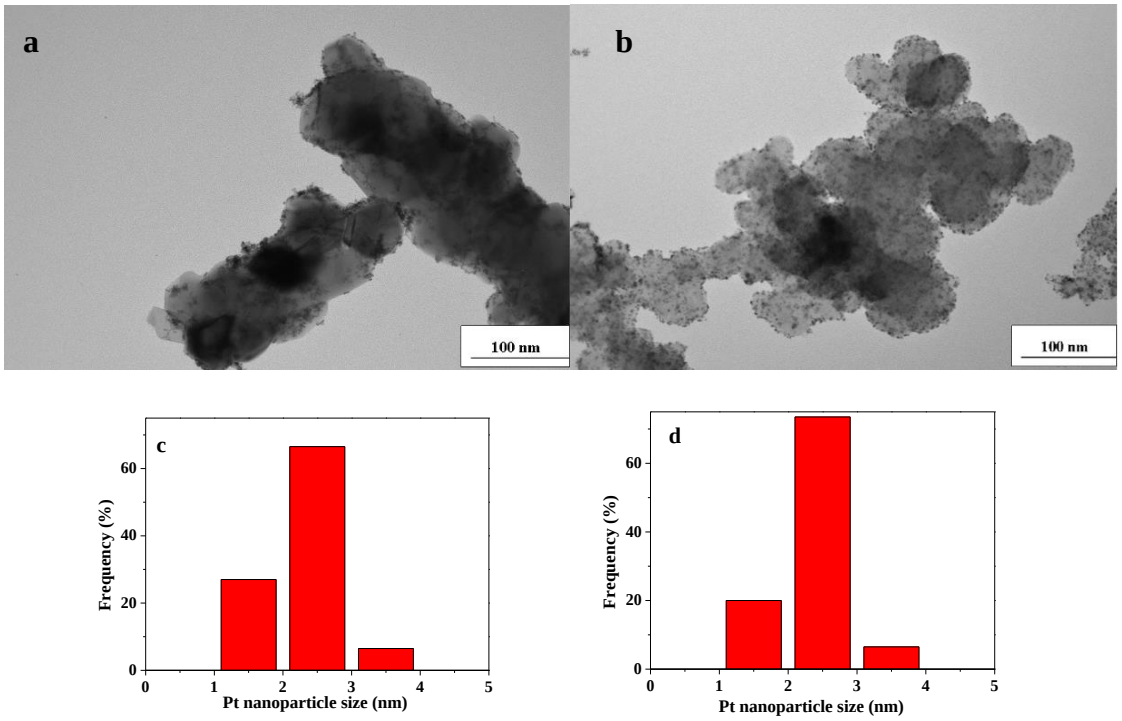

Figure 16: TEM micrographs of 16 %Pt/TNFs (a) and 33%Pt/Vulcan XC-72R (b) and corresponding Pt nanoparticle size distribution histograms obtained from measurements of 100 nanoparticles (c, d), respectively.

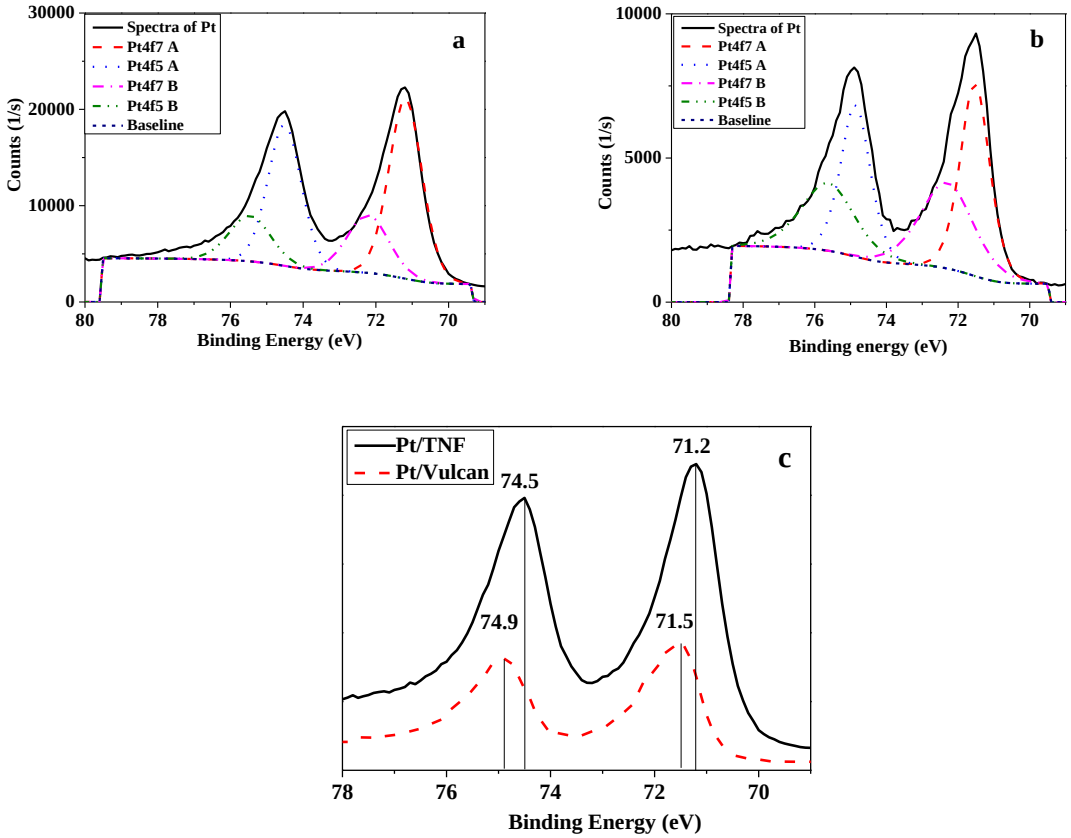

Figure 17: XPS spectra of Pt for Pt on TNFs (a) and Pt on Vulcan XC-72R (b) and comparison of both of them (c).

Surface analysis

The electronic interactions between metal catalysts and supports can be characterised by using XPS. Figure 17 shows high resolution XPS spectra of the Pt 4f region recorded for Pt/TNFs and Pt/Vulcan XC-72R. The Pt 4f signal consists of two doublets. The intense doublet Pt 4f7/2 (at 71.2 eV for Pt/TNFs and 71.5 eV for Pt/Vulcan XC-72R) corresponds to metallic Pt. The small shift of both doublets to higher binding energies is typical for small Pt particles [34]. The small doublet at 72.2 eV for Pt/TNFs and 72.3 eV for Pt/Vulcan XC-72R can be attributed to PtO and $Pt(OH)_2$ [35]. The slight negative shift of 0.3 eV may be attributed to an increase of electron density on the Pt surface due to the electron transfer from TiO_2 to Pt. Such result is usually associated with the strong metal-support interaction (SMSI) between Pt and TiO_2 (Figure 17c) [36], [37].

2.2 Electrochemical characterisation of Pt/TNFs

The activity and stability of the Pt/TNFs electrocatalyst was evaluated using cyclic voltammetry and linear sweep voltammetry at rotating disk electrode and compared to that of commercial Pt/C and Pt/Vulcan XC-72R.

2.2.1 Determination of the electrochemical surface area

The cyclic voltamograms of Pt/TNFs, Pt/C and Pt/Vulcan XC-72R are shown in Figure 18. The platinum oxidation-reduction region of TNFs was suppressed in comparison to that of Pt/Vulcan XC-72R. Moreover, the electrochemically active surface area (ECSA) of Pt/TNFs (36 m^2/g) is lower than that of Pt/Vulcan XC-72R (47 m^2/g) with similar Pt nanoparticles size. This could be a result of lower electrical conductivity (10^{-3} S/cm for TNFs and 6 S/cm for Vulcan XC-72R) and low surface area of the TNFs. Chhina et al. [27] also reported smaller ECSA of 10 wt % Pt supported on titania compared to commercial 40 wt. % Pt/C. Furthermore, Subban et al. [38] reported that the ECSA of Pt on $Ti_{0.7}W_{0.3}O_2$ was lower than Pt on Vulcan, which was attributed to insufficient electrical conductivity of $Ti_{0.7}W_{0.3}O_2$ and to aggregation of Pt particles. The ECSA of Pt/TNFs was higher than that reported by Senevirathne et al. [9] for Pt supported on electrospun Ti_4O_7 (~6 m^2/g), probably due to the difference in Pt nanoparticles size (2.3 and 7 nm).

The PtO reduction peak of Pt/TNFs was shifted to lower voltage compared to that of Pt/C and Pt/Vulcan XC-72R. This result may be attributed to lower ORR activity for Pt/TNFs.

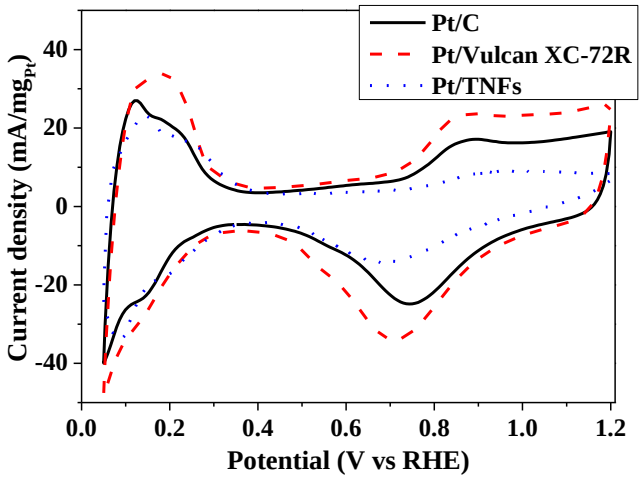

Figure 18: Cyclic voltammograms of Pt/TNFs, Pt/C and Pt/Vulcan XC-72R obtained at a scan rate of 50 mV/s in 0.1 M $HClO_4$.

2.2.2 Evaluation of ORR activity

The ORR polarisation curves for Pt supported on TNFs and carbon based supports (Figure 19) show onset potentials at around 0.9 V. In the region from 0.95 to 0.60 V for Pt/C and Pt/Vulcan XC-72R, the ORR curves were under mixed kinetic and diffusion control. The mixed kinetic-diffusion controlled region of Pt/TNFs was between 0.85 and 0.40 V. It is slightly shifted to lower potentials. The $E_{1/2}$ of Pt/TNFs, Pt/C and Pt/Vulcan XC-72R was 0.78, 0.82 and 0.81 at 900 rpm, respectively. This result indicates lower ORR activity of Pt/TNFs compared to that of Pt/C and Pt/Vulcan XC-72R. Indeed, Pt/TNFs show lower mass activity than other electrocatalysts (Table 5), which could be related to lower conductivity of the support. Bauer et al. [39] also demonstrated that both Nb doped as well as H_2 reduced electrospun titania supported Pt provided lower ORR activity than Pt/C due to lower conductivity and surface area of the oxide support. Furthermore, Subban et al. [38] reported that ORR mass activity of $Pt/Ti_{0.7}W_{0.3}O_2$ was lower than that of Pt/Vulcan.

Figure 19d shows the current density as a function of the square root of the rotation rate of the RDE. The number of electrons involved in the reaction was 2.8, 3.6 and 3.7 for Pt/TNFs, Pt/Vulcan XC-72R and Pt/C, respectively. For the oxide based catalyst, a contribution of both 2 and 4 electron mechanisms is then possible. The RRDE studies could be envisaged for the future to estimate the amount of hydrogen peroxide produced during the oxygen reduction.

Table 5 : Comparison of ORR mass activities and Tafel slopes for ORR on different catalysts.

Electrocatalyst	Pt/C	Pt/Vulcan XC-72R	Pt/TNFs
ORR mass activity at 0.8 V (A/g_{Pt})	61.4	36.5	29.3
Tafel slopes	-55	-52	-94

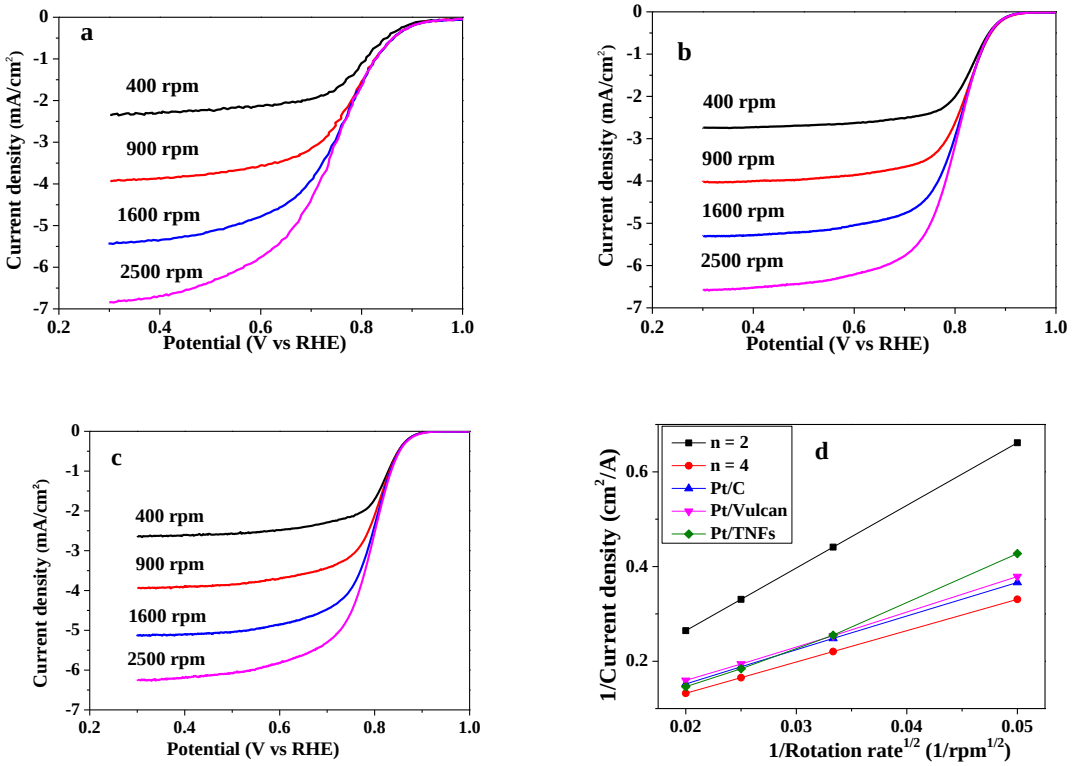

Figure 19: Oxygen reduction reaction polarization curves obtained on Pt/TNFs (a), Pt/C (b) and Pt/Vulcan XC-72R (c) and current densities as a function of the inverse of the square root of the rotation rate (d).

Figure 20 shows Tafel plots for the ORR on Pt/TNFs, Pt/C and Pt/Vulcan XC-72R at 900 rpm in 0.1 M $HClO_4$. Pt/TNFs show higher slope (Table 5) than the Pt/C and Pt/Vulcan XC-72R electrocatalysts, which may indicate a different ORR mechanism.

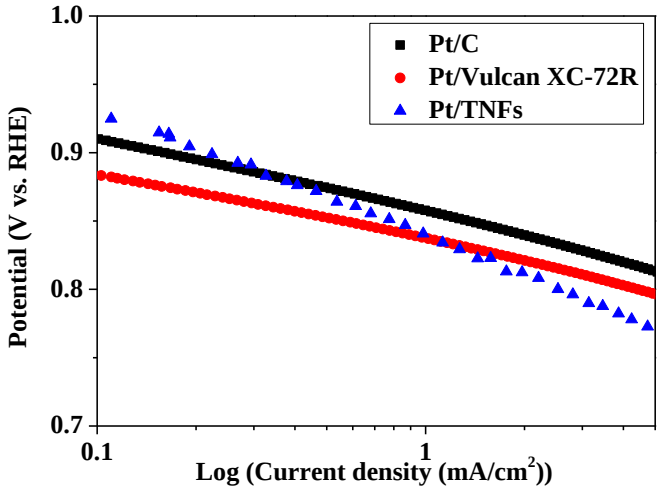

Figure 20 : Tafel plots for ORR on Pt/TNFs, Pt/C and Pt/Vulcan XC-72R at 900 rpm in 0.1 M $HClO_4$.

2.2.3 Evaluation of the electrochemical stability

In order to compare the stability of Pt/TNFs with Pt supported on carbon-based materials, 1000 potential cycles were recorded between 0.05 and 1.2 V. Cyclic voltammograms before and after the stability test are shown in Figure 21. The decrease in ECSA after voltage cycling was lower for Pt/TNFs (25 % ECSA loss) than for Pt/C (39 %) and Pt/Vulcan XC-72R (32 %), as shown in Table 6.

Bauer et al. also observed lower ECSA loss for electrospun Nb doped TiO_2 supported Pt after 1000 cycles (40 % ECSA loss) [39] compared to commercial Pt/C. This result is usually attributed to superior stability of oxide-based support. Also, Senevirathne et al. [9] reported similar ECSA loss of 23 % for electrospun H_2 reduced Ti_4O_7 supported Pt after 1000 cycles. The drop of ECSA was attributed to the decrease of the support electrical conductivity and to Pt nanoparticles agglomeration.

Furthermore, in the case of Pt/TNFs, the oxygen reduction peak was shifted to lower voltage, which suggests poor ORR activity after voltage cycling.

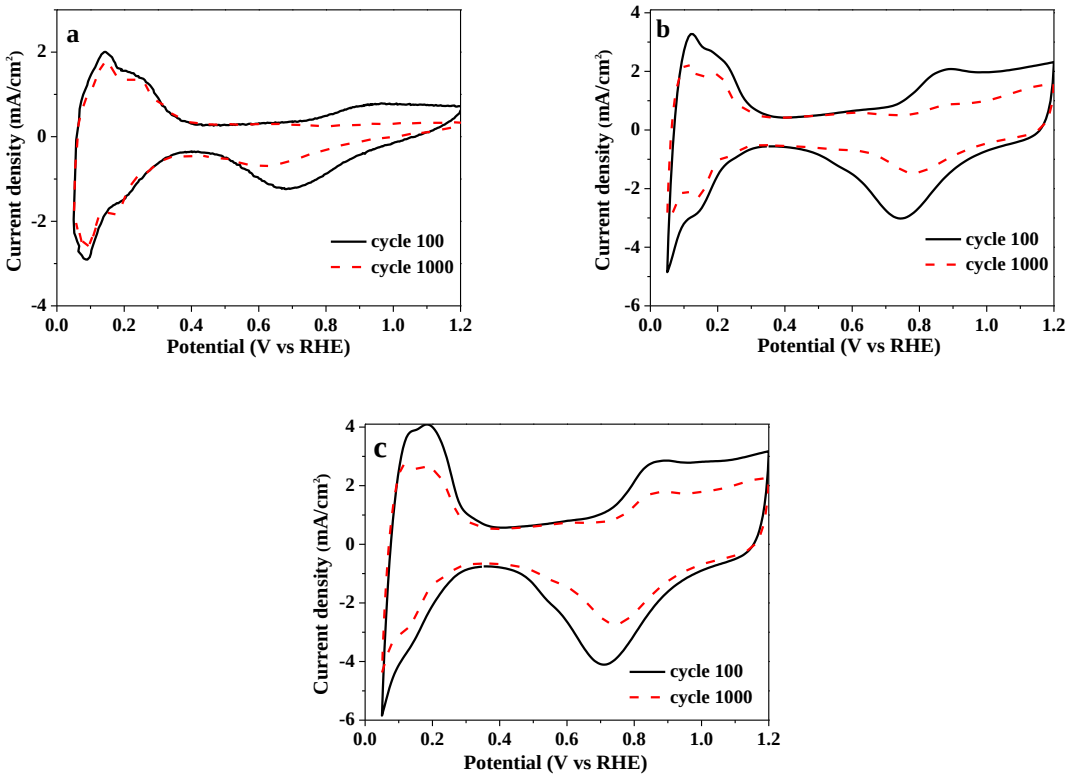

Figure 21: Cyclic voltammograms obtained after 100 and 1000 cycles on Pt/TNFs (a), Pt/C (b) and Pt/Vulcan XC-72R (c).

Table 6: ECSA of Pt/TNFs, Pt/Vulcan XC-72R and Pt/C before and after the stability test.

Electrocatalyst	Pt/C	Pt/Vulcan XC-72R	Pt/TNFs
ECSA before voltage cycling, m^2/g	33	47	36
ECSA after voltage cycling, m^2/g	20	32	27
ECSA loss, %	39	32	25

ORR activity loss after stability test

Figure 22 shows ORR mass activities calculated from the polarisation curves at a rotation speed of 900 rpm before and after the voltage cycling. In terms of percent loss of mass activity, the losses for all materials are similar, although slightly less for Pt/Vulcan XC-72R (Table 7). Given the higher resistance of the oxide support to electrochemical corrosion, these observations suggest that Pt dissolution/migration/agglomeration phenomena have occurred at the electrode surface (see TEM characterisation in the next paragraph).

A further explanation is the possible formation of non-conductive TiO_2 layer on the surface of Ti_4O_7 after voltage cycling, as reported by Li et al. [40]. Comparable ORR mass loss of 86% for electrospun Ti_4O_7 supported Pt was observed by Senevirathne et al. [9].

The agglomeration of Pt nanoparticles can be also a cause of such activity loss. Therefore, TEM analysis was performed before and after the voltage cycling.

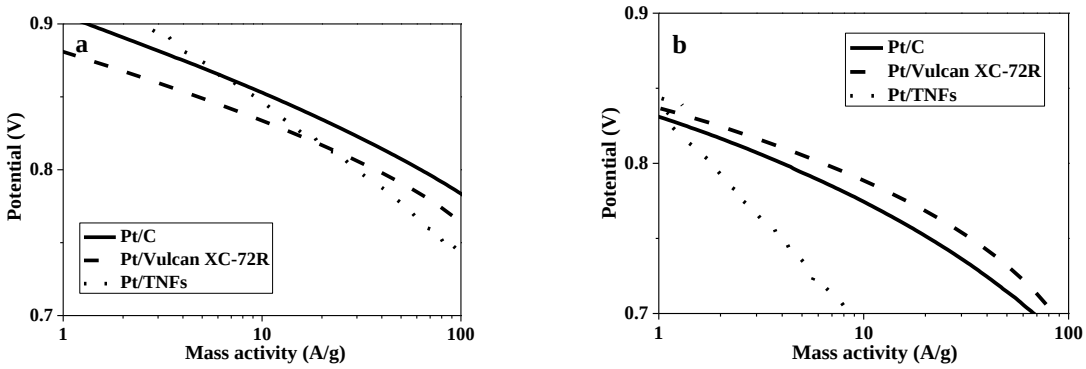

Figure 22: Mass activities of ORR measurements before (a) and after (b) the stability test.

Table 7: ORR mass activities before and after voltage cycling at 0.8 V_{RHE}.

Electrocatalyst	Pt/C	Pt/Vulcan XC-72R	Pt/TNFs
ORR mass activity before voltage cycling, A/g	61.4	36.5	29.3
ORR mass activity after voltage cycling, A/g	3.9	5.5	1.8
ORR mass activity loss, %	94	81	94

Transmission electron micrographs before and after voltage cycling

TEM images (Figure 23) show that the Pt particle size of all samples increased after the voltage cycling. The average particle size increased from 2.3 to 5.0 nm for Pt/TNFs, from 2.4 to 5.0 nm for Pt/Vulcan XC-72R and from 3.8 to 5.3 nm for Pt/C (see Chapter 2). All platinum particles therefore showed similar growth. However, there are areas with huge Pt particles agglomerations for Pt/C electrocatalyst. Such agglomeration is attributed to carbon corrosion at high potential.

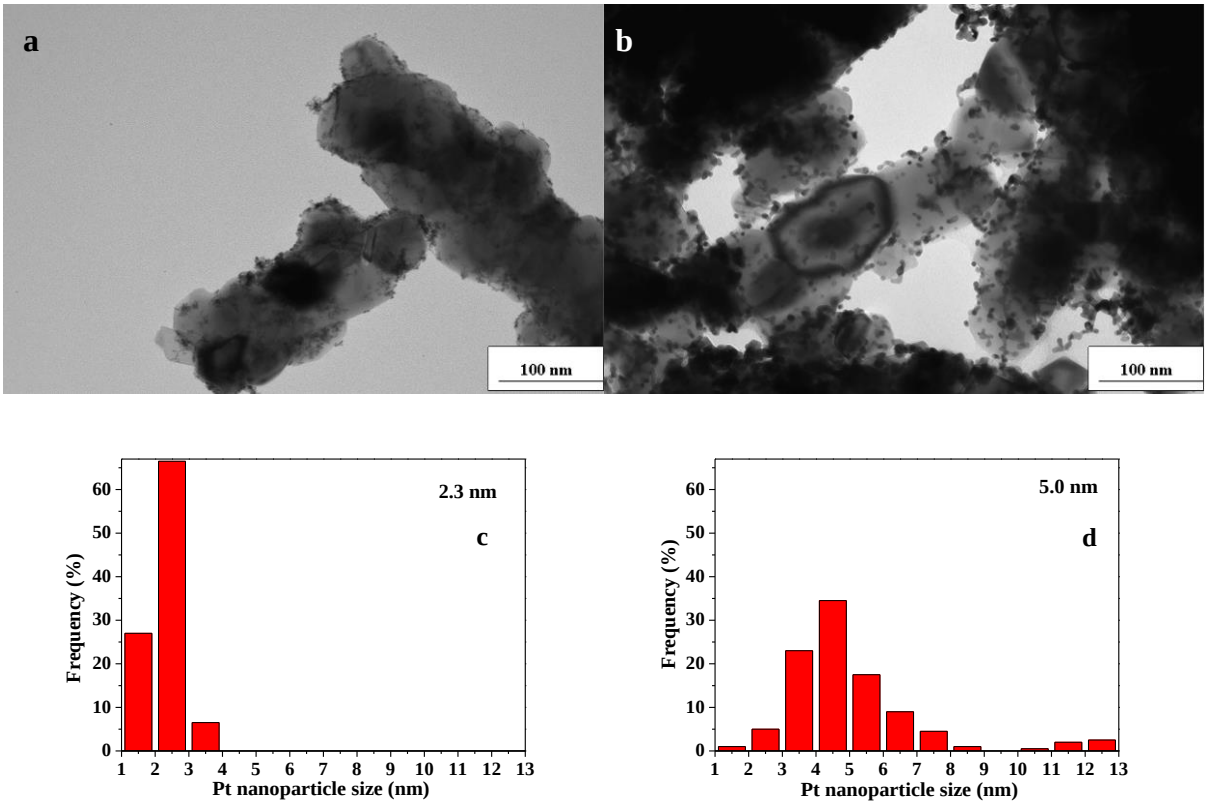

Figure 23: TEM micrographs of Pt/TNFs before (a) and after potential cycling (b) and corresponding Pt nanoparticle size distribution histograms obtained from the measurements of 100 particles (c and d).

Conclusions

Niobium-doped titania nanofibres were prepared by electrospinning and under various heat-treatment conditions used in order to establish a good compromise between the electrical conductivity and specific surface area. Structural and surface properties of the obtained fibres were characterised by nitrogen adsorption/desorption, Raman, XPS and XRD analysis and conductivity measurements. The effect of Nb on the morphology, specific surface area, phase transition and the electrical conductivity was investigated. The 10 at. % Nb doped HTR sample was selected for Pt deposition due to its high conductivity. The obtained Pt/TNFs electrocatalyst retained 73 % of its initial ECSA after accelerated stress test, but showed high ORR mass activity loss, which may be attributed to the formation of the resistive stoichiometric oxide layer on the surface of the nanofibres as well as to platinum dissolution and agglomeration.

Perspectives

Electrospinning provides the possibility to obtain supported or free-standing mat. These 3 D interconnected nanofibrous networks can be used as catalyst support. However, ceramic nanofibres mats are too fragile (compared to carbon nanofibres mat) to be handled as a free-standing film. The use of composite electrospun mats such as polymer/TiO_2 or carbon/TiO_2 can be a solution to this problem.

The electrical conductivity and surface area of the titanium oxide need to be improved, in order to enhance ORR activity of Pt/TNF. For instance, TiO_2 nanofibres can be heated at 800 °C under pure H_2 atmosphere and in the presence of catalyst such as cobalt [41], in order to increase the amount of suboxide, while maintaining specific surface area of TiO_2. However, the use of doping such as W and Mo is preferred to avoid oxidation of suboxide at the cathode.

Furthermore, the composite carbon/TiO_2 fibres can be obtained by adding of corrosion resistive CNTs or graphene into the electrospinning solution in order to increase conductivity and surface area of TiO_2-based fibres.

Another strategy is to replace TiO_2 by more conductive oxide such as indium tin oxide (ITO) or doped tin oxide. Therefore, Nb and Sb doped SnO_2 was prepared by electrospinning and characterised as electrocatalyst support for PEMFC, as described in the next chapter.

References

[1] Z. Zhang, J. Liu, J. Gu, L. Su, and L. Cheng, "An Overview on Metal Oxide Materials as Electrocatalysts and Supports for Polymer Electrolyte Fuel Cells," *Energy & Environmental Science*, pp. 1–95, 2014.

[2] X. Wang, Z. Li, J. Shi, and Y. Yu, "One-Dimensional Titanium Dioxide Nanomaterials: Nanowires, Nanorodes, and Nanobelts," *Chemical reviews*, 2014.

[3] I. Savych, J. Bernard d'Arbigny, S. Subianto, S. Cavaliere, D. J. Jones, and J. Rozière, "On the Effect of Non-Carbon Nanostructured Supports on the Stability of Pt Nanoparticles during Voltage Cycling: a Study of TiO_2 Nanofibres," *Journal of Power Sources*, vol. 257, pp. 147–155, Feb. 2014.

[4] S. Cavaliere, S. Subianto, L. Chevallier, D. J. Jones, and J. Rozière, "Single step elaboration of size-tuned Pt loaded titania nanofibres," *Chemical communications*, vol. 47, no. 24, pp. 6834–6, Jun. 2011.

[5] D. Li and Y. Xia, "Electrospinning of Nanofibers: Reinventing the Wheel?," *Advanced Materials*, vol. 16, no. 14, pp. 1151–1170, Jul. 2004.

[6] D. Li and Y. Xia, "Fabrication of Titania Nanofibers by Electrospinning," *Nano Letters*, vol. 3, no. 4, pp. 555–560, Apr. 2003.

[7] D. Li and Y. Xia, "Direct Fabrication of Composite and Ceramic Hollow Nanofibers by Electrospinning," *Nano Letters*, vol. 4, no. 5, pp. 933–938, May 2004.

[8] Y. Xiong, B. T. Mayers, and Y. Xia, "Some recent developments in the chemical synthesis of inorganic nanotubes," *Chemical communications*, no. 40, pp. 5013–22, Oct. 2005.

[9] K. Senevirathne, R. Hui, S. Campbell, S. Ye, and J. Zhang, "Electrocatalytic activity and durability of Pt/NbO_2 and Pt/Ti_4O_7 nanofibers for PEM fuel cell oxygen reduction reaction," *Electrochimica Acta*, vol. 59, pp. 538–547, Jan. 2012.

[10] S.-Y. Huang, P. Ganesan, and B. N. Popov, "Electrocatalytic activity and stability of niobium-doped titanium oxide supported platinum catalyst for polymer electrolyte membrane fuel cells," *Applied Catalysis B: Environmental*, vol. 96, no. 1–2, pp. 224–231, Apr. 2010.

[11] H. Chhina, "Oxidation-resistatnt catalyst supports for Proton exchnge membrane fuel cells," 2009.

[12] Y.-J. Wang, D. P. Wilkinson, A. Guest, V. Neburchilov, R. Baker, F. Nan, G. a. Botton, and J. Zhang, "Synthesis of Pd and Nb–doped TiO_2 composite supports and their corresponding Pt–Pd alloy catalysts by a two-step procedure for the oxygen reduction reaction," *Journal of Power Sources*, vol. 221, pp. 232–241, Jan. 2013.

[13] K. A. Michalow, D. Flak, A. Heel, M. Parlinska-Wojtan, M. Rekas, and T. Graule, "Effect of Nb doping on structural, optical and photocatalytic properties of flame-made TiO_2 nanopowder," *Environmental Science and Pollution Research*, vol. 19, no. 9, pp. 3696–3708, 2012.

[14] A. M. Ruiz, G. Dezanneau, J. Arbiol, A. Cornet, and J. R. Morante, "Insights into the Structural and Chemical Modifications of Nb Additive on TiO_2 Nanoparticles," *Chemistry of Materials*, vol. 16, no. 17, pp. 862–871, 2004.

[15] T. Yuan, B. Zhao, R. Cai, Y. Zhou, and Z. Shao, "Electrospinning based fabrication and performance improvement of film electrodes for lithium-ion batteries composed of TiO_2 hollow fibers," *Journal of Materials Chemistry*, vol. 21, no. 38, p. 15041, 2011.

[16] D. A. H. Hanaor and C. C. Sorrell, "Review of the anatase to rutile phase transformation," *Journal of Materials Science*, vol. 46, no. 4, pp. 855–874, Dec. 2010.

[17] V. Guidi, M. C. Carotta, M. Ferroni, G. Martinelli, D. Fisica, V. Paradiso, I. Ferrara, C. Ercole, and I. Este, "Effect of Dopants on Grain Coalescence and Oxygen Mobility in Nanostructured Titania Anatase and Rutile," *The Journal of Physical Chemistry B*, vol. 107, pp. 120–124, 2003.

[18] H. Song, A. O. Sjastad, H. Fjellvag, H. Okamoto, Ø. B. Vistad, B. Arstad, and P. Norby, "Exfoliation and thermal transformations of Nb-substituted layered titanates," *Journal of Solid State Chemistry*, vol. 184, no. 12, pp. 3135–3143, Dec. 2011.

[19] S. Karvinen, "The effects of trace elements on the crystal properties of TiO_2," *Solid State Sciences*, vol. 5, no. 5, pp. 811–819, May 2003.

[20] G. Q. Wang, W. Lan, G. J. Han, Y. Wang, Q. Su, and X. Q. Liu, "Effect of Nb doping on the phase transition and optical properties of sol–gel TiO_2 thin films," *Journal of Alloys and Compounds*, vol. 509, no. 10, pp. 4150–4153, Mar. 2011.

[21] H. An and H.-J. Ahn, "Fabrication of wrinkled Nb-doped TiO_2 nanofibres via electrospinning," *Materials Letters*, vol. 93, pp. 88–91, Feb. 2013.

[22] M. Hirano and Y. Ichihashi, "Phase transformation and precipitation behavior of niobium component out of niobium-doped anatase-type TiO_2 nanoparticles synthesized via hydrothermal crystallization," *Journal of Materials Science*, vol. 44, no. 22, pp. 6135–6143, Sep. 2009.

[23] A. Kumar, R. Jose, K. Fujihara, J. Wang, and S. Ramakrishna, "Structural and Optical Properties of Electrospun TiO2 Nanofibers," *Chemistry of Materials*, vol. 19, no. 26, pp. 6536–6542, Dec. 2007.

[24] P. S. Archana, R. Jose, T. M. Jin, C. Vijila, M. M. Yusoff, and S. Ramakrishna, "Structural and Electrical Properties of Nb-Doped Anatase TiO_2 Nanowires by Electrospinning," *Journal of the American Ceramic Society*, vol. 93, no. 12, pp. 4096–4102, Dec. 2010.

[25] P. C. Ricci, C. M. Carbonaro, L. Stagi, M. Salis, A. Casu, S. Enzo, F. Delogu, and I. Italiano, "Anatase-to-Rutile Phase Transition in TiO_2 Nanoparticles Irradiated by Visible Light," *The Journal of Physical Chemistry C*, vol. 117, p. 7850 − 7857, 2013.

[26] M. Z. Atashbar, H. T. Sun, B. Gong, W. Wlodarski, and R. Lamb, "XPS study of Nb-doped oxygen sensing TiO_2 thin films prepared by sol-gel method," *Thin Solid Films*, vol. 326, pp. 238–244, 1998.

[27] H. Chhina, S. Campbell, and O. Kesler, "Ex Situ and In Situ Stability of Platinum Supported on Niobium-Doped Titania for PEMFCs," *Journal of The Electrochemical Society*, vol. 156, no. 10, p. B1232, 2009.

[28] M. Wesselmark and C. Lagergren, "Degradation Studies of PEMFC Cathodes Based on Different Types of Carbon," *ECS Transactions*, vol. 25, no. 1, pp. 1241–1250, 2009.

[29] C. A. Reiser, L. Bregoli, T. W. Patterson, J. S. Yi, J. D. Yang, M. L. Perry, and T. D. Jarvi, "A Reverse-Current Decay Mechanism for Fuel Cells," *Electrochemical and Solid-State Letters*, vol. 8, no. 6, p. A273, 2005.

[30] M. P. Gurrola, J. Gutiérrez, S. Rivas, M. Guerra-Balcázar, J. Ledesma-García, and L. G. Arriaga, "Evaluation of the corrosion of Sb-doped SnO_2 supports for electrolysis systems," *International Journal of Hydrogen Energy*, pp. 2–9, Mar. 2014.

[31] S. Siracusano, a. Stassi, E. Modica, V. Baglio, and a. S. Aricò, "Preparation and characterisation of Ti oxide based catalyst supports for low temperature fuel cells," *International Journal of Hydrogen Energy*, vol. 38, no. 26, pp. 11600–11608, Aug. 2013.

[32] H.-S. Oh, J.-G. Oh, Y.-G. Hong, and H. Kim, "Investigation of carbon-supported Pt nanocatalyst preparation by the polyol process for fuel cell applications," *Electrochimica Acta*, vol. 52, no. 25, pp. 7278–7285, Sep. 2007.

[33] H. Chhina, D. Susac, S. Campbell, and O. Kesler, "Transmission Electron Microscope Observation of Pt Deposited on Nb-Doped Titania," *Electrochemical and Solid-State Letters*, vol. 12, no. 6, p. B97, 2009.

[34] C. Roth, M. Goetz, and H. Fuess, "Synthesis and characterization of carbon-supported Pt-Ru-WOx catalysts by spectroscopic and diffraction methods," *Journal of Applied Electrochemistry*, vol. 31, pp. 793–798, 2001.

[35] A. K. Shukla, M. K. Ravikumar, A. Roy, S. R. Barman, and D. D. Sarma, "Electro-oxidation of Methanol in Sulfuric Acid Electrolyte on Platinized-Carbon Electrodes with Several Functional-Group Characteristics," *Journal of Electrochemical Society*, vol. 141, no. 6, pp. 463–467, 1994.

[36] A. Lewera, L. Timperman, A. Roguska, and N. Alonso-vante, "Metal-Support Interactions between Nanosized Pt and Metal Oxides (WO_3 and TiO_2) Studied Using X-ray Photoelectron Spectroscopy," *The Journal of Physical Chemistry C*, vol. 115, pp. 20153–20159, 2011.

[37] A. Rabis, P. Rodriguez, and T. J. Schmidt, "Electrocatalysis for Polymer Electrolyte Fuel Cells: Recent Achievements and Future Challenges," *ACS Catalysis*, vol. 2, no. 5, pp. 864–890, May 2012.

[38] C. V Subban, Q. Zhou, A. Hu, T. E. Moylan, F. T. Wagner, and F. J. DiSalvo, "Sol-gel synthesis, electrochemical characterization, and stability testing of $Ti_{0.7}W_{0.3}O_2$ nanoparticles for catalyst support applications in proton-exchange membrane fuel cells.," *Journal of the American Chemical Society*, vol. 132, no. 49, pp. 17531–6, Dec. 2010.

[39] A. Bauer, K. Lee, C. Song, Y. Xie, J. Zhang, and R. Hui, "Pt nanoparticles deposited on TiO_2 based nanofibers: Electrochemical stability and oxygen reduction activity," *Journal of Power Sources*, vol. 195, no. 10, pp. 3105–3110, May 2010.

[40] X. Li, A. L. Zhu, W. Qu, H. Wang, R. Hui, L. Zhang, and J. Zhang, "Magneli phase Ti_4O_7 electrode for oxygen reduction reaction and its implication for zinc-air rechargeable batteries," *Electrochimica Acta*, vol. 55, no. 20, pp. 5891–5898, Aug. 2010.

[41] Y. Lee, D. Kwak, A. Park, B. Roh, I. Hwang, and G. Cao, "Facile and Catalytic Synthesis of Conductive Titanium Suboxides for Enhanced Oxygen Reduction Activity and Stability in Proton Exchange Membrane Fuel Cells," *Int. J. Electrochem. Sci.*, vol. 8, pp. 9499–9507, 2013.

CHAPTER 4:

Tin dioxide as electrocatalyst support

1 Introduction

This chapter describes the preparation of niobium doped tin oxide nanotubes by combining conventional electrospinning with a specific thermal treatment in air. The effect of Nb and Sb doping on the tin oxide conductivity, morphology and surface area was investigated. Structure and properties of obtained doped SnO_2 fibre-in-tubes were characterised by XRD, SEM, XPS, Raman analysis, nitrogen adsorption/desorption analysis and electronic conductivity measurements.

Platinum nanoparticles were prepared using microwave-assisted polyol method and deposited on 5 at. % Nb doped SnO_2 support. ORR activity and stability of the obtained Pt/Nb-SnO_2 electrocatalysts were evaluated using a RDE technique and compared with a commercial Pt/C.

The influence of niobium doping on morphology and properties of tin oxide has been published in the following paper:

S. Cavaliere, S. Subianto, I. Savych, M. Tillard, D. J. Jones, J. Rozière, Dopant-Driven Nanostructured Loose-Tube SnO_2 Architectures: Alternative Electrocatalyst Supports for Proton Exchange Membrane Fuel Cells. *The Journal of Physical Chemistry C*, 117 (2013) 18298 − 18307 [1].

State-of-the-art on the preparation of nanotubes by single-needle electrospinning

Electrospun core-shell and tubular structures are usually prepared using a coaxial setup (see Chapters 1 and 3). However, this technique requires a strict control of the working parameters, complicated spinnerets and the appropriate precursor solution pairs [2]. Therefore, a new method was proposed, that allows hollow structures formation during heat treatment. Li et al. were the first authors who, in 2007, obtained nanotubes using a simple single-needle electrospinning [3]. Recently, various hollow oxide fibres, including Fe_2O_3 [4],[5], In_2O_3-Fe_2O_3 [6], Cu-doped WO_3 [7], SnO_2-ZnO [128],[129], ZnO [10],[11], CuO [12], Al_2O_3 [13] and Y_2O_3:$Yb^{3+}Er^{3+}$ [14] were prepared using conventional electrospinning, followed by calcination in air. This method also allows the fabrication of wire-in-tube (nickel–zinc ferrite) [15], as well as tube-in-tube (TiO_2, SiO_2, In_2O_3, SnO_2 [16] and Fe_2O_3 [2]) structures. In particular, hollow tin oxide fibres have gained significant attention in various fields such as gas sensing, lithium ion batteries and solar cells, as shown in Table 1.

Two mechanisms have been proposed in the literature to explain the formation of hollow structures during the calcination process. The first is based on the Kirkendall effect [17],[18],[19] and the second on the effects of polymer decomposition [20],[21]. Gao et al. [22] demonstrated that both mechanisms play a key role for the formation of hollow fibres. The lack of the oxygen inside the fibre causes the precursor concentration gradient, which leads to the diffusion of $SnCl_2$ molecules to the fibre surface (Kirkendall effect - diffusion via vacancies). Furthermore, the decomposition of a polymer results in release of carbon dioxide, which facilitates the hollow structure formation. An et al. [23], Cheng et al. [24] and Mou et al. [2] have prepared hollow and dense fibres by changing the heating rate. At low heating rate (1 °C/min) dense fibres were obtained, while at high heating rates hollow fibres were observed due to an increase in the rate of PVP decomposition. In addition, fibre-in-tube and tube-in-tube structures were prepared using very high heating rate of 100 °C/min and 250 °C/min, respectively. The formation mechanism was attributed to the generation of rigid shell due to the enhanced temperature gradient inside the fibre caused by large heating rates. Such dense shell is believed to prevent further decrease of the fibre diameter, whereas inner gel will shrink due to the decomposition of the polymer [2]. Finally, Lang et al. [16] and Gao et al. [22] observed that the precursor concentration has also a significant impact on fibre morphology.

Table 1: SnO_2 tubes by conventional electrospinning.

Reference	Composition	Temperature, time and heating rate	Diameter (nm)	Surface area (m^2/g)	Application
Li 2010 [25]	SnO_2	500 °C, 3 h, 2.8 °C/min	220	27.9	lithium ion batteries
Choi 2010 [26]	Pd-doped SnO_2	600 °C, 2 h	200 - 300	-	gas sensing
Kong 2011 [27]	SnO_2	700 °C, 1 h, 10 °/min	100	37.5 – 42.3	-
Xia 2012 [17]	SnO_2	600 °C, 3 h, 0.5 °C/min	50 - 300	35.8	-
Jiang 2012 [21]	SnO_2	600 °C, 5 h, 10 °C/min	200	-	NOx sensing
Gao 2012 [22]	SnO_2	500 °C, 2 h, 3.5 °C/min	110	39	solar cells
Lang 2012 [16]	SnO_2	500 °C, 4 h, 2 °C/min	-	-	-
Mohanapriya 2013 [28]	Ce-doped SnO_2	600 °C, 5 h	110 - 234	16.7 – 38.5	ethanol sensing
Wu 2013 [29]	Al-doped SnO_2	600 °C, 2 h 2 °C/min	200 - 250	-	gas sensing
Miao 2013 [30]	SnO_2	600 °C, 3 h	150 - 250	-	H_2O_2 sensing
An 2013 [23]	Nb-doped SnO_2	500 °C 0.4–0.5 °C/min	180 - 293	-	-
Cheng 2014 [24]	Ni-doped SnO_2	600 °C, 2 h 2 to 10 °C/min	150 - 250	21.66	acetone sensing
Tang 2014 [9]	SnO_2-ZnO	600 °C, 3 h 1 °C/min	160 - 380	17.42	gas sensing
Aravindan 2014 [31]	SnO_2	500 °C, 6 h	-	-	lithium ion batteries
Kadir 2014 [32]	SnO_2	500 °C, 4 h 5 °C/min	80 - 400	-	H_2 gas sensing

2 Synthesis and characterisation of electrospun Nb doped SnO_2

Niobium doped SnO_2 was explored by the group of Sasaki as a corrosion resistant catalyst support for PEM fuel cell cathodes [33],[34]. Pt/Nb-SnO_2 based MEAs demonstrated excellent start-stop cycle durability retaining 99 % of their initial cell voltage, even after 60,000 cycles (1.0–1.5 V_{RHE}) [35]. This was the starting point for this work where the aim was to develop tin oxide based supports with one-dimensional morphology, high surface area and improved conductivity.

2.1 Synthesis of Nb doped SnO_2

The synthesis protocol of niobium doped tin oxide electrospun fibres is shown in Figure 1. $SnCl_2$ and $NbCl_5$ were dissolved in ethanol, while PVP polymer in DMF. The obtained mixture was stirred and electrospun. As-prepared $SnCl_2$/PVP fibres were calcinated at 600 °C in order to remove carrier polymer and to allow formation of hollow fibres.

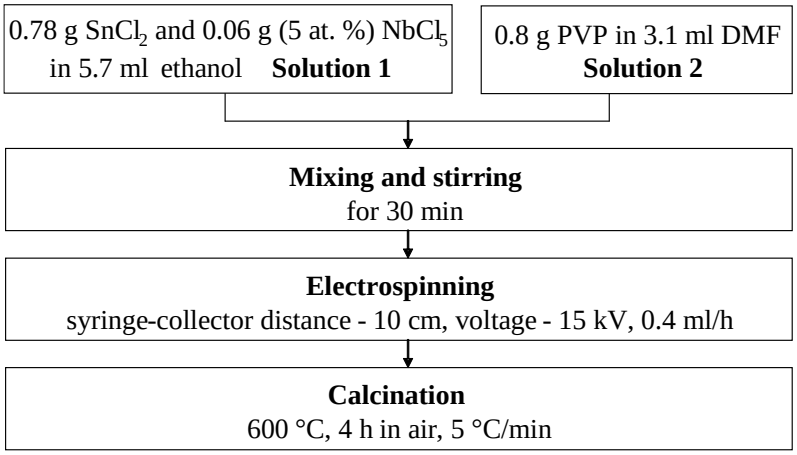

Figure 1: Schema of the nanofibre/nanotube niobium-doped tin oxide synthesis protocol.

In order to determine the polymer decomposition temperature, thermogravimetric analysis (TGA) of the obtained electrospun PVP/$SnCl_2$ composite fibres was carried out in the temperature range from 25 to 750 °C at a heating rate of 10 °C/min (Figure 2). The weight loss between 50 and 250 °C was attributed to the solvent evaporation. The main weight loss between 250 and 500 °C was assigned to the decomposition of the PVP polymer. No significant mass changes were observed at higher temperatures. Therefore, the calcination temperature higher than 500 °C was selected for fabrication of pure ceramic fibres without polymer matrix.

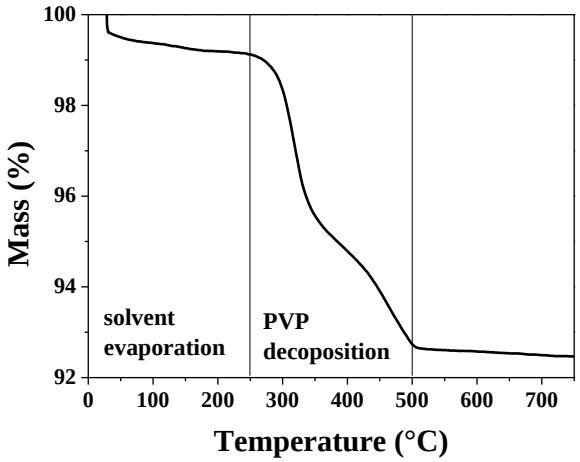

Figure 2: Thermogravimetric analysis of $SnCl_2$/PVP with 5 at. % Nb precursor electrospun fibres.

After the thermal treatment, the polymer was decomposed, while Sn^{2+} and Nb^{5+} were oxidised into Nb doped SnO_2 fibres. An unusual fibre-in-tube structure was obtained in the case of Nb doped samples, as shown in Figure 3. Larger grains formed the outer tube, while smaller grains formed a fibre inside the tube.

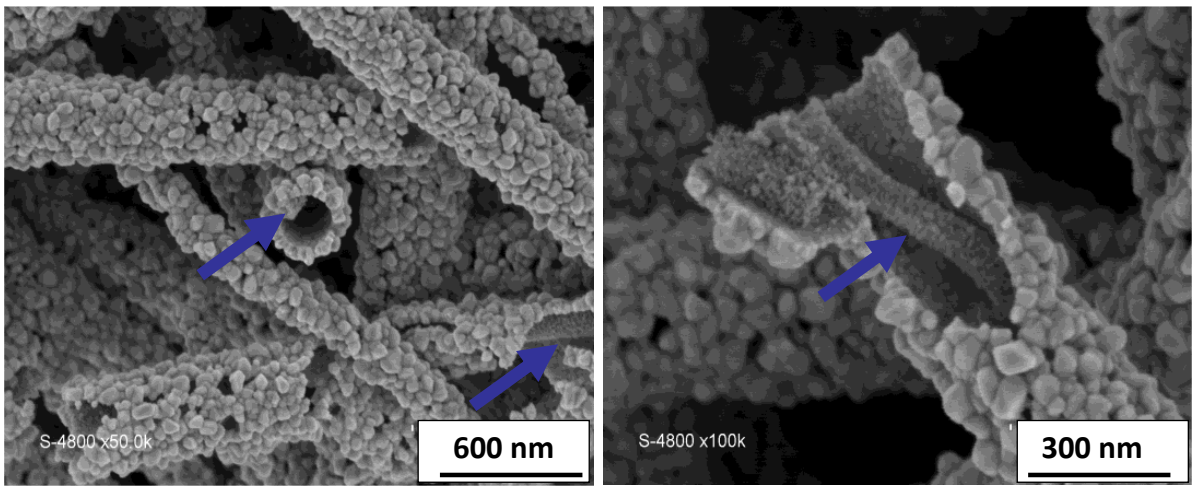

Figure 3: SEM images of 5 at. % Nb doped SnO_2 fibre-in-tube structures.

In the case of undoped SnO_2, dense fibres with smaller diameter of around 190 nm were obtained from the solution with 10 wt. % $SnCl_2$. However, when the concentration of the precursor was increased up to 15 wt. %, fibre-in-tube morphology with average tube diameter of 510 nm was the dominant structure, as shown in Figure 4.

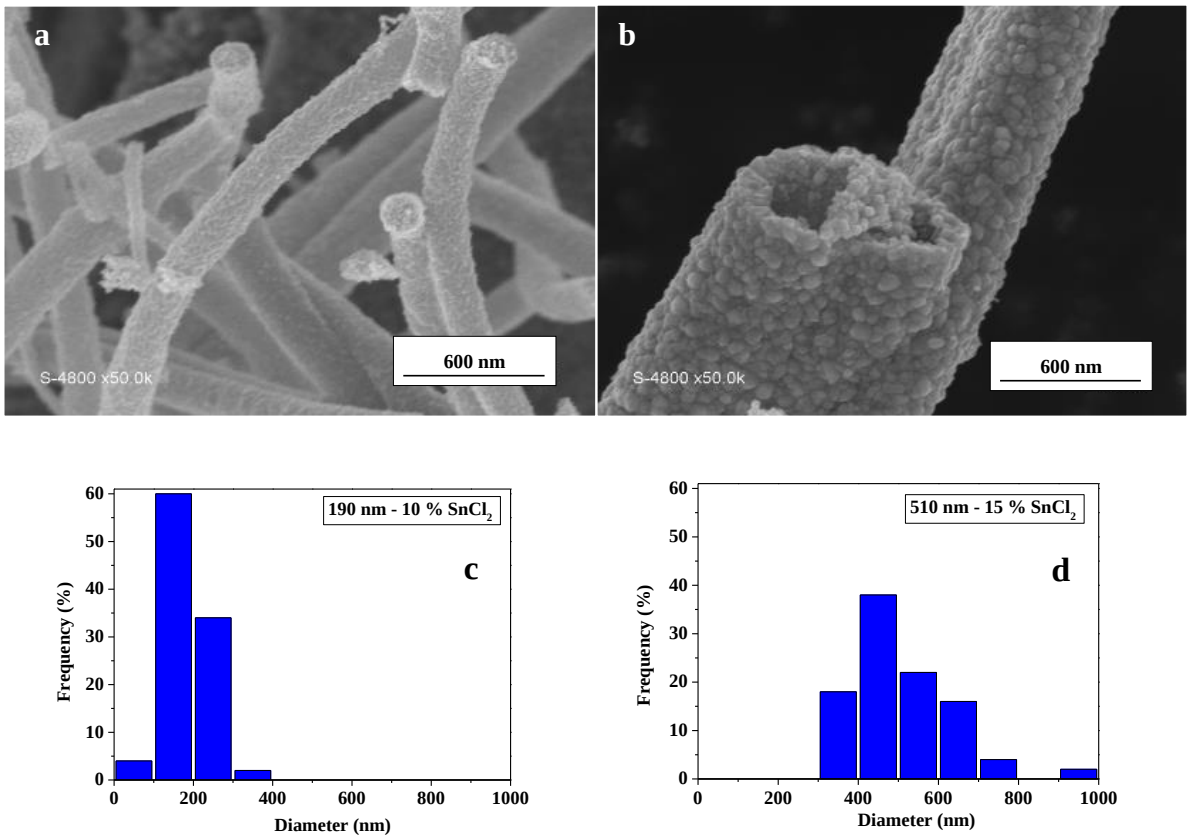

Figure 4: SEM images of SnO_2 fibres obtained from the solution with 10 (a) and 15 (b) wt. % $SnCl_2$ and then calcined at 600 °C for 4 h and corresponding fibre diameter distribution histograms (c and d).

The SEM images of Nb doped SnO_2 fibres with varying $SnCl_2$ concentrations are shown in Figure 5. Unlike undoped SnO_2, Nb doped SnO_2 has hollow structure for all precursor concentrations. This result may be attributed to the presence of Nb and the increased heating rate, which might facilitate formation of the hollow structure.

The diameter of the hollow fibres as well as the grain size increased with increasing the concentration of the precursor due to the increased viscosity of the solution. For instance, fibres obtained from the solution containing 3 wt. % $SnCl_2$ had small diameters of ~60 nm, whereas the fibres prepared from the solution containing 15 wt. % $SnCl_2$ showed larger diameters between 1 and 2 µm and are folded.

The effect of the precursor concentration on grain size distributions of the undoped and Nb doped SnO_2, estimated from the SEM images, is shown in Figure 6. The average grain size increases with higher precursor concentration from 25 nm for fibres prepared from a solution containing 3 wt. % $SnCl_2$, to 50 - 60 nm in the case of 15 wt. % $SnCl_2$ due to the increased viscosity of the solution. It can be concluded that the diameter and grain size of hollow fibres can be controlled by changing the precursor concentration.

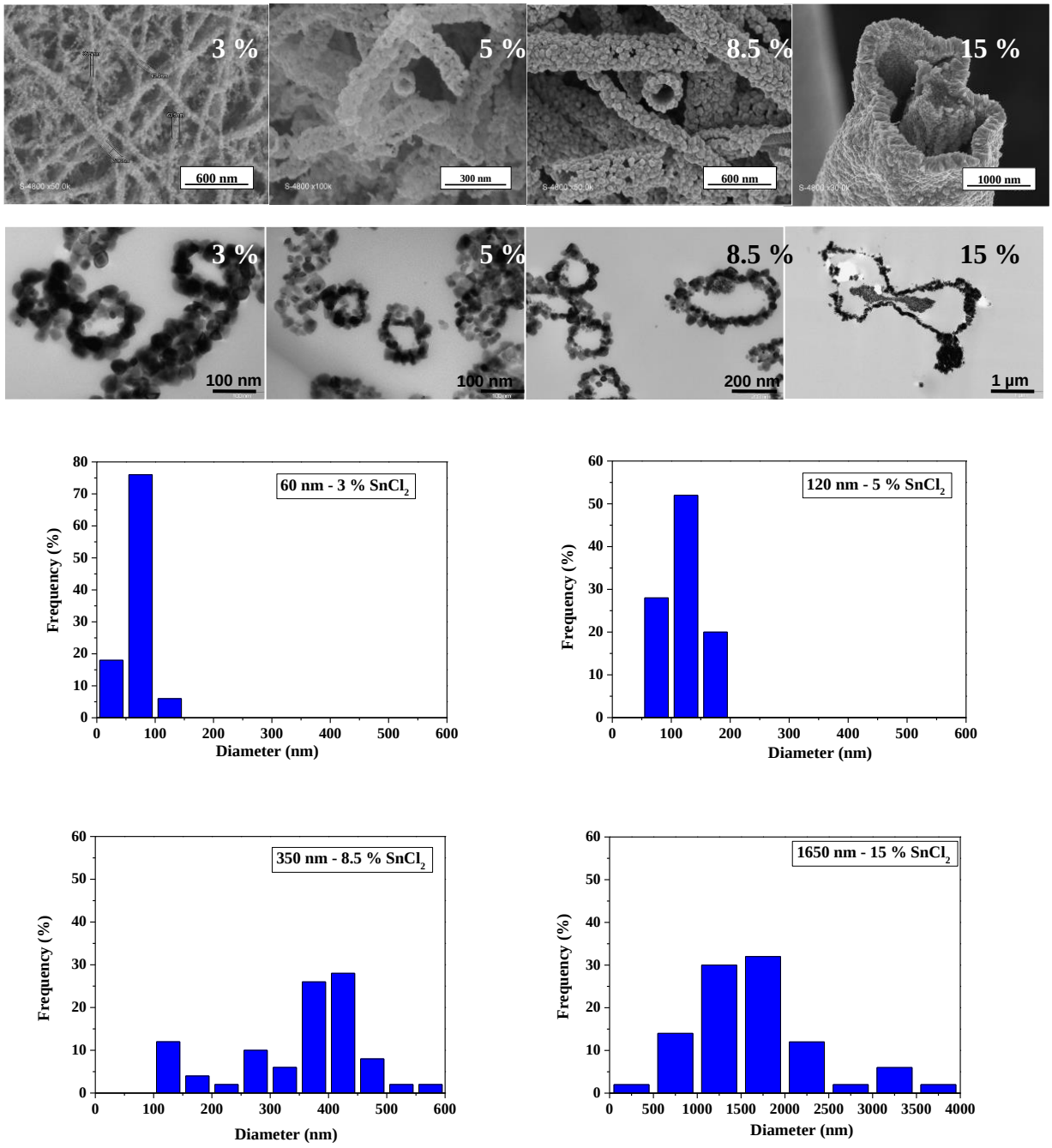

Figure 5: SEM (top) and TEM cross section (middle) images of 5 at. % Nb doped SnO_2 fibres prepared from solutions with 3, 5, 8.5 and 15 wt. % $SnCl_2$ from left to right, respectively, and corresponding fibre diameter distribution histograms obtained from measurement of 100 tubes (bottom).

2.2 Mechanism of nanotube formation

As described previously, the formation of hollow electrospun fibres is usually attributed to Kirkendall effect (diffusion in the solid state takes place via vacancies) followed by gas release caused by the decomposition of the polymer [22]. Therefore, the effect of heating rate used in the thermal treatment step, as well as influence of Nb doping on tin oxide morphology, were investigated.

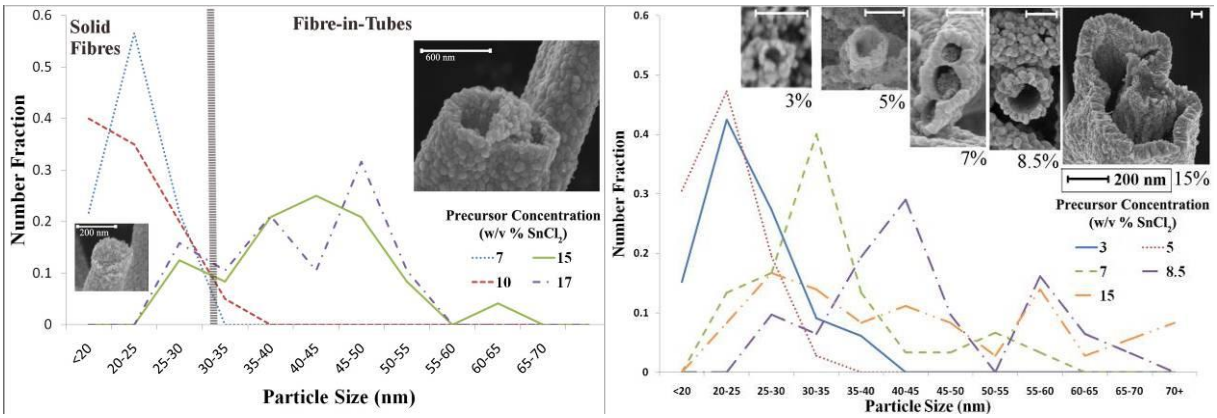

Figure 6: Grain size distribution of the undoped (left) and 5 at. % Nb doped SnO_2 (right) electrospun fibres obtained from the solution with different inorganic precursor concentration.

2.2.1 Effect of the degree of niobium doping on tin oxide morphology

Tin oxide electrospun materials with 0.5, 2, 5 and 10 at. % Nb were prepared, in order to understand the influence of Nb concentration on the SnO_2 morphology. TEM images show the cross sections of the obtained fibres (Figure 7). The fibre-in-tube structure was observed when the Nb concentration was between 5 and 10 at. %, while dense fibres were obtained when the Nb doping was between 0.5 and 2 at. %. Therefore, it can be concluded that Nb promotes formation of fibre-in-tube morphology.

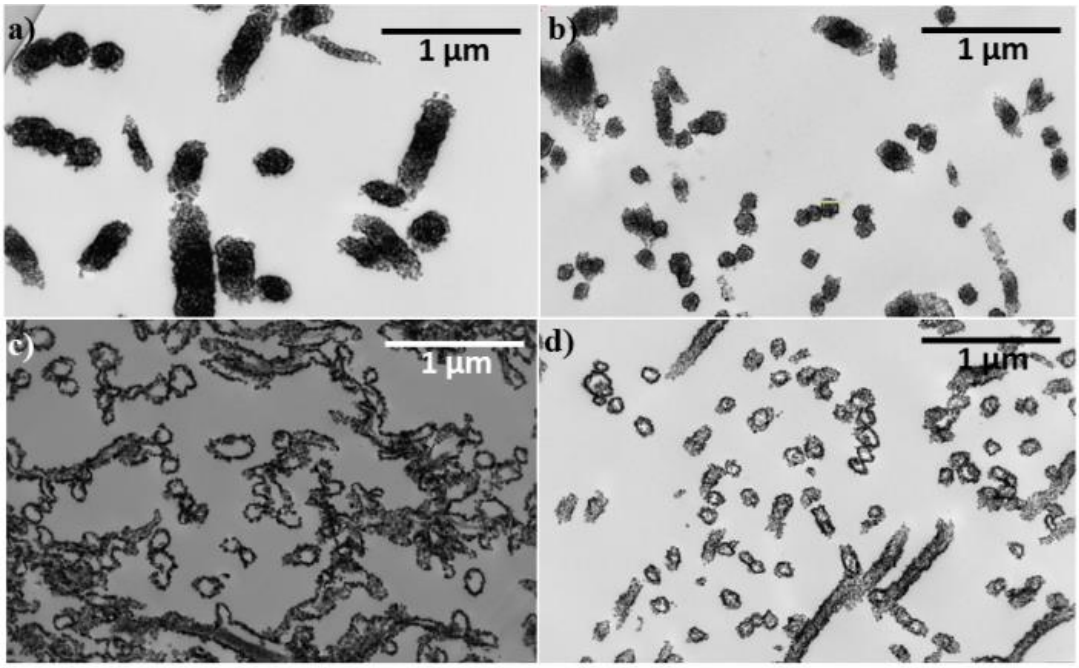

Figure 7: TEM micrographs of cross sections of SnO_2 doped with 0.5 (a), 2 (b), 5 (c), and 10 at. % Nb (d). All fibres were obtained from solution with 8.5 wt. % of $SnCl_2$.

In order to gain a better understanding of the tube formation mechanism in the presence of Nb, doped and undoped fibres were calcined at 300 °C. At this temperature, the fibres still contained the carrier polymer, as indicated by the TGA curve (Figure 2). Cross sections of the PVP/SnO_2 composite fibres are shown in Figure 8. In the case of the undoped SnO_2, the grain

size (2 – 4 nm) was homogeneous inside as well as on the surface of the fibre. Therefore, it can be concluded that tube formation takes place mainly at temperature higher than 300 °C due to gas expansion caused by PVP decomposition, as shown in Figure 9.

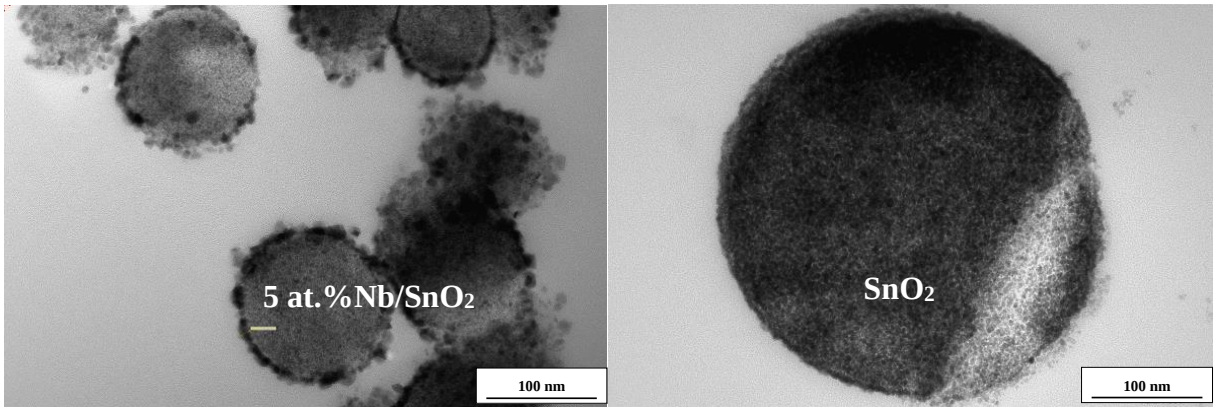

Figure 8: TEM cross section of 5 at. % Nb-SnO_2 (8.5 wt. % $SnCl_2$) and undoped SnO_2 fibres (15 wt. % $SnCl_2$) thermally treated at 300 °C for 4 h.

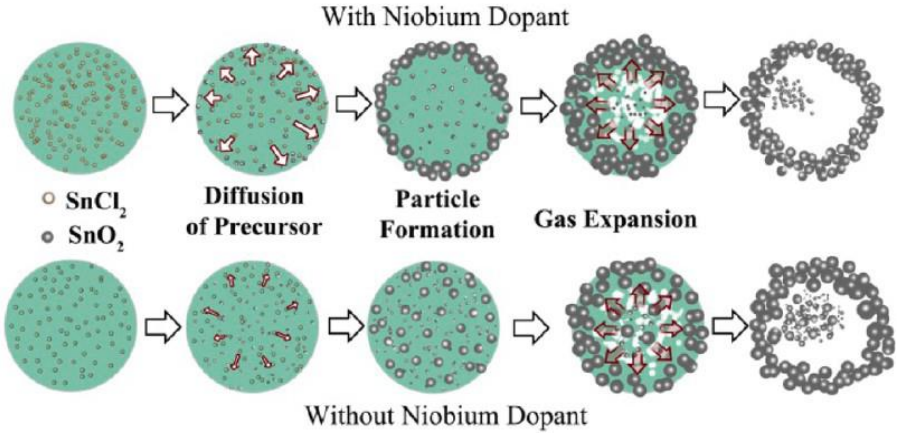

Figure 9: Scheme of the proposed mechanism of the formation of fibre-in-tube structures for undoped and Nb-doped SnO_2 [1]**.**

In the case of Nb doped SnO_2, at 300 °C larger grains were observed on the fibre surface compared to grains in the core structure. Such significant size difference between external and inner grain size, is attributed to inhibition of particle growth by niobium doping [36]. After removal of PVP at 500 °C, small particles form a fibre inside the tube, whereas the larger particles remain on the exterior, forming the shell of the fibre-in-tube structure.

Finally, the Nb concentration in the external tubes and in the inner fibres was determined using high resolution TEM coupled with an energy-dispersive X-ray spectroscopy (EDX). The average Nb content was 2.5 ± 0.6 at. % in the inner fibre, whereas it was 0.6 ± 0.4 at. % in the outer shell. This result is in agreement with the decreased SnO_2 particles size inside the tube due to the presence of Nb. Therefore, it can be concluded that Kirkendall effect plays a dominant role for Nb doped SnO_2 tube formation. The proposed mechanism is introduced in Figure 9.

2.2.2 Effect of the heating rate during thermal treatment on tin oxide morphology

The heating rate has also a significant influence on the fibre morphology as reported previously [22],[24]. Therefore, Nb doped SnO_2 was calcined at various heating rates. The obtained dense and hollow fibres are shown in Figure 10. At a heating rate of 1 °C/min, compact tubes with large inner fibre (solid core) and small diameter were obtained, while when heating rate was increased up to 5 °C/min and 10 °C/min, hollow fibres with smaller inner fibre and larger diameter were observed due to the effect of gas expansion. An increase in the heating rate enhances the decomposition of the polymer, which leads to an increase in carbon dioxide evolution and thus allows formation of hollow fibres with increased diameter. Consequently, hollow fibres can be obtained by using an appropriate heating rate. Other recent articles, published after the completion and publication of the present work [1], describe fabrication of electrospun Nb doped SnO_2 [23] and Ni doped SnO_2 [24] hollow-fibres using an appropriate heating rate.

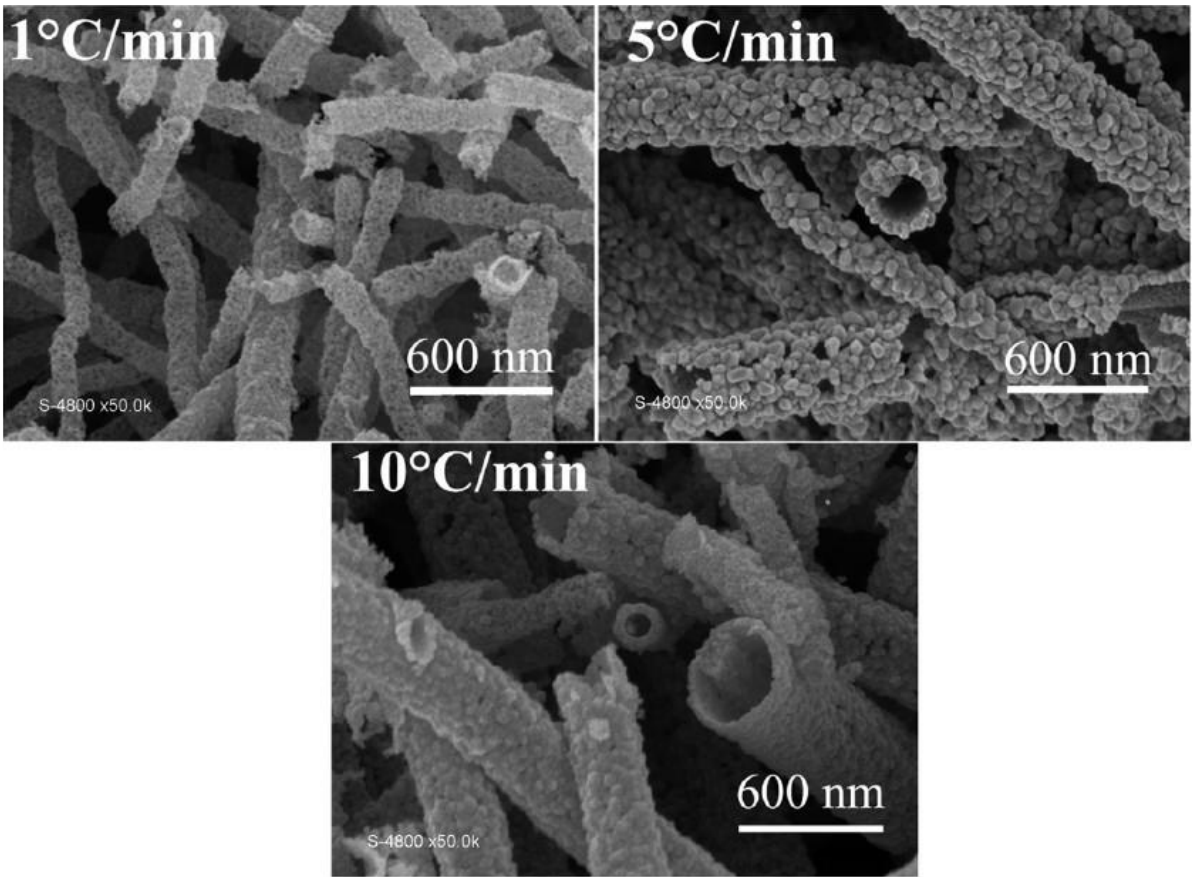

Figure 10: Nb-doped SnO_2 tubes prepared using heating rates of 1, 5, and 10 °C/min.

2.3 Structure and properties of Nb doped SnO_2

In order to find the sample with the highest specific surface area and electrical conductivity, SnO_2 with different amount of niobium doping was prepared.

2.3.1 Electronic conductivity

Nb has been chosen as an n-type dopant due to the similarities in Nb^{5+} (0.62 Å) and Sn^{4+} (0.69 Å) ionic radii [23]. The 5 at. % Nb doped sample showed electronic conductivity of 0.02 S/cm, which was much higher than that of the undoped sample. Table 2 lists the conductivities of the samples doped with different amounts of Nb. The measured conductivity was lower than that reported by Kakinuma et al. [37] for 4 at. % Nb doped tin oxide obtained by a flame combustion method (0.7 S/cm). Various conductivity values for Nb doped SnO_2 can be found in bibliographic data, probably due to the difference in the measurement method (in-plane/through-plane conductivity, pressure during the measurements) as well as in the porosity and thickness of the pellets.

Table 2: Electrical conductivity (RT) of the SnO_2 fibre-in-tube samples with different Nb concentrations.

Nb at. %	0	0.5	2	5	8
Conductivity (S/cm)	0.0011	0.0028	0.0086	0.021	0.0078

The electrical conductivity of SnO_2 with different Nb amount was measured as a function of temperature, as shown in Figure 11. The increase in the conductivity of the sample with temperature indicates semiconducting behaviour of Nb doped SnO_2. The 5 at. % Nb-SnO_2 showed the highest conductivity of 0.026 S/cm at 150 °C.

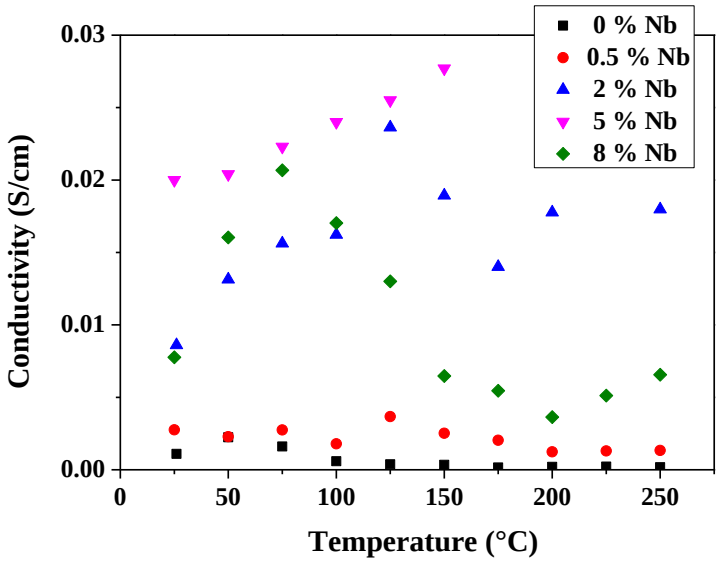

Figure 11: Conductivity of the undoped and Nb doped SnO_2 as a function of the temperature.

2.3.2 Specific surface area

The nitrogen adsorption/desorption isotherms of undoped and doped SnO_2 (Figure 12) were measured, in order to evaluate their specific surface area and porosity. All isotherms showed a hysteresis in the relative pressure range between 0.6 – 1.0 (type-IV isotherms), which is typical for mesoporous materials. The samples with 5 and 8 at. % Nb doping showed the highest surface areas of 42 m^2/g. This result may be attributed to the tubular structure of fibres with Nb doping higher than 5 at. % and to the inhibition of grain growth by Nb. Such improved surface area should enhance the capability of the support to achieve higher catalyst dispersion. The values of specific surface area are listed in Table 3. Comparable surface areas for undoped tin oxide hollow fibres (usually between 20 and 40 m^2/g) prepared using single-needle electrospinning have been reported [25],[27],[17],[22]. Also Nb doped SnO_2 nanoparticles with similar surface area were obtained by Kakinuma et al. (37 m^2/g) [37] and by Takasaki et al. (<50 m^2/g) [33].

Table 3: Specific surface areas of the SnO_2 samples with different Nb amount.

Nb at. %	0	0.5	5	8
Surface area (m^2/g)	26	31	42	42

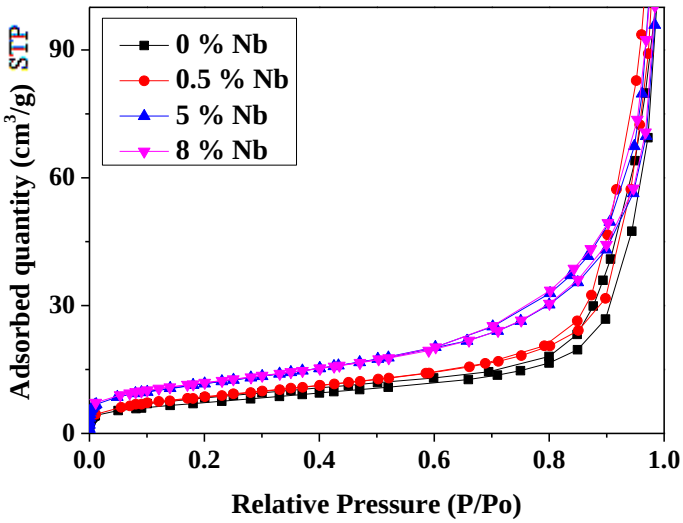

Figure 12: Nitrogen adsorption/desorption isotherms of the SnO_2 with different degrees of Nb doping.

2.3.3 XRD and Raman analysis

XRD patterns of Nb doped and undoped SnO_2 are shown in Figure 13. There is no significant crystallographic variation between these two samples. The calculated lattice parameters of undoped (a = 4.735 Å, c = 3.185 Å) and Nb doped (a = 4.737 Å, c = 3.185 Å) samples are very similar and consistent with the bibliographic data [38]. Due to the similar ionic radii of Sn^{4+} (0.69 Å) and Nb^{5+} (0.64 Å), replacement of tin by niobium takes place

without significant changes in the cell volume. Such substitutional doping is possible due to the similar outer shell electronic configuration of Nb and Sn, as reported previously for Fe doped tin oxide [39]. All the diffraction peaks were in agreement with standard data (JCPDS: 41-1445) for the tetragonal $P4_2/mnm$ cassiterite structure. No trace of a separate niobium-containing phase was observed.

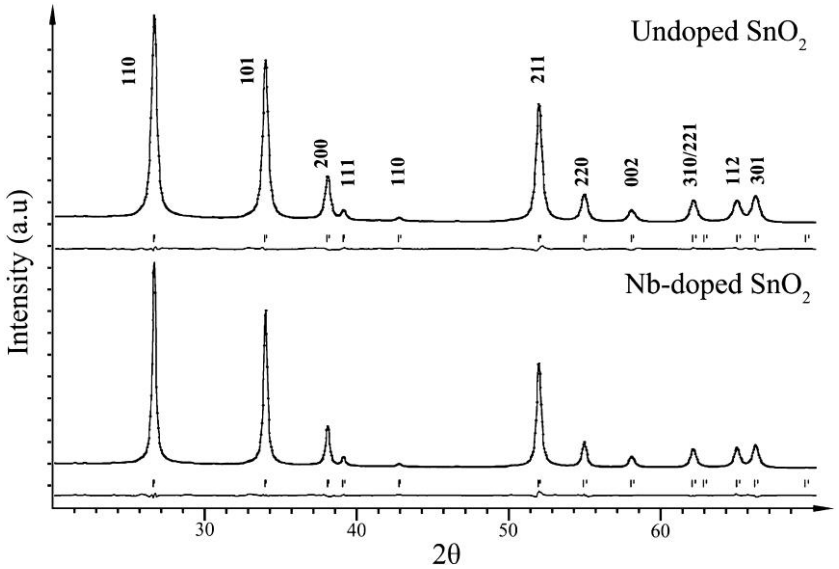

Figure 13: Experimentally observed (crosses) and calculated (solid line) X-ray diffraction (Cu K*α*) X-ray diffraction patterns for undoped and 5 at. % Nb-doped SnO_2 samples. The (observed – calculated) difference is plotted at the bottom of the diagram, and positions of Bragg possible reflections are indicated with vertical markers. Structures were refined using the Rietveld method.

The broadening of the diffraction peaks is commonly attributed to the small particle size. The average crystallite size of undoped and 5 at. % Nb doped SnO_2 calculated using the Scherrer equation was around 31 and 16 nm, respectively (Table 4). As already mentioned above, Nb doping decreases the size of the tin oxide crystallites [40],[36]. An et al. also observed that the grain size of SnO_2 hollow fibres decreases with increasing Nb concentration [23]. Also, Segawa et al. reported similar grain size for undoped and Ce doped SnO_2 tubes (41 and 22 nm respectively) [28].

Table 4: Size of undoped and Nb doped SnO_2 crystallite calculated from the X-ray diffraction lines given by (110), (101) and (211) planes.

Peak	Peak position (2θ)	FWHM (2θ)	Crystallite size (nm)
Non-doped SnO_2			
(110)	26.5127	0.3225	33.2
(101)	33.8012	0.3409	31.3
(211)	51.7065	0.3748	29.5
5 at. % Nb doped SnO_2			
(110)	26.5627	0.6113	15.6
(101)	33.8392	0.5790	16.8
(211)	51.7701	0.6298	16.3

Raman spectra of undoped and Nb doped SnO_2 are shown in Figure 14. Characteristic for SnO_2 cassiterite structure, peaks at 475, 631 and 772 1/cm can be identified as the E_g, A_{1g} and B_{2g} mode, respectively [41]. Similar Raman spectra were observed by Jiang et al. for electrospun SnO_2 tubes [21].

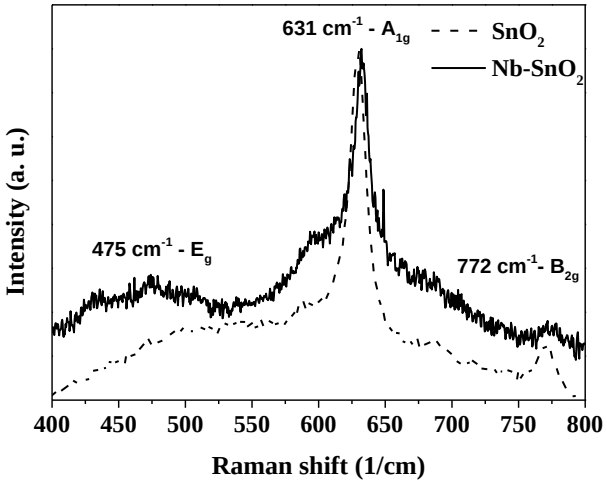

Figure 14: Raman spectra of SnO_2 and 5 at. % Nb doped SnO_2 calcined at 600 °C.

2.3.4 X-ray-photoelectron spectroscopy

An XPS spectrum of the Sn 3d region with spin-orbital split doublet peak is shown in the Figure 15a. The Sn $3d_{5/2}$ signal at 486.6 eV is usually attributed to the Sn^{4+}. However, it is not possible to distinguish between Sn^{4+} and Sn^{2+} species using the position of this peak [42]. The stoichiometric Sn/O ratios are: 0.77 for non-doped and 0.55 for doped sample. These values were obtained by integration of Sn $3d_{5/2}$ and O 1s peaks (O 1s signal at 530.7 eV in Figure 16 is attributed to the oxides). Therefore, it can be concluded that Sn^{2+} is present on the surface of pure and doped SnO_2. Kaciulis et al. [43] obtained similar stoichiometric ratio of 0.7 for undoped tin oxide calcined at 500 °C.

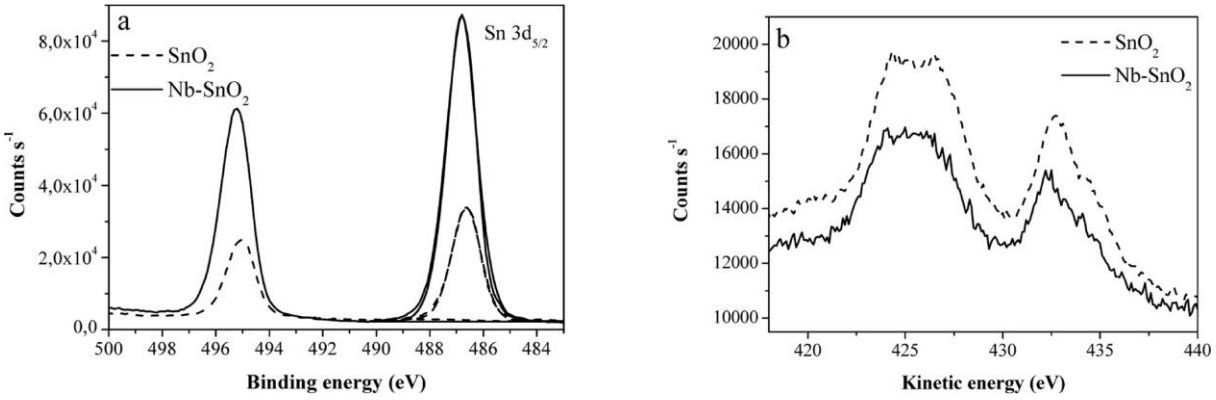

Figure 15: XPS (a) and Auger emission (b) spectra of the Sn region for non-doped and 5 at. % Nb doped SnO_2 electrospun materials.

The Auger emission spectra (Figure 15b) were recorded in order to investigate whether all tin species are present as Sn^{4+} at the surface of the tin oxide fibres. The Auger peaks at 432.7 eV and 432.4 eV are attributed to the undoped and doped samples, respectively.

The Auger parameter α first introduced by Wagner [44] as a sum of binding and kinetic energies was calculated to be 919.3 eV and 919.2 eV for the pure and doped samples, respectively:

$$\alpha = \text{BE Sn } 3d_{5/2} + \text{KE Sn},$$

where: BE is the binding energy of the photoelectron and KE is the kinetic energy of the Auger transition. Gonzalez-Elipe et al. observed similar Auger parameter of 919.2 eV for SnO and 918.5 eV for SnO_2 [45]. Also, Kaciulis et al. [43] and Mahmoudi Chernari et al. [38] reported the comparable value of 918.8 for nanostructured SnO_x. It can be concluded, that both Sn^{4+} and Sn^{2+} species are present on the surface of doped and undoped tin oxides (oxygen deficient surfaces) prepared in this work.

The presence of Nb in the sample was also confirmed using XPS analysis. The Nb 3d region is shown in Figure 16. The doublet at 207.5 and 210.1 eV is attributed to the Nb^{5+} [46].

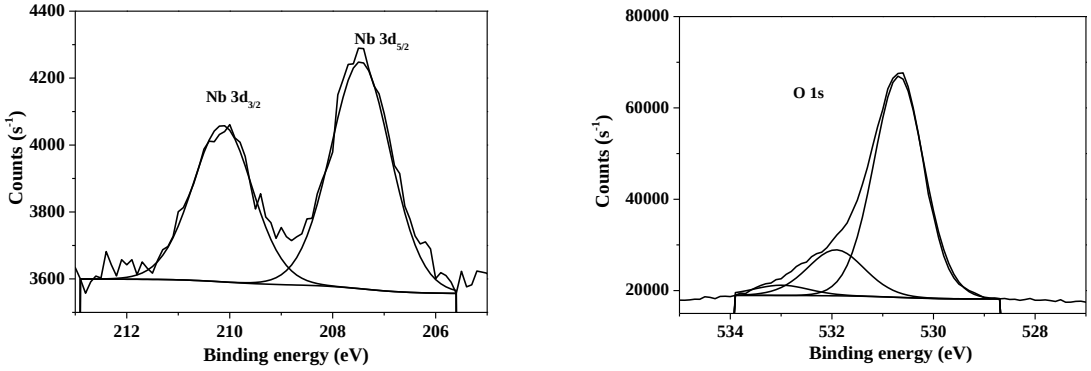

Figure 16: XPS spectra of the niobium and oxygen regions for 5 at. % Nb doped SnO_2.

2.3.5 Electrochemical characterisation of niobium doped tin oxide fibres

In order to evaluate the stability of the support under conditions similar to that in a PEMFC, an accelerated stress test (80 °C, 2h, 0.5 M H_2SO_4, 1.4 V) was performed, as described in the experimental part (Annex A). The oxidation charges were obtained by integrating the area under the chronoamperometric curves shown in Figure 17. The oxidation charge normalised by weight of the support was significantly lower for Nb doped SnO_2 (0.9 C/mg) than for Vulcan XC-72R (3.9 C/mg). This result indicates the high corrosion resistance of tin oxide support.

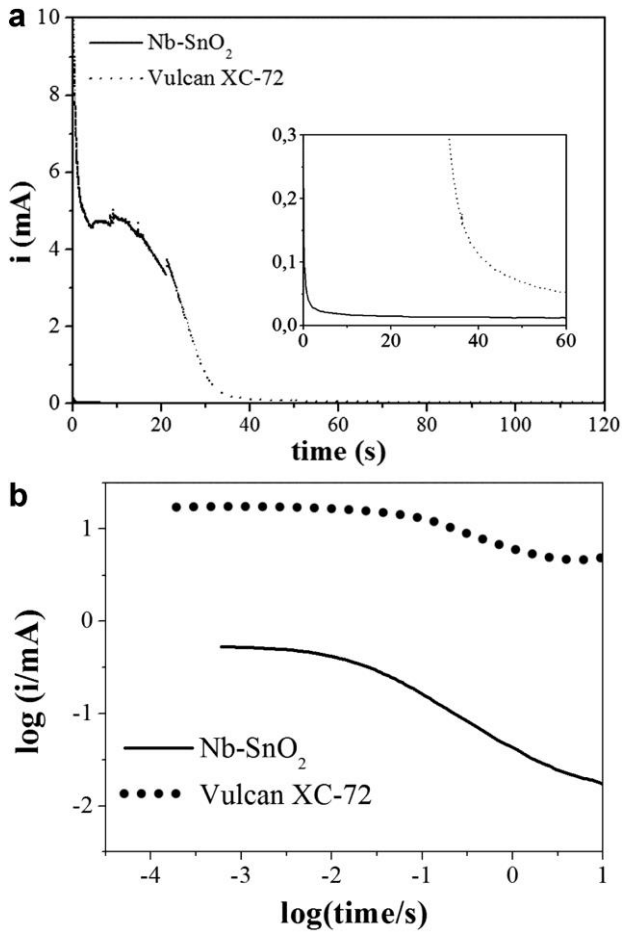

Figure 17: Chronoamperometric curves in linear (a) and logarithmic (b) scales for electrospun 5 at. % Nb–SnO_2 and Vulcan XC-72 at 1.4 V_{RHE} at 80 °C.

Conclusions

Addition of Nb leads to an improved electrical conductivity of SnO_2. Moreover, Nb doping has significant impact on SnO_2 fibre morphology such as the formation of the fibre-in-tube structure and inhibition of SnO_2 grain growth. This leads to improved specific surface area of the support. The most conductive sample (5 at. % Nb doped SnO_2) demonstrated also enhanced surface area. Therefore, this composition was chosen for the Pt deposition by a microwave-assisted polyol method.

3 Synthesis and characterisation of electrospun antimony doped SnO_2

Antimony is one of the most used dopants for SnO_2 due to the high electrical conductivity of antimony doped tin oxide (ATO). For instance, Kakinuma et al. [37] reported that Sb doped SnO_2 provides much higher conductivity compared to Nb-SnO_2 and similar to commercial carbon blacks. Therefore, Sb doped SnO_2 was explored as an alternative support that can potentially replace carbon in PEM fuel cell [47],[48],[49],[50],[37]. ATO recently obtained by a sol-gel method provides not only high conductivity, but high surface area while maintaining high stability towards a long-term test, during which a potential of 1.8 V_{RHE} was imposed [51]. Therefore, in our work Sb doped SnO_2 hollow fibres were obtained by electrospinning and characterised as alternative catalyst support for PEMFC.

3.1 Synthesis of Sb doped SnO_2

Figure 18 shows the synthesis protocol for 5 and 10 at. % Sb doped SnO_2 nanofibres, which is similar to that of Nb-SnO_2. Briefly, $SbCl_3$ precursor was added to the $SnCl_2$ and PVP solution in ethanol and DMF. The obtained mixture was stirred and electrospun. As-prepared $SnCl_2$/PVP fibres were calcinated at 600 °C in order to remove carrier polymer and to allow formation of hollow fibres.

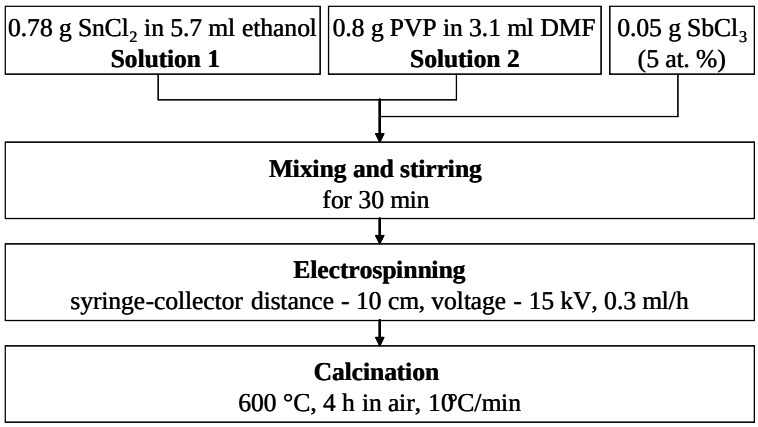

Figure 18: Schema of the Sb doped SnO_2 synthesis protocol.

SEM images of 5 and 10 at.% of Sb doped SnO_2 calcined at 600 °C at a heating rate of 10 °C/min for 4 h are shown in Figure 19. Similar to Nb doping, Sb also promotes the formation of fibre-in-tube structures. Indeed, more hollow fibres were obtained when the Sb concentration was increased up to 10 at. %. Furthermore, the average diameter of 10 at. % Sb-SnO_2 hollow fibres (~180 nm) was smaller than that of 5 at. % Sb-SnO_2 fibres (~230 nm).

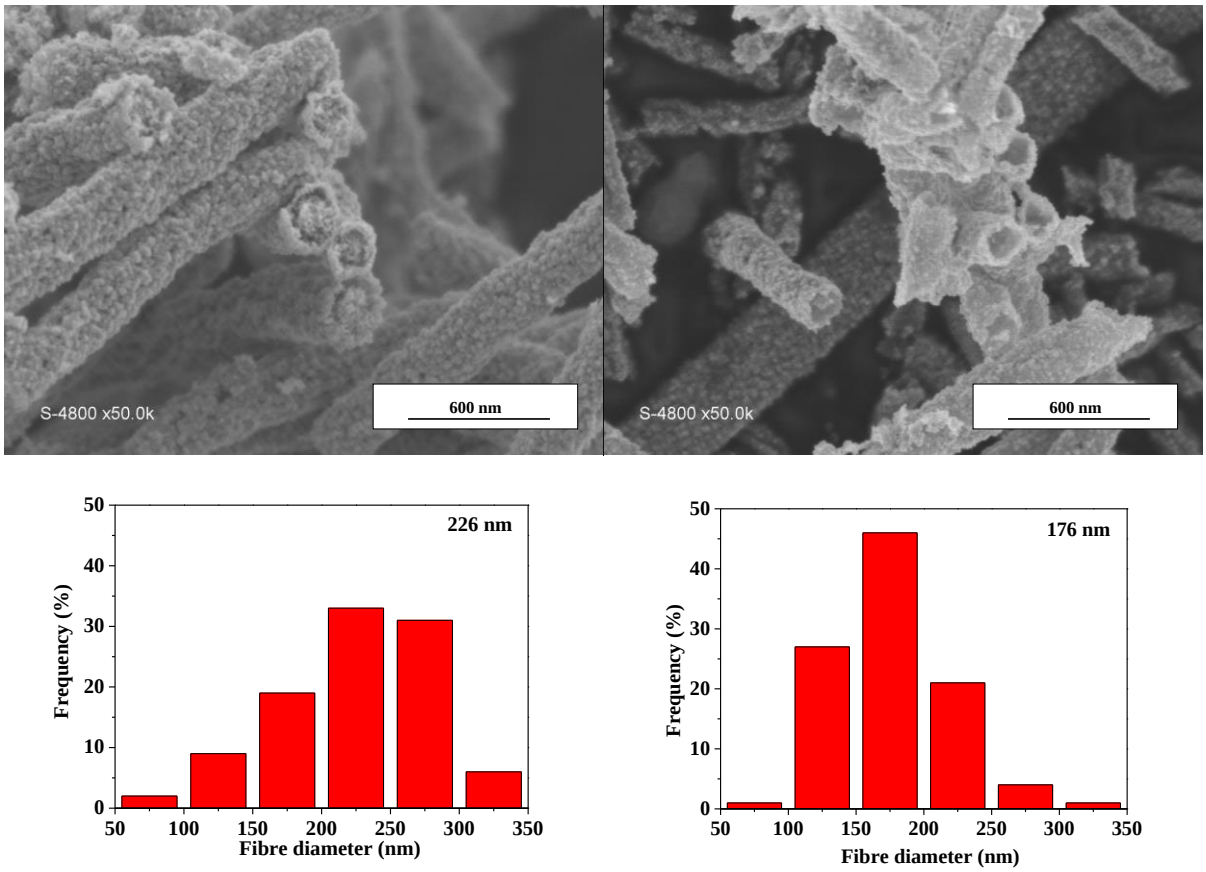

Figure 19: SEM images of 5 (left) and 10 (right) at.% of Sb doped SnO_2 calcined with a heating rate of 10 °C/min at 600 °C for 4 h and corresponding fibre diameter distribution histograms.

3.2 Structure and properties of Sb doped SnO_2

Structural, surface area and electrical properties of the obtained Sb-SnO_2 fibres were characterised by using XRD, nitrogen adsorption/desorption analysis and electrical conductivity measurements.

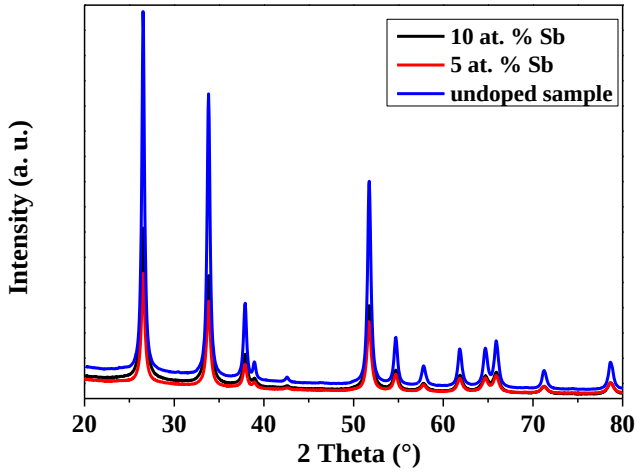

Figure 20: XRD diffractogramms of undoped, 5 and 10 at. % Sb doped SnO_2 tubes.

3.2.1 Structural analysis

Figure 20 shows the XRD patterns of undoped and Sb doped SnO_2 samples. For undoped, 5 and 10 at. % Sb doped samples, all diffraction peaks can be indexed as tetragonal cassiterite SnO_2 structure. No separate phases containing antimony were detected. This result indicates that the antimony ions might have substituted the tin ions in the SnO_2 lattice.

The XRD peak broadening with increasing Sb concentration indicates a decrease in the grain size of SnO_2 doped with Sb. Indeed, the crystallite sizes calculated using Scherrer equation were ca 31, 22 and 18 nm for undoped, 5 and 10 at. % Sb doped SnO_2, respectively, as displayed in Table 5. Like Nb doping, also Sb inhibits grain growth, as reported previously [52].

Table 5: Size of the Sb doped SnO_2 crystallite calculated from XRD pattern.

Peak	Peak position (2θ)	FWHM (2θ)	Crystallite size (nm)
Undoped SnO_2			
(110)	26.5127	0.3225	33
(101)	33.8012	0.3409	31
(211)	51.7065	0.3748	29
5 at. % Sb doped SnO_2			
(110)	26.5149	0.4300	23
(101)	33.7957	0.4493	22
(211)	51.6991	0.5153	20
10 at. % Sb doped SnO_2			
(110)	26.5380	0.5077	19
(101)	33.8075	0.5568	18
(211)	51.7158	0.5998	17

3.2.2 Electrical properties

The electrical conductivity increases significantly from ca 0.001 S/cm for SnO_2 to 0.7 S/cm for 5 at. % Sb doped SnO_2 and to 1 S/cm for 10 at. % Sb doped SnO_2 sample.

Antimony can be incorporated into the SnO_2 lattice as Sb^{5+} or as Sb^{3+}. Terrier et al. [53] reported that antimony was present only as Sb^{5+} (donor-doping), when the Sb concentration was 3.8 %. However, the Sb^{3+} (acceptor-doping) amount increases with increasing doping level. Therefore, further addition of Sb may result in the compensating effect and thus no further increase in conductivity with increasing Nb concentration. Therefore, the high Sb concentrations (> 10 at. %) were not characterised in this work.

Figure 21 shows conductivities of 5 and 10 at. % Sb doped SnO_2 as a function of temperature. A small increase in the conductivity of the material with temperature indicates semiconductor behaviour of Sb doped SnO_2. Similar electrical conductivity was measured by

Kakinuma et al. (1.2 S/cm) [54] and Yin et al. (0.99 S/cm at 80 °C) [48] for Sb doped SnO_2 nanoparticles.

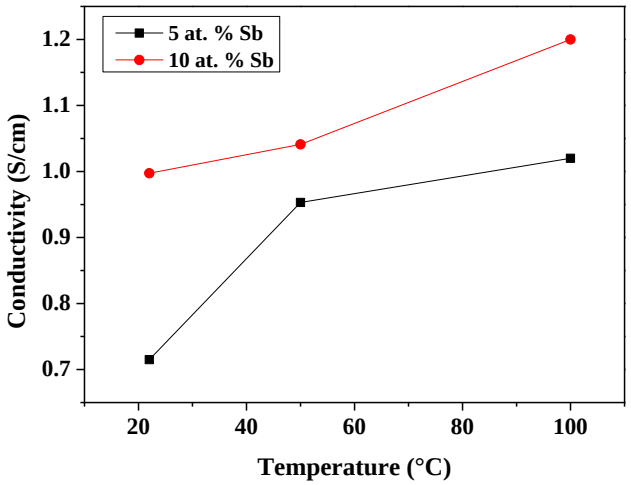

Figure 21: Electrical conductivity of 5 and 10 at. % Sb doped SnO_2 as a function of temperature.

3.2.3 Surface properties

The nitrogen adsorption/desorption isotherms of 5 and 10 at. % Sb doped SnO_2 are displayed in Figure 22. Both isotherms showed hysteresis in the relative pressure range between 0.7 – 1.0 (type-IV isotherms), which is typical for mesoporous materials. The specific surface areas obtained using BET analysis were 26, 27 and 35 m^2/g for undoped, 5 and 10 at. % Sb doped SnO_2, respectively. Like Nb doped SnO_2, 10 at. % Sb doped SnO_2 exhibits enhanced surface area compared to 5 at. % Sb doped and undoped SnO_2, probably due to its smaller grain size and more hollow structure.

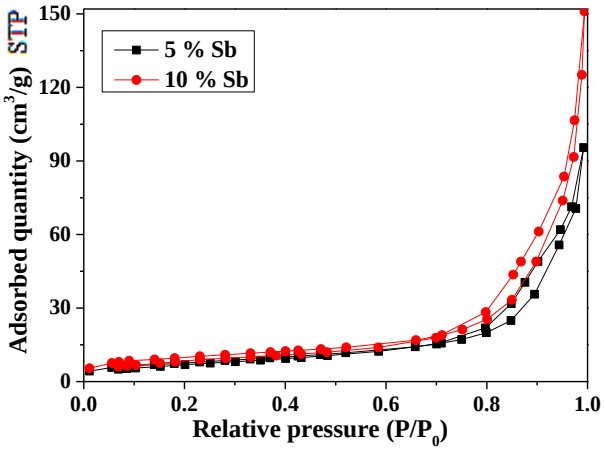

Figure 22: Nitrogen adsorption/desorption isotherms of Sb-SnO_2 samples calcined at 600 °C for 4 h.

Modification of calcination time

Fabbri et al. [55] reported that Sb-SnO_2 calcined at 550 °C for 2 h provide superior electrochemical stability than Sb-SnO_2 calcined at 550 °C for 10 h. Such behaviour was attributed to the sublimation or dissolution of Sb during heat treatment or potential cycling. Therefore, in this work, the calcination time was decreased from 4 to 1 h. Such change in thermal treatment resulted in an improvement of the surface area from 35 to 42 m^2/g (Figure 23), probably due to smaller grain size of Sb-SnO_2 calcined for 1 h.

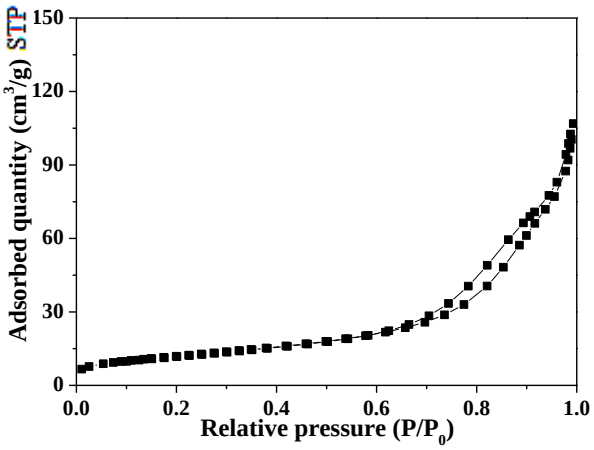

Figure 23: Nitrogen adsorption/desorption isotherms of 10 at. % Sb doped SnO_2 calcined for 1 h.

Conclusions

Sb doping leads to a dramatic increase in electrical conductivity of SnO_2. Furthermore, it promoted hollow structure formation and decreased grain growth of SnO_2, which lead to higher surface area of Sb-doped SnO_2 fibres. The calcination time was decreased from 4 to 1 h, to limit grain growth and to avoid sublimation of Sb. The 10 at. % Sb doped SnO_2 provided higher conductivity and surface area than the 5 at. % Sb doped SnO_2. Therefore, it was selected for deposition of Pt nanoparticles obtained by microwave-assisted polyol method. The obtained electrocatalyst was *in situ* characterised in a single PEMFC (see Chapter 5). Sb-SnO_2 demonstrated similar morphology and specific surface area, but much higher electrical conductivity than Nb-SnO_2, which might lead to an improved performance of a Sb-SnO_2 based cathode.

4 Synthesis and characterisation of Pt supported on Nb-SnO_2

Pt nanoparticles were prepared by microwave-assisted polyol method as described in the experimental part. The target Pt loading was ~30 wt. % for Nb and Sb doped SnO_2 hollow fibres with surface area of 42 m^2/g (see calculations in the experimental part – Anex A). High Pt loadings allow fabrication of thin catalyst layer, which leads to decreased mass transport losses.

4.1 Pt deposition and physico-chemical characterisation of Pt/Nb-SnO_2

Zeta potential measurements

The surface charge of the Nb-SnO_2 and Pt colloids were measured as a function of pH (Figure 24), in order to estimate the optimal pH, which favours Pt nanoparticles adsorption on the surface of Nb-SnO_2, as described in the experimental part. The surface charge of the Pt nanoparticles was negative over the whole pH range, whereas zeta potential of tin oxide was positive at pH 2. Therefore, after the synthesis of Pt nanoparticles and addition of the Nb-SnO_2 support, sulphuric acid was added drop-wise until the pH reached the value of 2.

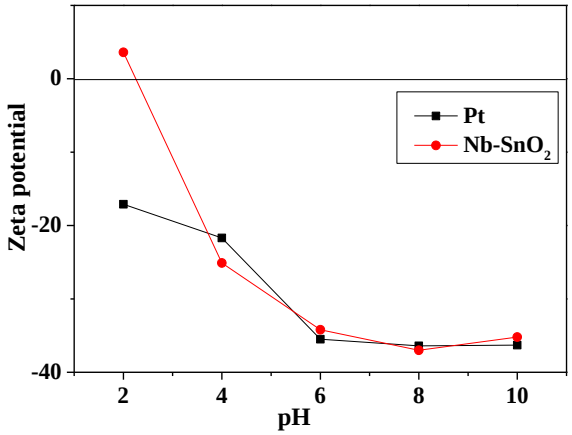

Figure 24: Zeta potential as a function of pH for Pt nanoparticles and Nb doped SnO_2 hollow fibres.

Morphological characterisation

TEM cross section images of 21 wt. % Pt/Nb-SnO_2 is shown in Figure 25. The Pt nanoparticles are evenly distributed on both the outer surface as well as the inner surface of the hollow fibres. This result indicates that the inner surface of the tube is also accessible to platinum particles, which allows high Pt dispersion. The average particle diameter was ca 3 nm, which is close to the particle size calculated from the XRD patterns (4 nm, see Table 6).

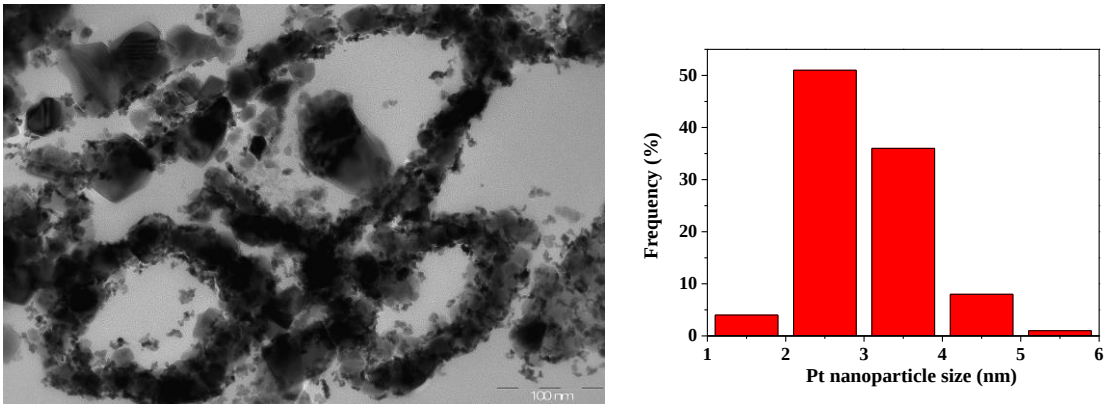

Figure 25: TEM cross section micrographs of 21 wt. % Pt/Nb-SnO_2 (left) and corresponding Pt nanoparticle size distribution histograms obtained from measurement of 100 nanoparticles (right).

XPS analysis of Pt/Nb-SnO_2 and Pt/Vulcan XC-72R

The XPS spectra of Pt4f for Pt/Nb-SnO_2 and Pt/Vulcan XC-72R are shown in Figure 26. After the curve fitting, a signal assigned to the Pt^0 form is observed at 71.5 eV for both of the electrocatalysts, while signals attributed to Pt^{2+} for Pt/Nb-SnO_2 and Pt/Vulcan XC-72R are observed at 72.6 and 72.3 eV, respectively. In the literature, a negative shift in the Pt 4f binding energies for the Pt/C and Pt/oxide have been observed, which is generally attributed to the strong metal support interactions [56]. However, in this work, peak assigned to Pt^0 appears at the same position.

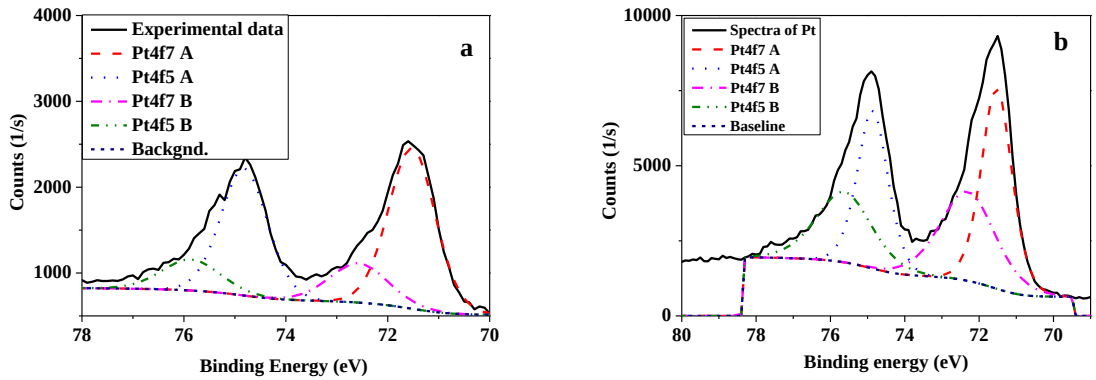

Figure 26: The Pt 4f region of the XPS spectrum of the Pt/Nb-SnO_2 (a) and Pt/Vulcan XC-72R (b).

XRD analysis

As shown in Figure 27, the characteristic diffraction peaks of (111) and (200) facets of Pt are observed at 39° 2θ and 46° 2θ, respectively. The broadening of the diffraction peaks indicates small size of Pt nanoparticles. Indeed, the Pt coherence length was around 4 nm calculated from XRD spectra using the Scherrer equation. The obtained results are summarised in Table 6.

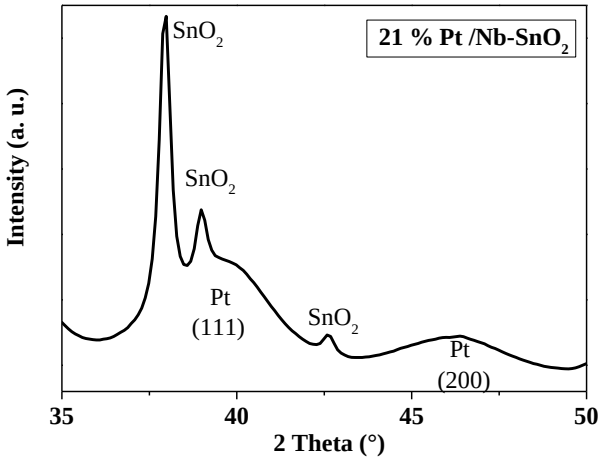

Figure 27: XRD patterns of Pt/Nb-SnO_2 sample.

Table 6: Pt crystallite size calculated from XRD pattern.

Peak	Peak position (2θ)	Crystallite size (nm)
(111)	40.016	4.4
(200)	46.169	4.1

4.2 Electrochemical characterisation of Pt/Nb-SnO_2

The electrochemical characterisation of Pt/Nb-SnO_2 was performed using a RDE, in order to evaluate its ECSA, ORR activity and stability to potential cycling and compared to that of commercial Pt/C electrocatalyst. Amounts of Pt and Nafion® on the RDE are showed in Table 7.

Table 7: Mass of the Pt and Nafion on the electrode.

	50 % Pt/C (JM)	33 % Pt/Vulcan	21 % Pt/Nb-SnO_2
Mass of Pt (µg)	23.8	23.7	23.9
Pt loading (µg/cm^2)	121.2	120.7	121.7
Mass of Nafion (µg)	10.4	15.5	9.9
Nafion loading (µg/cm)	53.1	79	50.5

4.2.1 Determination of ECSA

Figure 28a shows the cyclic voltammograms of Nb-SnO_2 and Pt/Nb-SnO_2. The hydrogen adsorption-desorption peaks between 0.05 and 0.4 V were observed only for Pt/Nb-SnO_2 and not for the oxide support alone. Therefore, the ECSA calculated from the hydrogen desorption peak was attributed to the Pt nanoparticles only and not to the Nb-SnO_2. Similar behaviour for tin oxide has been previously reported in the literature [57], although Zhang et al. [58] have reported hydrogen adsorption-desorption signals for SnO_2.

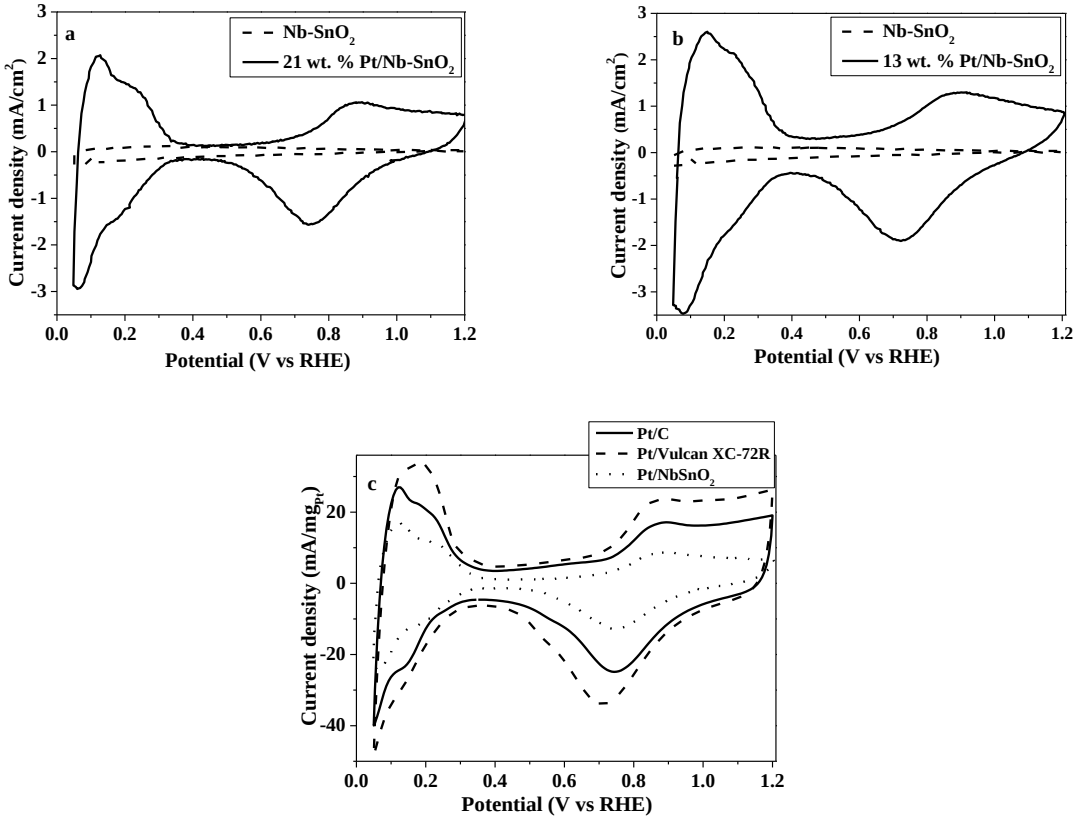

Figure 28: Cyclic voltammograms obtained for $NbSnO_2$ and 21 wt. % Pt/Nb-SnO_2 (a), 13 wt. % Pt/Nb-SnO_2 (b), Pt/Nb-SnO_2, Pt/C and Pt/Vulcan XC-72R (c) at a scan rate of 50 mV/s in 1 M $HClO_4$.

The oxidation-reduction and hydrogen adsorption/desorption region of Pt/Nb-SnO_2 were suppressed compared to that of Pt/C and Pt/Vulcan XC-72R, as shown in Figure 28b, giving a lower electrochemically active surface area of Pt on Nb-SnO_2 (25 m^2/g) than that of Pt on Vulcan XC-72R (47 m^2/g), Table 8. The difference in ECSAs may be attributed to a slightly higher Pt nanoparticles size for Pt/Nb-SnO_2 (3 nm) compared with that on Pt/Vulcan XC-72R (2.4 nm) and to a lower surface area and electrical conductivity of Nb-SnO_2 (42 m^2/g and ca 10^{-2} S/cm). Sasaki et al. [34] reported a similar ECSA of 21.4 m^2/g for 20 wt. %Pt/$Sn_{0.98}Nb_{0.02}O_2$, which was lower than that of Pt/Vulcan. This result was attributed to high Pt loading and to low surface area of $Sn_{0.98}Nb_{0.02}O_2$, which was not high enough for good Pt nanoparticles dispersion (the specific surface area of tin oxide was much lower than that of Vulcan). Lee et al. [47] also reported that ECSA of Pt/Vulcan was much higher than that of Pt on tin oxide due to the lower surface are of the oxide support (99.7 m^2/g). An increase of ECSA with decreasing Pt loading was attributed to the better dispersion of Pt nanoparticles on tin oxide. In our work higher ECSA of 53 m^2/g was obtained when the Pt loading was reduced from 21 to 13 wt. % and when the Pt nanoparticles size was reduced

from ~3 to 2.4 nm. This result indicates that the Pt nanoparticles are more homogeneously dispersed when Pt loading was relatively low.

Table 8: ECSA of Pt/Nb-SnO_2, Pt/Vulcan XC-72R and Pt/C.

Electrocatalyst	50%Pt/C	33%Pt/Vulcan	13%Pt/Nb-SnO_2	21%Pt/Nb-SnO_2
ECSA (m^2/g)	33	47	53	25
Pt particles size (nm)	3.8	2.4	2.4	3.0

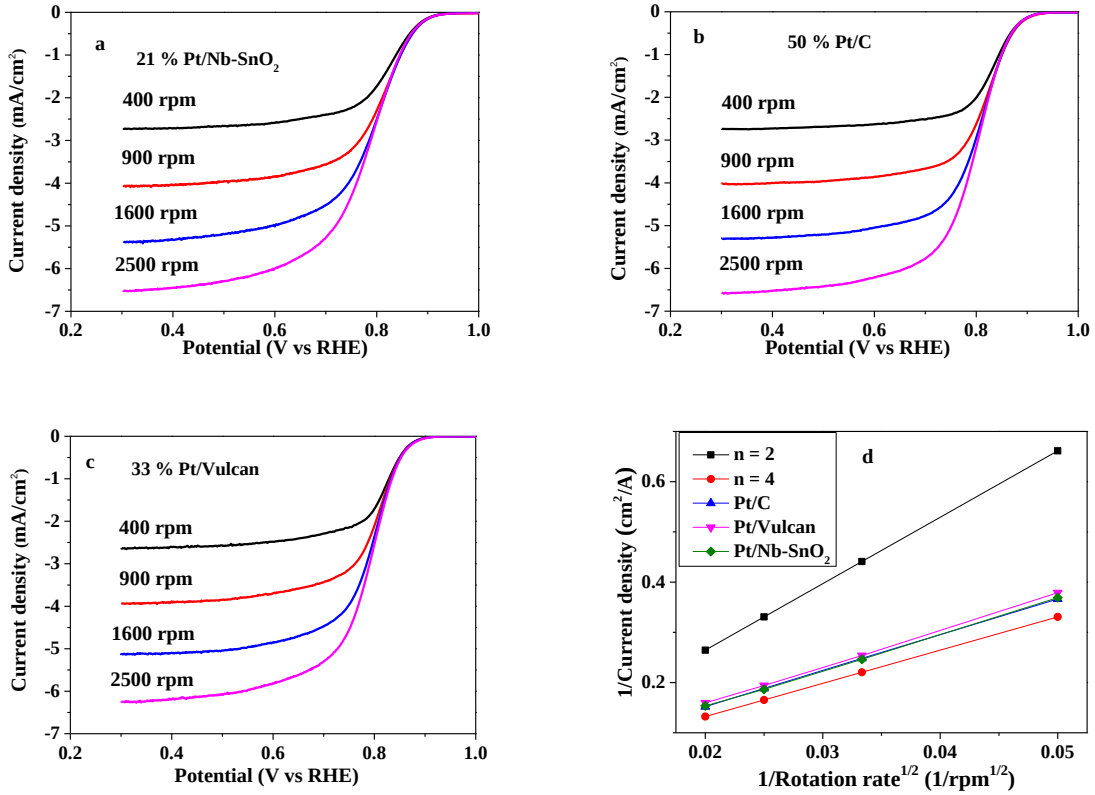

Figure 29: Linear sweep voltammograms of Pt/Nb-SnO_2 (a), Pt/C (b) and Pt/Vulcan XC-72R (c) at different rotation rates and the inverse current densities as a function of the inverse of the square root of the rotation rate (d).

4.2.2 Evaluation of ORR activity

Linear sweep voltammograms of Pt/Nb-SnO_2, Pt/C and Pt/Vulcan XC-72R are presented in Figure 29. All polarisation curves show an onset potential at around 0.9 V_{RHE}. The $E_{1/2}$ of Pt/Nb-SnO_2, Pt/C and Pt/Vulcan XC-72R was 0.81, 0.82 and 0.81 V_{RHE}, respectively, at 900 rpm, indicating similar ORR activity for all electrocatalysts. The ORR mass activities of the different electrocatalysts at 0.8 V_{RHE} are listed in Table 9. Pt/Nb-SnO_2 showed lower ORR mass activity than the commercial Pt/C electrocatalyst. This result may be related to higher ECSA and higher conductivity of the Pt/C compared to the Pt/Nb-SnO_2. Zhang et al. [58] and Sasaki et al. [59],[34] also obtained higher ORR activities for commercial Pt/C compared to the Pt supported on tin oxide.

Table 9: ORR mass activities and Tafel slopes for ORR on Pt/C, Pt/Vulcan XC-72R and Pt/Nb-SnO_2.

Electrocatalyst	Pt/C	Pt/Vulcan XC-72R	Pt/Nb-SnO_2
ORR mass activity at 0.8 V (A/g_{Pt})	61.4	36.5	42.7
Tafel slope (mV/dec)	-55	-52	-64

The number of electrons involved in the reaction was around 3.6, 3.6 and 3.7 for Pt/Nb-SnO_2, Pt/Vulcan XC-72R and Pt/C, respectively. Thus, it can be concluded that oxygen reduction occurs mainly via a 4 electron pathway.

Figure 30 shows Tafel plots obtained from ORR measurements at 900 rpm. Pt/Nb-SnO_2 has higher Tafel slope (Table 9) compared to other electrocatalysts, which may indicate a slightly different mechanism of oxygen reduction.

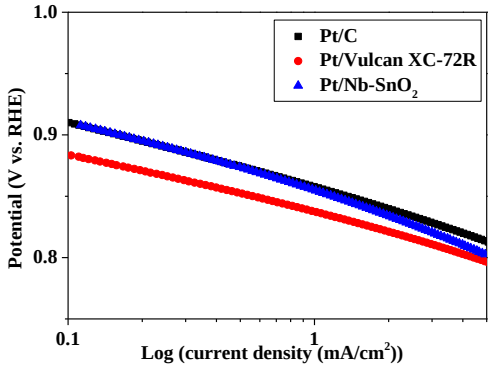

Figure 30: Tafel plots for ORR on Pt/Nb-SnO_2, Pt/C and Pt/Vulcan XC-72R at 900 rpm in 0.1 M $HClO_4$.

4.2.3 Evaluation of the electrochemical stability

The ECSA was evaluated before and after prolonged voltage cycling, in order to compare the stability of the Pt/Nb-SnO_2 with Pt/C and Pt/Vulcan XC-72R electrocatalysts. Figure 31 shows the voltammograms of Pt/Nb-SnO_2, Pt/C and Pt/Vulcan XC-72R after 100, 1000 and 2000 cycles. The ECSA loss before and after the stability test are listed in Table 10. The ECSA decreases with the number of cycles for all samples. Generally, this phenomenon is assigned to dissolution, migration, agglomeration and growth of Pt nanoparticles. However, the Pt/Nb-SnO_2 demonstrated a significantly lower ECSA loss of 24 % after 2000 cycles than Pt/C (86 %) and Pt/Vulcan XC-72R (51 %) electrocatalysts, indicating better electrochemical durability of the Pt/Nb-SnO_2 to cycling to high potential. Similar ECSA loss of 20 % after 1600 cycles was demonstrated by Zhang et al. [58] for Pt/SnO_2 catalyst, while Lee et al. [47] reported higher ECSA loss of 40% after 1000 cycles for 20 wt. % Pt/Sb-SnO_2. This result can be attributed to the high electrochemical corrosion resistance of the support, and also suggests a strong interaction between Pt nanoparticles and the oxide support.

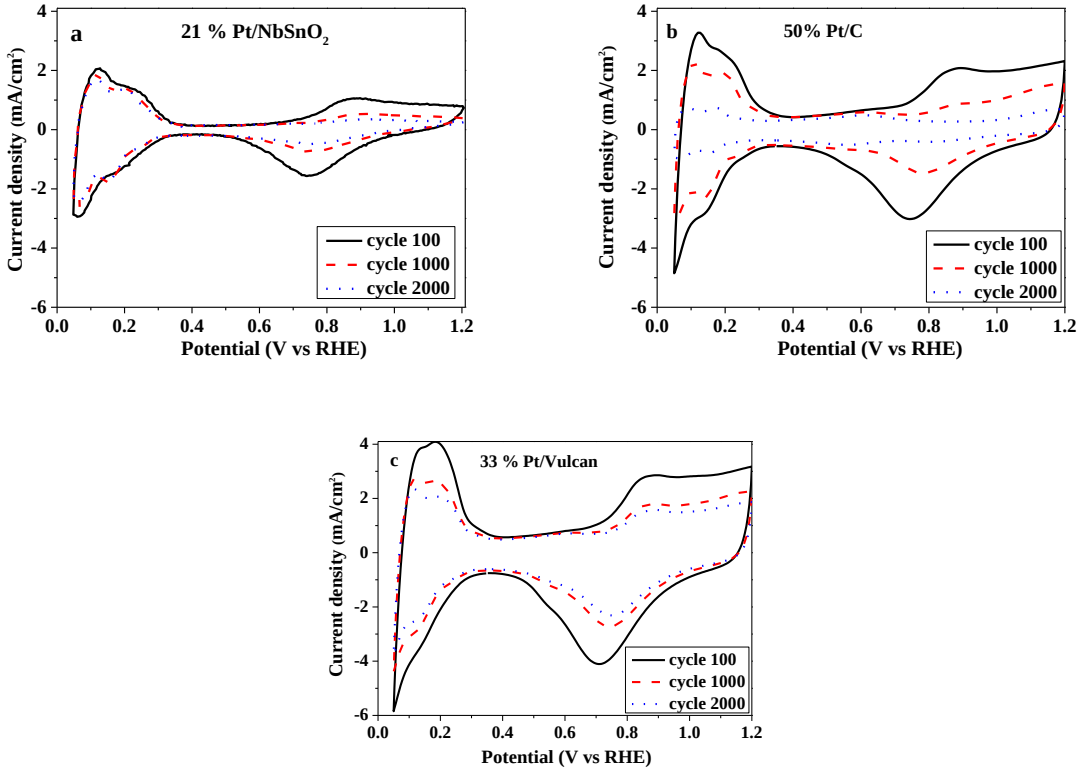

Figure 31: CV curves of Pt/Nb-SnO_2 (a), Pt/C (b) and Pt/Vulcan XC-72R (c) at a scan rate of 50 mV/s.

Table 10: ECSA of Pt/Nb-SnO_2, Pt/C and Pt/Vulcan before (fresh catalyst) and after (aged catalyst) 2000 potential cycles.

Sample	ECSA (m^2/g)		ECSA loss (%)
	before cycling	after cycling	after cycling
Pt/Nb-SnO_2	25	19	24
Pt/C	33	4	86
Pt/Vulcan XC-72R	47	23	51

ORR activity loss after stability test

The ORR mass activity was evaluated before and after these prolonged cycles, as shown in Table 11 and Figure 32. The Pt/Nb-SnO_2 electrocatalyst showed ca 90 % loss in ORR mass activity after 2000 cycles, while Pt/C showed a 99 % loss in ORR mass activity after 2000 electrochemical cycles indicating a slightly better stability of the Pt/Nb-SnO_2. High ORR activity loss can be related to strong adsorption of anions or other molecules on the platinum surface.

Table 11: ORR mass activities before and after the stability test at 0.8 V_{RHE}.

Electrocatalyst	Pt/C	Pt/Vulcan XC-72R	Pt/Nb-SnO_2
ORR mass activity before stability test (A/g)	61.4	36.5	42.7
ORR mass activity after stability test (A/g)	0.3	4.3	4.3

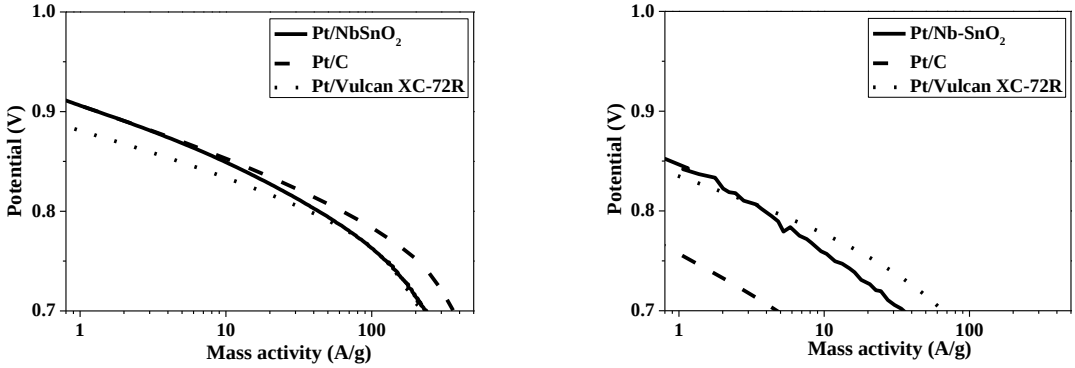

Figure 32: Mass activities of ORR measurements at 900 rpm for Pt/Nb-SnO_2, Pt/Vulcan XC-72R and Pt/C before (left) and after (right) stability test. Pt loading on the electrodes was ca 120 µg/cm^2.

Transmission electron micrographs before and after stability test

Figure 33 shows the TEM images of the Pt/Nb-SnO_2 as well as the distribution of the Pt particles before and after potential cycling. The average size of Pt nanoparticles increases after potential cycling from 3.0 to 5.3 nm. Similar particle growth during potential cycles was observed by Lee et al. [47] for Pt loaded on Sb doped SnO_2. Higher increase in average Pt nanoparticle size after stability test is observed for Pt/Vulcan XC-72R (from 2.4 to 5.8 nm) and for Pt/C (from 3.8 to 6.6 nm), as shown in Figure 34 and Figure 35, with broader particle size distributions. This result is consistent with the ECSA loss as described above.

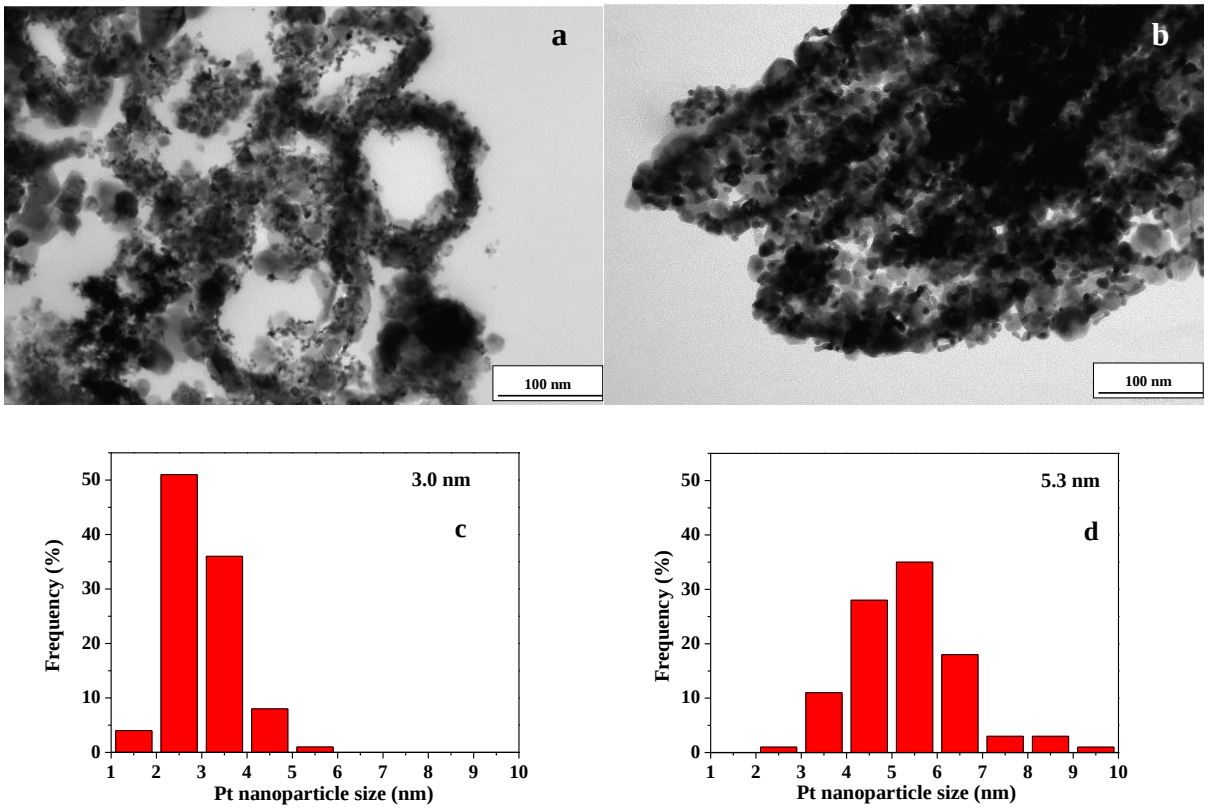

Figure 33: TEM micrographs of Pt/Nb-SnO_2 before (a) and after voltammetric cycling (b) and corresponding Pt nanoparticle size distribution histograms (c and d), respectively.

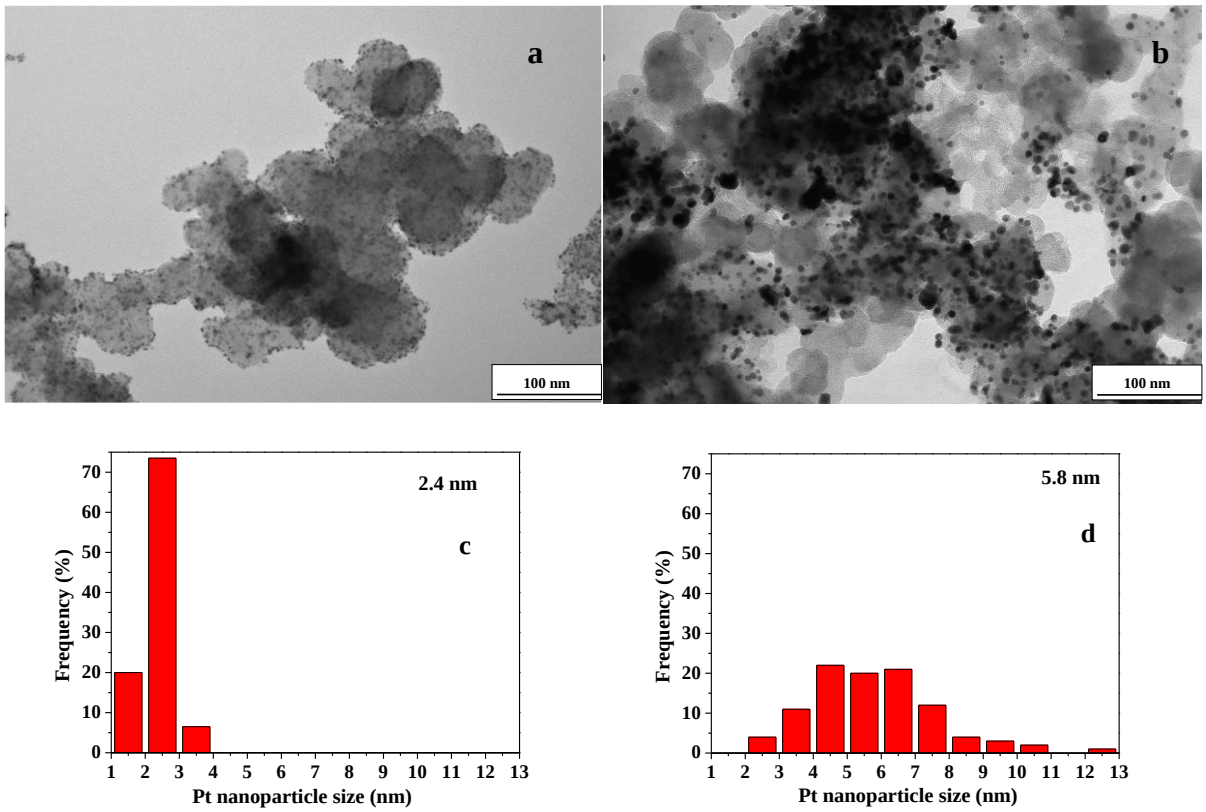

Figure 34: TEM micrographs of Pt/Vulcan XC-72R before (a) and after potential cycling (b) and corresponding Pt nanoparticle size distribution histograms (c and d), respectively.

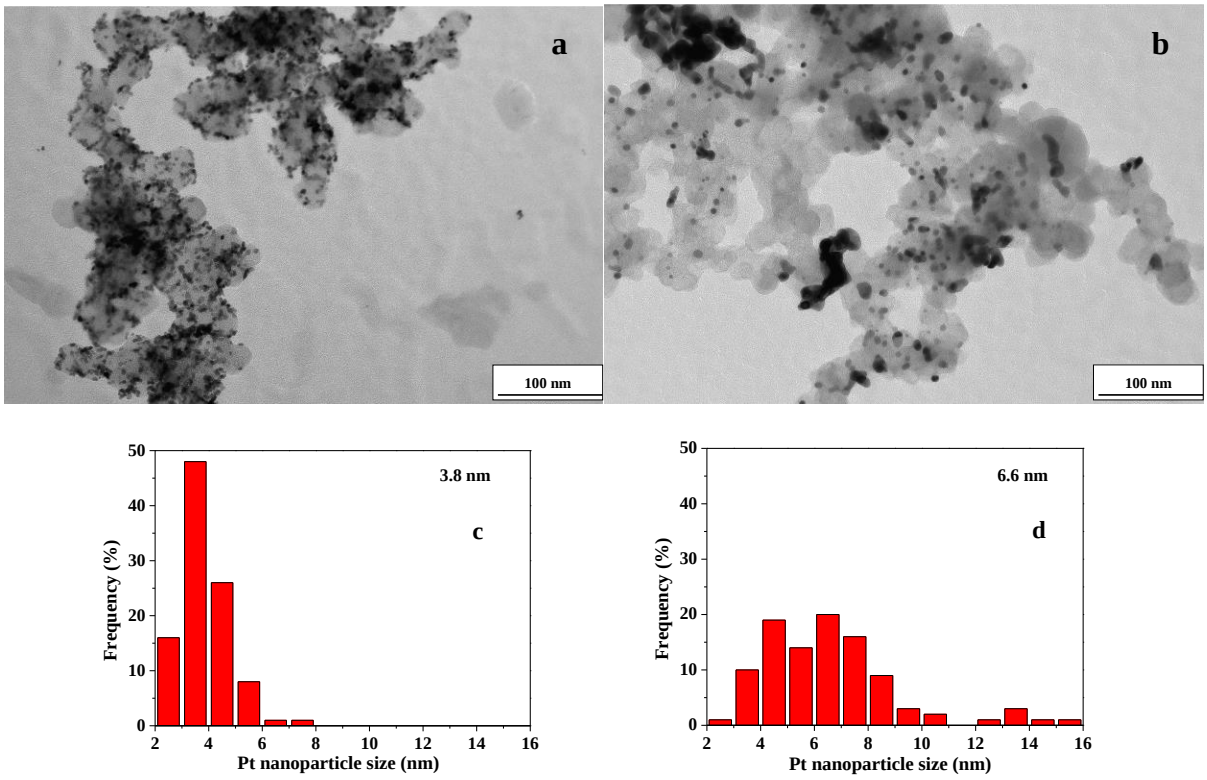

Figure 35: TEM micrographs of Pt/C before (a) and after voltammetric cycling (b) and corresponding Pt nanoparticle size distribution histograms (c and d), respectively.

Conclusions

Nb and Sb doped SnO_2 fibre-in-tubes were obtained by conventional single-needle electrospinning, without using complicated coaxial setup. The diameter of these 1 D structures increased with increasing precursor concentration. The addition of the doping agents such as Nb and Sb enhanced electrical conductivity of SnO_2. In particular, Sb-SnO_2 exhibits high conductivity of ca 1 S/cm at room temperature. In addition, electrical conductivity of doped materials increased with the temperature, while that of carbon decreased. Furthermore, addition of Nb and Sb doping promoted formation of hollow fibres and inhibited SnO_2 grain growth leading to an enhanced surface area of the doped materials.

Pt nanoparticles were synthesised by microwave-assisted polyol method and deposited on Nb-SnO_2. The obtained Pt/Nb-SnO_2 was characterised *ex situ* using RDE. The electrocatalyst exhibited higher durability upon potential cycling compared to the commercial Pt/C. The improved durability can be attributed to the high resistance of the oxide-based materials to corrosion and strong metal support interactions. Therefore, Nb-SnO_2 hollow fibres can be an alternative support materials, which might be able to replace carbon and therefore lead to an enhancement of the PEMFC lifetime.

Perspectives

Pt/Sb-SnO_2 electrocatalyst should be characterised by RDE, in order to evaluate its ORR activity and electrochemical stability and to compare it with that of Pt/Nb-SnO_2.

Further improvement of oxide surface area and porosity is necessary in order to disperse Pt particles more homogeneously and to enhance ECSA of Pt on oxide support. In addition, the optimal Pt loading on the oxide needs to be determined.

The further optimisation of Pt synthesis using microwave-assisted polyol method is also envisaged, in order to control the Pt nanoparticle size distribution.

The Pt loading on the oxide support should be confirmed by more reliable technique such as for example inductively coupled plasma-mass spectrometric analysis (ICP-MS), after dissolving these Pt catalysts in hot aqua regia. This method is commonly used to determine Pt mass %.

References

[1] S. Cavaliere, S. Subianto, I. Savych, M. Tillard, D. J. Jones, and J. Rozie, "Dopant-Driven Nanostructured Loose-Tube SnO_2 Architectures: Alternative Electrocatalyst Supports for Proton Exchange Membrane Fuel Cells," *The Journal of Physical Chemistry C*, vol. 117, p. 18298 − 18307, 2013.

[2] F. Mou, J. Guan, W. Shi, Z. Sun, and S. Wang, "Oriented contraction: a facile nonequilibrium heat-treatment approach for fabrication of maghemite fiber-in-tube and tube-in-tube nanostructures," *Langmuir*, vol. 26, no. 19, pp. 15580–5, Oct. 2010.

[3] X. H. Li, C. L. Shao, and Y. C. Liu, "A simple method for controllable preparation of polymer nanotubes via a single capillary electrospinning," *Langmuir*, vol. 23, no. 22, pp. 10920–3, Oct. 2007.

[4] Y. Cheng, B. Zou, C. Wang, Y. Liu, X. Fan, L. Zhu, Y. Wang, H. Ma, and X. Cao, "Formation mechanism of Fe_2O_3 hollow fibers by direct annealing of the electrospun composite fibers and their magnetic, electrochemical properties," *CrystEngComm*, vol. 13, no. 8, p. 2863, 2011.

[5] S. Chaudhari and M. Srinivasan, "1D hollow α-Fe_2O_3 electrospun nanofibers as high performance anode material for lithium ion batteries," *Journal of Materials Chemistry*, vol. 22, no. 43, p. 23049, 2012.

[6] C. Zhao, G. Zhang, W. Han, J. Fu, Y. He, Z. Zhang, and E. Xie, "Electrospun In_2O_3/α-Fe_2O_3 heterostructure nanotubes for highly sensitive gas sensor applications," *CrystEngComm*, vol. 15, no. 33, p. 6491, 2013.

[7] X. Bai, H. Ji, P. Gao, Y. Zhang, and X. Sun, "Morphology, phase structure and acetone sensitive properties of copper-doped tungsten oxide sensors," *Sensors and Actuators B: Chemical*, vol. 193, pp. 100–106, Mar. 2014.

[8] S. Wei, Y. Zhang, and M. Zhou, "Toluene sensing properties of SnO_2–ZnO hollow nanofibers fabricated from single capillary electrospinning," *Solid State Communications*, vol. 151, no. 12, pp. 895–899, Jun. 2011.

[9] W. Tang, J. Wang, P. Yao, and X. Li, "Hollow hierarchical SnO_2-ZnO composite nanofibers with heterostructure based on electrospinning method for detecting methanol," *Sensors and Actuators B: Chemical*, vol. 192, no. 2, pp. 543–549, Mar. 2014.

[10] Z. Zhang, X. Li, C. Wang, L. Wei, Y. Liu, and C. Shao, "ZnO Hollow Nanofibers: Fabrication from Facile Single Capillary Electrospinning and Applications in Gas Sensors," *The Journal of Physical Chemistry C*, vol. 113, no. 45, pp. 19397–19403, Nov. 2009.

[11] S. Wei, M. Zhou, and W. Du, "Improved acetone sensing properties of ZnO hollow nanofibers by single capillary electrospinning," *Sensors and Actuators B: Chemical*, vol. 160, no. 1, pp. 753–759, Dec. 2011.

[12] H. Xiang, Y. Long, X. Yu, X. Zhang, N. Zhao, and J. Xu, "A novel and facile method to prepare porous hollow CuO and Cu nanofibers based on electrospinning," *CrystEngComm*, vol. 13, no. 15, pp. 4856–4860, 2011.

[13] P. Liu, Y. Zhu, J. Ma, S. Yang, J. Gong, and J. Xu, "Preparation of continuous porous alumina nanofibers with hollow structure by single capillary electrospinning," *Colloids and Surfaces A: Physicochemical and Engineering Aspects*, vol. 436, pp. 489–494, Sep. 2013.

[14] D. Li, X. Dong, W. Yu, J. Wang, and G. Liu, "Synthesis and upconversion luminescence properties of YF_3:Yb^{3+}/Er^{3+} hollow nanofibers derived from Y_2O_3:Yb^{3+}/Er^{3+} hollow nanofibers," *Journal of Nanoparticle Research*, vol. 15, no. 6, p. 1704, May 2013.

[15] J. Fu, J. Zhang, Y. Peng, C. Zhao, Y. He, Z. Zhang, X. Pan, N. J. Mellors, and E. Xie, "Wire-in-tube structure fabricated by single capillary electrospinning via nanoscale Kirkendall effect: the case of nickel-zinc ferrite," *Nanoscale*, vol. 5, no. 24, pp. 12551–7, Dec. 2013.

[16] L. Lang, D. Wu, and Z. Xu, "Controllable fabrication of TiO_2 1D-nano/micro structures: solid, hollow, and tube-in-tube fibers by electrospinning and the photocatalytic performance," *Chemistry*, vol. 18, no. 34, pp. 10661–8, Aug. 2012.

[17] X. Xia and G. X. J., "Formation mechanism of porous hollow SnO_2 nanofibers prepared by one-step electrospinning," *Express Polymer Letters*, vol. 6, no. 2, pp. 169–176, Dec. 2012.

[18] Y. Yin, R. M. Rioux, C. K. Erdonmez, S. Hughes, G. A. Somorjai, and A. P. Alivisatos, "Formation of hollow nanocrystals through the nanoscale Kirkendall effect," *Science*, vol. 304, no. 5671, pp. 711–4, Apr. 2004.

[19] H. J. Fan, U. Gösele, and M. Zacharias, "Formation of nanotubes and hollow nanoparticles based on Kirkendall and diffusion processes: a review," *Small*, vol. 3, no. 10, pp. 1660–71, Oct. 2007.

[20] Y. Cheng, W. Huang, Y. Zhang, L. Zhu, Y. Liu, X. Fan, and X. Cao, "Preparation of TiO_2 hollow nanofibers by electrospining combined with sol–gel process," *CrystEngComm*, vol. 12, no. 7, p. 2256, 2010.

[21] C. Jiang, G. Zhang, Y. Wu, L. Li, and K. Shi, "Facile synthesis of SnO_2 nanocrystalline tubes by electrospinning and their fast response and high sensitivity to NOx at room temperature," *CrystEngComm*, vol. 14, no. 8, p. 2739, 2012.

[22] C. Gao, X. Li, B. Lu, L. Chen, Y. Wang, F. Teng, J. Wang, Z. Zhang, X. Pan, and E. Xie, "A facile method to prepare SnO_2 nanotubes for use in efficient SnO_2-TiO_2 core-shell dye-sensitized solar cells," *Nanoscale*, vol. 4, no. 11, pp. 3475–81, Jun. 2012.

[23] H. An and H. Ahn, "Processing Research Morphology control of Nb-doped SnO_2 nanofibres formed via electrospinning: From hollow nanofibres to dense nanofibres," *Journal of Ceramic Processing Research*, vol. 14, no. 3, pp. 371–375, 2013.

[24] J. P. Cheng, B. B. Wang, M. G. Zhao, F. Liu, and X. B. Zhang, "Nickel-doped tin oxide hollow nanofibers prepared by electrospinning for acetone sensing," *Sensors and Actuators B: Chemical*, vol. 190, pp. 78–85, Jan. 2014.

[25] L. Li, X. Yin, S. Liu, Y. Wang, L. Chen, and T. Wang, "Electrospun porous SnO_2 nanotubes as high capacity anode materials for lithium ion batteries," *Electrochemistry Communications*, vol. 12, no. 10, pp. 1383–1386, Oct. 2010.

[26] J.-K. Choi, I.-S. Hwang, S.-J. Kim, J.-S. Park, S.-S. Park, U. Jeong, Y. C. Kang, and J.-H. Lee, "Design of selective gas sensors using electrospun Pd-doped SnO_2 hollow nanofibers," *Sensors and Actuators B: Chemical*, vol. 150, no. 1, pp. 191–199, Sep. 2010.

[27] J. Kong, S. Y. Wong, Y. Zhang, H. R. Tan, X. Li, and X. Lu, "One-dimensional carbon–SnO_2 and SnO_2 nanostructures via single-spinneret electrospinning: tunable morphology and the underlying mechanism," *Journal of Materials Chemistry*, vol. 21, no. 40, p. 15928, 2011.

[28] P. Mohanapriya, H. Segawa, K. Watanabe, K. Watanabe, S. Samitsu, T. S. Natarajan, N. V. Jaya, and N. Ohashi, "Enhanced ethanol-gas sensing performance of Ce-doped SnO_2 hollow nanofibers prepared by electrospinning," *Sensors and Actuators B: Chemical*, vol. 188, pp. 872–878, Nov. 2013.

[29] J. Wu, D. Zeng, and S. Zhang, "Mesoporous Al-doped SnO_2 nanotubes with enhanced gas-sensing properties fabricated by electrospinning," in *AMA Conferences - Sensor Materials*, 2013, pp. 257–262.

[30] Y.-E. Miao, S. He, Y. Zhong, Z. Yang, W. W. Tjiu, and T. Liu, "A novel hydrogen peroxide sensor based on Ag/SnO_2 composite nanotubes by electrospinning," *Electrochimica Acta*, vol. 99, pp. 117–123, Jun. 2013.

[31] V. Aravindan, J. Sundaramurthy, E. N. Kumar, P. S. Kumar, W. C. Ling, R. von Hagen, S. Mathur, S. Ramakrishna, and S. Madhavi, "Does carbon coating really improves the electrochemical performance of electrospun SnO_2 anodes?," *Electrochimica Acta*, vol. 121, pp. 109–115, Mar. 2014.

[32] R. A. Kadir, Z. Li, A. Z. Sadek, R. A. Rani, A. S. Zoolfakar, M. R. Field, J. Z. Ou, A. F. Chrimes, and K. Kalantar-zadeh, "Electrospun Granular Hollow SnO_2 Nano fibers Hydrogen Gas Sensors Operating at Low Temperatures," *The Journal of Physical Chemistry C*, vol. 118, pp. 3129–3139, 2014.

[33] F. Takasaki, S. Matsuie, Y. Takabatake, Z. Noda, a. Hayashi, Y. Shiratori, K. Ito, and K. Sasaki, "Carbon-Free Pt Electrocatalysts Supported on SnO_2 for Polymer Electrolyte Fuel Cells: Electrocatalytic Activity and Durability," *Journal of The Electrochemical Society*, vol. 158, no. 10, p. B1270, 2011.

[34] T. Tsukatsune, Y. Takabatake, Z. Noda, A. Hayashi, and K. Sasaki, "Electrochemical Properties and Durability of Electrocatalysts Supported on SnO_2," *ECS Transactions*, vol. 58, no. 1, pp. 1251–1257, 2013.

[35] K. Kanda, Z. Noda, Y. Nagamatsu, T. Higashi, S. Taniguchi, S. M. Lyth, a. Hayashi, and K. Sasaki, "Negligible Start-Stop-Cycle Degradation in a PEFC Utilizing Platinum-Decorated Tin Oxide Electrocatalyst Layers with Carbon Fiber Filler," *ECS Electrochemistry Letters*, vol. 3, no. 4, pp. F15–F18, Feb. 2014.

[36] I. T. Weber, R. Andrade, E. R. Leite, and E. Longo, "A study of the SnO_2 Nb_2O_5 system for an ethanol vapour sensor: a correlation between microstructure and sensor performance," *Sensors and Actuator*, vol. 72, pp. 180–183, 2001.

[37] K. Kakinuma, Y. Chino, Y. Senoo, M. Uchida, T. Kamino, H. Uchida, S. Deki, and M. Watanabe, "Characterization of Pt catalysts on Nb-doped and Sb-doped $SnO_{2-\delta}$ support materials with aggregated structure by rotating disk electrode and fuel cell measurements," *Electrochimica Acta*, vol. 110, pp. 316–324, Nov. 2013.

[38] H. Mahmoudi Chenari, L. Weinhardt, N. S. Rodriguez Lastra, M. a. Ernst, F. Reinert, M. M. Golzan, and A. Hassanzadeh, "Structural properties and x-ray photoelectron spectroscopic study of SnO_2 nanoparticles," *Materials Letters*, vol. 85, pp. 168–170, Oct. 2012.

[39] T. S. Ribeiro, J. M. Sasaki, and I. F. Vasconcelos, "Structural disorder of ball-milled, nanosized, Fe-doped SnO_2: X-ray diffraction and Mössbauer spectroscopy characterization," *Journal of Materials Science*, vol. 47, no. 6, pp. 2630–2636, Nov. 2012.

[40] W. Fliegel, G. Behr, J. Werner, and G. Krabbes, "Preparation, development of microstructure, electrical and gas- sensitive properties of pure and doped SnO_2, powders," *Sensors and Actuators*, vol. 19, pp. 18–19, 1994.

[41] A. Diéguez, A. Romano-Rodríguez, A. Vilà, and J. R. Morante, "The complete Raman spectrum of nanometric SnO_2 particles," *Journal of Applied Physics*, vol. 90, no. 3, p. 1550, 2001.

[42] J.-M. Themlin, M. Chtaib, L. Henrard, P. Lambin, J. Darville, and J. Gilles, "Characterization of tin oxides by x-ray-photoemission spectroscopy," *Physical Review B*, vol. 46, no. 4, pp. 2460–2466, 1992.

[43] S. Kaciulis, L. Pandolfi, E. Comini, G. Faglia, M. Ferroni, G. Sberveglieri, S. Kandasamy, M. Shafiei, and W. Wlodarski, "Nanowires of metal oxides for gas sensing applications," *Surface and Interface Analysis*, vol. 40, no. 3–4, pp. 575–578, Mar. 2008.

[44] D. Wagner, "Chemical Shifts of Auger Lines, and the Auger Parameter," *Farad. Discuss. Chem. Soc.*, vol. 60, p. 291, 1975.

[45] V. M. Jiménez, J. A. Mejias, J. P. Espinds, and A. R. Gonzfilez-Elipe, "Interface effects for metal oxide thin films deposited on another metal oxide II SnO_2 deposited on SiO_2," *Surface Science*, vol. 366, pp. 545–555, 1996.

[46] S. G. Kim, M. J. Ju, I. T. Choi, W. S. Choi, H.-J. Choi, J.-B. Baek, and H. K. Kim, "Nb-doped TiO_2 nanoparticles for organic dye-sensitized solar cells," *RSC Advances*, vol. 3, no. 37, p. 16380, 2013.

[47] K. Lee, I. Park, Y. Cho, D. Jung, N. Jung, H. Park, and Y. Sung, "Electrocatalytic activity and stability of Pt supported on Sb-doped SnO_2 nanoparticles for direct alcohol fuel cells," *Journal of Catalysis*, vol. 258, no. 1, pp. 143–152, Aug. 2008.

[48] M. Yin, J. Xu, Q. Li, J. O. Jensen, Y. Huang, L. N. Cleemann, N. J. Bjerrum, and W. Xing, "Highly active and stable Pt electrocatalysts promoted by antimony-doped SnO_2 supports for oxygen reduction reactions," *Applied Catalysis B: Environmental*, vol. 144, pp. 112–120, Jan. 2014.

[49] J. Suffner, S. Kaserer, H. Hahn, C. Roth, and F. Ettingshausen, "Sb-Doped SnO_2 Hollow Spheres Offering Micro- and Nanoporosity in Fuel Cell Electrode Structures," *Advanced Energy Materials*, vol. 1, no. 4, pp. 648–654, Jul. 2011.

[50] M. P. Gurrola, M. Guerra-Balcázar, L. Álvarez-Contreras, R. Nava, J. Ledesma-García, and L. G. Arriaga, "High surface electrochemical support based on Sb-doped SnO_2," *Journal of Power Sources*, vol. 243, pp. 826–830, Dec. 2013.

[51] M. P. Gurrola, J. Gutiérrez, S. Rivas, M. Guerra-Balcázar, J. Ledesma-García, and L. G. Arriaga, "Evaluation of the corrosion of Sb-doped SnO_2 supports for electrolysis systems," *International Journal of Hydrogen Energy*, pp. 2–9, Mar. 2014.

[52] V. Senthilkumar, P. Vickraman, M. Jayachandran, and C. Sanjeeviraja, "Structural and electrical studies of nano structured $Sn_{1-x}Sb_xO_2$ (x = 0.0, 1, 2.5, 4.5 and 7 at%) prepared by co-precipitation method," *Journal of Materials Science: Materials in Electronics*, vol. 21, no. 4, pp. 343–348, Jun. 2009.

[53] C. Terriera, J. P. Chatelon, R. Berjoan, and J. A. Rogera, "Sb-doped SnO_2, transparent conducting oxide from the sol-gel dip-coating technique," *Thin Solid Films*, vol. 263, pp. 37–41, 1995.

[54] K. Kakinuma, M. Uchida, T. Kamino, H. Uchida, and M. Watanabe, "Synthesis and electrochemical characterization of Pt catalyst supported on Sn0.96Sb0.04O2−δ with a network structure," *Electrochimica Acta*, vol. 56, no. 7, pp. 2881–2887, Feb. 2011.

[55] E. Fabbri, A. Rabis, R. Kötz, and T. J. Schmidt, "Pt nanoparticles supported on Sb-doped SnO_2 porous structures: developments and issues," *Physical Chemistry Chemical Physics*, 2014.

[56] N. Zhang, S. Zhang, C. Du, Z. Wang, Y. Shao, F. Kong, Y. Lin, and G. Yin, "Pt/Tin Oxide/Carbon Nanocomposites as Promising Oxygen Reduction Electrocatalyst with Improved Stability and Activity," *Electrochimica Acta*, vol. 117, pp. 413–419, Jan. 2014.

[57] M. Dou, M. Hou, D. Liang, W. Lu, Z. Shao, and B. Yi, "SnO_2 nanocluster supported Pt catalyst with high stability for proton exchange membrane fuel cells," *Electrochimica Acta*, vol. 92, pp. 468–473, Mar. 2013.

[58] P. Zhang, S.-Y. Huang, and B. N. Popov, "Mesoporous Tin Oxide as an Oxidation-Resistant Catalyst Support for Proton Exchange Membrane Fuel Cells," *Journal of The Electrochemical Society*, vol. 157, no. 8, p. B1163, 2010.

[59] F. Takasaki, Z. Noda, A. Masao, Y. Shiratori, K. Ito, and K. Sasaki, "Carbon-free Pt Electrocatalysts Supported on Doped SnO_2 for Polymer Electrolyte Fuel Cells," *ECS Transactions*, vol. 25, no. 1, pp. 831–837, 2009.

CHAPTER 5:

In situ characterisation of platinum supported on doped tin oxide nanotube as a cathode electrocatalyst for PEMFC

1 Introduction

Most of the electrochemical characterisation of doped oxide supported Pt reported in the literature has been performed *ex situ* using RDE. There are few studies focused on the characterisation of Pt/tin oxide as a cathode in a single fuel cell with Nafion® [1],[2],[3] and even fewer with PBI membrane [4], as listed in Table 1.

In these studies, Pt/C at the cathode side usually provides better performance in PEMFC than oxide supported Pt, due to the lower electrical conductivity and surface area of oxide compared with that of carbon support. Several approaches have been developed to overcome the problem of low conductivity of the support. On the one hand, Popov's group [1],[5],[6] used high Pt loadings of around 60 wt.% on oxide supports (namely TiO_2 and SnO_2), in order to obtain a very thin catalyst layer (~1 µm). In this case, Pt nanoparticles not only play the role of a catalyst, but also ensure the electron transport [5]. Furthermore, oxide-based supports provide the ability to obtain thin catalyst layers due to their higher density compared with that of carbon. Thin electrodes allow an increase of the current density at potentials lower than 0.7 V due to improved mass transport kinetics. For instance, the 3M NSTF-type catalysts [7] are ultrathin cathode layers (~0.27 µm) based on sputtered platinum on stacked perylene red nano-whiskers, which showed 100 % catalyst utilisation with low mass transport losses at high current densities. On the other hand, composite support materials containing both carbon and oxide are widely used to improve conductivity and surface area of ceramic supports. For instance, Sb doped SnO_2 (ATO) loaded on carbon nanotubes (CNT) provided improved surface area and conductivity compared to pure ATO support, which resulted in enhanced HT-PEMFC performance of a Pt/ATO-CNT based MEA [4]. Furthermore, Pt/ATO-C provides higher ECSA and ORR activity than Pt/ATO [8].

In this chapter, the performance and the stability of Pt/Nb-SnO_2 based catalyst layers were evaluated with Nafion® and PBI membranes in a single PEMFC. The effect of addition of Vulcan XC-72R to the catalyst layer was evaluated in terms of initial performance and performance after potential cycling. Later in this chapter, Pt supported on more conductive electrospun Sb-SnO_2 (compared to Nb-SnO_2) was also characterised as cathode catalyst in a single PEMFC.

Table 1: Characterisation of tin oxide supported Pt *in situ* in single PEMFC

Reference	Electrocatalyst on the cathode side	Pt loading, mg_{Pt}/cm^2	Catalyst deposition method	Operating conditions	Comparison with commercial Pt/C
with PFSA membrane					
Masao 2009 [9]	Pt/SnO_2	0.6	spray-printing on carbon paper	H_2/air, 80 °C, 100 % RH	comparable performance to that of Pt/C
Zhang 2010 [1]	Pt/SnO_2	0.5	spray-coated onto a GDL	H_2/O_2, 75 °C, 100 % RH	0.74 W/cm^2, lower power density, but higher stability than that of Pt/C
Sasaki 2010 [10]	Pt/SnO_2	-	-	H_2/air, 80 °C, 100 % RH, 1 bar	comparable performance to that of Pt/C
Suchsland 2012 [11]	Pt/Sb-SnO_2	0.1	CCM method by decal process	H_2/air, 85 °C, 50 % RH, 1.5 bar	lower performance than that of Pt/C (Sb leaches out of Sb-SnO_2)
Kakinuma 2013 [3]	Pt/$Sn_{0.96}Nb_{0.04}O_\delta$ Pt/$Sn_{0.96}Sb_{0.04}O_\delta$	0.2	sprayed onto a GDL	H_2/air, 80 °C, 53 % RH	lower than that of Pt/C (Sn cation dissolution of $Sn_{0.96}Sb_{0.04}O_\delta$)
Higashi 2013 [12]	Pt/$Sn_{0.96}Nb_{0.04}O_2$	0.5	by pulse laser deposition(oxide) sputtering (Pt)	H_2/air, 80 °C	lower power density, but higher stability than that of Pt/C
Kanda 2014 [2]	Pt/Nb-SnO_2 with carbon nanofibre filler	0.5	spray printing	H_2/air, 80 °C 44 % RH (cathode)	higher performance than that of Pt/Nb-SnO_2 without carbon
with PBI/H_3PO_4 membrane					
Xu 2013 [4]	Pt/Sb-SnO_2	0.7	spraying	H_2/air, 120 – 200 °C	Lower performance than that of Pt/CNT and Pt/Sb-SnO_2-CNT

2 Characterisation of Pt/Nb-SnO_2 based MEA with Nafion® membrane

Electrodes were prepared using the catalyst coated substrate (CCS) method. For this purpose, Pt/Nb-SnO_2 or commercial Pt/C electrocatalysts were dispersed in ethanol and Nafion® solution by ultra-sonication. The obtained catalyst inks were sprayed onto the GDL (Sigracet 10 BC, 4 cm^2) and dried at 80 °C on a hot plate protected by aluminium foil. Spraying was performed using a BADGER 360 air brash. The thickness of obtained electrodes was around 10 µm. The porosities were ca 43 and 45 % for Pt/Nb-SnO_2 and Pt/C based cathodes, respectively, as calculated in the experimental part (Annex A). The loading of Pt and Nafion® are listed in Table 2.

Table 2: Cathode catalyst layer composition.

Composition of 50 wt. % Pt/C based MEA	
Pt loading	0.5 mg/cm^2
Nafion® loading	0.5 mg/cm^2
Carbon loading	0.5 mg/cm^2
Pt loading on the anode (GDE) provided by JM	0.4 mg/cm^2
Composition of 21 wt. % Pt/Nb-SnO_2 based MEA with Vulcan XC-72R	
Pt loading	0.5 mg/cm^2
Nafion® loading	0.5 mg/cm^2
Nb-SnO_2 loading	2 mg/cm^2
Vulcan XC-72R loading	0.125 mg/cm^2
Pt loading on the anode (GDE) provided by JM	0.4 mg/cm^2

The obtained cathodes were hot-pressed at 140 °C for 2 min at 250 kg/cm^2 together with a Nafion® 212 membrane (thickness ~50 µm) and an anode provided by Johnson Matthey (JM), in order to prepare Pt/Nb-SnO_2, Pt/Nb-SnO_2-Vulcan and Pt/C based MEAs. The MEAs were tested in a single PEMFC. Experimental conditions are listed in Table 3.

Table 3: **PEMFC testing conditions.**

Break-in	0.5 A/cm^2, 12 h, 80 °C, 100 % RH
FC temperature	80 °C
Relative humidity (RH)	100 %
Pressure	2 bar (abs)
Gases stoichiometry	H_2/O_2 – 1.5/2

2.1 Performance evaluation of Pt/Nb-SnO_2 based MEA

The polarisation curves for MEAs with Pt/Nb-SnO_2, Pt/Nb-SnO_2-Vulcan and Pt/C cathodes are shown in Figure 1. The Pt/Nb-SnO_2-MEA provided a maximum power density of 0.41 W/cm^2, which is relatively high given that the electrode was not optimised in terms of Pt or ionomer loading or its porosity. The Pt/C-MEA provides higher maximum power density of 0.96 W/cm^2 indicating higher Pt utilisation for the commercial catalyst. The initial voltage drop

at low current density for Pt/Nb-SnO_2-MEA is compatible with the lower ORR activity and ECSA of Pt/Nb-SnO_2 described in Chapter 4. Further voltage losses in the ohmic region can be attributed to the relatively low electron conductivity of tin oxide compared to the carbon-based support.

To enhance the cathode conductivity, Vulcan XC-72R was added to the catalyst ink. The obtained loading of Vulcan XC-72R was 0.125 mg/cm^2. This resulted in a higher fuel cell performance, particularly in the ohmic region, caused by the increased conductivity of the catalyst layer. Thus, the maximum power density was enhanced from 0.41 W/cm^2 for Pt/Nb-SnO_2-MEA to 0.61 W/cm^2 for Pt/Nb-SnO_2-Vulcan-MEA.

Sasaki et al. [12] and Popov et al. [1] also demonstrated that an MEA having a cathode of Pt supported on SnO_2 showed lower fuel cell performance than one with a Pt/C cathode. In a more recent work of Sasaki et al. [2], carbon fibres were added as a conducting filler to the catalyst layer which resulted in increased conductivity of the Pt/Nb-SnO_2 based electrodes and increased performance of the tin oxide based MEA.

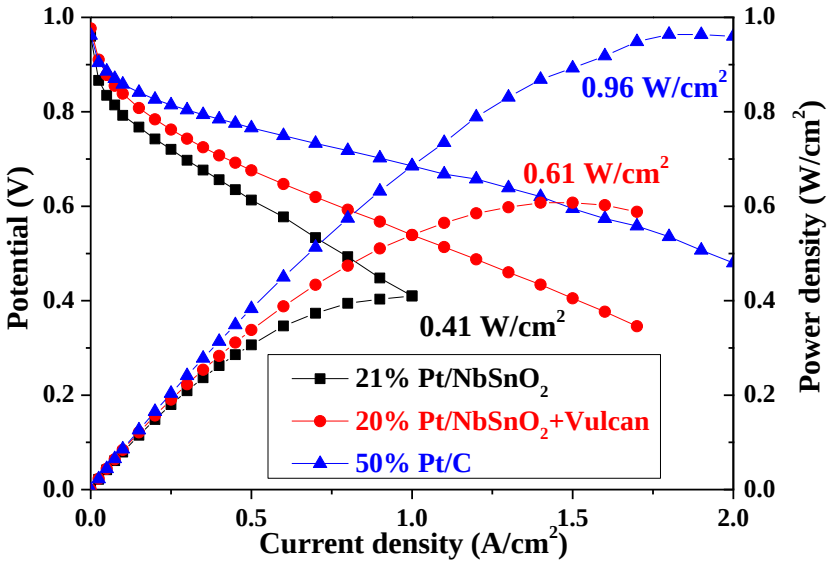

Figure 1: Polarisation curves for Pt/Nb-SnO_2 (100 % RH), Pt/Nb-SnO_2-Vulcan (50 % RH for cathode, 64 °C) and Pt/C (100 % RH) based MEAs at 80 °C under H_2/O_2 (1.5:2) and 2 bar (abs).

2.2 Electrochemical impedance spectroscopy (EIS)

During an EIS experiment, a sinusoidal current (I) or potential (E) is applied with a small amplitude (ΔI or ΔE):

$E = \Delta E \sin(2\pi ft)$, where f is frequency and t is time.

The response is also sinusoidal with the same frequency, but different amplitude (ΔI) and phase (φ):

$$I = \Delta I \sin(2\pi ft + \varphi)$$

The impedance is defined as:

$$Z = E/I$$

It can also be expressed in Cartesian coordinates as:

$Z = Z_{re} + iZ_{im}$, where Z_{re} and Z_{im} are real and imaginary parts, respectively.

An impedance spectrum is commonly plotted in Nyquist form, where the imaginary part of the impedance is plotted versus the real part at each frequency.

A Randles circuit [13] is often used to describe a single semicircle loop resulting from the impedance measurements (Figure 2). In the PEM fuel cell, the high frequency intercept of the semicircle with the real axis represents the total ohmic resistance ($\mathbf{R_{el}}$) of the cell components such as membrane, catalyst layer, GDL and bipolar plates. Generally, it is mostly related to the membrane proton conductivity. The diameter of the semicircle (also called as kinetic loop) corresponds to the charge transfer resistance of the cathode ($\mathbf{R_{ct}}$) (due to the fast kinetics of HOR compared to that of ORR).

In real systems, the electrode surface is porous leading to deformations of the impedance diagram. In this case, the double layer capacity ($\mathbf{C_{dl}}$) on the electrode-electrolyte interface) is often replaced by a constant phase element (**CPE**) to describe the depressed semicircle due to the distribution of double layer charging along the length of the pores [14]. An impedance of CPE can be expressed as [15]:

$$\boldsymbol{Z_{CPE}(\omega) = q^{-1}(i\omega)^{-\alpha}},$$

where: q is a factor of proportionality, and α is the CPE exponent that characterises the phase shift, $\omega = 2\pi f$. For porous electrodes $\alpha \sim 0.5$, whereas for a smooth electrodes $\alpha \sim 1$.

It is possible to evaluate double layer capacitance ($\mathbf{C_{dl}}$) using CPE ($\boldsymbol{q}$) [16]:

$$\boldsymbol{C_{dl} = [q\,(1/R_{el} + 1/R_{ct})^{\alpha-1}]^{1/\alpha}}$$

The impedance spectra in Figure 2 consist of one semicircle, which is attributed to oxygen reduction on the cathode due to the fast kinetics of hydrogen oxidation reaction.

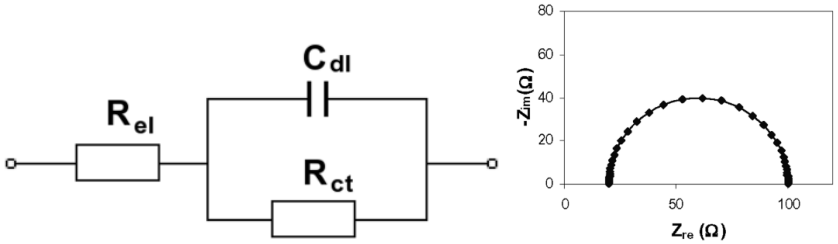

Figure 2: Randles circuit (left) and corresponding Nyquist plot (right) [15]**.**

Warburg impedance (**W**) is usually added to the Randles model, as shown in Figure 3 [15]. It describes the resistance associated with the mass and ionic transport process in the electrode.

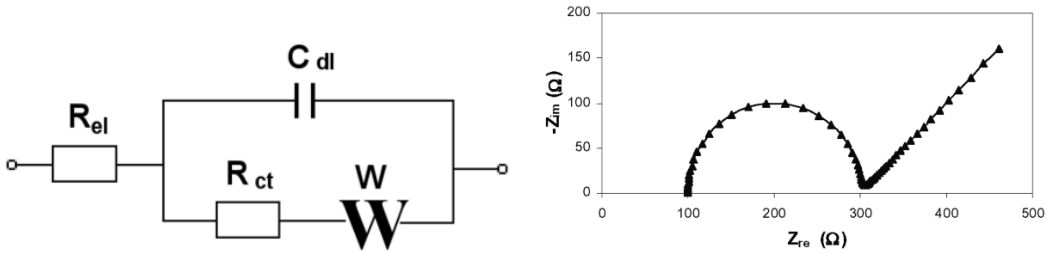

Figure 3: Mixed kinetic and diffusion control equivalent circuit (left) and corresponding Nyquist plot (right) [15].

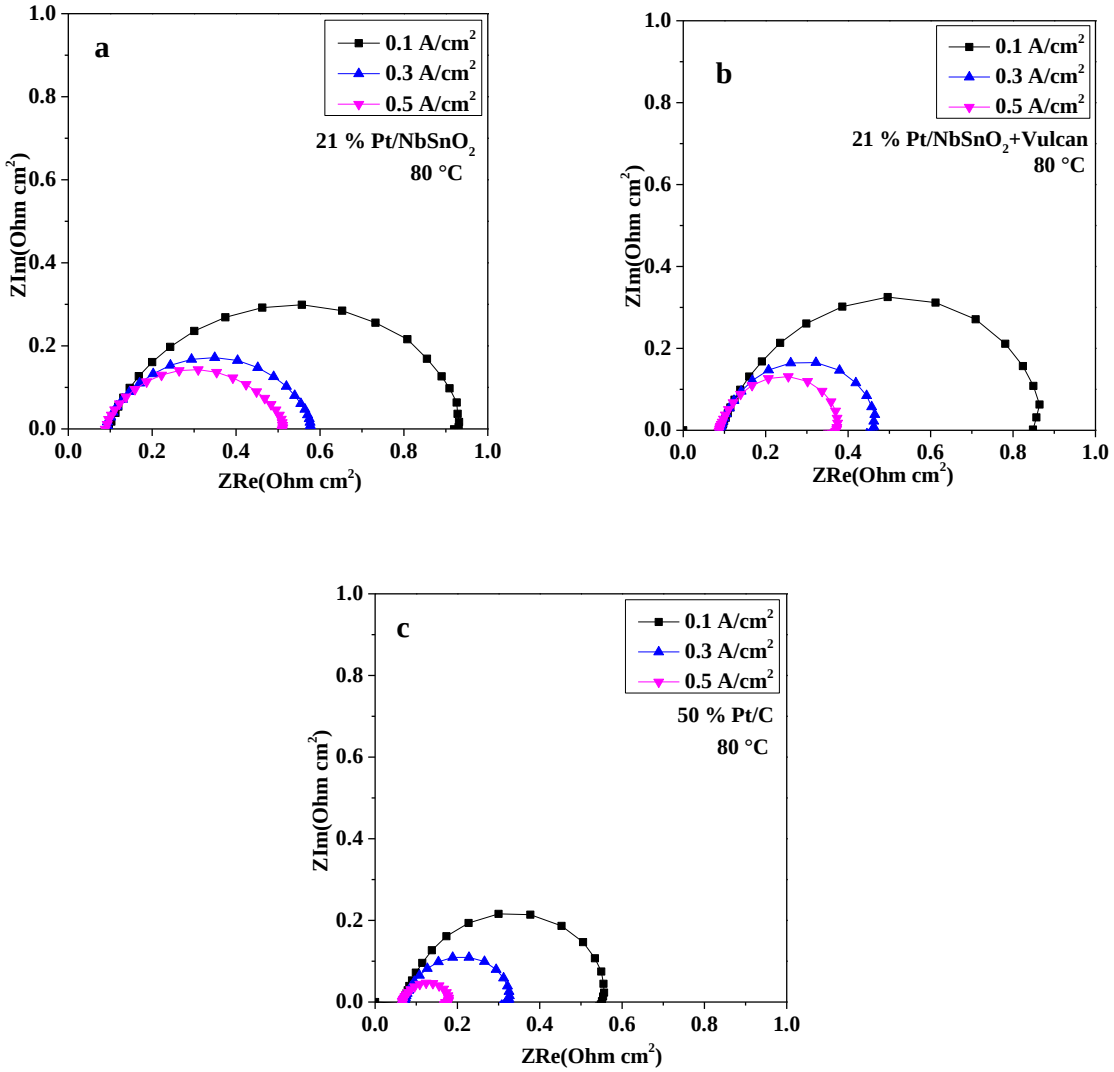

Figure 4: Nyquist plot of Pt/Nb-SnO₂ (a), Pt/Nb-SnO₂-Vulcan (b) and Pt/C (c) based MEAs for different current densities, over the frequency range from 20 kHz to 100 mHz.

Figure 4 shows the impedance spectra of the Pt/C, Pt/Nb-SnO_2 and Pt/Nb-SnO_2-Vulcan based MEAs obtained at different current densities. The Randles circuit was used to fit the single semicircle loop measured at low current densities. Parameters obtained using simulation in EC-Lab software (Randomized + Simplex method) are summarised in Table 4. The relative uncertainty (χ^2) was ca 10^{-2}, which was considered as acceptable. The ohmic resistance mainly attributed to the membrane resistance was ca 70 mΩ cm^2 for Pt/C-MEA, which is expected for Nafion® 212 membrane (50 µm). In the case of the Pt/Nb-SnO_2 based MEA, the ohmic resistance was higher (88 - 95 mΩcm^2). This could result from lower membrane hydration caused by slower electrocatalysis with the Pt/Nb-SnO_2. In addition, high $\mathbf{R_{el}}$ can be attributed to presence of Nb-SnO_2 in the MEA, which provides higher resistance than carbon support. Relatively low Nb-SnO_2 conductivity can also cause higher charge transfer resistance of Pt/Nb-SnO_2-MEA compared to that of Pt/C-MEA. However, addition of Vulcan XC-72R results in decrease of $\mathbf{R_{ct}}$, as shown in Table 4. The $\mathbf{R_{ct}}$ decreases with increasing current density from 0.1 to 0.5 A/cm^2 for all MEAs due to the increasing driving force for the charge transfer reaction.

Table 4: The values of the Randles cell components obained by fitting the impedance spectra.

A/cm²	**R_{el}, Ωcm²**	**R_{ct}, Ωcm²**	**CPE**	**α**	**C_{dl}, Fcm²**
Pt/Nb-SnO_2					
0.1	0.095	0.835	0.092	0.79	0.021
0.3	0.090	0.460	0.120	0.78	0.025
0.5	0.088	0.404	0.145	0.78	0.027
Pt/Nb-SnO_2-Vulcan					
0.1	0.093	0.820	0.521	0.84	0.260
0.3	0.090	0.386	0.375	0.88	0.203
0.5	0.090	0.292	0.327	0.91	0.200
Pt/C					
0.1	0.071	0.503	0.287	0.88	0.152
0.3	0.072	0.180	0.296	0.87	0.123
0.5	0.070	0.114	0.282	0.88	0.120

2.3 Durability evaluation of the Pt/Nb-SnO_2 based MEA

In order to investigate the stability of MEAs, an accelerated stress test was performed. During each cycle, the potential was stepped between 0.9 and 1.4 V with a holding period of 3 s at each potential on the cathode side. Kakinuma et al. [17] performed a similar test protocol for durability evaluation of the Pt/Sb-SnO_2 based MEA, where the potential was stepped between 0.9 V and 1.3 V with a holding period of 30 s at each potential. Experimental conditions for the stability test are listed in Table 5.

Table 5: **Accelerated stress test conditions.**

T, °C	80 °C
RH	100 %
Pressure	2 bar (abs)
Gases stoichiometry	H_2/O_2 – 1.5/2
Protocol of one cycle	0.9 V for 3 s and then 1.4 V for 3 s
Number of cycles	1200

The polarisation curves of MEAs based on Pt/Nb-SnO_2 and Pt/C cathode catalysts before and after this accelerated stress test are depicted in Figure 5. The initial open circuit voltage (OCV) was around 0.96 V for both MEAs and remained practically unchanged after the accelerated stress test, indicating that membrane conductivity was not affected by the stability test.

The performance of the MEA with the cathode comprising Pt/Nb-SnO_2 stayed almost unchanged, whereas for that with Pt/C cathode, a dramatic drop in performance was observed already after 400 cycles. The performance loss particularly in the ohmic and mass-transfer regions is attributed to a decrease in the conductivity of the catalyst layer and to mass-transport losses. At high potential (1.4 V), oxidation leads to functionalisation of the carbon surface, which results in an increase in the hydrophilicity of the catalyst layer and high mass-transport overpotentials [18] (see Chapter 1). The loss of the fuel cell performance is also related to the thinning of catalyst layer due to detachment, migration and three-phase-boundary isolation of Pt nanoparticles as a result of carbon corrosion (see paragraph 2.6). In contrast to the results with the Pt/oxide-only cathode, the Pt/Nb-SnO_2-Vulcan-MEA also shows a significant voltage drop upon potential cycling which, it may be deduced, is due to Vulcan XC-72R corrosion leading to a decrease of cathode conductivity.

A slight increase in performance of the Pt/Nb-SnO_2-MEA was observed after 400 cycles, probably caused by the improved mass-transfer properties of the cathode. Sasaki et al. [12] also reported an increase in performance of Pt/SnO_2 based MEA in the mass transport region after

potential cycling between 1.0 and 1.5 V for 2 sec per cycle. However, a slight voltage decrease was observed at low current densities after the stability test for Pt/Nb-SnO_2-MEA, indicating a decrease in ORR activity probably caused by some agglomeration and growth of Pt nanoparticles (see paragraph 2.5).

The greater stability of the tin oxide based electrocatalyst at high potentials can be assigned to the corrosion resistance of such support, already demonstrated in *ex situ* tests (see Chapter 4) and strong metal support interactions.

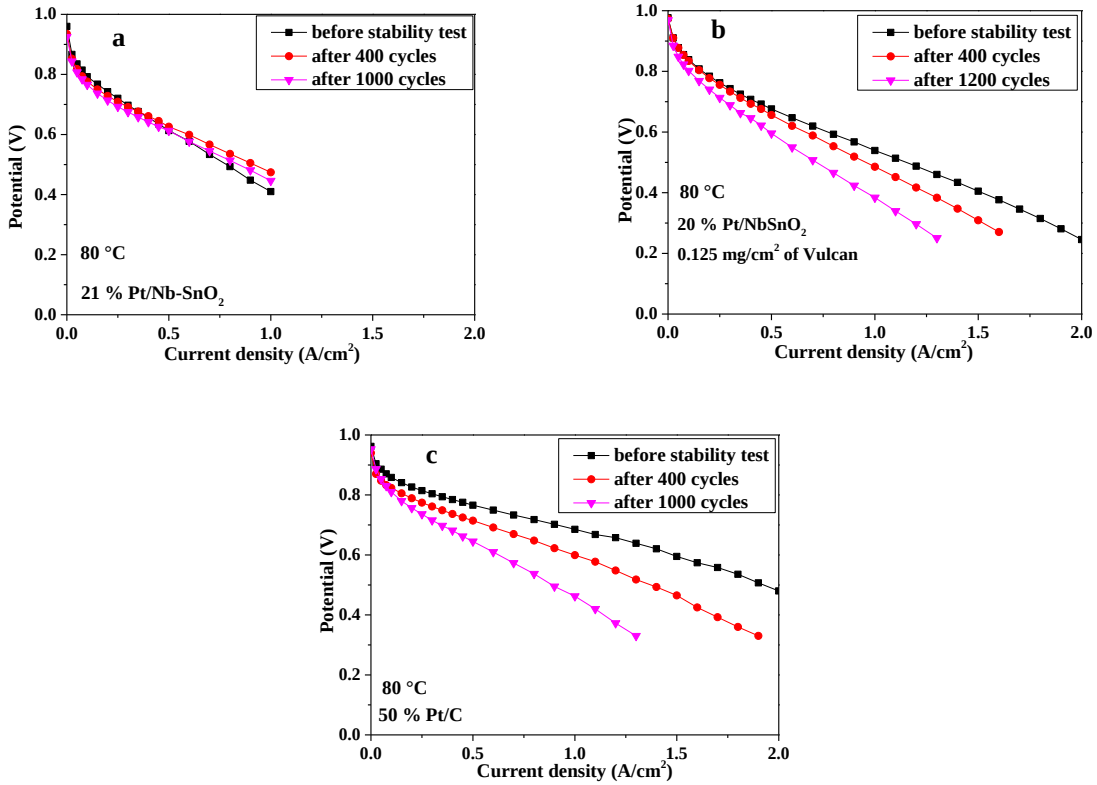

Figure 5: Polarisation curves for PEMFCs with Pt/Nb-SnO_2 (a), Pt/Nb-SnO_2-Vulcan (b) and Pt/C (c) electrocatalysts before and after potential cycling 0.9-1.4 V at 80 °C.

2.4 Evaluation of MEA durability using impedance spectroscopy

In order to investigate the durability over time of the catalyst layer, electrochemical impedance spectroscopy was carried out before and after the stability test. Impedance spectra of Pt/Nb-SnO_2, Pt/C and Pt/$NbSnO_2$-Vulcan based MEAs at 80 °C are shown in Figure 6. Ohmic and charge transfer resistance obtained after the fitting using Randles model are summarised in Table 6.

The charge transfer resistance increases significantly with the number of potential cycles from 0.5 to 0.9 Ω cm^2 for Pt/C-MEA, whereas it remains almost unchanged upon cycling for the Pt/Nb-SnO_2-MEA, indicating its high stability.

Table 6: The values of the Randles circuit components obained by fitting the impedance spectra at 0.1 A/cm² for Pt/Nb-SnO₂, Pt/Nb-SnO₂-Vulcan and Pt/C based MEAs before and after stability test.

A/cm²	R_{el}, Ωcm²	R_{ct}, Ωcm²
Pt/Nb-SnO₂		
0	0.095	0.835
1200	0.098	0.810
Pt/Nb-SnO₂-Vulcan		
0	0.093	0.820
1200	0.144	0.808
Pt/C		
0	0.071	0.503
1200	0.070	0.900

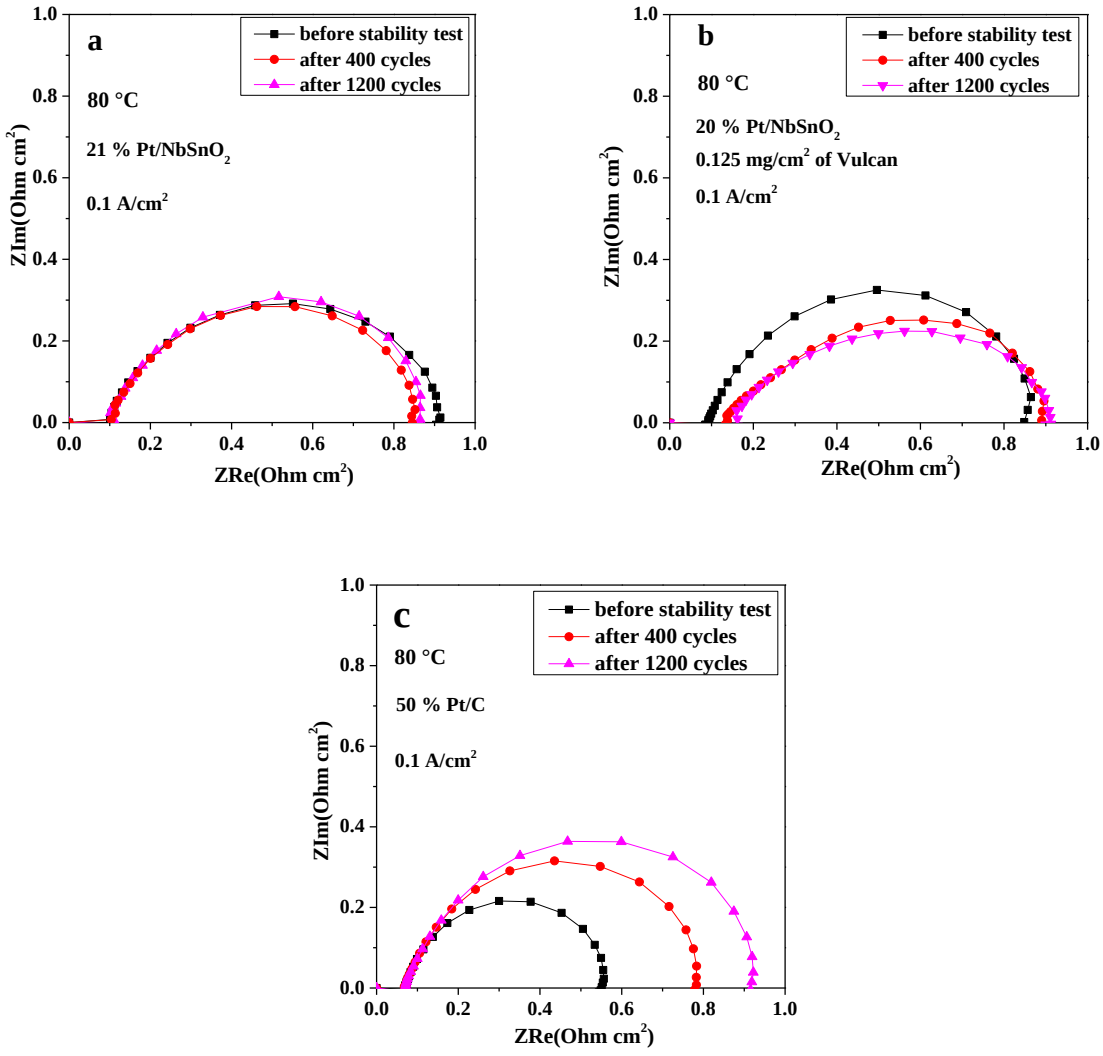

Figure 6: Electrochemical impedance spectra of Pt/Nb-SnO₂ (a) and Pt/Nb-SnO₂-Vulcan (b) and Pt/C (c) catalyst before and after potential cycling test at 80 °C.

2.5 TEM characterisation before and after durability test

TEM micrographs of Pt/Nb-SnO$_2$, Pt/C and Pt/Nb-SnO$_2$-Vulcan before and after 1200 cycles are shown in Figure 8, Figure 9 and Figure 10, respectively. All samples demonstrated similar platinum particle growth from 2-4 nm to ~ 5 nm, although the distribution of Pt particle size remains slightly narrower for the Pt/Nb-SnO$_2$ support (Figure 7). In addition, in the case of the commercial Pt/C electrocatalyst, a higher amount of Pt nanoparticles are unsupported after potential cycling. Such detachment and isolation of Pt nanoparticles may be caused by carbon degradation.

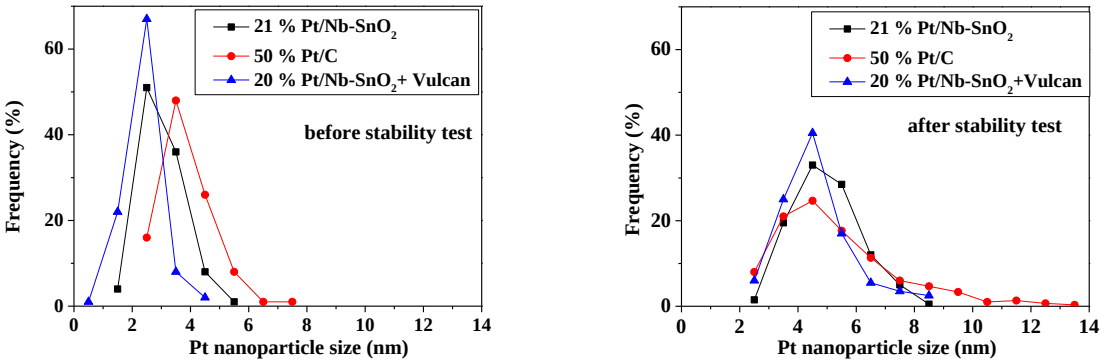

Figure 7: Comparison of Pt nanoparticle size distribution histograms before (left) and after (right) the stability test.

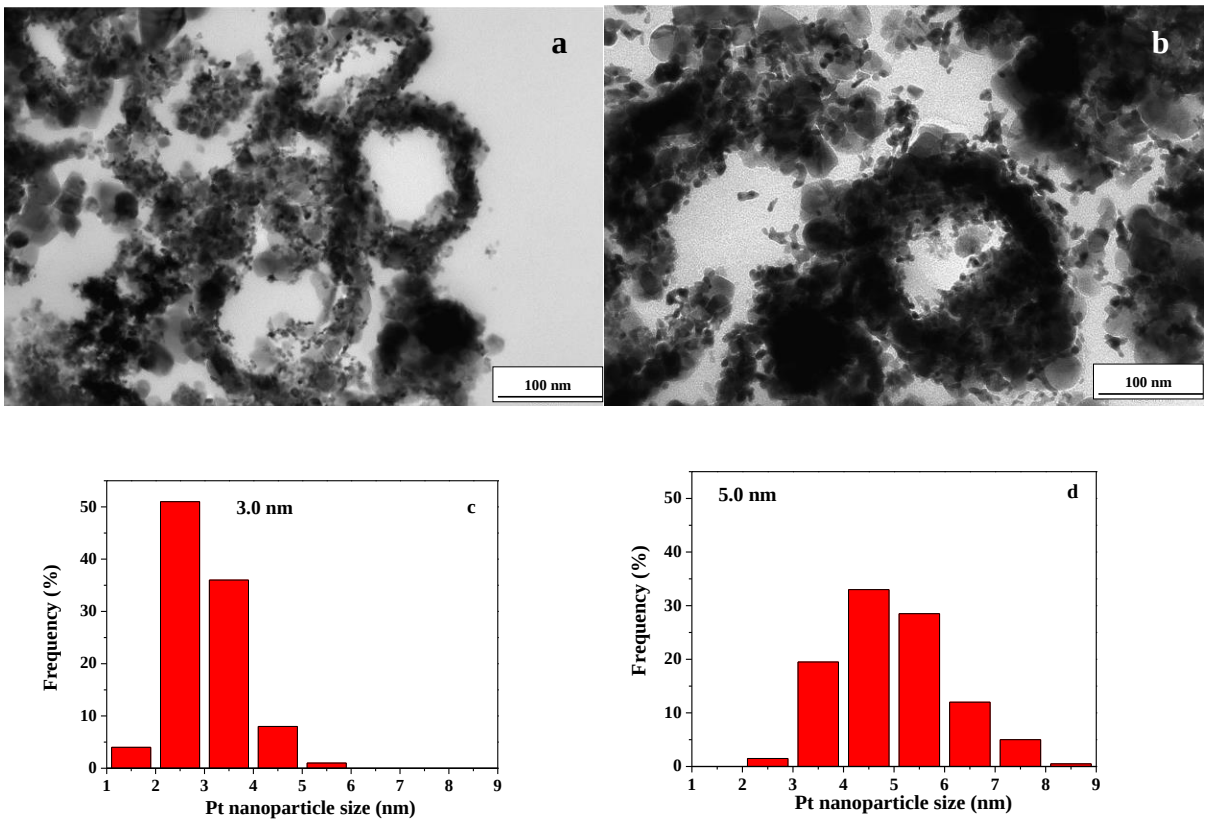

Figure 8: TEM micrographs of 21 % Pt/Nb-SnO$_2$ before (a) and after 1200 cycles (b) and corresponding Pt nanoparticle size distribution histograms (c and d, respectively).

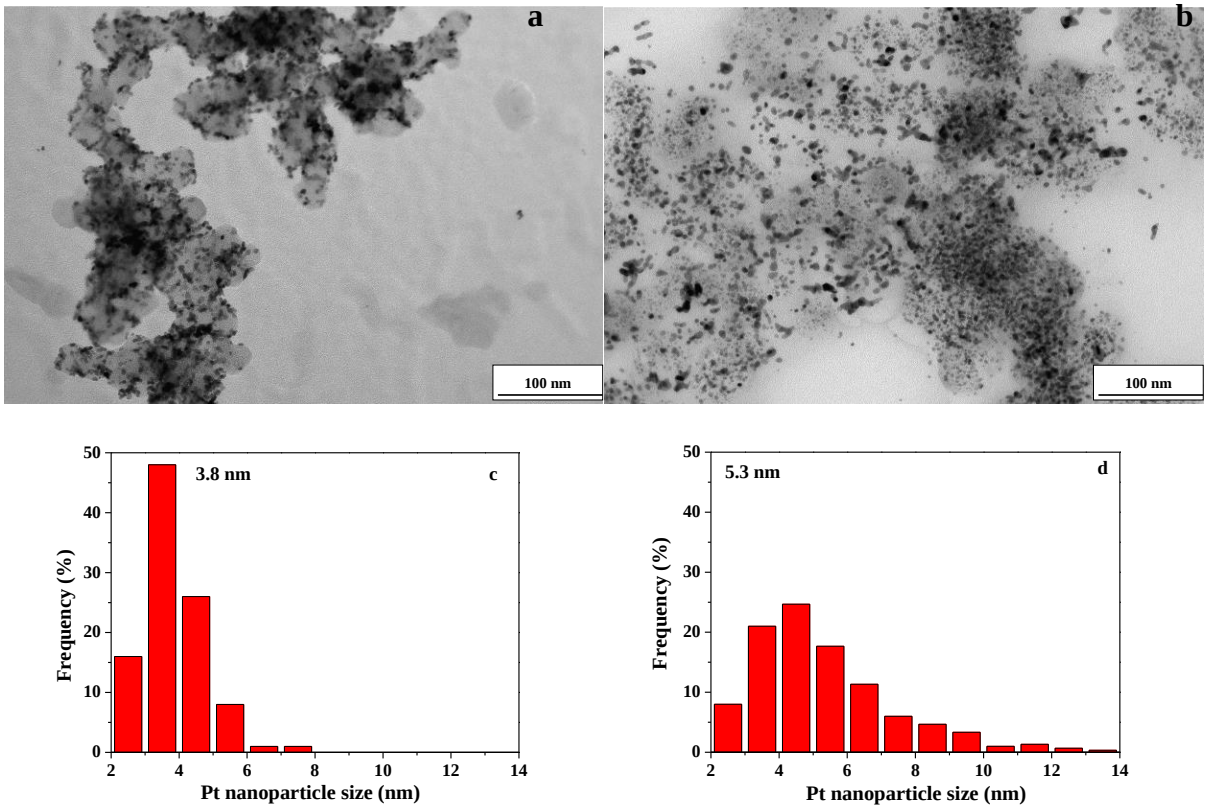

Figure 9: TEM micrographs of 50 % Pt/C before (a) and after 1200 cycles (b) and corresponding Pt nanoparticle size distribution histograms (c and d, respectively).

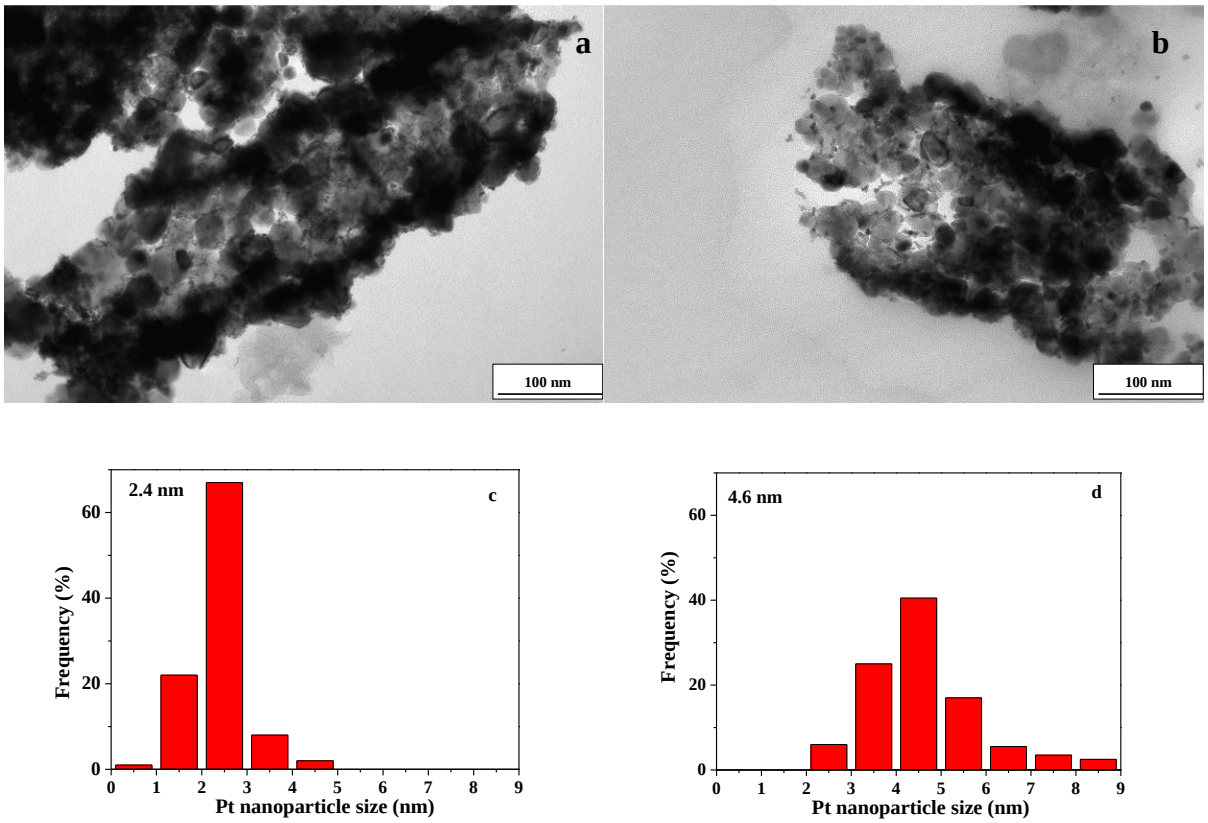

Figure 10: TEM micrographs of 20 % Pt/Nb-SnO$_2$-Vulcan before (a) and after 1200 cycles (b) and corresponding Pt nanoparticle size distribution histograms (c and d, respectively).

2.6 SEM characterisation of the catalyst layer after durability test

BSE-SEM images of the cross-section of Pt/Nb-SnO$_2$, Pt/Nb-SnO$_2$-Vulcan and Pt/C based cathodes after potential cycling are shown in Figure 11. The Pt/C cathode catalyst layer shows a significant aggregation of the Pt nanoparticles, whereas no particular aggregation of the Pt nanoparticle can be observed for the Pt/Nb-SnO$_2$ cathode, where the presence of the hollow fibres at the cathode is clearly visible. It is observed that the tubular structure of the support material is retained during electrode development and assembly of the MEA. Either or both of these steps, involving ink formation (ultra-sound treatment) and lamination under pressure could have caused physical degradation to the morphology. This is also true after the accelerated ageing cycling, where the tubes supporting the Pt nanocatalyst are clearly observed. In particular, Figure 8b shows the dispersion of the Pt particles all over the internal and external tube surfaces. Thus, the stability of these alternative supports to the MEA preparation route used, during polarisation and electrochemical cycling is then established.

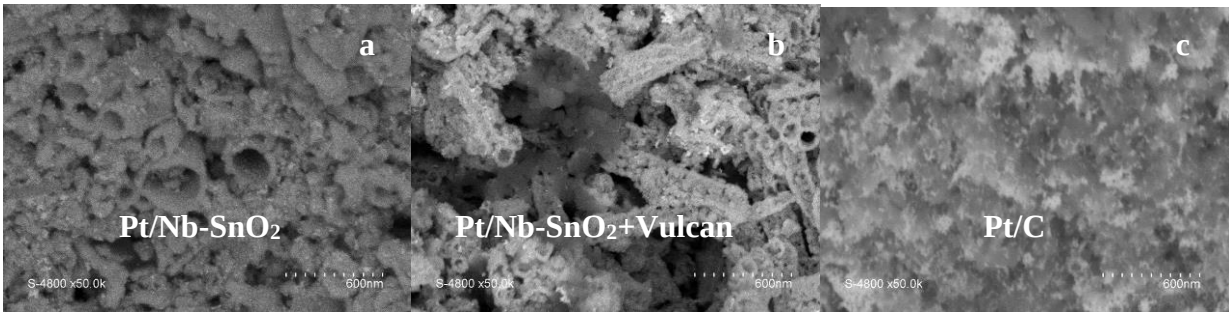

Figure 11: BSE-SEM images of 21 % Pt/Nb-SnO$_2$ (a), 20 % Pt/Nb-SnO$_2$-Vulcan (b), and 50 % Pt/C (c) based cathode after 1200 cycles.

Figure 12 shows SEM micrographs of the cross-sections of Pt/Nb-SnO$_2$, Pt/Nb-SnO$_2$-Vulcan and Pt/C based MEAs. For all MEAs Pt bands can be observed in the middle of the membrane. They are caused by Pt dissolution from the cathode and migration through the membrane, where it precipitates as Pt nanoparticles at the point where it meets crossover hydrogen. The presence of Pt in the membrane results in generation of peroxide radicals, which can attack the Nafion® membrane [19].

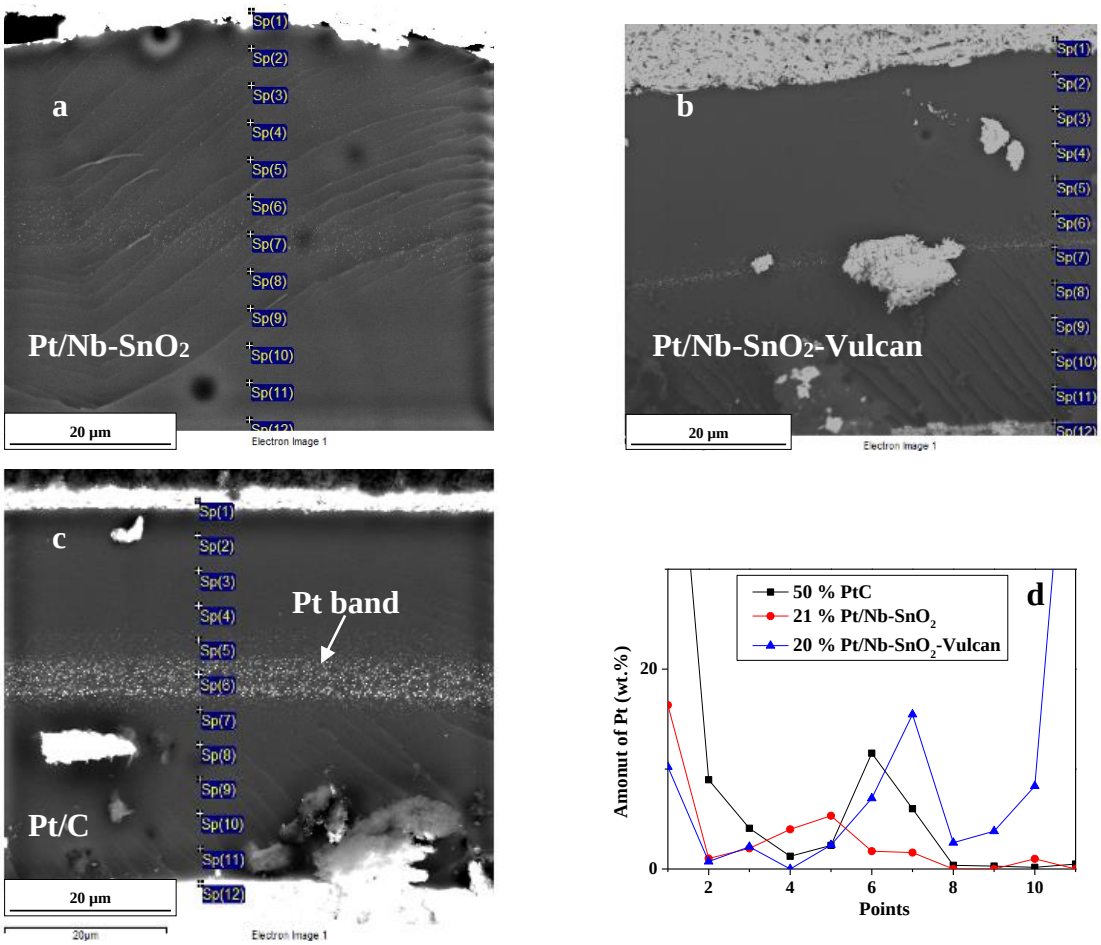

Figure 12: BSE-SEM cross-sections images of 21 % Pt/Nb-SnO$_2$ (a), 20 % Pt/Nb-SnO$_2$-Vulcan (b), and 50 % Pt/C (c) based MEAs after 1200 cycles and Pt amount measured by EDX analysis in the membrane (d).

For the MEA having the oxide support at the cathode, however, significantly less Pt is detected in the membrane (both visually and by EDX, Figure 12d.), and it may be concluded that the resistance to electrochemical oxidation of the support material at the cathode directly impacts the stability of the supported Pt catalyst with regard to dissolution and migration. This observation is important, and is interpreted as indicating that a strong metal support interaction has formed between Pt and Nb-SnO$_2$ that is effective in stabilising the Pt to dissolution at high cell voltage. Since support oxidation and Pt dissolution could, in principle, each be considered as separate degradation phenomena, this observation further shows that these degradation phenomena are in fact related when carbon supports are used, but can be decoupled by use of an oxide support.

Conclusions

The MEA based on Pt/Nb-SnO_2 (at the cathode) exhibits encouraging fuel cell performance and significantly enhanced durability compared to the MEA having Pt/C cathode. Such behaviour can be ascribed to carbon corrosion leading to platinum dissolution, migration and re-deposition of oxidised Pt into the membrane. Furthermore, carbon surface oxidation at high potentials leads to increased hydrophobicity of the catalyst layer, resulting in water management problems. SEM analysis after potential cycling indicated that the Pt/Nb-SnO_2 enables higher resistance to Pt dissolution than commercial Pt/C electrocatalyst, which is undoubtedly ascribable to a strong platinum-Nb-SnO_2 support interaction. Further effort will be made to identify this interaction by spectroscopic means.

Although addition of Vulcan XC-72R results in the improvement in PEMFC performance caused by increased cathode conductivity, the carbon component undergoes rapid corrosion at high potentials leading to performance degradation.

Perspectives

Further improvements in the electronic conductivity of tin oxide based cathodes are necessary to improve the performance of the corresponding MEAs. The use of different doping agents and in different proportions may increase this property.

A higher Pt loading on SnO_2 could also improve the electron transfer. This could be achieved by novel deposition methods (e.g. thin continuous metal layers) or by increasing the Pt adsorption (e.g. by using high surface area support). This would allow decreasing the catalyst layer thickness (see for instance [1]) for a fixed cathode loading and reducing the resistive issues (see paragraph 4).

Another possibility would be the use of carbon-based additives into the electrodes. For example Vulcan XC-72R can be replaced by CNT or highly graphitised CNF, which provide improved corrosion resistance. Utilisation of more conductive support material can lead to higher voltage in ohmic region and thus to enhanced power density (see paragraph 4).

Addition of Nafion® ionomer leads to the improvement in proton conductivity of the catalyst layer. However, at high Nafion® loading, some Pt active sites may be covered by a thick layer of ionomer, which hinders the reactants diffusion to the catalyst surface. Therefore, Nafion® amount needs to be optimised for each new catalyst support depending on its surface area and density to achieve better performance of Pt/Nb-SnO_2 based MEA.

3 Characterisation of Pt/Nb-SnO_2 based MEA with PBI/H_3PO_4 membrane

The HT-PEMFCs have gained a great interest due to easier water management and higher tolerable amount of impurities in the fuel. However, carbon oxidation rate increases with increasing temperature [20] and alternative support materials are therefore also of considerable interest for HT-PEMFCs. Amongst these, tin oxide has been studied as a corrosion resistant catalyst support for high temperature applications such as HT-PEMFC [4], regenerative PEMFC [21], and PEM electrolysers [22].

In this work, a brief evaluation was made of Pt/Nb-SnO_2-MEA performance and durability in HT-PEMFC. Electrocatalyst powders were mixed with Nafion® ionomer and sprayed onto the GDL (Sigracet 10 BC, 4 cm^2), in order to prepare cathode with Pt loading of 0.8 mg/cm^2. The thicknesses of obtained cathodes were between 20 - 22 µm. The cathodes were assembled without pressing with an in-house developed PBI/H_3PO_4 membrane and anode provided by Johnson Matthey with Pt loading of 0.8 mg/cm^2. The PBI/H_3PO_4 membrane was prepared by Aurélien Kreisz with thickness of ca 40 µm, proton conductivity ~ 160 S/cm at 140 °C and acid doping level (ADL) of 25. Experimental conditions are listed in Table 7.

Table 7: **HT-PEMFC testing conditions.**

Break-in	160 °C, 1 bar (abs), 0.2 A/cm^2
FC temperature	140 - 180 °C
Pressure	1 bar (abs)
Gases stoichiometry	H_2/O_2 – 1.5/2
Pt loading on the cathode	0.8 mg/cm^2
Nafion® loading on the cathode	0.17 mg/cm^2
Pt loading on the anode provided by JM	0.8 mg/cm^2

3.1 Performance evaluation at high temperature

The polarisation curves of Pt/Nb-SnO_2 and Pt/C based MEAs at temperatures ranging from 140 to 180 °C are shown in Figure 13. The fuel cell performance increases with increasing temperature for both MEAs, which is due to the higher membrane conductivity and improved reaction kinetics for both ORR and HOR at higher temperatures. Both types of MEAs show a dramatic voltage drop at low current densities compared to MEAs prepared with the Nafion® membrane and tested at 80 °C. Such high activation overpotential is well known for HT-PEMFCs, and can be attributed to the blocking of the Pt active sites in the electrode by phosphoric acid.

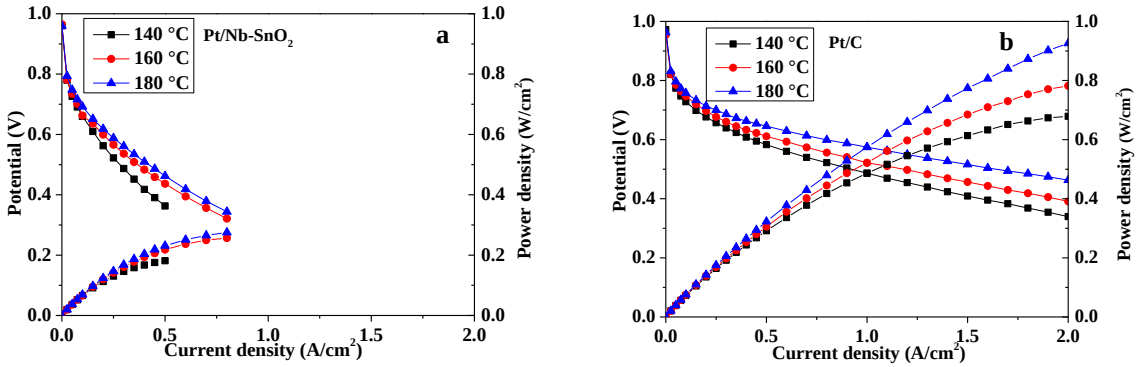

Figure 13: Polarisation curves of the Pt/Nb-SnO_2 (a) and Pt/C (b) at 140, 160 and 180 °C with Pt loading of 0.8 mg/cm^2.

The Pt/Nb-SnO_2-MEA provided a current density of ca. 0.6 V at 0.3 A/cm^2 (160 °C, H_2-O_2), which is lower than that for the Pt/C-MEA, and the electrode formulation requires optimisation. Parrondo et al. [23] also reported that at high concentrations of tin oxide in the cathode catalyst layer, the performance of HT-PEMFC decreased as a result of mass transport limitations within the electrode. Furthermore, $\mathbf{R_{el}}$ increased when tin oxide concentration increased from 7 to 18 wt. %.

In addition, low performance of Pt/Nb-SnO_2-MEA can be attributed to high electrode thickness of Pt/Nb-SnO_2-based cathode (ca 20 µm), which may lead to high ohmic and charge transfer resistances as well as high mass transport losses.

3.2 Electrochemical impedance spectroscopy

The electrochemical impedance spectra of Pt/Nb-SnO_2 and Pt/C at 140, 160 and 180 °C are depicted in Figure 14. The ohmic and charge transfer resistances of both MEAs were calculated using Randles model and listed in Table 8. The Pt/Nb-SnO_2-MEA provides higher ohmic and charge transfer resistances than Pt/C-MEA probably due to the presence of the less conductive oxide and lower ORR activity of Pt/Nb-SnO_2. The charge transfer resistance decreases with increasing temperature due to the improved ORR kinetics for both MEAs.

Despite of improved ORR kinetics at high temperatures, the charge transfer resistance of Pt/C-PBI/H_3PO_4 based MEA (0.64 mΩ cm^2 at 140 °C and 0.1 A/cm^2) is higher than that of Pt/C-Nafion® based MEA (0.50 mΩ cm^2 at 80 °C and 0.1 A/cm^2). This behaviour is consistent with low performance in activation region, which is attributed to adsorption of phosphates on the Pt surface and blocking of Pt active sites [24],[25].

Table 8: Ohmic and charge transfer resistance before and after stability test obtained from Nyquist plots at 0.1 A/cm² for Pt/Nb-SnO₂ and Pt/C based MEAs at different temperatures.

T °C	R_{el}, Ωcm²	R_{ct}, Ωcm²	CPE	α	C_{dl}, Fcm²
Pt/Nb-SnO₂					
180	0.237	0.810	0.478	0.65	0.061
160	0.211	0.960	0.520	0.64	0.076
140	0.175	1.150	0.564	0.63	0.088
Pt/C					
180	0.049	0.570	0.692	0.91	0.485
160	0.053	0.592	0.722	0.90	0.491
140	0.054	0.641	0.740	0.91	0.515

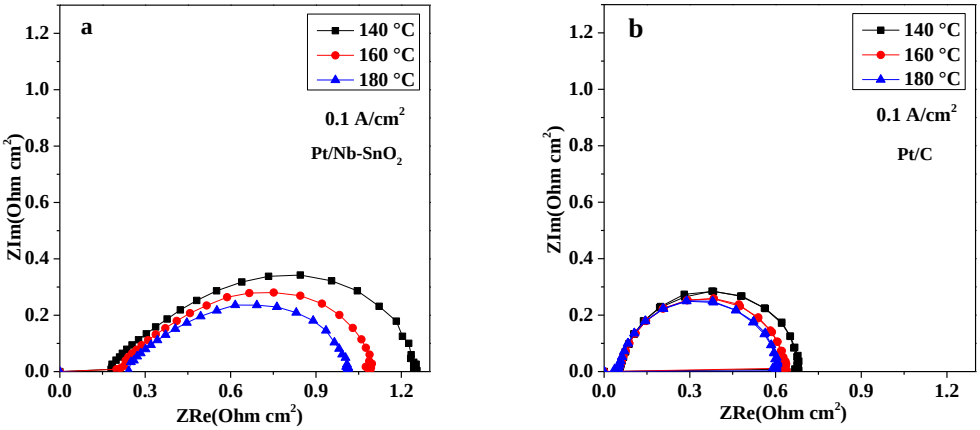

Figure 14: Electrochemical impedance spectra of Pt/Nb-SnO₂ (a) and Pt/C (b) at 140, 160 and 180 °C.

3.3 Durability evaluation of the Pt/Nb-SnO₂ based MEA at high temperature

The polarisation curves for Pt/Nb-SnO₂ and Pt/C based MEAs before and after stability test are shown in Figure 15. Both MEAs undergo degradation after potential cycling, particularly Pt/C-MEA exhibits a huge performance loss already after 400 cycles caused by carbon corrosion.

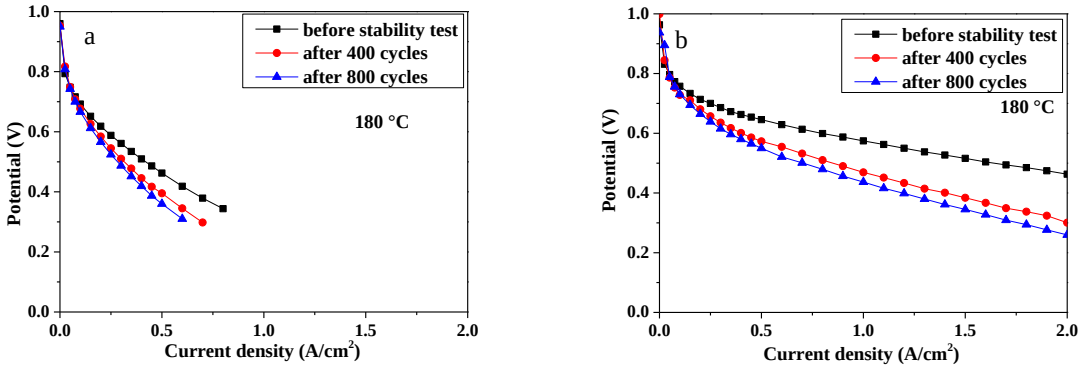

Figure 15: Polarisation curves for PEMFCs with Pt/Nb-SnO₂ (a) and Pt/C (b) catalyst before and after potential cycling test at 180 °C under H₂ and O₂.

3.4 Evaluation of MEA durability using impedance spectroscopy

The ohmic and charge transfer resistances calculated from the impedance spectra of Pt/C and Pt/Nb-SnO_2 based MEAs (Figure 16) are summarised in Table 9. The Pt/C-MEA shows an increase in charge transfer resistance of 0.353 Ωcm^2, whereas Pt/Nb-SnO_2-MEA provides smaller increase of 0.229 Ωcm^2, which may be related to the block of catalyst pore structure by phosphoric acid. In addition, $\mathbf{R_{el}}$ increases dramatically from ca 0.24 to 0.4 Ωcm^2 for Pt/Nb-SnO_2-MEA. This behaviour can be attributed to the H_3PO_4 leaching from the PBI/H_3PO_4 membrane, which results in a decrease in proton conductivity [26].

Table 9: Ohmic and charge transfer resistance before and after stability test obtained from Nyquist plots at 0.1 A/cm² for Pt/Nb-SnO₂ and Pt/C based MEAs at 180 °C before and after stability test.

Cycles	R_{el}, Ωcm^2	R_{ct}, Ωcm^2
Pt/Nb-SnO₂		
0	0.237	0.811
800	0.396	1.04
Pt/C		
0	0.049	0.570
800	0.071	0.927

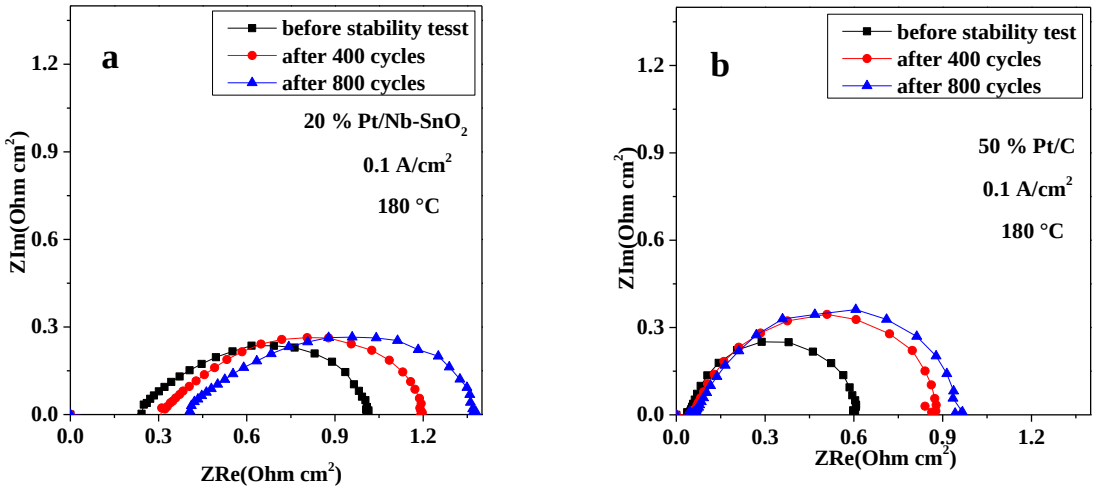

Figure 16: Electrochemical impedance spectra of Pt/Nb-SnO_2 (a) and Pt/C (b) catalyst at 180 °C.

3.5 TEM and SEM characterisation of MEAs after durability test

SEM and TEM micrographs of Pt/C and Pt/Nb-SnO$_2$ catalysts after stability test and the corresponding Pt nanoparticle size distribution histograms are shown in Figure 17, Figure 18 and Figure 19. Both catalysts show comparable Pt nanoparticle growth from 2.4 to 4.1 for Pt/Nb-SnO$_2$ (Figure 18) and from 3.8 to 4.5 nm for Pt/C (Figure 19).

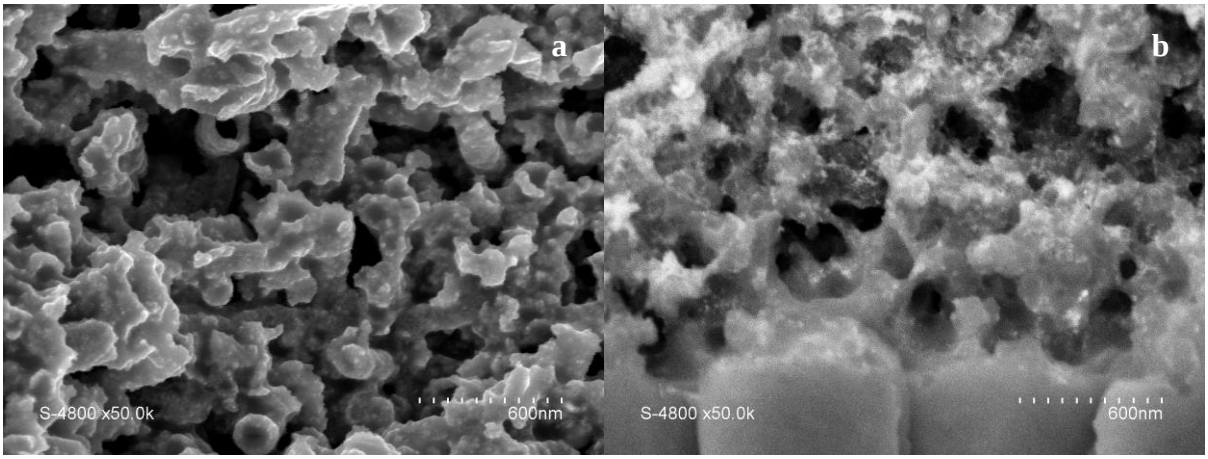

Figure 17: SEM micrographs of Pt/Nb-SnO$_2$ (a) and Pt/C (b) after 800 cycles at 180 °C.

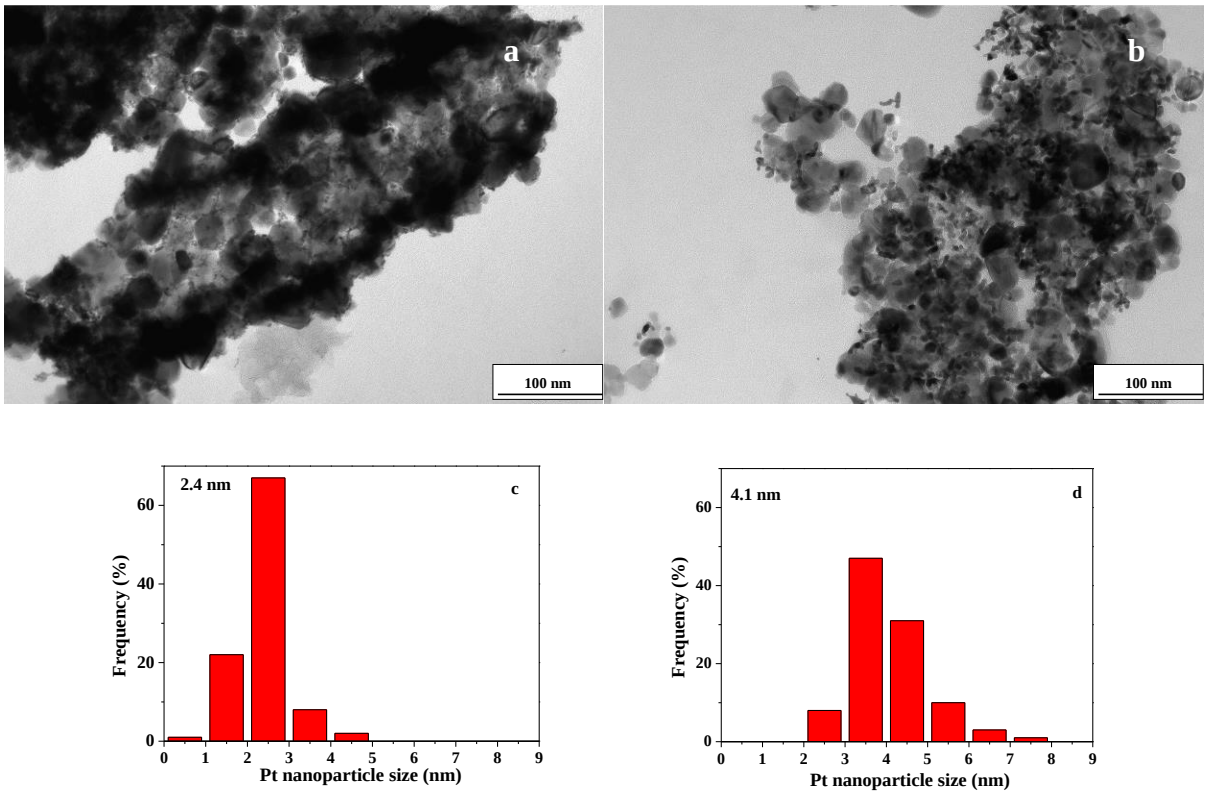

Figure 18: TEM micrographs of 20 % Pt/Nb-SnO$_2$ before (a) and after 800 cycles (b) and corresponding Pt nanoparticle size distribution histograms (c and d, respectively).

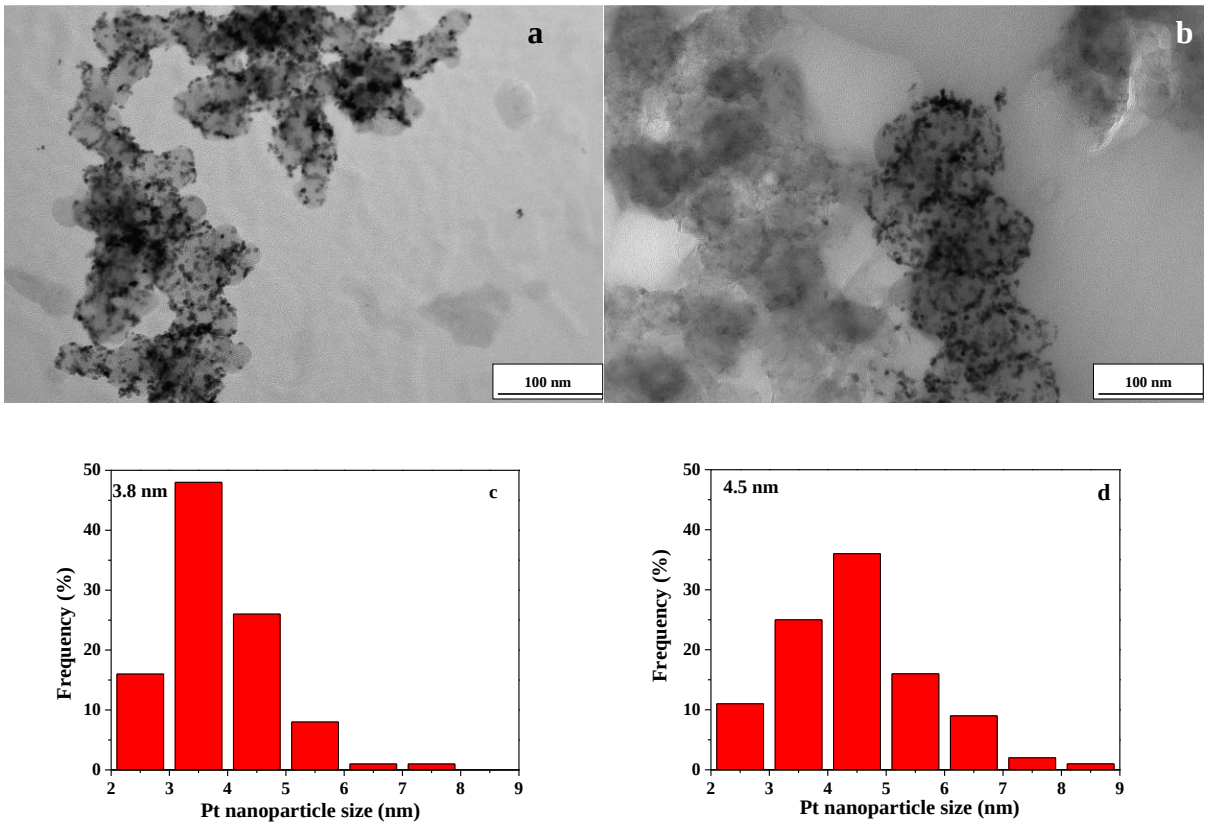

Figure 19: TEM micrographs of 50 % Pt/C before (a) and after 800 cycles (b) and corresponding Pt nanoparticle size distribution histograms (c and d, respectively).

SEM cross-section images of Pt/Nb-SnO_2 and Pt/C based MEAs after the stability test are shown in Figure 20. Unlike for Pt/Nb-SnO_2-MEA, for Pt/C-MEA the Pt band is next to the cathode side of Pt/C based MEA. Thus, a greater Pt amount in the membrane for Pt/C-MEA was measured using EDX analysis (Figure 20c). This result is attributed to the Pt nanoparticles dissolution from the cathode and re-deposition into the membrane, which leads to the thinning of the cathode layer and MEA performance drop, as described previously.

Conclusions

The Pt/Nb-SnO_2-MEA provides lower HT-PEMFC performance and higher ohmic and charge transfer resistances compared to the Pt/C-MEA. However, the electrode was non-optimised in terms of composition and porosity. The Pt/C-MEA undergoes severe degradation upon potential cycling caused by carbon corrosion, with Pt seen by electron microscopy to be detached in the electrode and to have migrated to form a Pt band in the membrane. Pt/Nb-SnO_2-MEA also shows significant performance degradation and an increase in ohmic and charge transfer resistances upon potential cycling, but the support is observed to remain unmodified, with low platinum migration into the membrane.

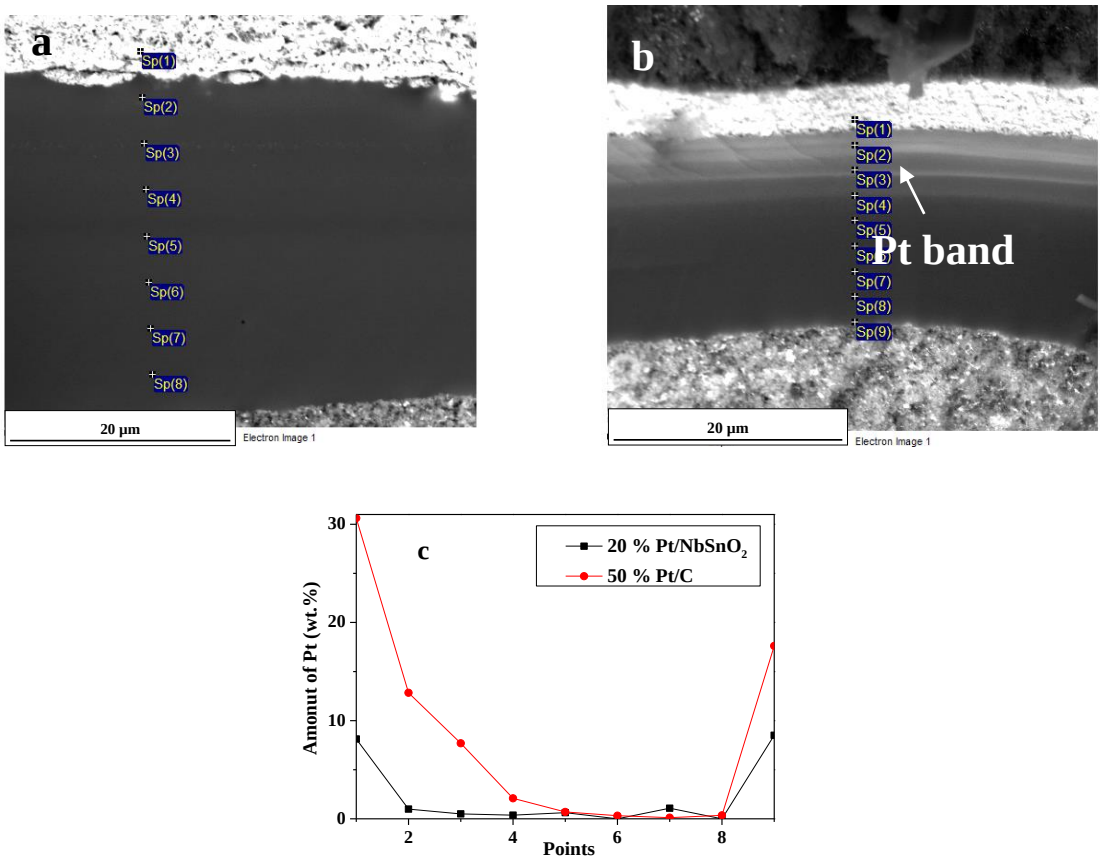

Figure 20: SEM cross-section micrographs of 20 % Pt/Nb-SnO$_2$ (a) and 50 % Pt/C (b) based MEAs after 800 cycles between 0.9-1.4 V at 180 °C and Pt amount measured by EDX in the membrane (c).

The ink formulation and the deposition method for the electrode preparation should be optimised. At the operating temperature of HT-PEMFC the conductivity of metal oxide is increasing due to their semi-conducting nature. While, the addition of a carbon additive in the catalyst layer could improve the cathode conductivity, a more promising route is to implement more highly conducting alternative supports such as the antimony doped tin oxide prepared in this work.

4 Characterisation of Pt/Sb-SnO₂ based MEA with Nafion® membrane

Following the calculation of Chhina et al. [27], we have estimated that Pt loading on Sb-SnO_2 hollow fibres with surface area of 42 m^2/g should be around 30 wt. %. The obtained Pt loading (33 wt. %) was determined using XRF, as described in the experimental part (Annex A).

4.1 Performance of Pt/Sb-SnO₂ based MEA

The polarisation curves obtained for MEAs with Pt/Nb-SnO_2 and Pt/Sb-SnO_2 cathodes are plotted in Figure 21. They show similar behaviour at low current densities, result that can be attributed to the similar ORR activity of both electrocatalysts. However, there is a markedly improved performance in the ohmic region for the MEA with the Pt/Sb-SnO_2 cathode, which is caused by the improved conductivity of the Sb-SnO_2. The maximum power density is 0.61 W/cm^2 for the MEA with Pt/Sb-SnO_2 cathode, what is a significant increase over the 0.41 W/cm^2 for the MEA with the Pt/Nb-SnO_2 cathode. In addition, high Pt loading on Sb-SnO_2 (33 wt. %) allows fabrication of thin catalyst layer, which may lead to lower ohmic and mass transport losses. Although the performance of Pt/Sb-SnO_2-MEA is still lower than that of Pt/C-MEA, this result clearly identifies the conductivity of the support as a one of the main factors driving MEA performance.

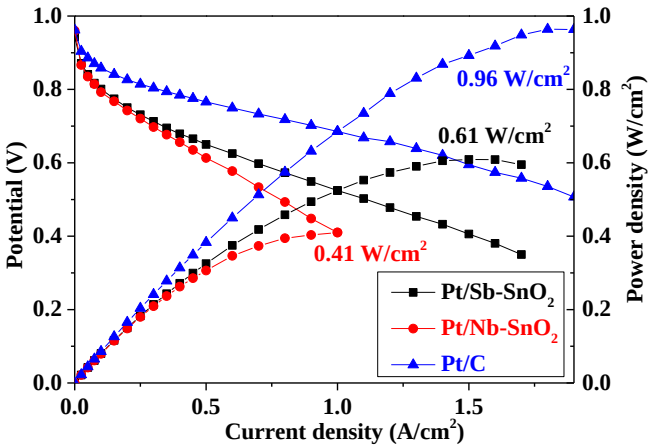

Figure 21: Polarisation curves of MEA with 21 wt. % Pt/Nb-SnO_2, 33 wt. % Pt/Sb-SnO_2 and 50 wt. % Pt/C cathodes at 80 °C and 100 % RH.

4.2 Electrochemical impedance spectroscopy

The ohmic and charge transfer resistances obtained from impedance spectra in Figure 22 are listed in Table 10. The Pt/Sb-SnO_2-MEA exhibits lower $\mathbf{R_{ct}}$ than Pt/Nb-SnO_2-MEA due to the improved conductivity of Sb doped SnO_2. This result is in agreement with the improved PEMFC performance for the Pt/Sb-SnO_2-MEA.

Table 10: Elements of the equivalent circuit obtained by fitting the impedance spectra.

A/cm²	R_{el}, Ωcm²	R_{ct}, Ωcm²	CPE	α	C_{dl}, Fcm²
Pt/Nb-SnO₂					
0.1	0.095	0.835	0.092	0.79	0.021
0.3	0.090	0.460	0.120	0.78	0.025
0.5	0.088	0.404	0.145	0.78	0.027
Pt/Sb-SnO₂					
0.1	0.091	0.789	0.117	0.85	0.046
0.3	0.092	0.371	0.093	0.88	0.041
0.5	0.092	0.296	0.088	0.89	0.41
Pt/C					
0.1	0.071	0.503	0.287	0.88	0.152
0.3	0.072	0.180	0.296	0.87	0.123
0.5	0.070	0.114	0.282	0.88	0.120

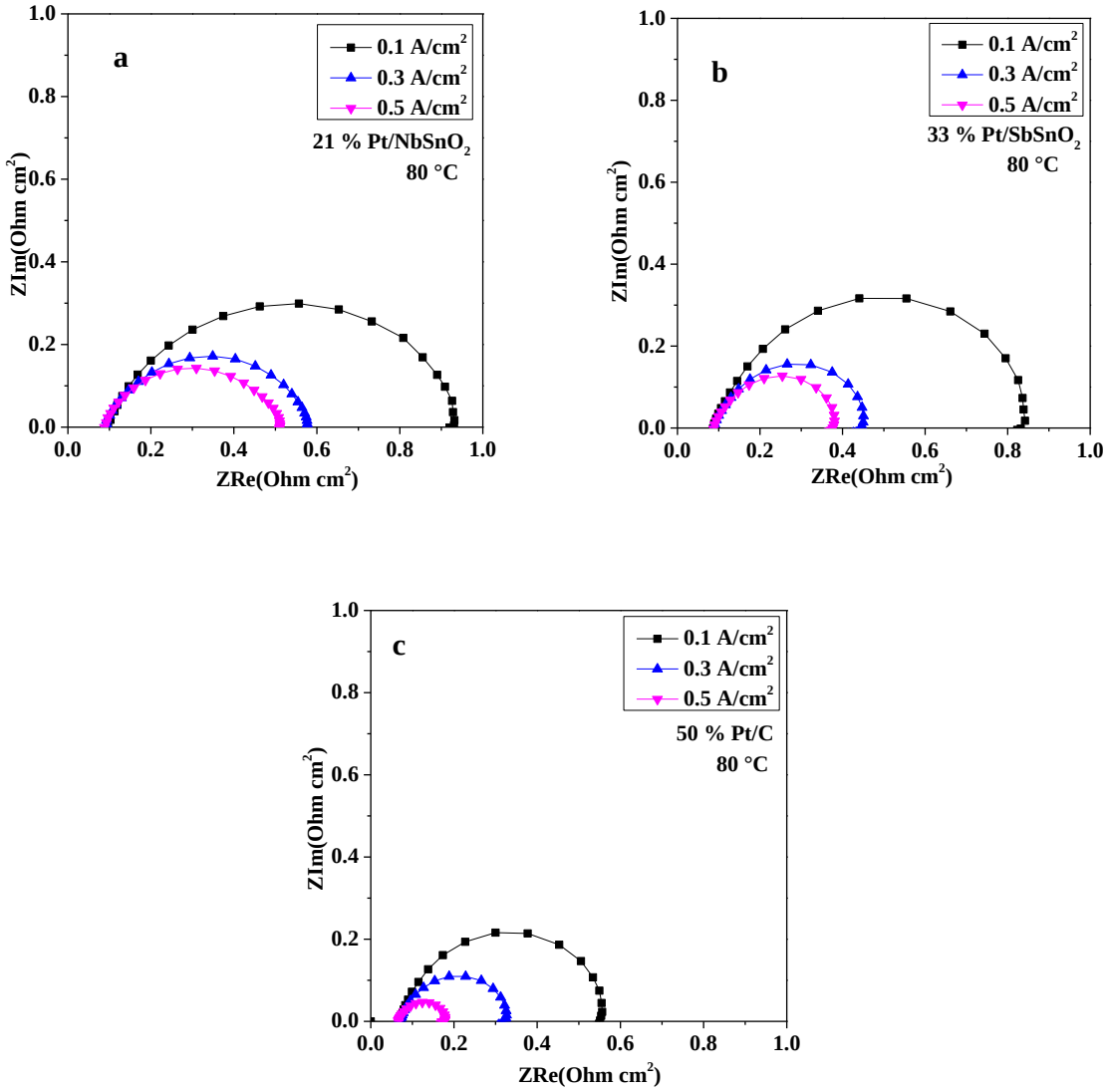

Figure 22: Nyquist plot of Pt/Nb-SnO₂ (a) Pt/Sb-SnO₂ (b) and Pt/C (c) based MEA for different current densities, over the frequency range from 20 kHz to 100 mHz.

4.3 Stability to potential cycling

The polarisation curves obtained before and after the potential cycling test for Pt/Sb-SnO_2, Pt/Nb-SnO_2 and Pt/C based MEAs are shown in Figure 23. After potential cycling, the performance of the Pt/C based MEA decreased dramatically, while only a slight performance decrease was observed for MEA based on Pt/Sb-SnO_2.

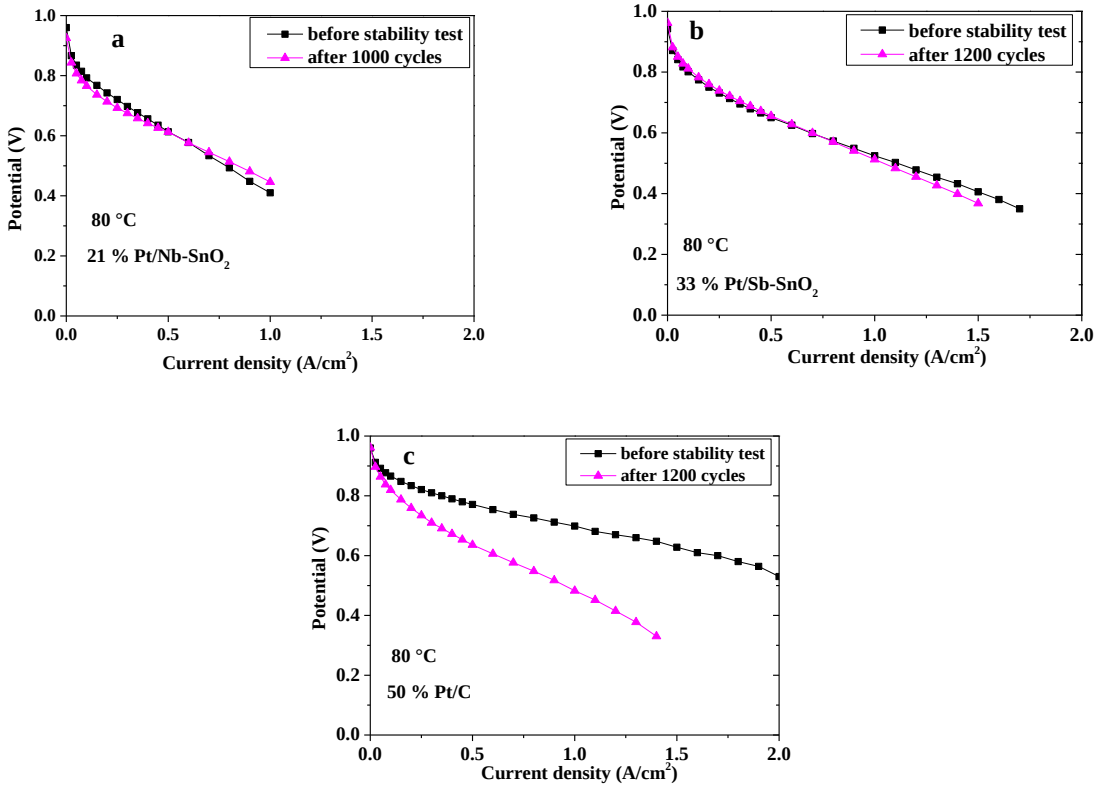

Figure 23: Polarisation curves of the Pt/Nb-SnO_2 (a), Pt/Sb-SnO_2 (b) and Pt/C (c) based MEAs before and after stability test at 80 °C and 100 % RH.

4.4 Evaluation of MEA durability using impedance spectroscopy

The ohmic and charge transfer resistances obtained from impedance spectra in Figure 24 are listed in Table 11. The ohmic resistances remained almost unchanged after the potential cycling test for all MEAs. However, Pt/Sb-SnO_2-MEA showed a lower decrease of charge transfer resistance than Pt/C-MEA, but higher than Pt/Nb-SnO_2-MEA, which can be attributed to the slightly lower stability of Pt/Sb-SnO_2 compared to Pt/Nb-SnO_2 based MEA. Sasaki et al. [10] and Kakinuma et al. [3] also have shown that Pt supported on Sb doped SnO_2 is less stable than Pt on Nb doped SnO_2, due to Sn dissolution from the Sb doped SnO_2, leading to performance degradation caused by Pt poisoning by Sn [3]. In addition, Suchsland et al. [11] reported that antimony leached out of the tin oxide, leading to the poisoning of the Pt surface and activity loss.

Table 11: Elements of the equivalent circuit obtained by fitting the impedance spectra.

Cycles	R_{el}, Ω cm^2	R_{ct}, Ω cm^2
Pt/Sb-SnO$_2$		
0	0.095	0.835
1200	0.092	0.888
Pt/C		
0	0.071	0.503
1200	0.070	0.900
Pt/Nb-SnO$_2$		
0	0.095	0.835
1200	0.098	0.810

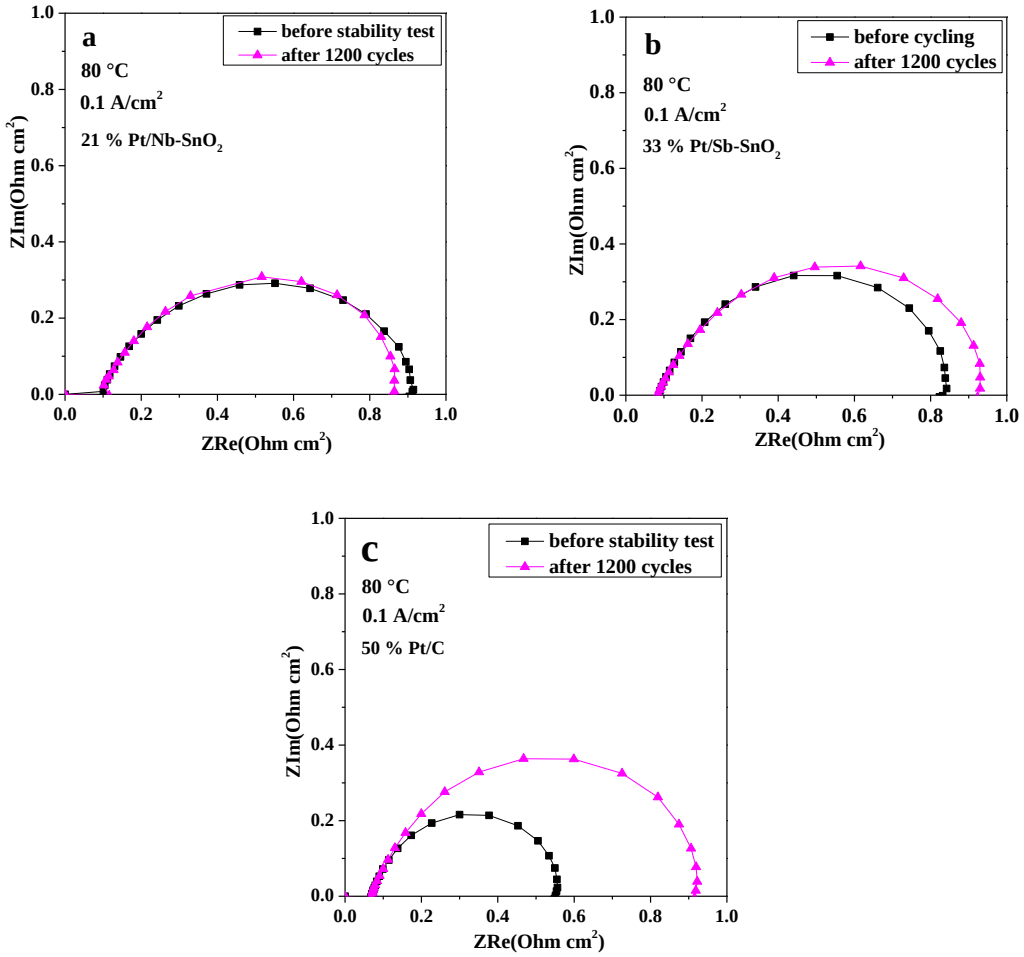

Figure 24: Electrochemical impedance spectra of Pt/Nb-SnO$_2$ (a), Pt/Sb-SnO$_2$ (b) and Pt/C (c) based MEA before and after potential cycling test.

MEAs integrating Nb- or Sb-SnO$_2$ based cathodes provide similar cell voltage at low current density, but Pt/Sb-SnO$_2$-MEA shows significantly higher performance in ohmic region, as a result of the improved conductivity of the catalyst. Although it provides lower maximum power density compared to Pt/C-MEA, the results clearly show promise.

Conclusions and perspectives

This chapter describes *in situ* characterisation of doped tin oxide supported Pt in a single test station. The cathodes based on Pt/Nb-SnO_2, Pt/Sb-SnO_2 and Pt/C were prepared by CCS method, in which the catalyst ink was spray-coated onto GDL. The obtained gas diffusion electrodes (GDE) were hot-pressed with Nafion® or PBI/H_3PO_4 membranes and anode, in order to fabricate MEA. Performance of the obtained MEAs was evaluated before and after accelerated stress test, which was performed to simulate potential changes during start-up and shutdown of fuel cell. In addition, impedance spectroscopy was used to evaluate the charge transfer resistance at the cathode before and after the stability test. Finally, presence of Pt band in the membrane after stability test was determined by SEM microscopy.

A strong dependence of PEMFC durability on the catalyst supports was observed**.** The Pt/Nb-SnO_2-Nafion based MEA exhibited better stability than Pt/C based MEA, which can be attributed to higher corrosion resistance and stronger interactions between Pt nanoparticles and oxide-based support. However, it showed higher ohmic and charge transfer resistances and thus lower maximum power density than Pt/C based MEA, probably due to the lower conductivity and surface area of Nb-SnO_2 compared to that of carbon. In order to enhance conductivity of the catalyst layer, commercial Vulcan XC-72R was mixed with Pt/Nb-SnO_2 before spray-coating. This led to enhanced maximum power density, but decreased stability indicating rapid corrosion of Vulcan XC-72R support, which should be replaced by graphitised carbon or more conductive ceramic support such as Sb doped SnO_2.

Therefore, Sb-SnO_2 supported Pt was characterised in a single PEMFC test station and compared to Pt/Nb-SnO_2-MEA. Both oxide based MEAs provide similar performance at low current density, but different slopes indicating improved conductivity of Sb-SnO_2 based cathode. As expected, it exhibited higher performance than Pt/Nb-SnO_2-MEA maintaining high durability. However, Pt/Sb-SnO_2-MEA provides lower maximum power density than Pt/C-MEA. Therefore, ORR activity of the oxide supported Pt needs to be improved by increasing surface area and conductivity of the oxide support.

It was expected that at elevated temperature Nb-SnO_2 based cathode will provide higher conductivity and thus improved fuel cell performance. However, the Pt/Nb-SnO_2-PBI/H_3PO_4 based MEA provided decreased performance at 180 °C. This behaviour can be attributed to the blocking of cathode pore structure and Pt active sites by phosphoric acid.

For the future work, Pt loading on the oxide-based support and Nafion® amount in the catalyst layer as well as cathode thickness and porosity need to be optimised, in order to improve PEMFC performance of oxide based MEA. Finally, PTFE can be added to the catalyst ink, in order to increase hydrophobicity of the electrode. In the case of HT-PEMFC, Nafion® in the catalyst layer should be replaced by more efficient binder such as polyvinylidene difluoride (PVDF), which allows to achieve lower ohmic and charge transfer resistance leading to improved maximum power density [28].

References

[1] P. Zhang, S.-Y. Huang, and B. N. Popov, "Mesoporous Tin Oxide as an Oxidation-Resistant Catalyst Support for Proton Exchange Membrane Fuel Cells," *Journal of The Electrochemical Society*, vol. 157, no. 8, p. B1163, 2010.

[2] K. Kanda, Z. Noda, Y. Nagamatsu, T. Higashi, S. Taniguchi, S. M. Lyth, a. Hayashi, and K. Sasaki, "Negligible Start-Stop-Cycle Degradation in a PEFC Utilizing Platinum-Decorated Tin Oxide Electrocatalyst Layers with Carbon Fiber Filler," *ECS Electrochemistry Letters*, vol. 3, no. 4, pp. F15–F18, Feb. 2014.

[3] K. Kakinuma, Y. Chino, Y. Senoo, M. Uchida, T. Kamino, H. Uchida, S. Deki, and M. Watanabe, "Characterization of Pt catalysts on Nb-doped and Sb-doped $SnO_{2-\delta}$ support materials with aggregated structure by rotating disk electrode and fuel cell measurements," *Electrochimica Acta*, vol. 110, pp. 316–324, Nov. 2013.

[4] J. Xu, D. Aili, Q. Li, C. Pan, E. Christensen, J. O. Jensen, W. Zhang, G. Liu, X. Wang, and N. J. Bjerrum, "Antimony doped tin oxide modified carbon nanotubes as catalyst supports for methanol oxidation and oxygen reduction reactions," *Journal of Materials Chemistry A*, vol. 1, no. 34, p. 9737, 2013.

[5] S.-Y. Huang, P. Ganesan, and B. N. Popov, "Electrocatalytic Activity and Stability of Titania-Supported Platinum–Palladium Electrocatalysts for Polymer Electrolyte Membrane Fuel Cell," *ACS Catalysis*, vol. 2, no. 5, pp. 825–831, May 2012.

[6] S.-Y. Huang, P. Ganesan, and B. N. Popov, "Titania supported platinum catalyst with high electrocatalytic activity and stability for polymer electrolyte membrane fuel cell," *Applied Catalysis B: Environmental*, vol. 102, no. 1–2, pp. 71–77, Feb. 2011.

[7] M. K. Debe, A. K. Schmoeckel, G. D. Vernstrom, and R. Atanasoski, "High voltage stability of nanostructured thin film catalysts for PEM fuel cells," *Journal of Power Sources*, vol. 161, no. 2, pp. 1002–1011, Oct. 2006.

[8] M. Yin, J. Xu, Q. Li, J. O. Jensen, Y. Huang, L. N. Cleemann, N. J. Bjerrum, and W. Xing, "Highly active and stable Pt electrocatalysts promoted by antimony-doped SnO_2 supports for oxygen reduction reactions," *Applied Catalysis B: Environmental*, vol. 144, pp. 112–120, Jan. 2014.

[9] A. Masao, S. Noda, F. Takasaki, K. Ito, and K. Sasaki, "Carbon-Free Pt Electrocatalysts Supported on SnO_2 for Polymer Electrolyte Fuel Cells," *Electrochemical and Solid-State Letters*, vol. 12, no. 9, p. B119, 2009.

[10] K. Sasaki, F. Takasaki, and Z. Noda, "Alternative Electrocatalyst Support Materials for Polymer Electrolyte Fuel Cells Thermochemical stability of support materials," *ECS Transactions*, vol. 33, no. 1, pp. 473–482, 2010.

[11] J. P. Suchsland, B. Klose-Schubert, D. Herein, T. Martin, C. Eickes, and M. Lennartz, "The Potential of Non Carbon Based Catalysts for Automotive Fuel Cells," *ECS Transactions*, vol. 50, no. 2, pp. 1659–1667, 2012.

[12] T. Higashi, Z. Noda, A. Hayashi, and K. Sasaki, "Pulse Laser Deposition and Sputtering of Carbon-free Pt/SnO_2 Electrocatalysts for PEFC," *ECS Transactions*, vol. 58, no. 1, pp. 1293–1299, 2013.

[13] J. E. B. Randels, "Kinetics of rapid electrode reactions," *Discussions of the Faraday Society*, vol. 1, pp. 11–19, 1947.

[14] X. Yuan, H. Wang, J. Colinsun, and J. Zhang, "AC impedance technique in PEM fuel cell diagnosis - A review," *International Journal of Hydrogen Energy*, vol. 32, no. 17, pp. 4365–4380, Dec. 2007.

[15] X.-Z. Yuan, C. Song, H. Wang, and J. Zhang, *Electrochemical Impedance Spectroscopy in PEM Fuel Cells*. London: Springer-Verlag, 2010, pp. 1–413.

[16] G. J. Brug, A. L. G. Van der Eeden, M. Sluyters-Rehbach, and J. H. Sluyters, "The analysis of electrode impedances complicated by the presence of a constant phase element," *J. Electroanal. Chem.*, vol. 176, pp. 275–295, 1984.

[17] K. Kakinuma, M. Uchida, T. Kamino, H. Uchida, and M. Watanabe, "Synthesis and electrochemical characterization of Pt catalyst supported on $Sn_{0.96}Sb_{0.04}O_{2-\delta}$ with a network structure," *Electrochimica Acta*, vol. 56, no. 7, pp. 2881–2887, Feb. 2011.

[18] K. Kinoshita and J. A. S. Bett, "Influence of electrochemical treatment in phosphoric acid on the wettability of carbons," *Carbon*, vol. 13, pp. 405–409, 1975.

[19] J. Peron, Y. Nedellec, D. Jones, and J. Roziere, "The effect of dissolution, migration and precipitation of platinum in Nafion®-based membrane electrode assemblies during fuel cell operation at high potential," *Journal of Power Sources*, vol. 185, no. 2, pp. 1209–1217, Dec. 2008.

[20] L. M. Roen, C. H. Paik, and T. D. Jarvi, "Electrocatalytic Corrosion of Carbon Support in PEMFC Cathodes," *Electrochemical and Solid-State Letters*, vol. 7, no. 1, p. A19, 2004.

[21] J. C. Cruz, S. Rivas, D. Beltran, Y. Meas, R. Ornelas, G. Osorio-Monreal, L. Ortiz-Frade, J. Ledesma-García, and L. G. Arriaga, "Synthesis and evaluation of ATO as a support for Pt–IrO_2 in a unitized

regenerative fuel cell," *International Journal of Hydrogen Energy*, vol. 37, no. 18, pp. 13522–13528, Sep. 2012.

[22] A. T. Marshall and R. G. Haverkamp, "Electrocatalytic activity of IrO_2–RuO_2 supported on Sb-doped SnO_2 nanoparticles," *Electrochimica Acta*, vol. 55, no. 6, pp. 1978–1984, Feb. 2010.

[23] J. Parrondo, F. Mijangos, and B. Rambabu, "Platinum/tin oxide/carbon cathode catalyst for high temperature PEM fuel cell," *Journal of Power Sources*, vol. 195, no. 13, pp. 3977–3983, Jul. 2010.

[24] A. Kamat, M. Herrmann, D. Ternes, O. Klein, U. Krewer, and S. Scholl, "Experimental Investigations into Phosphoric Acid Adsorption on Platinum Catalysts in a High Temperature PEM Fuel Cell," *Fuel Cells*, vol. 11, no. 4, pp. 511–517, Aug. 2011.

[25] S. Kaserer, K. M. Caldwell, D. E. Ramaker, and C. Roth, "Analyzing the Influence of H_3PO_4 as Catalyst Poison in High Temperature PEM Fuel Cells Using in-operando X-ray Absorption Spectroscopy," *The Journal of Physical Chemistry B*, vol. 117, pp. 6210–6217, 2013.

[26] G. Liu, H. Zhang, J. Hu, Y. Zhai, D. Xu, and Z. Shao, "Studies of performance degradation of a high temperature PEMFC based on H_3PO_4-doped PBI," *Journal of Power Sources*, vol. 162, no. 1, pp. 547–552, Nov. 2006.

[27] H. Chhina, "Oxidation-resistatnt catalyst supports for Proton exchnge membrane fuel cells," 2009.

[28] H. Su, S. Pasupathi, B. Bladergroen, V. Linkov, and B. G. Pollet, "Optimization of gas diffusion electrode for polybenzimidazole-based high temperature proton exchange membrane fuel cell: Evaluation of polymer binders in catalyst layer," *International Journal of Hydrogen Energy*, vol. 38, no. 26, pp. 11370–11378, Aug. 2013.

CONCLUSIONS
AND
FUTURE PERSPECTIVES

CONCLUSIONS AND FUTURE PERSPECTIVES

Carbon blacks are the state-of-the-art electrocatalyst support materials for PEMFC technology due to their high surface area and electrical conductivity. However, they suffer from severe corrosion in particular during start-up and shut-down of the PEMFC. Thus, the objective of this thesis is to develop corrosion resistant support materials that can potentially replace carbon. Therefore, three types of materials: graphitised carbon, TiO_2 and SnO_2 nanofibres were selected due to their stability and strong metal support interactions. Nanofibres and nanotubes were prepared using electrospinning technique, in order to exploit the directional properties of this nanometric 1D materials. The obtained materials were characterised using various techniques such as SEM, TEM, XRD, XPS, Raman spectroscopy, N_2 adsorption/desorption analysis, and electrical conductivity measurements. The conductivity of the oxide-based materials was improved by doping the support with aliovalent ions and by specific thermal treatments. In a further step, Pt nanoparticles were prepared by microwave-assisted polyol method and deposited onto the selected electrospun fibres and a commercial carbon based support (Vulcan XC-72R). The Pt loading on the carbon-based and on the oxide-based supports was determined using TGA and XRF, respectively. ORR activity and stability of the obtained electrocatalysts were characterised using RDE and compared to that of the commercial Pt/C. The size of Pt nanoparticles before and after prolonged potential cycling was estimated using TEM. The sample with the best electrochemical properties was selected for further *in situ* characterisation in a fuel cell setup. Electrochemical impedance spectroscopy was used to evaluate charge transfer resistance of the cathode before and after stability test.

As described in Chapter 2, CNFs were carbonised at three different temperatures (700, 1000 and 1500 °C) in order to find a compromise between higher electrochemical stability and specific surface area. CNF_{700} showed higher surface area, but was not conductive enough to be used as catalyst support in PEMFC. CNF_{1000} and CNF_{1500} gave much higher conductivity, but lower surface area than CNF_{700}. CNF_{1500} was more stable than $CNFs_{1000}$ and commercial support (Vulcan XC-72R).

ORR activity and stability of Pt supported on CNF_{1000} was lower than that of the Pt supported on Vulcan XC-72R and of the commercial Pt/C electrocatalyst due to the low corrosion resistance of the support and agglomeration of Pt nanoparticles.

For future work, nitrogen doping can be used to improve electrochemical stability, conductivity and interaction between Pt nanoparticles and CNFs. Furthermore, steam activation during the carbonisation step could allow fabrication of CNFs with improved surface area. Also, it would be interesting to obtain interconnected free-standing carbon nanofibres mat, which can be directly used as support for PEMFC. Finally, the stability of Pt/CNF could be improved by increasing carbonisation temperature of the carbon materials. Even though, the use of graphitised carbons slow down corrosion kinetics, but it cannot be completely avoided. Therefore, development of more stable ceramic supports such as metal oxides is required.

Thus, in Chapter 3, electrospun titania 1 D structures were explored as an alternative catalyst supports. Titania nanofibres and tubes were prepared by single-needle and coaxial electrospinning, respectively. TiO_2 nanofibres were selected for further characterisation due to their high surface area. The electrical conductivity of TiO_2 nanofibres was improved by Nb doping and thermal treatment at 800 °C in the presence of hydrogen. In addition, Nb doping inhibited TiO_2 grain growth leading to the enhancement of the surface area of the nanofibres. However, the surface area decreased significantly after calcination at high temperatures. These reduced Nb doped titania nanofibres provided better electrochemical stability at high potentials than carbon-based supports. However, the stability of Pt supported on Nb doped titania towards potential cycling was lower compared to Pt supported on Vulcan XC-72R and to the commercial Pt/C, probably due to the formation of a nonconductive TiO_2 layer on the surface of the TiO_x fibres. Furthermore, ORR activity of the titania supported Pt was lower than that of the Pt/C. This behaviour was attributed to lower conductivity and surface area of the oxide-based support. Therefore, electrical conductivity of TiO_2 can be further increased by using different doping agents (e.g. Ta and W). In order to improve the surface area of titania, addition of porogens to electrospinning solution is envisaged.

In the next part of the work, SnO_2 was also characterised as catalyst support for PEMFC owing to its higher conductivity compared to TiO_2. Thus, tin oxide fibres and tubes were obtained by combining electrospinning with an appropriate thermal treatment. The formation of hollow structures during thermal treatment was attributed to gas expansion (using relatively high heating rates) and to Kirkendall effect (diffusion via vacancies). In addition, Nb and Sb doping promoted the formation of hollow fibres and inhibited SnO_2 grain growth leading to an increase in the surface area of doped SnO_2. Furthermore, the addition of Nb and Sb resulted in improved electrical conductivity of SnO_2. In particular, Sb doped SnO_2 presented

high electrical conductivity of ca 1 S/cm, which increased with the temperature approaching conductivity of Vulcan XC-72R.

As expected, Nb doped tin oxide exhibited higher electrochemical stability at high potentials than commercial carbon support. Consequently, Pt supported on Nb doped SnO_2 provided higher stability towards potential cycling than commercial Pt/C electrocatalyst. Therefore, it was chosen for further *in situ* characterisation in a single PEMFC test bench.

In the final part of this study, Pt supported on Nb doped SnO_2 was integrated in MEA with Nafion® and PBI/H_3PO_4 membranes, in order to investigate its performance and durability at 80 °C and 180 °C.

At 80 °C Pt/Nb-SnO_2-MEA showed lower maximum power density, but higher stability compared to Pt/C based MEA. In the case of Pt/C-MEA, Pt band was observed in the membrane after stability test indicating Pt dissolution from the cathode, migration and re-deposition into the membrane.

In order to increase the conductivity of the catalyst layer, Vulcan XC-72R support was added to the Pt/Nb-SnO_2. This resulted in improved fuel cell performance, but lower stability indicating corrosion of the Vulcan XC-72R, which can be replaced by more stable CNTs or graphitised CNFs.

As expected, Pt/Sb-SnO_2-MEA provided comparable stability, but higher performance than Pt/Nb-SnO_2-MEA, due to the higher conductivity of the Sb-SnO_2 support.

At 180 °C Pt/Nb-SnO_2-MEA provided poor performance and poor stability probably due to blocking of Pt active sites and electrode pore structure by phosphoric acid leaking out from the membrane.

In order to improve the MEA performance the optimisation of the cathode layer structure (thickness, porosity) and preparation technique (hot-pressing conditions, use of CCM method) should be performed in the case of the oxide based electrocatalysts. In addition, catalyst and ionomer loadings need to be optimised.

Despite the lower conductivity and surface area of the prepared Sb doped SnO_2 hollow fibres as compared to that of Vulcan XC-72R, they can be considered as promising catalyst support for PEMFC due to their better electrochemical stability. In order to increase surface area and conductivity of such supports, composite materials containing both oxide and graphitised carbon can be developed to combine stability and SMSI of oxide with high conductivity and surface area of carbon-based supports.

ANNEX A:

Experimental part

1. Synthesis of nanofibres and tubes via electrospinning

Elaboration of carbon nanofibres

A 7.5 wt. % polyacrylonitrile (PAN, Mw = 150,000, Sigma-Aldrich) solution in N,N-dimethylformamide (DMF, 98 %, Sigma-Aldrich) was stirred at 60 °C overnight, in order to dissolve polymer and obtain homogeneous solution. The obtained solution was loaded in a plastic syringe stainless steel needle. The needle was connected to a voltage supply (CZE 1000R, Spellman, High Voltage Electronics Corporation), which can generate voltages up to 30 kV. A syringe pump (kdScientific) was used to control the flow rate. A grounded aluminium collector plate was used to collect the fibres. The distance between the needle tip and the rotating drum was around 10 cm, the flow rate was 0.5 mL/h and the applied voltage was 10 kV. The resulting white electrospun nanofibres were stabilised in air at 280 °C for 1 h with a heating rate of 1 °C/min, leading to a brown material. Afterwards stabilised nanofibres were carbonised at 700, 1000 and 1500 °C for 1 h in a nitrogen atmosphere with a heating rate of 5 °C/min. Obtained powder was black in colour.

Elaboration of titania nanofibres

In order to obtain carrier polymer solution, 0.23 g of polyvinyl pyrrolidone (PVP with average molar mass of ~1,300,000 g/mol, Aldrich) was dissolved in 3.3 mL of absolute ethanol (Sigma-Aldrich). This solution was then added to a precursor mixture made of 0.52 mL of titanium (IV) isopropoxide (97 %, Aldrich, stored in a glove box), 0 to 0.16 mL (for 0 to 20 at. % doping) of niobium ethoxide (99.95 %, Aldrich, stored in a glove box) and 1 mL of acetic acid (Sigma-Aldrich). The obtained yellow solution was stirred for 1 hour at room temperature.

Electrospinning of the solution containing slightly hydrolysed alkoxide was carried out in air with a plastic syringe and a grounded aluminium collector plate. The distance between the needle tip and the collector plate was 10 cm, the applied voltage was 15 kV and the flow rate was 0.5 mL/h. The as-prepared fibres were calcined in air at 500 °C or 800 °C at 5 °C/min for 6 h, in order to remove carrier polymer. The powders calcined at 500 °C were homogenised by using a mortar and a pestle and put in to the ceramic boat, which then was placed in a tubular oven and heated at 800 °C under 95 % Ar / 5 % H_2 atmosphere for 2 h with a heating rate of 5 °C/min. Afterwards, the oven was cooled down to room temperature.

Elaboration of hollow titania nanofibres via coaxial electrospinning

In order to obtain a hollow structure, 0.6 g of polyvinyl pyrrolidone (PVP with average Mw ~1,300,000 g/mol, Aldrich) was dissolved in 10 mL ethanol (Sigma-Aldrich), while 6.3 mL of Ti(O*i*Pr)$_4$ (97 %, Aldrich) and 0.6 mL of niobium ethoxide (10 at.% doping) were dissolved in 4 mL acetic acid. The two solutions were mixed together and stirred for at least 1 h and then put into the syringe. Another syringe was filled with mineral oil (WD-40 Company). Two syringes were connected with two pumps and two capillaries. The diameters of the coaxial needles were 0.8 and 1.83 mm. The flow rate was 0.3 mL/h for the mineral oil and 0.1 mL/h for the PVP solution. The applied voltage was 15 kV. The distance between the needle and aluminium collector was 10 cm. The as-spun fibres were immersed in n-hexane overnight in order to extract the oil phase and calcined at 500 °C for 6 h and then reduced under 95 % Ar / 5 % H_2 atmosphere at 800 °C for 2 h in 5 % H_2/Ar with a heating rate of 5 °C/min.

Elaboration of tin oxide nanofibres

In order to obtain Nb-SnO_2 hollow fibres, 0.78 g of tin (II) chloride (98 %, Sigma-Aldrich) was dissolved 5.7 mL of absolute ethanol (puriss., Sigma-Aldrich). For Nb doped materials niobium (V) chloride (98 % min., Merck, 0.5 – 10 at. %) was added to the solution. The obtained solution was mixed with 0.8 g of polyvinylpyrrolidone (average Mw ~ 1,300,000 g/mol, Aldrich) in 3.1 mL of N,N-dimethylformamide (98 % min., Fluka). For Sb doped materials antimony (III) chloride (99 % min., Sigma-Aldrich, 5 – 10 at. %) was added to the mixture. The obtained mixture was stirred at least for 1 h, in order to obtain homogeneous solution. This solution was electrospun at RT using an applied voltage of 15 kV, a needle-collector distance of 10 cm and a flow rate of 0.4 mL/h. The obtained materials were calcined at 600 °C for 4 h or 1 h in air with a heating rate of 5 °C/min.

2. Characterisation of the support

Electron microscopy

The morphology of the electrospun materials was analysed using a Hitachi S-4800 scanning electron microscope (SEM), a FEI Quanta FEG 200 equipped with energy-dispersive spectroscopy analysis (EDX) and a JEOL 1200 EXII transmission electron microscope (TEM) operating at 120 kV, equipped with a CCD camera SIS Olympus Quemesa (11 million pixels). For TEM analyses, the samples were suspended in ethanol and ultrasonicated before deposition onto carbon-coated copper grids. The diameters of the Pt nanoparticles and diameters of the fibres were determined by measuring at least 100 selected particles using an ImageJ software.

X-ray diffraction

Powder X-ray diffraction (XRD) patterns were recorded during ca 12 hours at room temperature in Bragg-Brentano configuration using a PANAlytical X'pert diffractometer, equipped with a hybrid monochromator, operating with CuKα radiation (λ = 1.541 Å).

Specific surface area determination

Nitrogen adsorption/desorption isotherms were determined by using Micromeritics ASAP 2020 apparatus after outgassing overnight at 200 °C. The specific surface area was calculated using the Brunauer-Emmett-Teller (BET) equation, taking 0.162 nm^2 as the cross-sectional area of one N_2 molecule.

Raman spectroscopy

Raman analysis was performed on a LabRAM Aramis IR2 (Horiba Jobin Yvon) equipped with a He/Ne laser (λ = 633 nm, 17 mW on titania and on tin oxide and 4 mW on carbon nanofibres) and a long work distance objective × 50.

X-ray photoelectron spectroscopy

The surface composition of the electrospun fibres was monitored by X-ray photoelectron spectroscopy (XPS) on an ESCALAB 250 (Thermo Electron). The X-ray excitation was provided by a monochromatic Al Kα (1486.6 eV) source and the analysed surface area was 400 μm^2. A constant analyser energy mode was used for the electron detection (20 eV pass energy). Detection of the emitted photoelectrons was performed perpendicularly to the sample surface. Data quantification was performed in the Avantage software, removing the background signal using the Shirley method. The surface atomic concentrations were

determined from photoelectron peaks areas using the atomic sensitivity factors reported by Scofield. Binding energies of all core levels are referred to the C-C bond of C 1s at 284.8 eV.

Electrical conductivity measurements

Pellets of 13 mm in diameter and of 250 - 600 μm thick (measured using a micrometer) were obtained by using a cylindrical die and then compressed using a manual hydraulic press during 5 or 10 minutes at 370 - 740 MPa. The thickness of the pellet was measured using a micrometer. The electrical conductivity of the obtained pellets was measured using Van der Pauw method with an in-house developed conductivity cell.

In the case of carbon-based materials 558 mg of 5 wt. % Nafion® dispersion (Aldrich) was added as a binder to 96 mg of carbon (CNFs or Vulcan XC-72R, Cabot). Nafion® ionomer was added in order to achieve a suitable cohesion of the pellet. The obtained mixture was oven dried at 70 °C overnight.

Electrochemical characterisation

The electrochemical analyses were carried out in a three-electrode cell equipped with a thermostat comprising a gold rotating disk electrode (RDE) with surface area of 0.03 cm^2 (working electrode), a saturated calomel electrode (SCE, reference electrode), a platinum wire (counter electrode), and a Bio-Logic SP-150 potentiostat.

In order to estimate stability of various supports, accelerated stress test was performed by holding the working electrode potential at 1.4 V vs RHE for 2 h in 0.5 M H_2SO_4 at 80 °C. An ink was first prepared by dispersing (ultrasonication, 30 min) 20 mg of the support material (CNF_{1000}, CNF_{1500}, TNFs, 5%at Nb−SnO_2 tubes or Vulcan XC-72, from Cabot) in 1 mL of ethanol (Aldrich) and 200 μL of 5 wt. % Nafion® dispersion in alcohol (Aldrich). A 3 μL portion of the ink was then deposited onto the RDE surface using a micropipette and dried in air.

3. Synthesis and deposition of Pt nanoparticles

Microwave-assisted polyol method

177 mg of hexachloroplatinic acid (H_2PtCl_6 $6H_2O$, 99.9 % Alfa Aesar) were dissolved in 80 ml of ethylene glycol (99.5 %, Fluka) and adjusted to a pH of 11.5 by addition of NaOH (98 %, Sigma Aldrich) dissolved in ethylene glycol. The resulting solution was heated at 110 °C for 6 minutes in microwave reactor (MiniFlow 220SS Sairem) to obtain Pt nanoparticles.

It is possible to control Pt nanoparticles size by changing concentration of the platinum salt or changing pH of the solution. When the concentration of hexachloroplatinic acid was increased up to 0.0068 mol/L, Pt particle diameter increased from 2.4 nm to 3 nm for 21 wt. % Pt/Nb-SnO_2 electrocatalyst.

Zeta potential measurements

In order to determine a suitable pH for the Pt adsorption on the surface of the supports, 0.5 mg of the support was dispersed in 40 ml of MilliQ-water and the resulting suspension was sonicated for at least 10 minutes and the zeta potential of the carbon supports and Pt particles was measured as a function of pH using a Malvern Zetasizer 3000 device.

Deposition of Pt on electrospun nanofibres

A suspension containing 100 mg of the support material (carbon, titania, tin oxide nanofibres or Vulcan XC-72R) in 5 ml ethylene glycol was sonicated for 10 min and added to the Pt nanoparticle solution, and the solution was adjusted to pH 2 (pH = 4 for Vulcan XC-72R) by the addition of 1M H_2SO_4 (aq solution, 95-98 %, Aldrich) solution in ethylene glycol and stirred for at least 24 h to allow the Pt adsorption onto the support. After 24 hours the product was recovered by centrifugation (4000 rpm, 20 min), washed with milli-Q water and ethanol on filter, and dried in an oven at 80 °C for 24 h in air.

Thermogravimetric analysis

Thermogravimetric analysis was performed in air up to 800 °C (10 °C/min) using a Netzsch TG 439 thermobalance to determine the Pt loading on CNF electrospun fibres and on commercial Vulcan XC-72R support.

In order to determine characteristic weight loss profiles of composite SnO_2/PVP electrospun fibres and polymer decomposition temperature, thermogravimetric analysis was performed in air up to 1000 °C at 10 °C/min.

X-ray fluorescence

Pt/oxide catalyst was analysed by X-ray fluorescence, in order to determine the Pt amount, which was adsorbed on the tin oxide or titania nanofibres after polyol synthesis. The samples were prepared by grinding 50 mg of Nb-SnO_2 with 25 mg of cellulose to facilitate the formatting of the pellet. The recovered powder was then placed in a cavity in the H_3BO_3 matrix subsequently pressed, in order to obtain a pellet of 32 mm diameter with scanned surface of ca. 12 mm. The same protocol was utilised to prepare four standard samples using 15, 20, 25 and 30 wt. % of Pt black (Alfa Aesar) and tin oxide hollow fibres or 5, 10, 15 and 20 wt. % of Pt black and titania nanofibres to obtain a calibration lines. Figure 1 shows the calibration curve that was used to estimate the amount of Pt adsorbed on the Nb doped SnO_2 support after polyol synthesis. The analyses were performed with a PANalytical Axios Max spectrometer fitted with a Rh (4kW) tube. Omnian software and LiF200 crystal have been used for the analysis.

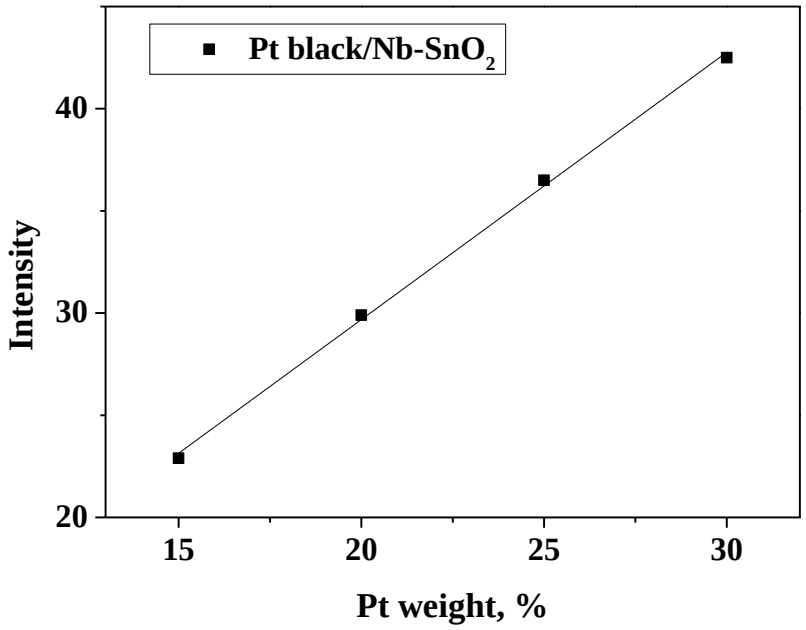

Figure 1: Calibration curve obtained after XRF analysis of standard samples.

Calculation to determine the amount of Pt added

Carbon blacks exhibit large specific surface area (~230 m^2/g for Vulcan XC-72R). However, significant part of this area is not accessible for Pt (usual size of 3-5 nm) or Nafion® ionomer, due to high microporosity of carbon blacks (pores < 2 nm). Therefore, only the external surface area (~100 m^2/g) of the carbon was accounted for in our calculations, following the methodology of Chhina et al. [1],[2].

Average Pt crystallite size for 50 wt. % PT/C (XRD) = 3 nm

Assuming spherical particles:

Volume of one Pt particle = $4/3\pi\ r^3$ = *$1.13*10^{-25}\ m^3$*

Surface area of one Pt particle - $4\ \pi\ r^2$ = *$1.13*10^{-16}\ m^2$*

For 50 wt. % Pt/C there is 1 g Pt g^{-1} of C

Volume of Pt g^{-1} of C

= 1 g Pt g^{-1} of C/Pt density (ρPt = 21.45 g cm^{-3}) = volume of Pt g^{-1} of C

= *$4.66*10^{-8}\ m^3$ Pt g^{-1} of C*

No. of Pt crystallites g^{-1} of C

= Volume of Pt required g^{-1} of C/Volume of one Pt particle

= $4.66*10^{-8}$ m^3 Pt g^{-1} of C / $1.13*10^{-25}$

= *$4.12*10^{17}$ crystallite g^{-1} C*

No. of Pt crystallites m^{-2} of C

= $4.12*10^{17}$ crystallite g^{-1} C/C external SA (100 m^2/g)

= *$4.12*10^{15}$ Pt crystallites m^{-2} of C*

Pt surface area/support surface area

= Pt crystallites m^{-2} of C * surface area of a crystallite

= $4.12*10^{15}$ m^{-2} of C * $1.13*10^{-16}$ m^2

= *0.466 m^2 Pt m^{-2} C*

For TiO_2

No. of Pt crystallites g^{-1} of TiO_2

No. of Pt crystallite m^{-2} C * TiO_2 BET SA (16 m^2/g)

Want $4.12*10^{15}$ Pt crystallite m^{-2} of support * 16 m^2/g

= $6.6*10^{16}$ crystallites g^{-1} TiO_2

Volume of Pt g^{-1} of TiO_2 needed

= No of Pt crystallites g^{-1} of TiO_2 * Vol. of one Pt particle

= $6.6*10^{16}$ crystallites g^{-1} * $1.13*10^{-25}$ m^3

= $7.46*10^{-9}$ m^3 Pt g^{-1} of TiO_2 * 21.45 g cm^{-3} $(100)^3$

= 0.16 g of Pt g^{-1} of TiO_2

~13.8 wt. % Pt/TiO_2

For SnO_2

No. of Pt crystallites g^{-1} of SnO_2

No. of Pt crystallite m^{-2} C * SnO_2 BET SA (42 m^2/g)

Want $4.12*10^{15}$ Pt crystallite m^{-2} of support * 42 m^2/g

= $1.73*10^{17}$ crystallites g^{-1} SnO_2

Volume of Pt g^{-1} of SnO_2 needed

= No of Pt crystallites g^{-1} of SnO_2 * Vol. of one Pt particle

= $1.73*10^{17}$ crystallites g^{-1} * $1.13*10^{-25}$ m^3

= $1.95*10^{-8}$ m^3 Pt g^{-1} of SnO_2 * 21.45 g cm^{-3} $(100)^3$

= 0.42 g of Pt g^{-1} of SnO_2

~29.6 wt. % Pt/SnO_2

For Carbon nano-fibers (CNF)

No. of Pt crystallites g^{-1} of CNF

No. of Pt crystallite m^{-2} C * CNF BET SA (36 m^2/g)

Want $4.12*10^{15}$ Pt crystallites m^{-2} of support * 36 m^2/g

= $1.48*10^{17}$ crystallites g^{-1} CNF

Volume of Pt g^{-1} of CNF needed

= No of Pt crystallites g^{-1} of CNF * Vol. of one Pt particle

= $1.48*10^{17}$ crystallites g^{-1} * $1.13*10^{-25}$ m^3

= $1.67*10^{-8}$ m^3 Pt g^{-1} of CNF * 21.45 g cm^{-3} $(100)^3$

= 0.36 g of Pt g^{-1} of CNF

~26.5 wt. % Pt/CNF

4. *Ex situ* electrochemical characterisation of Pt supported on electrospun fibres

Cyclic voltammetry

Voltammograms were recorded using RDE glassy carbon electrode with surface area of 0.196 cm^2. Catalyst inks were prepared via the following procedure: 5 mg of the support material (Pt/CNFs, Pt/C, Pt/Vulcan XC-72R, Pt/TNFs or Pt/Nb-SnO_2) were dispersed in 0.20-0.35 mL of absolute ethanol (Aldrich), 10-25 μL of water and 10-25 μL of 5 %wt Nafion® dispersion (Aldrich) by ultrasonication for at least 30 minutes. 5 or 10 μL of these inks were then deposited onto the RDE surface with a micropipette and dried in air. The Pt loading was 86 $\mu g/cm^2$ for Pt/TNFs, 115 $\mu g/cm^2$ for Pt/CNFs, 122 $\mu g/cm^2$ for Pt/Nb-SnO_2, 121 $\mu g/cm^2$ for Pt/Vulcan XC-72R and 121 $\mu g/cm^2$ for commercial Pt/C to fully cover the glassy carbon RDE.

Cyclic voltammograms were carried out between 0.05 and 1.2 V vs RHE at a scan rate of 50 mV/s. The ECSA was evaluated from the hydrogen desorption peaks (between 0.05 0.4 V vs RHE), assuming a hydrogen desorption charge of 210 $\mu C/cm^2$ for the electroactive Pt surface. Each electrode was cycled at least 10 times in N_2-saturated 0.1 M $HClO_4$ in order to clean the Pt surface.

ORR activity measurements

The ORR polarisation curves were performed using linear sweep voltammetry at rotation rate varying from 400 to 2500 rpm in an O_2 saturated 0.1 M $HClO_4$. The potential was swept in the potential range from 1.0 V to 0.2 V vs RHE at a scan rate of 5 mV/s. The polarisation curves were obtained after subtracting the curve obtained in N_2 atmosphere from the curve obtained in an O_2 saturated electrolyte. All the potential values are referred to the reversible hydrogen electrode (RHE) and the current densities are reported as current per geometric electrode area. The pH = 1 for 0.1 M $HClO_4$ solution.

Stability test

For durability test the same cycles were performed 1000 times. In order to evaluate the stability of the electrocatalyst support, the variation of the ECSA was evaluated before and after these prolonged cycles. Its calculation was based on hydrogen desorption peaks in the range of 0.05 V to 0.4 V vs RHE, assuming a hydrogen desorption charge of 210 $\mu C\ cm^{-2}$ for the electroactive Pt surface.

In order to compare the stability of the different carbon-based supports, 1000 or 2000 cycles were performed between 0.05 and 1.2 V vs RHE at a scan rate of 50 mV/s in 0.1 M $HClO_4$. Nitrogen was bubbled into the solution during the stability test in order to remove any dissolved O_2. The ECSA was evaluated before and after the stability test as described previously.

TEM characterisation

In order to prepare a hard resin, 4.8 g of LV resin was mixed with 5.2 g hardener and 0.25 mL of accelerator (Agar Scientific, R1078). The mixture was sonicated for 60 min and stored in the freezer. The MEAs before and after 1000 cycles were immersed in the obtained resin for 24 h at 80 °C in a plastic form and then cut with diamond knife. The obtained layers were then deposited onto a copper grid.

5. *In situ characterisation of oxide based MEA*

Pre-treatment procedure

The Nafion® 212 membrane with 50 µm thickness was treated using following procedure: Nafion® 212 membranes were immersed in a 3 % v/v H_2O_2 solution (30 wt. %, Carlo Erba Reagents), which was then stirred for 1 h at 100 °C. After washing with water, the membranes were immersed in a 50 % w/w solution of HNO_3 (65 wt. %, Sigma Aldrich), which was then stirred for 30 min at room temperature. Finally, the membranes were washed, immersed in a 1 M solution of H_2SO_4 (95 wt. %, Sigma Aldrich) for 1 h at 100 °C. After such treatments, the membranes were washed last time and stored in the plastic bags.

Preparation and characterisation of Pt/Nb-SnO_2 and Pt/Sb-SnO_2 based MEA with Nafion® membrane

The cathodes loaded with 0.5 mg/cm^2 of Pt and 0.5 mg/cm^2 of Nafion® binder were prepared using the following procedure: a mixture of 9.5 mg of 21 wt. % Pt/Nb-SnO_2 or 6 mg of 33 wt. % Pt/Sb-SnO_2 or 4 mg of 50 wt. % Pt/C catalyst or 10 mg of 20 wt. % Pt/Nb-SnO_2 with 0.53 mg of Vulcan XC-72R, 46 µL of a 5 wt. % Nafion® solution (Sigma-Aldrich), 200 µL of Milli-Q water and 1 mL of ethanol was sonicated for at least 30 min and sprayed-coated on a GDL (4 cm^2, Sigracet 10 BC).

The GDE for anode side loaded with 0.4 mg/cm^2 of Pt used in this work was provided by Johnson Matthey for Maestro Project.

The MEA was assembled by pressing the electrodes and membrane at 140 °C for 2 min at 1 ton. The MEA was then incorporated in the fuel cell setup using fluorinated ethylene propylene (FEP) gaskets at 10 - 15 % compression, which prevent leakage of the reactants. The MEA break-in step was performed prior to the actual tests at 0.5 A/cm^2 overnight at 80 °C. H_2 and O_2 were bubbled through milli-Q water, which was heated at 80 °C. The humidity of the reactant gases was maintained at 100 % RH for both cathode and anode sides for all MEAs, except Pt/Nb-SnO_2-Vulcan-MEA. In the case of Pt/Nb-SnO_2-Vulcan-MEA, the RH on the cathode was 50 %, in order to avoid flooding, which may lead to the catalyst degradation. Polarisation curves and impedance measurements were carried out under H_2/O_2 (using a 1.5/2 stoichiometry) by setting the current density and measuring the cell potential. Tests were performed under the pressure of 1 bar (2 bar absolute pressure).

Accelerated stress test

The accelerated stress test consists of 1200 cycles at 80 °C in H_2 and O_2 for the anode and cathode. During each cycle potential of 0.9 V for 3 sec and of 1.4 V for 3 sec was applied on the cathode side (working electrode) in order to simulate the start-up and shutdown of the fuel cell. Kakinuma et al. [3] used similar test protocol for evaluation of the Pt/Sb-SnO_2 stability, according to which the potential was stepped between 0.9 V and 1.3 V with a holding period of 30 s at each potential. This test was proposed by Fuel Cell Commercialization Council of Japan.

Impedance spectroscopy

The impedance spectra were carried out with frequency in the range from 20 kHz to 100 mHz at 0.1, 0.3 and 0.5 A/cm² and with a sinusoidal amplitude of 10 % of applied current density. The two electrode configuration was used, where cathode was used as the working electrode, while anode was used as both reference and counter electrode.

Preparation and characterisation of Pt/Nb-SnO_2 based MEA with PBI membrane

PBI membrane was prepared by Aurélien Kreisz (ICGM Montpellier) with thickness of ca 40 µm, proton conductivity ~ 160 S/cm at 140 °C and acid doping level (ADL) of 25.

The cathodes loaded with 0.8 mg/cm^2 of Pt and 0.2 mg/cm^2 of Nafion® binder were prepared using the following procedure: a mixture containing 6.4 mg of 50 wt. % Pt/C or 16 mg of 20 wt. % Pt/Nb-SnO_2 was mixed with, 18 µL of a 5 %wt Nafion® solution (Sigma-Aldrich), 200 µL of water and 1 mL of ethanol, then it was sonicated for at least 30 min and sprayed-coated on a GDL (4 cm^2, Sigracet 10 BC).

GDEs with Pt loading of 0.8 mg/cm^2 provided by Johnson Matthey were used as anode. This GDE was assembled with PBI/H_3PO_4 membrane and cathode without pressing. The obtained MEA were tested in a single HT-PEMFC under atmosphere pressure with pure H_2 and O_2 gases.

Porosity measurements of the cathode

The porosity of the electrodes was calculated using following equations:

$$\textit{Volume of an electrode} = \textit{surface area} * \textit{thickness}$$

$$\textit{Volume of electrode materials} = \textit{mass/density (Pt)} + \textit{mass/density (support)} + \textit{mass/density (Nafion®)}$$

$$\textit{Porosity} = 1 - \textit{Volume of an electrode} / \textit{Volume of electrode materials}$$

Thickness of Pt/Nb-SnO_2 and Pt/C based cathode was ~10 µm (Figure 2). The densities of carbon, Nafion®, Pt, and tin oxide are 2, 21.45, 1.8 and 6.95, respectively. The obtained porosities were ca 43 % for Pt/Nb-SnO_2 and 45 % for Pt/C based cathode.

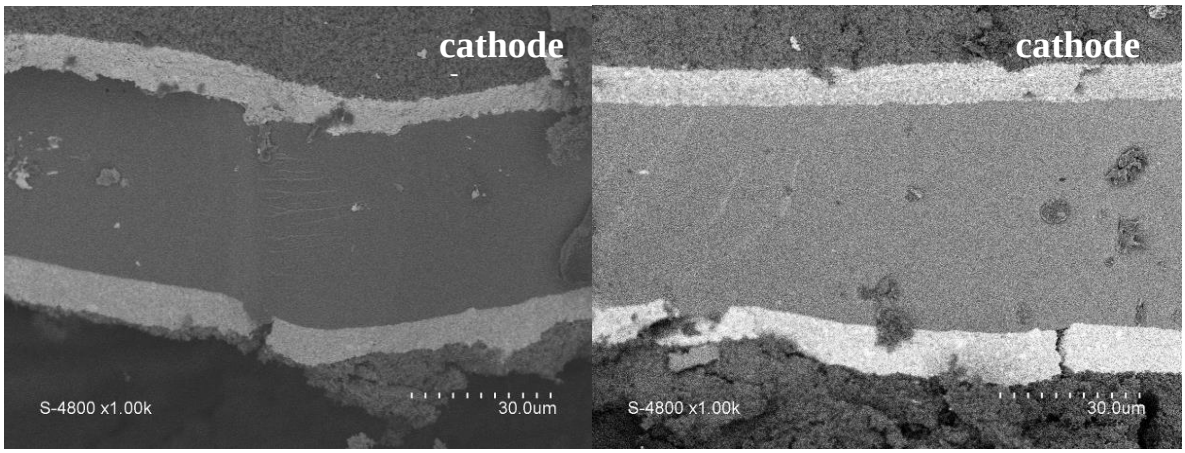

Figure 2: SEM cross-section images of the cathode based on Pt/Nb-SnO_2 (left) and Pt/C (right).

References:

[1] H. Chhina, "Oxidation-resistatnt catalyst supports for Proton exchnge membrane fuel cells," 2009.

[2] H. Chhina, S. Campbell, and O. Kesler, "Ex Situ and In Situ Stability of Platinum Supported on Niobium-Doped Titania for PEMFCs," *Journal of The Electrochemical Society*, vol. 156, no. 10, p. B1232, 2009.

[3] K. Kakinuma, M. Uchida, T. Kamino, H. Uchida, and M. Watanabe, "Synthesis and electrochemical characterization of Pt catalyst supported on $Sn_{0.96}Sb_{0.04}O_{2-\delta}$ with a network structure," *Electrochimica Acta*, vol. 56, no. 7, pp. 2881–2887, Feb. 2011.

Résumé

Cette thèse s'inscrit dans le contexte général des efforts de recherche pour développer des supports de catalyseur résistant à la corrosion qui peuvent potentiellement remplacer le carbone dans les piles à combustible à électrolyte polymère. Des nanofibres et des nanotubes à base de TiO_2 et SnO_2 dopés par Nb ont été préparés par filage électrostatique et caractérisés par diffraction des rayons X, spectroscopie des photoélectrons de rayons X, spectroscopie Raman, mesures de surface spécifique et de conductivité électronique. Les nanofibres de TiO_2 et SnO_2 dopées par Nb présentent une conductivité et une surface spécifique supérieure à celle des oxydes non dopés. Des nanoparticules de platine ont été préparées en utilisant une méthode polyol modifié par micro-ondes, et déposées sur les supports fibreux. La caractérisation électrochimique des électrocatalyseurs ainsi obtenus a été réalisée *ex situ* par voltampérométrie en utilisant une électrode à disque tournant. Le catalyseur supporté, Pt sur SnO_2 dopé par Nb a présenté une stabilité électrochimique supérieure à celle d'un catalyseur Pt sur carbone commercial (Vulcan XC-72R). Une cathode Pt/Nb-SnO_2 préparée par pulvérisation a pu être intégrée dans un assemblage membrane-électrode (AME) et caractérisée *in situ* dans une cellule de pile à combustible à électrolyte polymère. L'AME a présenté une durée de vie plus élevée mais une densité de puissance plus faible qu'un AME contenant Pt/C. Les nanotubes de SnO_2 dopés par Sb ont une conductivité plus élevée que celle des matériaux dopés par Nb et lorsqu'ils sont intégrés dans une cathode, fournissent une densité de puissance accrue par rapport à une cathode à base de Nb-SnO_2.

Mots clés: oxyde de titane / oxyde d'étain / nanofibres / filage électrostatique / support de électrocatalyseur / piles à combustible à électrolyte polymère.

Abstract

The objective of this thesis is to develop corrosion resistant catalyst support materials that can potentially replace carbon in Polymer electrolyte fuel cells. Therefore, Nb doped TiO_2 and SnO_2 nanofibres and nanotubes were prepared by electrospinning and characterised by X-ray diffraction, X-ray photoelectron spectroscopy, Raman spectroscopy, N_2 adsorption/desorption analysis and electronic conductivity measurements. The obtained Nb doped TiO_2 and SnO_2 one dimensional structures demonstrated higher conductivity and surface area than non-doped oxides. Pt nanoparticles were prepared using a modified microwave-assisted polyol method and deposited on the electrospun supports. Electrochemical characterisation of the obtained electrocatalysts was performed *ex situ* using a rotating disc electrode, and compared with a commercial carbon support (Vulcan XC-72R). Pt supported on Nb doped SnO_2 provided higher electrochemical stability in comparison to Pt on carbon. Thus, a cathode of Pt/Nb-SnO_2 prepared by spray-coating was integrated into Membrane Electrode Assembly (MEA) and characterised *in situ* in a single polymer electrolyte fuel cell. The MEA exhibited higher durability though lower power density compared to MEA with Pt/C based cathode. Sb doped SnO_2 nanotubes have higher conductivity than Nb doped material and when integrated into a cathode, provided enhanced power density in comparison to Nb-SnO_2 based cathode.

Keywords: titanium oxide / tin oxide / nanofibres / electrospinning / electrocatalyst supports / polymer electrolyte fuel cells.